

Beam-Induced Backgrounds in Detectors at the ILC

Dissertation zur Erlangung des Doktorgrades
des Departments Physik der Universität Hamburg

vorgelegt von Adrian Vogel
aus Dernbach im Westerwaldkreis

Hamburg
2008

Gutachter der Dissertation:	Prof. Dr. Joachim Mnich Prof. Dr. Peter Schleper
Gutachter der Disputation:	Prof. Dr. Joachim Mnich Prof. Dr. Eckhard Elsen
Datum der Disputation:	19. August 2008
Vorsitzender des Prüfungsausschusses: Vorsitzender des Promotionsausschusses:	PD Dr. Michael Martins Prof. Dr. Joachim Bartels
Leiter des Departments Physik: Dekan der MIN-Fakultät:	Prof. Dr. Robert Klanner Prof. Dr. Arno Frühwald

Abstract

There is general consensus in the high-energy physics community that the next particle collider to be built should be a linear electron-positron accelerator. Such a machine, colliding point-like particles with a well-defined initial state, would be an ideal complement to the Large Hadron Collider (LHC) and would allow high-precision measurements of the new physics phenomena that are likely to be discovered at the TeV energy scale (section 1). The most advanced project in that context is the International Linear Collider (ILC), aiming for a centre-of-mass energy of 500 GeV and a luminosity of $2 \cdot 10^{34} \text{ cm}^{-2}\text{s}^{-1}$ in its first stage (section 2).

In order to perform the intended measurements of the Higgs boson, supersymmetric particles, and other kinds of new physics that might be realised in nature, the ILC will need detectors of unprecedented performance in different aspects: secondary vertex reconstruction, momentum resolution, and jet energy resolution (section 4). One of the detector concepts that are currently being developed and studied is the so-called International Large Detector (ILD). A prime feature of the ILD concept is the usage of a Time Projection Chamber (TPC) as the main tracker, which allows to reach the required momentum resolution, but which also has excellent particle identification capabilities and a highly robust and efficient tracking (section 5).

As an electron-positron collider, the ILC will provide a very clean experimental environment. Background rates will be orders of magnitude lower than at hadron colliders, but nevertheless significantly higher than at previous lepton colliders: the beam-beam interaction of the strongly focused particle bunches at the ILC will produce beamstrahlung photons, which can in turn scatter to electron-positron pairs (section 3). These pairs are a major source of detector backgrounds, either because they hit the inner detector components directly or because they induce showers in the forward calorimeters from which secondaries can be backscattered.

This thesis explains the methods to study the effects of beam-induced electron-positron pair backgrounds with Mokka, a full detector simulation for the ILC that is based on Geant4 (section 6), and it presents the simulation results for different detector configurations and various small modifications (section 7). The main focus of the simulations and their analysis is on the vertex detector and the TPC, but results for the inner silicon trackers and the hadronic calorimeters are shown as well.

Using the nominal ILC beam parameters and a detector geometry with a crossing angle of 14 mrad and a specific configuration of the magnetic field, the simulations show that pair backgrounds will not be a severe problem for the detector: an amount of 400 hits per bunch crossing on the innermost

layer of the vertex detector (or $0.04 \text{ hits/mm}^2/\text{BX}$) is well within tolerable limits, and a TPC occupancy of less than 0.1 % should not affect the tracking capabilities. The neutron fluence in the vertex detector and in large parts of the HCAL is uncritical – only the innermost regions of the HCAL endcaps may suffer from radiation damage after several years of running. Concerning the gas in the TPC, a mixture containing hydrogen seems acceptable because neutron-proton scattering – producing short recoil tracks in the chamber – yields only a small contribution to the total beam-induced backgrounds in the TPC.

The thesis closes with a short summary (section 8), an outlook towards currently ongoing and planned studies (section 9), and a description of several technical details concerning the applied software tools (appendix).

PACS: 29.20.Ej, 29.40.Gx, 41.60.-m

Kurzfassung

In der Gemeinschaft der Hochenergiephysik herrscht Einigkeit darüber, dass als nächster Teilchenbeschleuniger ein Elektron-Positron-Collider gebaut werden sollte. Eine solche Maschine, die punktförmige Teilchen mit einem wohldefinierten Ausgangszustand zur Kollision bringt, wäre eine ideale Ergänzung zum Large Hadron Collider (LHC) und würde Präzisionsmessungen der neuen physikalischen Phänomene ermöglichen, die wahrscheinlich auf der TeV-Energieskala entdeckt werden (Abschnitt 1). Das in diesem Zusammenhang am weitesten fortgeschrittene Projekt ist der International Linear Collider (ILC), der in einer ersten Ausbaustufe eine Schwerpunktsenergie von 500 GeV und eine Luminosität von $2 \cdot 10^{34} \text{ cm}^{-2} \text{ s}^{-1}$ anstrebt (Abschnitt 2).

Um die vorgesehenen Messungen des Higgs-Bosons, supersymmetrischer Teilchen und anderer möglicher Arten von Neuer Physik durchführen zu können, braucht der ILC Detektoren von bisher unerreichter Leistungsfähigkeit, wobei verschiedene Gesichtspunkte wichtig sind: die Rekonstruktion sekundärer Vertizes, die Impulsauflösung und die Jetenergieauflösung (Abschnitt 4). Eines der Detektorkonzepte, die zurzeit entwickelt und untersucht werden, ist der sogenannte International Large Detector (ILD). Ein Hauptmerkmal des ILD-Konzepts ist die Verwendung einer Zeitprojektionskammer (TPC) als zentrale Spurkammer, die zum einen die notwendige Impulsauflösung erreichen kann, die zum anderen aber auch hervorragende Möglichkeiten zur Teilchenidentifizierung und zum hocheffizienten und robusten Tracking bietet (Abschnitt 5).

Als Elektron-Positron-Collider wird der ILC eine sehr saubere Experimentierumgebung bieten. Die Untergrundraten werden um viele Größenordnungen geringer als bei einem Hadroncollider sein, aber dennoch deutlich höher als bei früheren Leptoncollidern: Die Strahl-Strahl-Wechselwirkung der stark fokussierten Teilchenstrahlen produziert Beamstrahlungsphotonen, die dann miteinander streuen und Elektron-Positron-Paare erzeugen können (Abschnitt 3). Diese Paare sind eine Hauptquelle von Untergrund im Detektor, entweder indem sie die inneren Teile des Detektors auf direktem Wege treffen oder indem sie in den Vorwärtskalorimetern Teilchenschauer auslösen, aus denen Sekundärteilchen zurückgestreut werden können.

Diese Arbeit erläutert die Methoden, mit denen die Auswirkungen des strahlinduzierten Untergrunds aus Elektron-Positron-Paaren mit Mokka, einer Geant4-basierten vollen Detektorsimulation für den ILC (Abschnitt 6), untersucht werden können, und sie stellt die Simulationsergebnisse für unterschiedliche Detektorkonfigurationen und verschiedene kleine Abwandlungen dar (Abschnitt 7). Das Hauptaugenmerk der Simulationen und ihrer Auswertung liegt dabei auf dem Vertexdetektor und auf der TPC, daneben werden

aber auch Ergebnisse für die inneren Siliziumspurdetektoren und für das hadronische Kalorimeter gezeigt.

Für die nominellen ILC-Strahlparameter und eine Detektorgeometrie mit einem Kreuzungswinkel von 14 mrad und einer speziellen Magnetfeldkonfiguration zeigen die Simulationen, dass der Paaruntergrund kein schwerwiegendes Problem für den Detektor darstellen wird: Die Anzahl von 400 Treffern pro Strahlkreuzung auf der innersten Lage des Vertexdetektors (oder 0,04 Treffer/mm²/BX) liegt innerhalb der zulässigen Grenzen, und die TPC-Belegungswahrscheinlichkeit von weniger als 0,1 % sollte das Tracking nicht beeinträchtigen. Der Neutronenfluss ist im Vertexdetektor und in großen Teilen des hadronischen Kalorimeters unkritisch – lediglich der innerste Teil der HCAL-Endkappen könnte nach einigen Jahren Laufzeit Strahlenschäden erleiden. Im Hinblick auf das TPC-Gas erscheint eine Gasmischung mit einem Wasserstoffanteil akzeptabel, da die Neutron-Proton-Streuung, durch die kurze Rückstoßspuren in der Kammer erzeugt werden, nur einen kleinen Beitrag zum gesamten strahlinduzierten Untergrund in der TPC liefert.

Die Arbeit schließt mit einer kurzen Zusammenfassung (Abschnitt 8), einem Ausblick auf derzeit laufende und geplante Studien (Abschnitt 9) und der Beschreibung einiger technischer Details im Bezug auf die verwendete Software (Anhang).

PACS: 29.20.Ej, 29.40.Gx, 41.60.-m

Contents

Abstract	3
Kurzfassung	5
1 Introduction	11
1.1 The Standard Model of Particle Physics	11
1.2 Problems with the Standard Model	13
1.3 Extensions of the Standard Model	14
2 Particle Accelerators	16
2.1 Hadron vs. Lepton Colliders	16
2.2 Circular vs. Linear Accelerators	21
2.3 The International Linear Collider	22
2.4 ILC Beam Parameters	26
2.5 Other Projects	28
3 Detector Backgrounds	30
3.1 Beam-Beam Interaction and Beamstrahlung	30
3.2 Electron-Positron Pairs	32
3.3 Pairs in the Detector	34
3.4 Minijets	35
3.5 Other Sources	36
4 The Large Detector Concept	39
4.1 Performance Requirements	40
4.2 Particle Flow	41
4.3 Detector Layout	42
4.4 Magnetic Field Configuration	45
5 The Time Projection Chamber	47
5.1 Basic Concept	47
5.2 Ionisation and Drift	49
5.2.1 Interaction of Particles with Gas	49
5.2.2 Electric and Magnetic Fields	50
5.2.3 The Chamber Gas	51
5.3 Signal Amplification and Gating	53
5.3.1 Proportional Wires	53
5.3.2 Gas Electron Multipliers	54
5.3.3 Micromegas	56
5.3.4 Ion Backdrift and its Suppression	56

5.4	Pile-up and Readout	59
5.4.1	Anode Pads and Voxels	59
5.4.2	Overlay of Events	60
5.4.3	Timing and Event Decomposition	61
5.4.4	Track Reconstruction and Charge Sharing	62
5.5	Performance and Advantages	63
6	Simulation Tools	65
6.1	Guinea-Pig – Pairs Generator	65
6.2	Mokka – Full Detector Simulation	66
6.2.1	The Geant4 Framework	67
6.2.2	Detector Geometry in Mokka	67
6.2.3	Physics Models in Mokka	69
6.2.4	Primary Generator Particles in Mokka	72
6.2.5	Output of Simulation Results	73
6.3	Marlin – Analysis Framework	73
6.3.1	LCIO – Persistency Toolkit	74
6.3.2	Analysis of Background Simulations	75
6.3.3	Analysis for the TPC	75
6.3.4	MarlinTPC – Full Software Chain	77
6.4	Grid Computing – Mass Production	77
6.4.1	Computing in High-Energy Physics	77
6.4.2	The LHC Computing Grid	78
6.4.3	Profit and Experiences	79
7	Simulation Results	80
7.1	Remark on Statistics	80
7.2	Vertex Detector	81
7.2.1	Hits on the VTX	82
7.2.2	Particles Passing Through the VTX	88
7.3	Other Silicon Trackers	94
7.3.1	Silicon Intermediate Tracker	94
7.3.2	Forward Tracking Discs	95
7.4	Time Projection Chamber	98
7.4.1	Particles in the TPC	98
7.4.2	Hits in the TPC	103
7.4.3	Occupancy of the TPC	107
7.5	Electromagnetic Calorimeter	113
7.6	Hadronic Calorimeter	113
7.6.1	Neutrons in the Endcap	114
7.6.2	Photons in the Endcap	115

7.7	Design Options	115
7.7.1	Forward Region Layout	115
7.7.2	Crossing Angles	117
7.7.3	Beam Parameters	123
7.7.4	LumiCal Inner Radius	124
7.7.5	BeamCal Absorber	125
7.7.6	Support Tube	128
7.8	Comparative Studies	129
7.8.1	Nuclear Cascade Models	129
7.8.2	Methane Content of the TPC Gas	131
7.9	Uncertainty Estimation	131
7.9.1	Statistics	132
7.9.2	Generator Level	132
7.9.3	Modelling of Physics Processes	133
7.9.4	Geometry Variations	134
7.9.5	Other Sources	134
7.9.6	Safety Margins	135
7.10	Relation to Other Studies	135
8	Summary	137
9	Outlook	139
9.1	Ion Backdrift in the TPC	139
9.2	Event Reconstruction and Analysis	141
9.3	Further Simulations of Backgrounds	141
A	Guinea-Pig Parameter Settings	143
B	Mokka Technicalities	145
B.1	The Detector Geometry	145
B.1.1	Beam Tube	146
B.1.2	Vertex Detector	147
B.1.3	Silicon Intermediate Tracker	148
B.1.4	Forward Tracking Discs	148
B.1.5	Forward Mask	149
B.1.6	Time Projection Chamber	149
B.1.7	Endcap Tracking Discs	153
B.1.8	Silicon Envelope Tracker	153
B.1.9	Electromagnetic Calorimeter	153
B.1.10	Hadronic Calorimeter	154
B.1.11	Magnet Coil	154

B.1.12 Magnet Yoke	154
B.1.13 Magnetic Field	155
B.2 The Physics List QGSP_BERT_HP	156
B.2.1 Particles	156
B.2.2 Particle Decay	156
B.2.3 Standard Electromagnetic Physics	156
B.2.4 Extra Electromagnetic Physics	157
B.2.5 Elastic Hadron Physics	158
B.2.6 Inelastic Hadron Physics	158
B.2.7 Stopping Physics	159
B.2.8 Ion Physics	159
B.2.9 User Special Cuts	159
C Geometry Drivers for Mokka	160
C.1 The Beam Tube Driver	160
C.2 The Mask Driver	163
C.3 The Magnetic Field Driver	164
C.4 Geometry Parameter References	167
C.5 Error Checking	168
D Geometry Values	169
E Lorentz Boost for Crossing Angles	171
E.1 Purpose	171
E.2 Calculation	171
E.3 Implementation	173
List of Figures	175
List of Tables	178
Bibliography	179
Acknowledgements	197

1 Introduction

1.1 The Standard Model of Particle Physics

Today's Standard Model of particle physics provides a consistent and well-confirmed description of the fundamental particles and the forces that act between them. It contains twelve matter particles (figure 1.1), which can be arranged into two groups (six leptons and six quarks) of three generations (light, medium, heavy) each. The corresponding particles of the three generations differ substantially in their masses, but are identical with regard to most of their other properties. The leptons and quarks of one generation differ in their masses and their quantum numbers. The quarks come in three different colour states, and all particles (except possibly the neutrinos) have their respective antiparticles with identical masses and inverted quantum numbers. All matter particles are fermions with a spin of one half.

The forces of the Standard Model are described by means of mediating particles that act as force carriers (figure 1.2). They couple to the matter particles and in some cases also to each other (figure 1.3). The photon, γ , is the mediator of the electromagnetic force. It couples to all particles with electric charge, i.e. to all matter particles except the neutrinos and also to the W boson. The charged W boson and the neutral Z boson are the carriers of the weak force, coupling to all matter particles and to each other. The gluon, g, is the mediator of the strong force. It couples to all matter particles with colour charge, i.e. to the quarks. Gluons are electrically neutral, but

Leptons	$\dot{\nu}_e$ ○ e	$\dot{\nu}_\mu$ ○ μ	$\dot{\nu}_\tau$ ● τ	$Q = 0$ $Q = -1$
Quarks	○ u	● c	● t	$Q = +2/3$
	○ d	○ s	● b	$Q = -1/3$

Figure 1.1: Fermions in the Standard Model. The circle sizes reflect the approximate mass hierarchy, but they are not to scale. Masses and further properties can be found in [1]. Today, neutrinos are known to have non-zero mass, but the absolute mass scale of their eigenstates has not been measured yet.

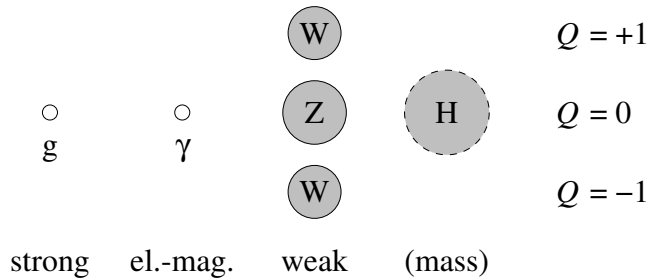


Figure 1.2: Bosons in the Standard Model. The gluon (g) and the photon (γ) are massless, whereas the W and the Z bosons acquire their large masses of 80.4 and 91.2 GeV through interaction with the (yet undiscovered) Higgs boson. The gluon is electrically neutral, but it carries colour charge.

they come in eight different colour states, which means that they also couple to each other. All force mediators are vector bosons with a spin of one.

The mathematical formulation of the Standard Model is that of a relativistic quantum field theory where the forces and their mediators are derived from the principle of local gauge invariance. The underlying symmetry structure is $SU(3)_C \times SU(2)_L \times U(1)_Y$, where $SU(3)_C$ is the symmetry group of QCD [2] with its three colours and $SU(2)_L \times U(1)_Y$ is the symmetry structure of the GSW theory [3], which combines the weak isospin of left-handed fermions and the weak hypercharge. Thereby the GSW – or “electroweak” – theory provides a common description for the electromagnetic and the weak force.

Using only these ingredients, the Standard Model has some fundamental problems: for example, the masses of the W and Z bosons cannot be taken into account without breaking the principle of gauge invariance, and certain scattering cross-sections (such as the scattering of longitudinally polarised W bosons) would violate the unitarity bound at energies around 1 TeV. To solve these issues, the Standard Model postulates an additional scalar particle, the so-called Higgs boson [4]. This particle has not been observed yet (the current lower mass limit from direct searches is $m_H > 114.4$ GeV [5]), but electroweak precision measurements that are sensitive to quantum loop corrections indicate that the Higgs boson should not be heavier than 150–200 GeV [6]. Other, rather general theoretical considerations suggest similar values for the Higgs mass [7]. This makes the Higgs boson one of the prime targets of current and future high-energy colliders.

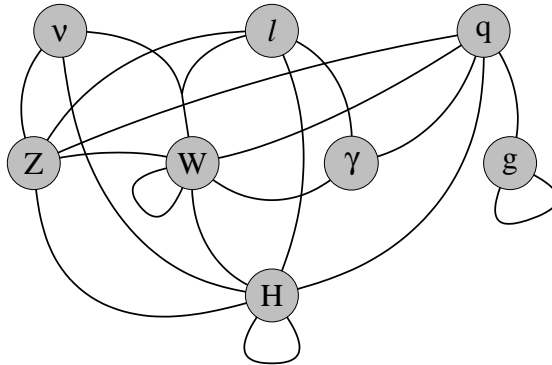


Figure 1.3: Interactions in the Standard Model, represented by possible couplings between the particles (adapted from [8]). The loops indicate self-couplings.

1.2 Problems with the Standard Model

The Standard Model has been tremendously successful (cf. e.g. [9]): there is not a single measurement made at high-energy physics experiments that would provide evidence for physics beyond the Standard Model. Many precision observables have been determined consistently in a variety of independent ways, and all particles that were predicted by the Standard Model (except the Higgs boson) have actually been found. Nevertheless, there are strong hints that the Standard Model cannot be the last word in the theory of fundamental particles.

Compelling evidence for new physics comes from rather recent observations in astroparticle physics and cosmology [10]: several independent measurements show that only around 5% of the energy density of the universe are due to matter as we know it, i. e. hydrogen gas, heavier elements, photons, and neutrinos. Around 25%, i. e. five times as much, must be caused by an unknown form of matter that is not described by the Standard Model: the so-called Dark Matter is subject to gravitation and influences the structures of galaxies and clusters, but it interacts neither strongly nor electromagnetically and is therefore invisible. The rest, i. e. 70% of the energy density of the universe, is of completely unknown origin. This phenomenon, which is responsible for the accelerated expansion of the universe, has been named Dark Energy, but until now it resists a manifest theoretical explanation – let alone one that could be verified by further experiments.

Another hint towards new physics comes from theory: the mass of the Higgs boson is very susceptible to self-energy quantum loop corrections. As a result, the loop contributions can be many orders of magnitude larger than

the Higgs mass itself, which should be of the order of 100 GeV and in no case larger than 1 TeV [11]. To keep the Higgs mass stable, it needs to be renormalised very precisely to cancel the large virtual contributions. This so-called fine-tuning problem is not a fundamental show-stopper of the Higgs theory, but it is aesthetically unpleasant and indicates that there should be some other, intrinsic mechanism to dispose of the loop corrections to the Higgs mass.

Gravity is the theory of space-time – it determines the structure of the universe and it is immediately perceivable in everyday life. On the one hand, gravity is extremely weak compared to the other forces, such that it is completely negligible for particle physics experiments. On the other hand, a comprehensive theory of fundamental particles and interactions must include all known forces if it is to remain valid up to very high energy scales. Furthermore, an explanation why gravity at low energies appears so much weaker than the other forces would be desirable.

Finally, it must not be forgotten that the Higgs boson has not been discovered yet. Even though many arguments indicate that the Higgs is not far away from the energy reach of past and present colliders, it cannot be taken for granted that it will really be discovered as predicted. If no Higgs boson is found in future experiments, or if a particle is found that has properties significantly different to those predicted by the Standard Model, the whole theory will need a thorough revision.

1.3 Extensions of the Standard Model

Over the years, theorists have developed a plethora of possible extensions and modifications of the Standard Model, each of which has its strengths and weaknesses. Presumably the most popular model is Supersymmetry (SUSY) [12], which postulates an additional fundamental symmetry between fermions and bosons, thereby introducing a bosonic partner to every fermion and vice versa. Perfect supersymmetry does obviously not exist in nature because no such superpartners have been found yet, but it could be that the symmetry is broken and the supersymmetric particles have higher masses than “ordinary” particles. However, theoretical arguments postulate that the supersymmetric energy scale should not be too high – at least some supersymmetric particles are expected to be lighter than 1 TeV.

Supersymmetry has some attractive features that could solve several problems of the Standard Model in a rather simple and elegant way: under the assumption that supersymmetric particles will always be produced in pairs, i. e. the so-called R -parity is conserved, the lightest supersymmetric particle would be an excellent candidate for Dark Matter [13]. Furthermore,

loop contributions from fermionic and bosonic superpartners would automatically cancel (as long as their mass difference is not too large), meaning that the fine-tuning problem disappears or is at least greatly reduced. A drawback, however, is that the most general form of supersymmetry will introduce a large number of free parameters, which would need to be measured and possibly linked to each other by further additions to the theory. Therefore, most of the current studies are focusing on the so-called Minimal Supersymmetric Extension of the Standard Model (MSSM) and further restrictions such as Minimal Supergravity (mSUGRA) [14] that are easier to handle.

Another idea is the existence of extra dimensions alongside the well-known three-plus-one dimensions of space-time [15, 16]. Gravitons, the hypothetical mediators of gravity, could move freely in all existing dimensions, whereas the other particles and forces would be confined to the ordinary subset of four dimensions. This could explain why gravity seems to be so weak, and it might also lead the way towards a grand unification of all forces. It should be noted that most of the more advanced extensions of (or alternatives to) the Standard Model, such as string theory, involve extra dimensions in one way or the other.

Many more models have been developed, including heavy partners of the weak gauge bosons (W' and Z' [17, 1]), new strong interactions at higher energy scales (e.g. technicolour [18]), or a connection of the lepton and quark sectors through new particles (leptoquarks [19]). It is the task of future experiments to determine which of these options are actually realised in nature and to measure the related parameters – e.g. particle masses and coupling strengths – in order to promote one of these theories to become the new, future standard model of particle physics.

2 Particle Accelerators

High energies are the key to particle physics: according to the de-Broglie equation $\lambda = h/p$, which relates wavelength λ and particle momentum p , high momenta are needed to resolve small structures, and according to the mass-energy equivalence $E = mc^2$, high energies are needed to produce heavy – and possibly unknown – particles. Therefore, many experiments use accelerators to bring particles to high energies and then let them interact with other particles. The most efficient experimental set-up is that of a particle collider, where two beams are shot towards each other such that they collide in a well-defined interaction point.

The most important characteristic values of a particle collider are its centre-of-mass energy \sqrt{s} and the luminosity

$$\mathcal{L} = \frac{n_b N^2 f_{\text{rep}}}{4\pi\sigma_x\sigma_y} H_D, \quad (1)$$

where n_b is the number of colliding particle bunches, N is the number of particles per bunch, f_{rep} is the repetition rate, σ_x and σ_y are the transverse bunch sizes (in the case of Gaussian beam profiles), and H_D is an enhancement factor that takes the mutual beam-beam interaction into account (section 3.1). For a process with a given cross-section σ , the luminosity \mathcal{L} immediately relates to the signal rate r :

$$r = \sigma \cdot \mathcal{L}$$

In order to observe a large number of events in a given amount of time, it is therefore desirable to have a collider with a luminosity that is as high as possible.

2.1 Hadron vs. Lepton Colliders

Several high-energy colliders have been successfully operated in the past – most recently LEP at CERN (1989–2000), HERA at DESY (1992–2007), and the Tevatron at Fermilab (since 1987). The next machine is the Large Hadron Collider (LHC) at CERN, which has been installed and commissioned in the LEP tunnel during the last years and which should start its operation in the second half of 2008. The LHC will accelerate two proton beams to an energy of 7 TeV each, resulting in a maximum centre-of-mass energy of 14 TeV [20]. Under nominal running conditions, it will be able to deliver a luminosity of $10^{34} \text{ cm}^{-2}\text{s}^{-1}$ to each of its two large multi-purpose detectors, ATLAS and CMS, and somewhat less to the two smaller, specialised detectors ALICE and LHCb.

The LHC will be the most powerful particle collider built up to now, delivering the highest energies ever achieved in a particle physics experiment. However, the fact that the LHC is a proton-proton – or rather a parton-parton – collider has several important consequences:

- Only a fraction of the centre-of-mass energy in the proton-proton system will actually be available for the hard interaction between two partons in each collision. This can be treated statistically by means of Parton Distribution Functions, but the initial state and the exact kinematics of an individual event are practically impossible to measure. Missing energy and similar discriminating event variables can only be evaluated in the transverse plane.
- The total cross-section for proton-proton scattering is very large, but completely dominated by QCD backgrounds [21]. Processes that the LHC is looking for, such as the production of top quark pairs or the Higgs boson, are eight to eleven orders of magnitude below the total proton-proton cross-section. On the one hand, the luminosity of the collider is large enough to still produce top quarks or Higgs bosons at sizable rates (around ten top pairs per second and several Higgs bosons per minute at the full design luminosity of $10^{34} \text{ cm}^{-2}\text{s}^{-1}$), but on the other hand, this also means that the LHC experiments will need powerful trigger systems to detect the interesting physics events among the huge amount of backgrounds.
- Directly related is the problem that many final states are practically inaccessible because they cannot be discriminated from background events and therefore cannot be triggered on. As a result, most of the relevant final states must contain one or more isolated high-energy leptons or photons – i. e. particles that usually do not appear in QCD processes – even though the corresponding branching fractions may be small or even tiny.

The most important example is the Higgs boson: a “light” Higgs with a mass around 120 GeV will dominantly decay into b quark pairs, but searching for events with this final state is futile in the LHC environment. The branching fraction into W pairs is very small for a light Higgs, and the decay into τ pairs is difficult to reconstruct, so the most promising decay mode is actually $H \rightarrow \gamma\gamma$, even though it is strongly suppressed by the fact that it can only happen on the one-loop level [22]. Likewise, the most important decay mode of a “heavy” Higgs boson around 200 GeV is the fully leptonic decay $H \rightarrow ZZ \rightarrow 4\mu$, even though hadronic or semileptonic modes have a much larger branching fraction.

- Finally, the large cross-section leads to a significant pile-up of events: every hard interaction will be accompanied by tracks from the proton remnants (so-called underlying events) and – running at the full design luminosity – also by 35 soft interactions (so-called minimum-bias events) that will happen in the same bunch crossing. This means that the LHC experiments will need a robust pattern recognition and event reconstruction in order to decompose the resulting disorder of particle tracks.

Still, the LHC collaborations are confident that they will be able to cope with these challenges, and various studies have shown that the LHC will very likely discover the Higgs boson if it exists. Likewise, the LHC should find at least some supersymmetric particles (typically the superpartners of quarks and gluons) in case supersymmetry is realised.

However, many other important measurements will be difficult to make at the LHC: in order to prove that the alleged Higgs boson really behaves as predicted by the electroweak theory, it will be necessary to determine its unique properties such as spin, coupling strengths to other massive particles, and the characteristic self-coupling. Strongly depending on the Higgs mass, some of these measurements are possible with more or less precision (mass, spin, parity). Other values (couplings) can only be measured making certain assumptions, and some properties (self-coupling) are most probably out of reach.

In order to perform these required measurements, a high-energy lepton collider in the TeV range would be the right tool. Lepton colliders in this energy regime have several important advantages compared to hadron machines:

- Because leptons are point-like, the full centre-of-mass energy is available in each collision. This also means that the initial state of the interaction is well-defined and that measured events can be fully reconstructed.
- The overall event rate is low, but the cross-sections of interesting physics processes are typically only one to two orders of magnitude lower than the total cross-section [23]. This means that trigger systems can be much less selective, and hence more sensitive to new and unexpected physics.
- The spin properties of the initial state can be defined if polarised beams are available. Since the electroweak interaction is spin-dependent, the sensitivity for particular processes can even be increased by selecting

the appropriate spin configuration of the initial state, thereby suppressing unwanted background processes or observing spin-dependent variations of the event rate [24].

- Due to the low event rate, the pile-up of multiple interactions from one bunch crossing – and even from subsequent bunch crossings that will be overlaid in slower detector components – is unlikely. Most of the recorded events contain only particles from a single interaction, making them more easy to reconstruct and to analyse. Related to this are much more relaxed requirements with respect to the radiation hardness of the detector equipment, because particle fluences and radiation doses in most of the detector components (except for the very forward instrumentation) will be orders of magnitude lower than at hadron machines.

All this means that lepton colliders can be used for high-precision measurements, which easily compensates for the fact that lepton colliders in the past typically had somewhat lower centre-of-mass energies than hadron machines that were running at the same time (figure 2.1). A good example are the Super Proton Synchrotron (running since 1976 at an initial energy of 630 GeV) and the Large Electron-Positron Collider (running 1989–1995 at 91 GeV and 1996–2000 at up to 209 GeV) at CERN: the experiments UA1 and UA2 at the SPS discovered the W and Z bosons in 1983 [25], but only the four LEP experiments were able to determine their properties with great precision and to provide a deeper insight into the Standard Model, e. g. by scanning the Z resonance and determining the parameters of its lineshape [26].

In a similar way, an electron-positron collider in the TeV range would be an ideal complement to the LHC [30, 31]: it could measure the properties of the Higgs boson with a significantly higher precision and it could confirm – or disprove – that the Higgs mechanism is really the origin of particle masses (figure 2.2). It could investigate supersymmetric particles that are difficult to study at the LHC (such as the superpartners of leptons and electroweak gauge bosons) by measuring the full range of their properties (such as mass, spin, parity, and mixing parameters) and it could also perform measurements in physics scenarios that would be extremely challenging to the LHC experiments, for example certain extra-dimensional models. Finally, a high-precision electron-positron collider could make use of its sensitivity to small quantum corrections in order to probe much higher energy scales that are directly accessible neither to itself nor to the LHC – a similar thing happened with the top quark: its mass was first predicted from electroweak measurements made at LEP and SLC, and later confirmed at the Tevatron [32].

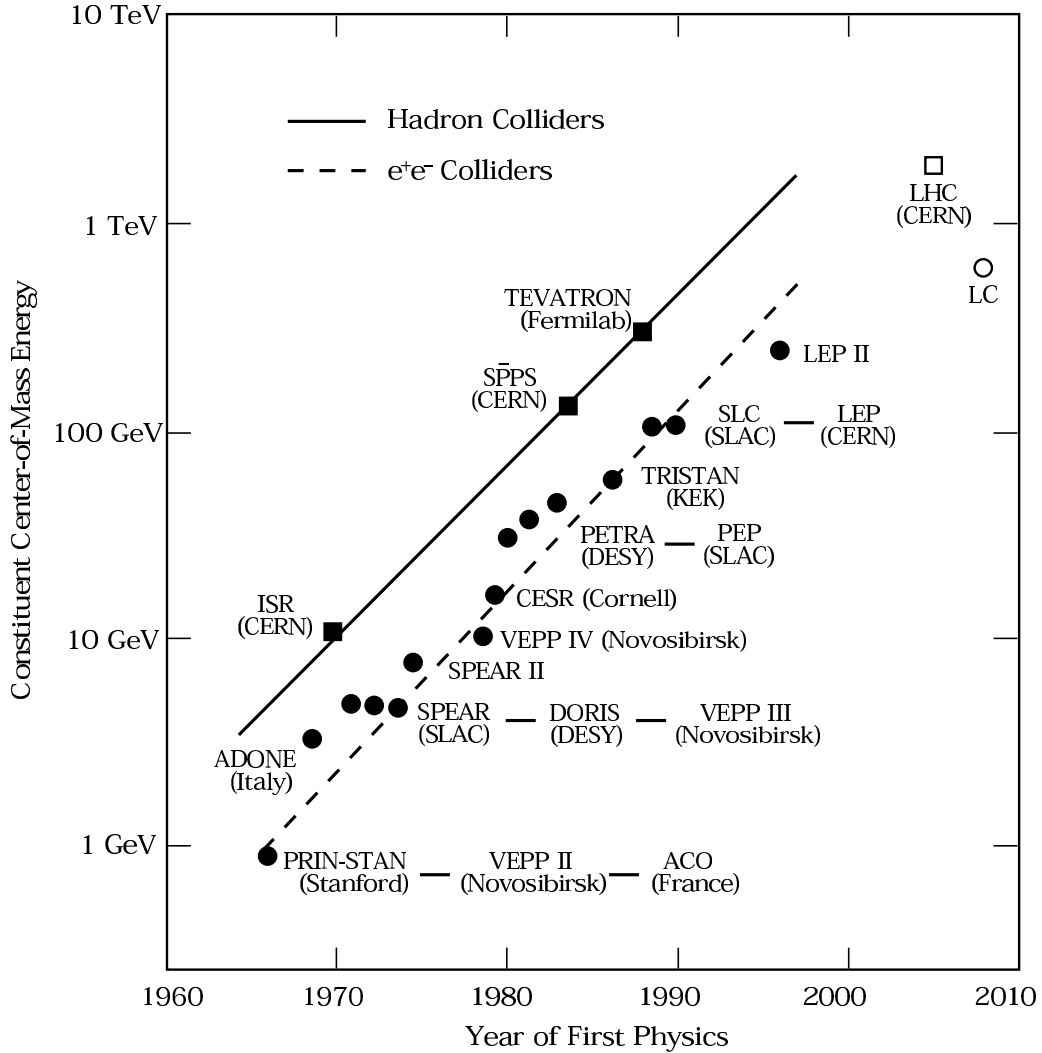


Figure 2.1: The so-called Livingston plot, adapted from [27, 28]: a history of hadron and lepton colliders, indicating an exponential increase of the available centre-of-mass energy in the course of time in the past, similar to Moore’s law of computing power. At the time of the drawing of this plot, the LHC was still believed to deliver first physics around 2005, and the subsequent lepton collider was foreseen for 2008. The former project is slightly delayed, the latter significantly. In any case, the progress of accelerator development seems to have slowed down in the recent years.

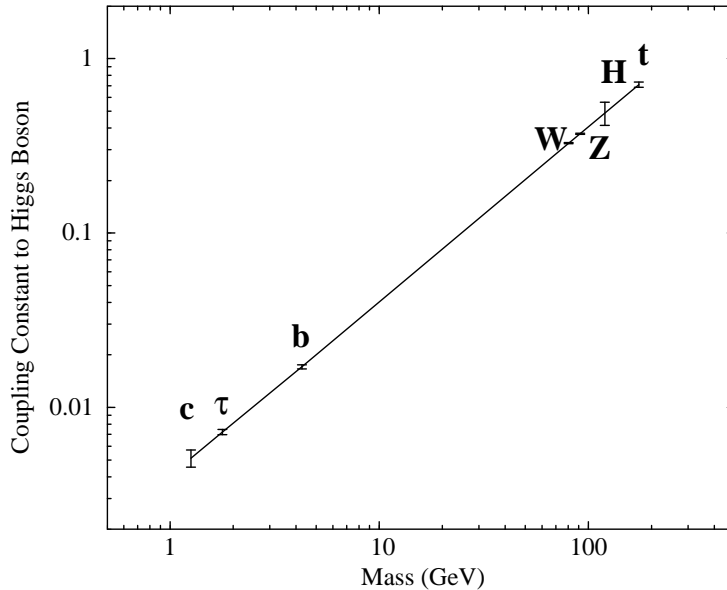


Figure 2.2: The relation between the Higgs coupling constants and the particle masses as they could be determined from high-precision ILC measurements [29]. If the couplings are proportional to the particles’ masses, this would prove that the Higgs mechanism is responsible for the generation of mass, as predicted by the Standard Model.

2.2 Circular vs. Linear Accelerators

These requirements may call for an upgraded version of the highly successful Large Electron-Positron Collider (LEP) at first sight, but it turns out that the construction of any circular electron-positron machine that goes well beyond the energy reach of LEP is practically impossible. The reason is that the energy loss per revolution due to synchrotron radiation increases with the fourth power of the beam energy [33]:

$$\Delta E_{\text{synch}} \propto \frac{1}{R} \cdot \frac{E^4}{m^4} \quad (2)$$

If electrons were to be accelerated to 250 GeV in a LEP-like ring, they would radiate a large fraction of their total energy during each single revolution, which renders the idea of a circular accelerator useless. This increase in losses cannot be compensated by increasing the accelerator radius R without making the accelerator unrealistically large (and expensive). Therefore, the only feasible solution to the problem of energy loss due to synchrotron radiation is to build a linear accelerator instead, even though this concept poses a lot of new challenges.

Equation (2) also shows that synchrotron radiation is completely negligible for a proton accelerator: since the mass of a proton is 2000 times larger than that of an electron, and since the mass also contributes with its fourth power, the synchrotron radiation losses of a 7-TeV proton in the LHC are of the order of 1 keV per revolution. This amount of energy can easily be restored.

2.3 The International Linear Collider

The International Linear Collider (ILC) is a proposed future electron-positron collider with a tunable centre-of-mass energy of 200–500 GeV and an overall length of 31 km. It emerged from three regional projects – the European TESLA collider [34, 23, 35], the American NLC [27], and the Japanese GLC [29] – and is now supported by large parts of the international high-energy physics community [36]. The ILC Reference Design Report (RDR) [37, 30, 38, 39], published in the middle of 2007, contains detailed studies of the ILC physics, accelerator technology, and detector concepts. It is supposed to be supplemented by an even more comprehensive Technical Design Report around 2012, so that the ILC would then be ready for construction if the upcoming LHC results support the scientific case.

The following list gives a short overview of the major components of the ILC accelerator (figure 2.3):

Particle Sources The electron and positron sources for the ILC have to meet stringent requirements: since the particles can only be used for one single shot (and not “re-cycled” as in a storage ring), the sources need to deliver a very large amount of particles ($2 \cdot 10^{10}$ electrons and positrons per bunch with a bunch spacing of 369 ns, figure 2.4). Furthermore, the particles must be produced with a low emittance so that they can afterwards be controlled by the beam optics of the main linac and the beam delivery system. Finally, it would be desirable to have polarised beams in order to influence the event rates of spin-dependent physics and background processes. The goal is to have an electron beam polarisation of 80 %, and an additional positron beam polarisation of 60 % would be a very interesting option [24].

The current plans foresee a laser-driven photoinjector that uses circularly polarised photons to produce polarised electrons. The positron source is placed in the middle of the main electron linac, where the electron beam (with an energy of already 150 GeV) is shot through an undulator to produce photons with energies of the order of 10 MeV. These photons are then converted to positrons in a thin target. If a

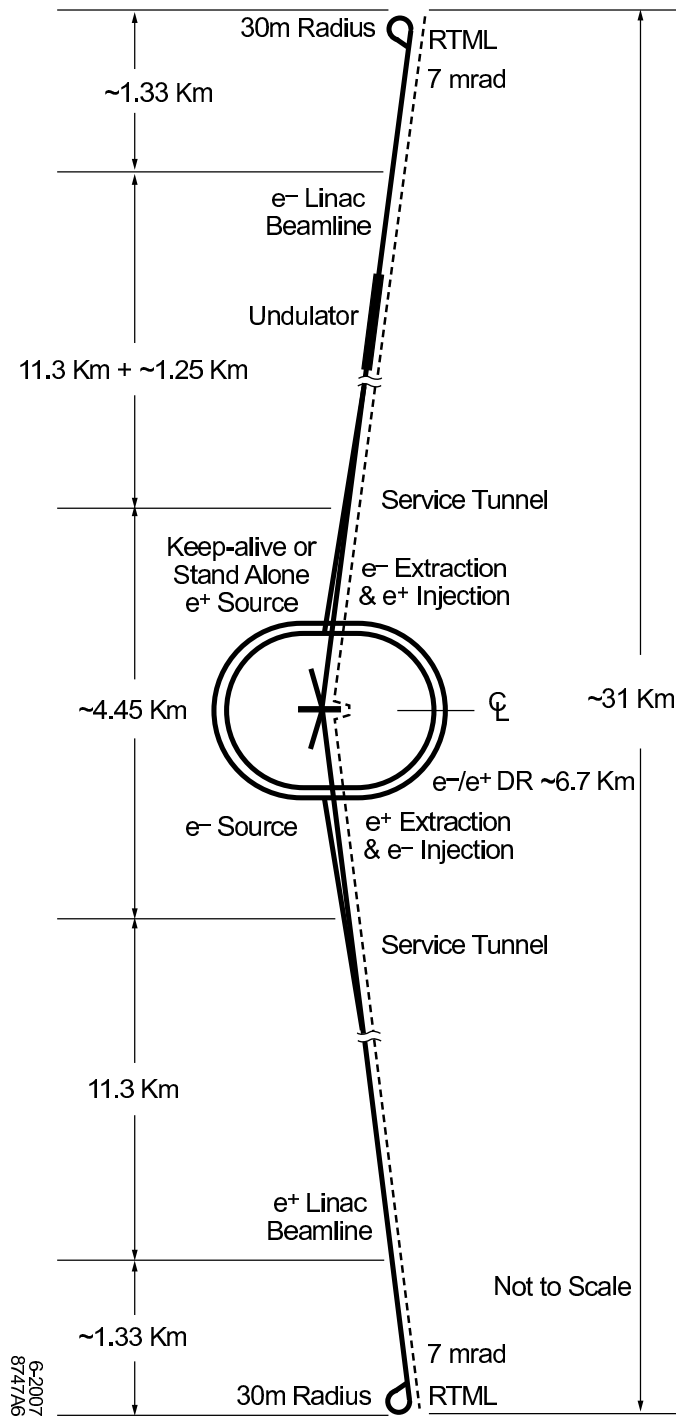


Figure 2.3: Schematic layout of the ILC complex for 500 GeV centre-of-mass energy [38]

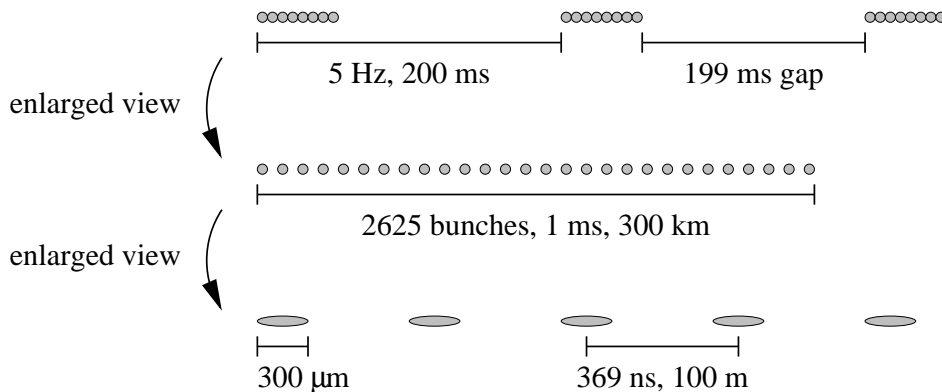


Figure 2.4: Bunch structure of the ILC: 2625 bunches with $2 \cdot 10^{10}$ particles per bunch form a so-called bunch train of about 1 ms length. Trains are accelerated at a repetition rate of 5 Hz.

helical undulator is used, polarised photons and positrons can be obtained.

Damping Rings After being pre-accelerated to 5 GeV, the beams are fed into two damping rings (DR). The particles are stimulated to emit synchrotron radiation (by the bending magnets and by additional wigglers) and the lost energy is restored by accelerating cavities. The emitted radiation can have a transverse component, but the energy is restored only in the longitudinal component, so the result is a reduction of the phase space volume that is occupied by the particle bunches, i. e. a reduction of the emittance.

Since the required amount of damping takes around 25 ms, the rings have to accommodate a whole bunch train of 2625 bunches, but the packing density is limited by the rise times of insertion and extraction kicker magnets (several nanoseconds). This means that the damping rings need a circumference of approximately 6 km, which already makes them a sizable facility in their own right.

Main Linac After damping, the beams pass through a long transfer line and the turning ring to the main linac (RTML). The main linac then accelerates the particles to their full energy of 250 GeV per beam. The ILC uses superconducting niobium cavities that are powered by a radiofrequency of 1.3 GHz, a technology taken over from the TESLA project. Since in a linear collider the final beam energy must be reached in one go, the foreseen average accelerating gradient of 31.5 MeV/m immediately determines the total length of the accelerating structures.

Including focusing quadrupoles and other beam instrumentation, each of the two linacs will have a length of 11 km.

Beam Delivery System The beam delivery system prepares the accelerated beams for their collision in the interaction point. It contains collimators to scrape off the beam halo, deflecting spoilers for halo muons, beam position monitors, presumably a polarimeter, other beam diagnostics, and finally the magnets that will focus the beams into a tiny spot at the interaction point (section 3.1). The last components of the beam delivery system are the final focus quadrupoles, which already reach into the detector itself. In total, each system is more than 2 km long.

Interaction Region The term “interaction region” usually comprises the detector and the innermost parts of the beam delivery system (at least all components that will be placed inside the experimental hall). Several different detector concepts are currently under discussion, one of which is described in more detail in section 4. The current plans foresee that the beams will not collide head-on, but under a small crossing angle of 14 mrad (section 7.7.2).

Since the particle bunches at the ILC have a very elongated shape (typically with a width-to-length ratio of 1 : 500, section 2.4), the angle of 14 mrad in the horizontal plane would already lead to a very poor mutual penetration of the colliding bunches, thus deteriorating the luminosity by more than a factor of three [40]. That effect can be compensated by rotating the bunches in the horizontal plane shortly before the interaction point (figure 2.5) such that their spatial overlap is restored and the full luminosity can (almost) be retained. This technique is commonly known as “crab crossing” since the rotated bunches appear to move sideways like a crab. Likewise, the device that applies the required radiofrequency kick to the bunches is called “crab cavity”.

Earlier designs of the ILC contained two independent interaction regions, each with its own detector, experimental hall, and beam delivery system. However, for reasons of cost saving, the current preference is to have only one interaction region that is shared by two detectors. These detectors will be exchanged regularly on a timescale of weeks to months to have alternating running and service periods. However, it is not yet sure whether such a “push-pull” scenario is technically feasible.

Extraction and Beam Dumps After their collision, the spent beams need to be safely disposed of. However, the beams are severely deformed due

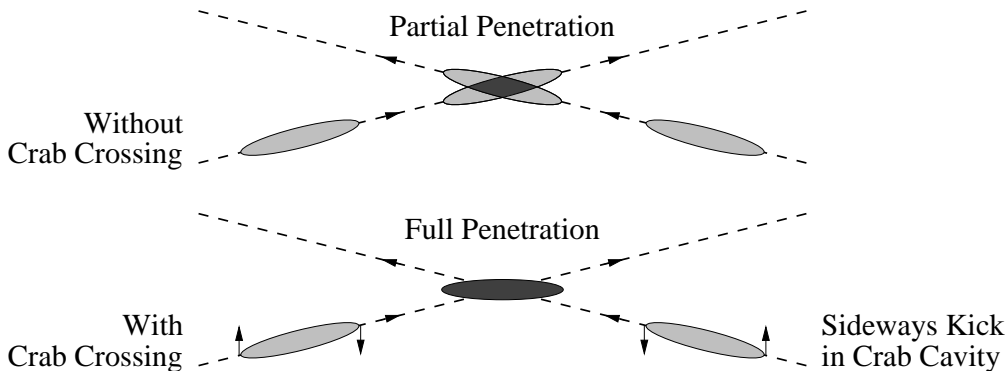


Figure 2.5: Sketch of the crab crossing technique. The crossing angle is greatly exaggerated, but the oblong shape of the bunches is under-exaggerated as well – the actual detriment caused by the crossing angle is similar to what this sketch may suggest.

to the strong beam-beam interaction during the collision of the bunches, and the mere power of the beams (about 10 MW each) makes them delicate to handle. The extraction system of the ILC contains additional focusing magnets, further beam diagnostics including a polarimeter, and finally the dumps for the main beams and photons (synchrotron radiation from the final focus and beamstrahlung from the interaction point, cf. section 3).

Apart from the nominal mode of operation, several run options and upgrade scenarios exist for the ILC. Besides the energy range of 200–500 GeV, which is interesting for the study of new physics like the Higgs boson and possibly supersymmetric particles, the ILC can also be operated as a “Giga-Z” machine: by running on the Z resonance or the WW threshold with an enormous luminosity, the ILC could be used for high-precision electroweak measurements that would improve the LEP results by approximately one order of magnitude. Furthermore, current plans for the ILC also foresee an upgrade to a centre-of-mass energy of 1 TeV. Other options are the transformation into an electron-electron, electron-photon, or photon-photon collider through Compton scattering of highly intense laser beams.

2.4 ILC Beam Parameters

Apart from the centre-of-mass energy and the luminosity that will be reached in particle collisions, a set of various other parameters defines the properties of the colliding beams. These beam parameters include the number of

particles per bunch (N), the number of bunches per bunch train (n_b) and their spacing in time (t_{sep}), the normalised emittance at the interaction point ($\gamma\varepsilon_x^*, \gamma\varepsilon_y^*$), and the bunch size at the interaction point ($\sigma_x^*, \sigma_y^*, \sigma_z^*$).

For a given centre-of-mass energy, a certain luminosity goal can be reached by many different parameter combinations such that there is always room for optimisation and trade-offs. In order to facilitate studies of different beam parameter settings and their impact on the overall accelerator and detector performance, five fixed beam parameter sets have been defined that can be used as reference points in the multi-dimensional parameter space. Starting from a nominal parameter set (“Nominal”) that is similar to the beam parameters in the TESLA TDR [34] and the US Technical Options Study [41], three scenarios are derived that address different critical issues with regard to the operation of the accelerator (“Low N”, “Large Y”, “Low P”). In each case, the remaining free parameters are adjusted to maintain the design luminosity of $2 \cdot 10^{34} \text{ cm}^{-2}\text{s}^{-1}$. The last set (“High L”) aims for maximum luminosity. The five parameter sets are:

Nominal The standard set in which none of the beam parameters is close to the supposed critical limits.

Low Charge (Low N) A scenario with only half the number of particles per bunch, but twice the number of bunches. On the one hand, this beam parameter set could reduce space charge effects in the damping rings, wakefield effects in the main linacs, or disruption effects at the interaction point. On the other hand, it would require the bunch spacing in the damping rings to be halved, the bunch length to be reduced, and also the beam delivery system to be made more flexible.

Large Spot (Large Y) This parameter set assumes that the intended – very small – vertical emittance cannot be achieved, resulting in a larger vertical size of the beam spot. To recover the luminosity, the beams are focused more tightly in the horizontal plane instead. A consequence are increased beam-induced backgrounds (section 3.1) and a stronger disruption of the beams in the interaction point.

Low Power (Low P) This parameter set takes into account possible limitations to the average beam power or problems with the bunch spacing in the damping rings or linacs. It has less than half the number of bunches per train and a larger bunch spacing, but the luminosity is recovered by a stronger focusing of the beams at the interaction point. A downside of this set is an increased amount of beam-induced backgrounds (sections 3.1 and 7.7.3).

	TESLA	Nominal	Low N	Large Y	Low P	High L
N (10^{10})	1.4	2.0	1.0	2.0	2.0	2.0
n_b	2820	2625	5120	2625	1320	2820
t_{sep} (ns)	337	369	189	369	480	308
$\gamma\varepsilon_x^*$ (mm mrad)	10	10	10	12	10	10
$\gamma\varepsilon_y^*$ (mm mrad)	0.03	0.04	0.03	0.08	0.036	0.03
σ_x^* (nm)	554	639	474	474	474	452
σ_y^* (nm)	5.0	5.7	3.5	9.9	3.8	3.5
σ_z^* (μm)	300	300	200	500	200	150
\mathcal{L} ($10^{34} \text{ cm}^{-2}\text{s}^{-1}$)	3.4	2.0	2.0	2.0	2.0	4.9

Table 2.1: The five predefined ILC beam parameter sets for a centre-of-mass energy of 500 GeV [38, 42]. The original TESLA parameters [34] are shown for comparison.

High Luminosity (High L) In this scenario, all parameters are pushed to the limits that are currently deemed feasible. The result is a much higher luminosity of almost $5 \cdot 10^{34} \text{ cm}^{-2}\text{s}^{-1}$, but also a more challenging operation of the accelerator and strongly increased backgrounds in the detector.

A brief overview of the parameters for a centre-of-mass energy of 500 GeV is given in table 2.1. The same parameter sets have also been defined for the increased centre-of-mass energy of 1 TeV.

Many of the physics studies for the ILC have been done with an integrated luminosity of 500 fb^{-1} , which should be collected during the first four years of running. This estimate assumes a collider availability of around 75 %, a physics run time of nine months per year, and a gradual ramp-up of the luminosity that is based on experiences from past collider experiments [42]. Regarding the detector hardware, that point in time might be suitable for the first detector upgrades, which is the reason why 500 fb^{-1} are sometimes considered as the design lifetime of the critical detector components. A single bunch crossing with nominal beam parameters yields an integrated luminosity of $1.46 \mu\text{b}^{-1}$, which means that the full integrated luminosity corresponds to a number of $3.4 \cdot 10^{11}$ bunch crossings in total.

2.5 Other Projects

It should be noted that the ILC is not the only approach towards an electron-positron collider in the TeV range. The superconducting cavities for the ILC

accelerator are supposed to run with an average operational field gradient of 31.5 MeV/m, which directly relates to the total length of the machine and therefore also has a significant impact on the cost. Currently ongoing prototype studies have shown that the accelerating gradient may eventually be increased up to 40–50 MeV/m [43], but it will not be possible to reach much higher values due to the intrinsic material properties of niobium, which will lose its superconductivity at a certain critical electric and magnetic field strength [44].

Consequently, the so-called Compact Linear Collider (CLIC) [45] aims towards a centre-of-mass energy of 3–5 TeV with a different acceleration technology: CLIC plans to transfer energy from an electron “drive beam” with relatively low energy and very high intensity to high-energy electron and positron beams by means of induced wakefields, thereby targeting for accelerating gradients of up to 150 MeV/m in room-temperature travelling-wave structures. This concept seems very elegant and could be a real breakthrough in accelerator technology, but a large-scale proof of principle still needs to be given. Nevertheless, the CLIC technology may definitely be an interesting way to reach even higher energies in electron-positron collisions in the future.

Equation (2) shows that the problem of synchrotron radiation losses in circular accelerators can also be solved by using heavier particles. This is of course already done in proton colliders, but it might also be possible to collide heavy leptons, i. e. muons, to benefit from the “best of both worlds”. However, the obvious problem is that muons are unstable, and up to now it is unknown how to prepare two muon beams that could be used in a particle collider. Still, even though it lies well beyond the timescale of the ILC or any similar project, a muon collider may become more than just science fiction [46].

3 Detector Backgrounds

As an electron-positron collider, the ILC may provide a very clean experimental environment compared to hadron colliders, but it is certainly not background-free. The rates for events from high-energy electron-positron interactions are low: at the nominal luminosity of $2 \cdot 10^{34} \text{ cm}^{-2}\text{s}^{-1}$, there will be less than one hard electroweak interaction per second at 500 GeV, even for processes that are not in the main focus of physical analyses. Consequently, the most important source of unwanted interactions are machine-induced backgrounds. This term denotes all particles that are produced due to the operation of the accelerator itself and due to collective effects from the collision of the particle bunches as a whole. A major contribution to machine-induced backgrounds are electron-positron pairs that are created in the scattering of beamstrahlung photons.

3.1 Beam-Beam Interaction and Beamstrahlung

The repetition rate of bunch trains at the ILC (5 Hz, cf. section 2.3 and figure 2.4) is rather low due to limitations in the available radiofrequency power for acceleration and the operation of superconducting cavities. Since the repetition rate immediately affects the luminosity of a collider (equation (1)), the colliding ILC beams need to be focused to an extremely small spot in order to reach a luminosity of $2 \cdot 10^{34} \text{ cm}^{-2}\text{s}^{-1}$: the nominal ILC beam parameters (table 2.1) foresee a horizontal size of $\sigma_x^* = 369 \text{ nm}$ and a vertical size of $\sigma_y^* = 5.7 \text{ nm}$, which is approximately a factor of 1000 less than the LEP beam spot size in each dimension [47].

The small bunch size implies that the bunches have a very high space charge and are thus accompanied by a strong electric field, which appears even stronger and compressed to a thin disc due to relativistic effects. This collective field of one bunch is strong enough to exert a significant force on the oncoming bunch of the opposite charge: the approaching bunches will attract each other so that the individual particles will be accelerated towards the centre of the oncoming bunch as shown in figure 3.1 – this mutual attraction is known as the pinch effect.

On the one hand, the pinch effect is helpful because it reduces the size of the colliding bunches – the luminosity increases even further, which is accounted for by the so-called beam enhancement factor H_D in equation (1). For typical ILC beam parameter sets, the beam enhancement factor is of the order of two, i.e. the luminosity is almost doubled by the beam-beam interaction [42].

On the other hand, the deflection of particles by the charge of the opposite

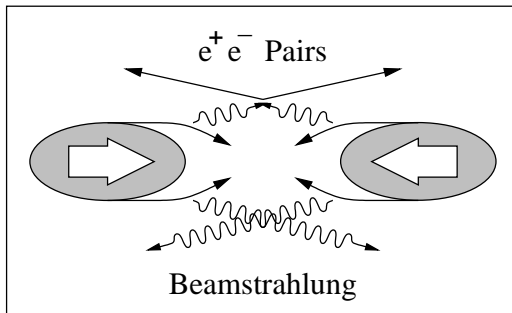


Figure 3.1: Illustration of the pinch effect in bunch collisions. The particles of one bunch are attracted by the electric space charge of the other and emit photons due to their deflection. Those photons can in turn scatter to produce electron-positron pairs.

bunch will cause them to radiate photons [48, 49], just like in any other deflection of charged particles. These photons – in principle a special kind of synchrotron radiation – are known as beamstrahlung, and they are produced in vast amounts: a total power of 250 kW, i. e. 10^8 TeV per bunch crossing, is carried away by beamstrahlung photons. The average energy loss δ of a particle in the colliding bunches is given by

$$\delta \propto \frac{\gamma}{E\sigma_z^*} \left(\frac{N}{\sigma_x^* + \sigma_y^*} \right)^2, \quad (3)$$

where γ denotes the relativistic factor of the beam particles, E is the beam energy, N is the number of particles per bunch, and σ_x^* , σ_y^* , σ_z^* are the bunch sizes at the interaction point in the respective dimensions. These energy losses – typically of the order of 1 GeV per particle – result in a reduced centre-of-mass energy that is available for the actual hard electron-positron interactions, thereby broadening the beam energy and the luminosity spectra in a similar way as initial-state radiation [50].

Equation (3) shows that the beamstrahlung can be reduced by increasing the bunch size. However, the longitudinal bunch size σ_z^* has an upper bound caused by the so-called hourglass effect [51], and the transverse bunch sizes have a direct influence on the luminosity, which must be kept large. Since the luminosity depends on the product of σ_x^* and σ_y^* and the beamstrahlung losses depend on their sum, the solution is to make one dimension very small and the other one much larger – as it is done for all ILC beam parameter sets that are under discussion. Circular accelerators like LEP have an elliptic beam profile due to the emission of synchrotron radiation in the horizontal plane, causing a beam jitter in the x -direction, but the ILC accelerator could

in principle deliver beams with a circular cross-section. The choice to have the horizontal size large and the vertical size small is related to the beam crossing angle and the crab crossing scheme (section 2.4): since the crossing angle will be in the horizontal plane for practical reasons, crab crossing would be extremely difficult if the beams were colliding with an upright shape.

Despite the large number of photons and the high total energy, the beamstrahlung itself is not a relevant source of detector backgrounds because it is strongly focused in the forward direction such that it will exit the detector through the beam tube [52]. Since photons cannot be deflected, there will always be a direct line of sight from the photon beam dump to the detector, but previous studies have shown that backscattering particles from the dump (and also other parts of the extraction system) will not cause significant backgrounds, either [53]. However, this is only true as long as there is another (much more powerful) dump for the main beams (section 3.5).

3.2 Electron-Positron Pairs

Instead of simply exiting the detector through the beam tube, the beamstrahlung photons can also create electron-positron pairs in the immediate vicinity of the interaction point. The two possible contributions are coherent [54] (CPC) and incoherent pair creation [55] (IPC): in the first case, the quantum fluctuations of a beamstrahlung photon are torn apart into a real electron-positron pair in the collective electric field of the bunch – similar to the usual process of photon conversion that can happen in the electric field of an atomic nucleus. In the second case, two photons scatter to produce an electron-positron pair (figure 3.1). Three different processes can be distinguished: the collision of two real beamstrahlung photons (Breit-Wheeler process), the collision of one real and one virtual photon that is emitted by an electron in the bunch (Bethe-Heitler process), and the collision of two virtual photons (Landau-Lifshitz process). It can be calculated that coherent pair creation is completely negligible for the collision of ILC-like beams and plays a role only for even higher space charges [49]. Of the incoherent processes, the latter two are dominant (with an approximate ratio of 2 : 1), whereas the real-real interaction contributes only on the percent level [56].

For ILC-like beam parameters, around 10^5 electron-positron pair particles are created per bunch crossing, carrying a total energy of approximately 100 TeV and an average energy of a few GeV per particle (figure 3.2). Numbers for the different ILC beam parameter sets (section 2.4) that have been simulated with Guinea-Pig (section 6.1) can be found in figure 3.4.

The pairs are also mainly focused in the forward direction, but not as strongly as the beamstrahlung photons – after all, if two photons with similar

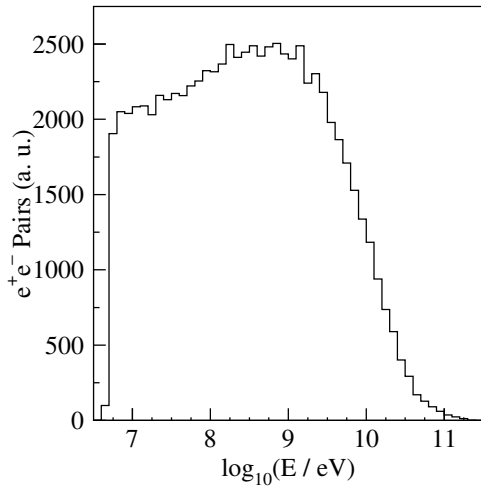


Figure 3.2: Energy spectrum of electron-positron pairs simulated with Guinea-Pig (section 6.1) for nominal beam parameters. The lower edge at 5 MeV corresponds to a momentum cut-off in the simulation.

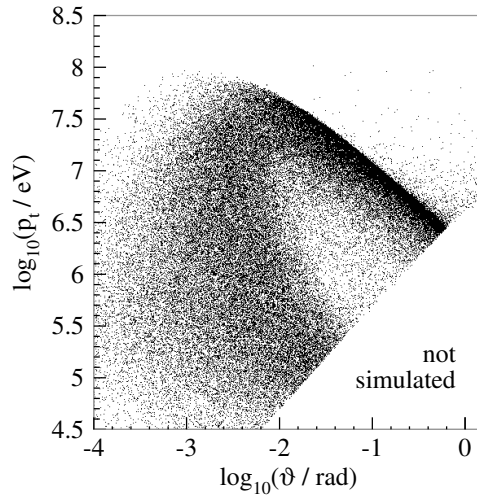


Figure 3.3: Transverse momentum of pairs vs. their polar angle. The void region in the lower right is caused by a momentum cut-off in the simulation. Particles in the upper dark band must be kept away from the vertex detector, but hits from the few particles that have even larger angles and momenta cannot be avoided [56].

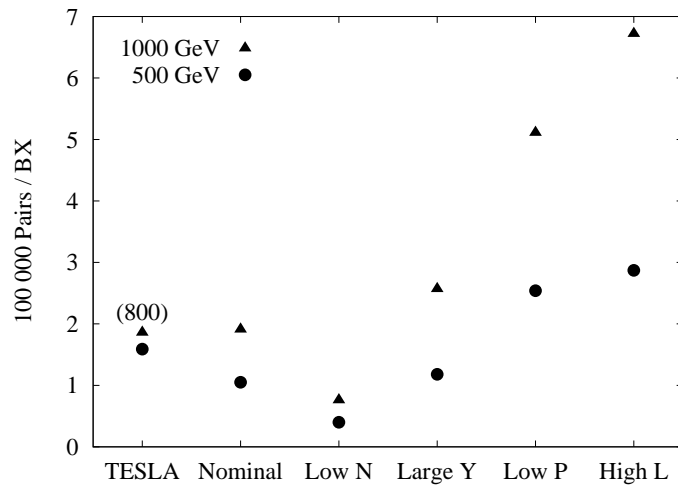


Figure 3.4: The number of electron-positron pairs created per bunch crossing for different beam parameter sets (adapted from [57])

energies collide to create an electron-positron pair, there is only a small longitudinal Lorentz boost between the centre-of-mass frame and the rest frame, such that all polar angles are in principle accessible. Even though most pair particles still have very small polar angles, and even though they are further confined by the magnetic field (section 4.4), they will not necessarily escape through the beam pipe. Pairs are therefore an important source of beam-induced backgrounds in the detector (see also [50, 58]).

3.3 Pairs in the Detector

Electron-positron pair particles will affect the detector in different ways:

- If their polar angle ϑ and transverse momentum p_t are large enough, some particles can immediately reach the vertex detector or even the main tracker. However, due to a rather strict upper bound in their ϑ - p_t -distribution (figure 3.3), the largest fraction of the pairs is confined to a cone that extends into the forward direction [56]. The opening angle of that cone can be influenced by the strength of the magnetic field, which will let the pair particles bend more or less tightly around the magnetic field lines. The beam tube wall should not touch the pairs cone, and the vertex detector must be kept clear of the main cone at all cost. Still, a few direct hits from particles with exceptionally high transverse momenta cannot be avoided (section 7.2.1). This is the dominant source of backgrounds in the vertex detector.
- Many of the particles with slightly larger polar angles or transverse momenta will hit the forward calorimeters of the detector, where they will deposit a large amount of energy (several TeV per bunch crossing or 10 MGy per year) and induce intense electromagnetic showers (figure 3.5). On the one hand, the geometrical pattern of the pairs can be utilised to calculate parameters of the bunch crossing itself (cf. section 4.3), but on the other hand, backscattering particles may be able to escape out of the showers in the forward calorimeters and reach the inner parts of the detector (described in various parts of section 7). This is the dominant source of backgrounds in the main tracker and affects the vertex detector as well.
- Pair particles that exit the inner detector through the beam tube are not necessarily harmless: most of the particles will be deflected too strongly in the first magnets of the beam extraction system because their energies are much lower than the nominal beam energy. They will hit the inside of the magnets and induce electromagnetic showers

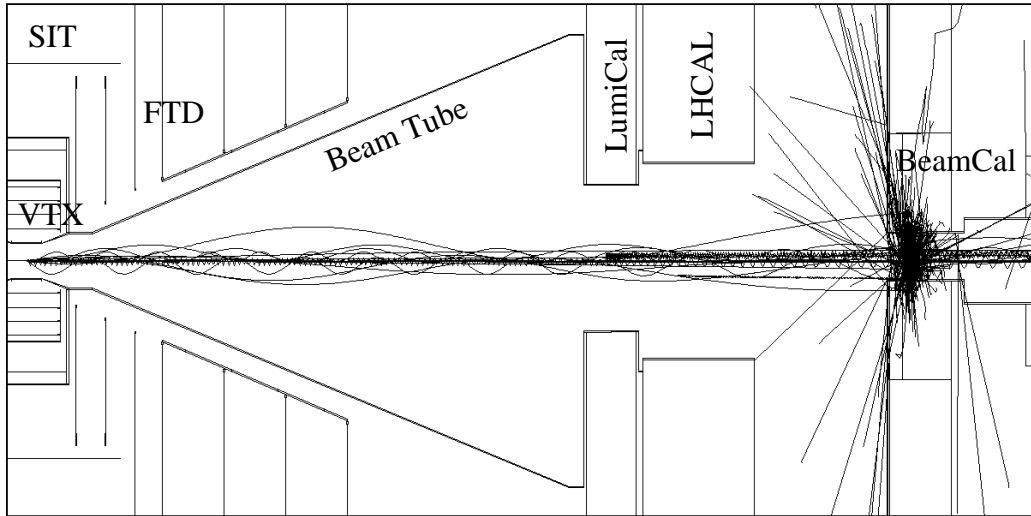


Figure 3.5: Twenty random particles from electron-positron pairs inside the detector (compressed by a factor of 5 in z -direction). Most particles are confined to a tight cone in which they curl around the magnetic field lines and hit the BeamCal. Only few particles (none of the ones shown here) can reach the LumiCal or even the vertex detector and other parts of the detector directly.

in the magnet material, and some particles (typically photons, which are not affected by the magnetic field) may be able to backscatter into the detector. However, it turns out that this is a negligible source of detector backgrounds (section 7.2.2).

All studies that are presented in section 7 deal with the impact of electron-positron pairs on various components of the detector.

3.4 Minijets

The beamstrahlung photons will not only scatter to electron-positron pairs, but they can also create quark pairs that will subsequently fragment into jets. Since these jets typically have rather low energies and low multiplicities, the hadronic scattering products are often called “minijets”. Previous studies have shown that these particles are not a significant source of backgrounds in terms of detector occupancies, but they might be misidentified as fake jets and therefore be confused with real physics events [58, 59]. Suppression algorithms in the event reconstruction and the possible impact on physics analyses still need to be studied in detail.

3.5 Other Sources

Apart from the beamstrahlung photons and their scattering products, there are several other sources of backgrounds that are related to the operation of the machine:

Beam Halo Muons The beams in the main linacs are accompanied by a beam halo of particles which have a significant deviation from the nominal beam orbit, but which are still accelerated up to the full beam energy. The halo is scraped away by collimators in the beam delivery system, but this process may create muons that basically have the full beam energy. Such high-energy muons cannot be easily absorbed and will strike through the experimental hall, including the detector. Beam halo muons will leave high-energy tracks in the detector that are almost parallel to the beam axis, and they will also contribute to the radiation levels in the experimental hall. It must be kept in mind that in case of a push-pull scenario (section 2.3), the hall should still be accessible to humans while the accelerator is running.

The amount of muons from the beam halo can be reduced by including so-called muon spoilers in the beam delivery system. These devices are large magnetised iron blocks which cannot stop the muons, but which can at least bend their trajectories in a way that a part of them will miss the experimental hall [38]. Simulations that use a best guess for the distribution and population of the beam halo give the result that only a few (about one to three) halo muons will cross the main tracking system per bunch crossing [60]. This number is believed to pose no problem for the tracker, but further studies are still needed.

Synchrotron Radiation The focusing and bending magnets in the beam delivery system and particularly the final focus quadrupoles will cause the beam particles to emit synchrotron radiation. Photons coming from further upstream need to be collimated, and photons from the final focus must be able to exit the detector through the beam tube on the opposite side. If the beam delivery and extraction systems are designed properly, photons from synchrotron radiation will not be a problem for detector backgrounds [52].

Beam-Gas Interaction The requirements on the beam tube vacuum of the beam delivery system are driven by beam-gas interactions. In order to avoid a significant contribution to detector backgrounds, the current specifications foresee a vacuum of approximately 10^{-9} mbar for the final parts of the beam delivery system [38].

Radiative Bhabha Scattering The process of electron-positron scattering with the initial-state radiation of a photon is called radiative Bhabha scattering and will affect several ten thousand particles per bunch crossing. These particles have an average energy of $\mathcal{O}(50\text{ GeV})$ and will typically hit magnets of the extraction system or collimators that are positioned even further downstream. They produce intense particle showers, but due to the large distance from the interaction point they are not relevant for detector backgrounds [53].

Extraction Line Losses Similarly, also particles from the main beams may deviate too far from the nominal orbit and hit pieces of the extraction system. This can easily happen because the particle bunches will be severely disrupted by the beam-beam interaction, introducing both an angular divergence and a significant energy spread. As in the case of radiative Bhabhas, these losses will mostly affect distant areas, but the number of involved particles (which would typically have energies close to the full beam energy) might be orders of magnitude larger.

Depending on the disruption of the bunches and the detailed design of the extraction system, backscattering particles might or might not play a role in terms of detector backgrounds. Recent simulations with the BDSIM simulation toolkit [61] suggested a very careful design of the extraction system, because otherwise detector backgrounds might in fact be dominated by extraction line losses [62]. Further work needs to be done on this issue.

Beam Dumps The hottest regions of the whole accelerator complex clearly are the beam dumps, which have to absorb a total power of approximately 10 MW each. In the case of water dumps, the incident particles will produce neutrons in amounts of the order of 10^{12} particles per bunch crossing. Earlier studies [53] showed that a small amount of these neutrons (around 10^7 particles) can escape from the dump and move back into the beam tunnel, but again only a tiny fraction (around 10^4 particles) can reach the detector. They hit the outer surface of the magnet yoke, but not the inner parts of the detector.

This means that the beam dumps are not a significant source of detector backgrounds, but it has to be kept in mind that the quoted studies were done for the case of separate dumps for the main beams and for photons. If there is only a single dump on each side of the detector, there will be a direct line of sight from the dump to the interaction point, making it impossible to introduce any kind of collimation or shielding. In this case, which is in fact the current default for the ILC, the impact on

the vertex detector might be non-negligible. Again, further studies are needed here.

As a conclusion it can be said that electron-positron pairs are an unavoidable source of backgrounds because they are immediately related to the collision of particle bunches – if a given luminosity is to be reached, a certain amount of pairs will be produced in any case (assuming that the optimisation of the parameters in equation (3) is limited by technical feasibilities such as the minimum achievable vertical bunch size). In contrast to that, several other sources depend critically on the design of the machine, with their possible impact on detector backgrounds ranging from negligible to dominant.

4 The Large Detector Concept

To exploit the potential of the accelerator in the best possible way, the ILC needs detectors of unprecedented performance. Even though the valuable experiences from earlier projects – especially from the highly successful LEP detectors – can provide some hints about which route to follow, there is no predefined way to reach the envisaged physics goals. It is only clear that none of the detectors from the past would have been powerful enough to meet the future requirements for the ILC.

Consequently, four collaboration-like communities have formed in the past few years to design different so-called “detector concepts”. These concepts, which are briefly compared in table 4.1, are the “Large Detector Concept” (LDC) [63, 64], mainly supported by European groups, the mostly US-based “Silicon Detector” (SiD) [65], the Japanese “Global Large Detector” (GLD) [66], and a fourth concept that is actually named “Fourth Concept” (4th) [67]. These concepts differ in several of their key features, which is in fact highly desirable in order to explore the full range of possible options. Moreover, the two detectors for the final experimental set-up should have been designed independently and should – where possible – be complementary to each other in order to produce more reliable results through the combination of their measurements.

Because of their relative similarity, two of the concepts – LDC and GLD – have recently started to merge into a new, common project named the “International Large Detector” (ILD) [68]. This process of merging is still

	LDC	GLD	SiD	4th
VTX	Si Pixel	Si Pixel	Si Pixel	Si Pixel
Main Tracker	TPC	TPC	Si strip	Cluster Counting
ECAL	Si/W	Si/W	Si/W	Crystal
HCAL	Sc/Fe	Sc/Pb	RPC/Fe	“DREAM”
Magnet	4 T	3 T	5 T	+3.5 T (inner) –1.5 T (outer)
Muons	Instr. Yoke	Instr. Yoke	Instr. Yoke	Cluster Counting
Radius	6.0 m	7.2 m	6.5 m	5.8 m
Half length	6.2 m	7.5 m	4.6 m	6.2 m

Table 4.1: Overview of the main features of the four detector concepts for the ILC. In all concepts, the technology choice for several components is not yet finalised.

underway because ILD should not just be the average of LDC and GLD or some other kind of arbitrary compromise, but already the next step towards an optimised detector [69].

Many of the following sections focus on the Large Detector Concept, which is strongly supported by DESY and which, to a certain extent, also carries some heritage from the former TESLA detector proposal [35].

4.1 Performance Requirements

The primary physics goals of the ILC are well defined [30]: the ILC should precisely determine the properties of the Higgs boson, it should likewise perform detailed studies of supersymmetric particles (provided they exist in nature), and it should be able to do high-precision measurements of the top quark and electroweak physics. On top of that, the ILC should also be prepared for less likely physics scenarios or even completely unexpected findings by having truly multi-purpose detectors, designed as generically as possible.

The following list gives some examples of physics items that drive the performance requirements for the major detector components. A much more detailed overview can be found in [39].

- One of the driving forces for the tracking system is the recoil mass measurement of the Higgs boson in the Higgsstrahlung process $e^+e^- \rightarrow Z^* \rightarrow ZH \rightarrow \mu^+\mu^-X$. Since the centre-of-mass energy is known at the ILC, the measurement of the two muons from the Z decay allows to determine the mass of the recoiling Higgs in a completely model-independent way, i. e. without any assumption about its decay modes and even without measuring the decay products themselves (here denoted by X). This process defines the requirement of $\Delta p_t/p_t^2 = 5 \cdot 10^{-5} \text{ GeV}^{-1}$ for the overall tracking resolution, which is about ten times better than the performance of the trackers at LEP.

Furthermore, the tracking system should have a large angular coverage, robust and highly efficient pattern recognition, and a low material budget in order to minimise unwanted interactions with the detector material.

- Many interesting physics processes at the ILC involve multiple jets in the final state. The precise reconstruction of the invariant masses of two or more jets is essential for the identification and separation of W, Z, H, and t decays. The performance goal of the calorimetric system is a jet energy resolution of $\Delta E/E \lesssim 3\text{--}4\%$ or $\Delta E/E = 30\%/\sqrt{E/\text{GeV}}$ for jet energies below 100 GeV. This is a factor of two better than

the resolution that could be achieved with the calorimetric techniques applied at LEP.

- A highly precise and efficient vertex detector is essential for the tagging of heavy-flavour quarks, i. e. bottom and charm. Efficient flavour identification is needed for the measurement of Higgs branching fractions, and it could also provide evidence for new physics. The required resolution of the track impact parameter is $\Delta\delta = 5 \mu\text{m} \oplus 10 \mu\text{m}/(p/\text{GeV}) \sin^{3/2} \vartheta$, which is a factor of 2–3 better than that of the SLD pixel vertex detector [70]. The vertex detector should be located as close to the interaction point as possible, it should have a very low material budget, and it must be able to handle a significant amount of background signals from the beam-beam interaction (sections 3.1 and 7.2).

Event though the ILC environment is not completely background-free (section 3), the background situation at an electron-positron collider is fundamentally different from that at the LHC: the LHC detectors have to cope with huge event rates and need highly selective hardware and software trigger systems to find interesting physics among the mostly QCD-related backgrounds. Moreover, the large expected radiation doses play an important role for the design of many detector components, e. g. silicon sensors and their readout electronics.

In contrast to that, event rates at the ILC are comparatively low – it is in fact planned to run the detectors without any conventional low-level trigger system, but to record the data from every single bunch crossing and to select interesting events only with the help of a software trigger. This approach sets high requirements for the data acquisition system, but it allows a very high efficiency and does not restrict the sensitivity for any kind of new physics on a basic level. Radiation hardness is generally not an issue, except for the components that are placed very close to the beams.

4.2 Particle Flow

Since hadronic showers are inherently subject to large statistical fluctuations, the envisaged jet energy resolution of $30\%/\sqrt{E}$ is a very ambitious goal for any conventional calorimetric system. Therefore, three of the detector concepts (LDC, GLD, and SiD) try to make an alternative approach towards the measurement of jets: on average, only 10% of the jet energy is carried by neutral hadrons, whereas all other particles in a jet – charged hadrons, photons, and possibly charged leptons – can also be measured by detector components other than the hadronic calorimeter.

Both the tracking system and the electromagnetic calorimeter have a much better momentum and energy resolution than the HCAL, at least in the typical energy range for jet particles. Consequently, the idea is to measure the momenta of all charged particles (also inside jets) with the tracker and the energies of photons with the ECAL, and then to disregard all related hits in the HCAL (i. e. all charged clusters and possible punch-through from the ECAL). Since the HCAL with its intrinsically worse resolution will effectively be used only for the measurement of neutral hadrons, the overall jet energy resolution can be significantly improved.

This novel approach has become known as “Particle Flow” [71, 72], and recent simulation studies have shown that the required jet energy resolution of $30\%/\sqrt{E}$ can actually be achieved with the current implementations (at least if the jet energies are not too high) [73]. Apart from a good tracking momentum resolution, Particle Flow needs a very high tracking efficiency, a reliable matching between tracks and calorimeter clusters, and highly granular calorimeters in order to separate energy deposits from charged clusters (which should be ignored) and energy deposits from neutral clusters (which must then be measured by the HCAL).

All this means that Particle Flow is not merely a calorimetry technique or an event reconstruction algorithm, but rather a complete paradigm for the overall design of the detector.

4.3 Detector Layout

The Large Detector Concept follows the basic layout of most modern particle detectors, but it has been specifically optimised with Particle Flow in mind. A cross-section of one quadrant is shown in figure 4.1. Its major detector components are listed below.

- The vertex detector (VTX) is a silicon pixel detector with five layers at radii of 15–60 mm. Details on the geometry can be found in appendix B.1.2. Various detector technologies are currently under consideration (section 7.2.1).
- The inner silicon tracking system supplements the vertex detector with two additional components: the Silicon Intermediate Tracker (SIT) consists of two cylindrical layers of silicon strip detectors that provide a link between the vertex detector and the main tracker. The Forward Tracking Discs (FTDs) are seven silicon discs, presumably with pixel sensors on the inner four discs and strip sensors on the outer three discs. They fill the space between the beam tube wall and the main

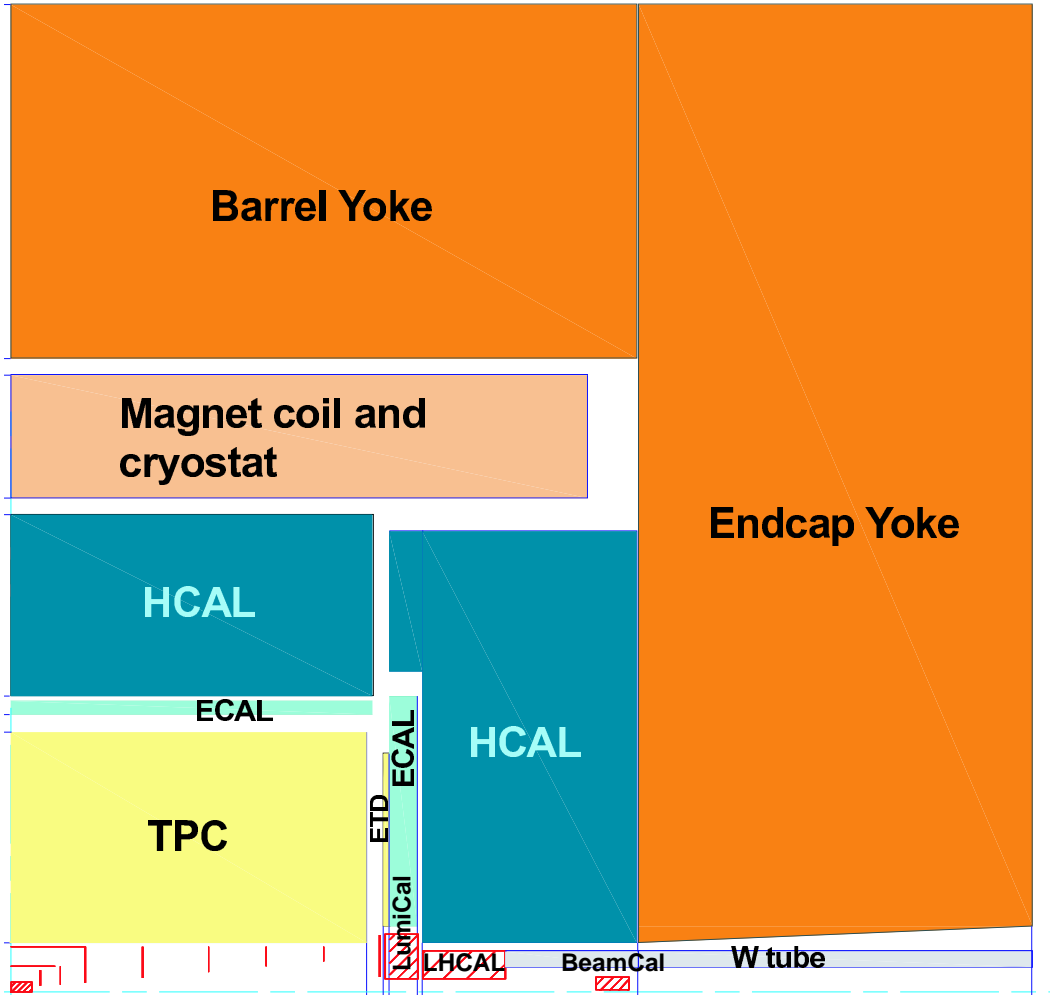


Figure 4.1: Quadrant of the Large Detector Concept [39]

tracker and they extend the tracking system towards small polar angles ($\vartheta \gtrsim 100$ mrad). Geometry values are given in appendix B.1.3.

- The main tracker is implemented as a Time Projection Chamber (TPC), i. e. a large-volume gaseous tracker with three-dimensional tracking capabilities. Strengths of a TPC are its low material budget, the very robust and highly efficient pattern recognition, and the possibility of a precise dE/dx measurement for particle identification. The resulting momentum resolution is comparable to that of a large silicon tracker, as used in SiD. The working principles of a TPC are described in section 5, some details on the TPC geometry in LDC can be found in appendix B.1.6.

- The outer silicon tracking system adds an additional layer of silicon strip detectors outside the main tracker. The Silicon Envelope Tracker (SET) should provide a precise link between the main tracker and the ECAL barrel, whereas the Endcap Tracking Discs (ETDs) should do the same in the endcap region. The actual need for these devices is still being debated.
- The ECAL is a tungsten-silicon sampling calorimeter, with alternating tungsten absorber layers and thin silicon sensor layers. In order to separate electromagnetic and hadronic showers, the ECAL material must have a large ratio of hadronic interaction length λ to electromagnetic radiation length X_0 and a small Molière radius. The current plans foresee an ECAL thickness of around $24X_0$, but it should be noted that the ECAL design is not fixed yet, and alternative technologies are under study as well.
- The HCAL is foreseen as a steel sampling calorimeter, either read out by scintillating tiles with built-in photomultipliers or by resistive plate chambers. The thickness of the HCAL corresponds to approximately 5λ , with the outer radius of the calorimetric system immediately determining the required magnet size. As for the ECAL, the final design is not fixed yet and several alternatives are currently being tested.
- The magnet coil is a superconducting solenoidal coil that creates a magnetic field of 4 T in the inner parts of the detector, i. e. everything up to the ECAL and the HCAL. Its mechanical design could be very similar to that of the CMS coil. Some details on the magnetic field can be found in the following section 4.4 and in appendix B.1.13.
- The magnet yoke, made of iron, will return the magnetic field lines of the coil. Apart from that, it will contain muon detectors (presumably resistive plate chambers), which can not only be used for lepton identification, but also as a tail catcher for shower leakage from the HCAL.
- Specific forward calorimeters are placed in the forward region of the detector to increase the total angular coverage down to very small values. The LumiCal is an ECAL-like device that is mainly designed to provide a precise luminosity determination by measuring Bhabha-scattered electrons and positrons from the interaction point [74], but it will also serve as an extension of the ECAL down to approximately $\vartheta = 40$ mrad. The BeamCal is a tungsten-silicon (or maybe even tungsten-diamond) sampling calorimeter that extends the angular coverage

further down to almost 5 mrad. It is the only detector component that has to face a massive amount of particles from the beam-beam interaction (section 3.1), and it uses the distinct pattern of these particles to determine the parameters of the corresponding bunch crossing (e. g. the relative alignment of the colliding bunches). The output of the BeamCal can then be used as a fast feedback for the beam delivery system to adjust the beam position and to achieve the maximum possible luminosity in the collisions [75]. Finally, the so-called LHCAL is an extension of the HCAL towards small polar angles.

4.4 Magnetic Field Configuration

The main solenoid field – with a strength of 4 T and a stored energy of 1.7 GJ – is certainly the dominant magnetic field in the LDC detector, but not the only contribution to the overall magnetic field configuration. Several other fields also play a role for the operation of the detector.

- The final focus quadrupoles are already placed inside the detector. Their high-gradient fields deflect the beam particles into the tiny focus spot at the interaction point, which has a size of only $500 \times 5 \text{ nm}^2$ (table 2.1). The final focus magnets are accompanied by higher-order correction magnets. Likewise, the first quadrupoles of the extraction system are placed immediately behind the detector, and directly next to the final doublet of the opposite beam. Details can be found in figure 6.4 on page 70 and in appendix D.
- The innermost quadrupole QD0 has a gradient of 65 T/m but only a bore of 10 mm radius, which means that the resulting field will be substantially weaker than the fringe field of the main solenoid in that region (figure B.3 on page 155). To protect the final focus from the influence of the main field, it has been considered to shield the whole forward region by an additional anti-solenoid field that would cancel the main solenoid [76].

However, these fields of opposite polarity would cause an immense magnetostatic repulsion, exerting a force equivalent to the weight of several tons. Since such a repulsive force would have to be absorbed by very stable mechanical structures, recent developments have focused on a force-neutral anti-solenoid design that can compensate the effects of an external field without receiving a repulsive force [77].

- The beams of the ILC will most likely collide under a crossing angle of 14 mrad. This causes a vertical deviation of the trajectory (including

the emission of synchrotron radiation and hence a deterioration of the emittance) and a small vertical angle at the interaction point, resulting in a small spin misalignment of polarised particles.

In order to avoid these effects, it has been suggested to superimpose an additional dipole field on the main solenoid field to bend it in the direction of the incoming particles – this would reduce the trajectory offset and also the spin misalignment between the upstream polarimeter and the interaction point. This special field configuration was initially called “Serpentine Field” (because of the serpent-shaped windings that would have to be added to the main coil), but today it is commonly known as a “Detector-Integrated Dipole”, or DID field [76, 78]. An example for a DID field configuration is shown in figure 7.53 on page 121.

Apart from beam polarisation, the DID field also has a significant impact on detector backgrounds and the performance of certain components – details are discussed in section 7.7.2.

- After the proposal of the DID field, it was also considered to flip its polarity such that the resulting detector field would be bent towards the holes for the outgoing beams [79, 78]. This configuration has become known under the name anti-DID field, and an example can be found in figure 6.2 on page 68. A possible field map is shown in figure B.4 on page 155.

The anti-DID field configuration will effectively double the spin misalignment of the incoming particles (so that it exactly contradicts the original purpose of the DID), but this effect could in principle be corrected [78].

Like the DID, the anti-DID has a strong influence on detector backgrounds and performance, and its beneficial effects are considered to outweigh the potential disadvantages – details can be found in section 7.7.2 as well. As a result, the anti-DID is currently the preferred field configuration for the LDC detector. Unless otherwise noted, it has been used for all studies that are presented in this thesis.

5 The Time Projection Chamber

A Time Projection Chamber (TPC) is a gaseous detector for charged particles which is primarily used for tracking, but which can also aid in the identification of particle types. Invented in the late 1970s [80], TPCs have already been used successfully for several large-scale experiments in the past (PEP-4 at PEP, TOPAZ at TRISTAN, ALEPH and DELPHI at LEP, STAR at RHIC), and several future experiments will use – or are planning to use – a TPC as well (ALICE at LHC, ND280 at T2K). A TPC is also under consideration as the main tracking device for a detector at the ILC.

5.1 Basic Concept

A typical TPC consists of a gas-filled, but otherwise empty volume, which is pervaded by a homogeneous electric field. When a charged particle traverses the TPC volume, gas atoms are ionised along the path of the particle. The resulting electrons and ions are separated by the electric field and drift in opposite directions towards the anode and the cathode, respectively. Shortly before arriving at the anode, the electron signal is amplified and finally sensed by a segmented readout structure (figure 5.1).

The charge pattern that is detected on the readout structure immediately yields a two-dimensional projection of the initial particle track along the – ideally parallel – drift lines onto the readout plane. Using an external timing trigger, the third coordinate can be reconstructed from the time interval

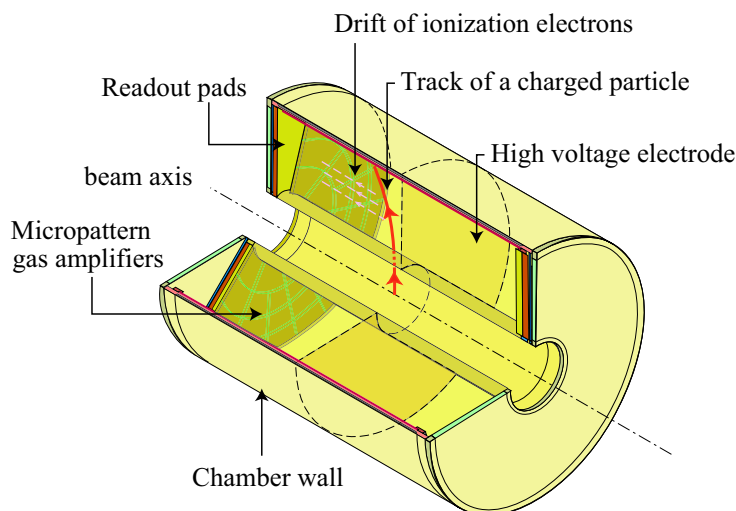


Figure 5.1: Schematic layout of a TPC [39]

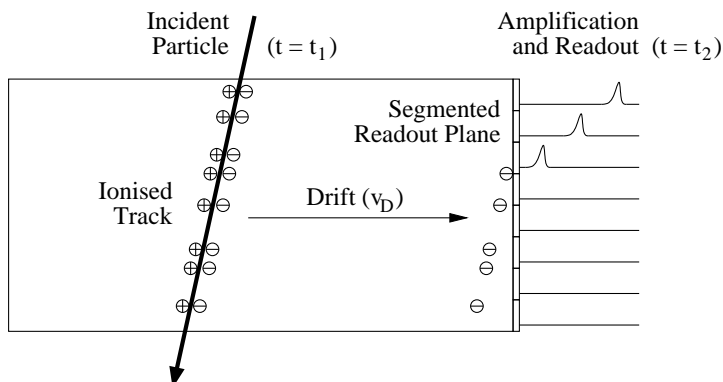


Figure 5.2: Basic principle of a TPC. The position of the track can be reconstructed from the drift time $\Delta t = t_2 - t_1$ and the drift velocity v_D .

between the incidence of the primary particle and the arrival of the charge signal on the readout plane, multiplied by the – ideally constant – drift velocity (figure 5.2). This makes the TPC a fully three-dimensional tracking device.

As a part of a large detector, TPCs typically have a tubular shape, with a cylindrical or polygonal inner and outer barrel and two parallel endplates. The cathode, consisting of two metal meshes or metallised plastic foils, is located at the centre plane of the chamber, whereas the anodes, including signal amplification, readout and front-end electronics, are located at the endplates.

To ensure a good, homogeneous electric field between the cathode and the anode, additional conductive field strips are attached to the barrels. Set to steadily increasing electric potentials by a resistor chain and acting as equipotential lines, these strips form a so-called “field cage”, which keeps the electric field lines straight on their way from the anode to the cathode.

In order to measure the momenta of particles from the curvature of their tracks, most large particle detectors have a magnetic field of the order of one up to a few Tesla. For the ILC detector, the TPC-based concepts currently foresee solenoidal field strengths ranging between 3 and 4 T. Such a homogeneous magnetic field that is parallel to the electric field can also improve the spatial resolution of a TPC significantly (section 5.2.2).

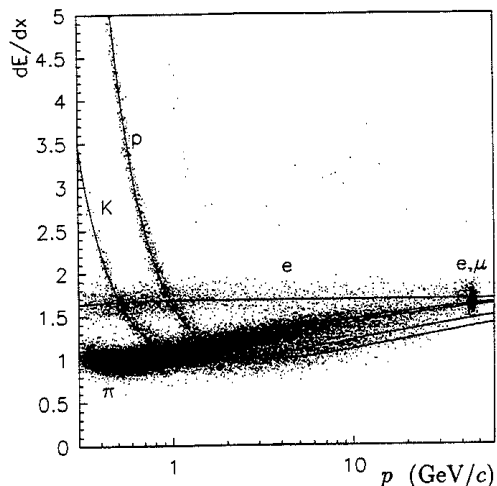


Figure 5.3: Energy loss of pions, kaons, protons, and electrons [84]. The solid lines correspond to the mean energy loss, calculated with the Bethe-Bloch formula. The dots correspond to particles measured in the ALEPH TPC.

5.2 Ionisation and Drift

5.2.1 Interaction of Particles with Gas

The basic process in a TPC is ionisation: incident particles interact with electrons of atoms in the chamber gas via their electric charge. Some electrons are merely excited without being detached from their atoms whereas others are released to leave an ionised atom behind. These electrons usually have more kinetic energy than is needed to break free from the atom, such that they can often ionise other atoms in turn and form so-called ionisation clusters [81]. If an electron has enough energy to travel a sizable distance away from the primary track, it is sometimes called a “delta ray”, even though no precise definition exists for this term.

The incident particles lose energy by ionising the chamber gas, even though this loss is hardly noticeable with respect to the curvature of the tracks, except for very low-energy particles. However, the mean energy loss per unit of length – described by the Bethe-Bloch formula [82] – is a characteristic property of each particle type, and the measurement of dE/dx is an essential quantity for particle identification. As an example, measurements made with the ALEPH TPC [83, 84] are shown in figure 5.3.

For a detector with a very low density (or thickness), as in the case of a TPC, the energy loss for a given thickness of the detector material is approximately described by a Landau probability distribution [85]. Its most

probable value is immediately related to the Bethe-Bloch prediction, but the overall distribution is strongly asymmetric with a long tail towards high energy losses: even though most of the ionisation clusters contain only a few electrons, every now and then the incident particle loses a lot of energy to form a very large cluster along its track or even a visible delta ray.

Neutral particles are not directly visible for a TPC because they do not ionise the chamber gas – they can only be detected if they interact with the gas and produce charged secondaries. Depending on their energy, photons can interact via the photoelectric effect (dominant for $E_\gamma < 100$ keV), Compton scattering (for $100 \text{ keV} < E_\gamma < 10 \text{ MeV}$), or conversion to an electron-positron pair (significant only for $E_\gamma > 1.02 \text{ MeV}$). Other neutrals with a mean lifetime of the order of 10^{-10} s (such as Λ^0) may decay inside the chamber, thereby possibly leaving tracks of charged decay products.

A special case are low-energy neutrons: since the cross-section for elastic nucleon-nucleon scattering rises towards low energies, neutrons may scatter with protons in the chamber gas. Due to the almost equal masses of both particles, this elastic scattering allows a nearly perfect momentum transfer from the neutron to the proton. Because of its large mass, the recoiling proton has a large dE/dx and a short range in the chamber gas, such that it deposits its kinetic energy quickly and produces a strong ionisation in a small volume. For example, a proton with a typical energy of 10 keV only has a range of the order of $100 \mu\text{m}$.

5.2.2 Electric and Magnetic Fields

After the ionisation process, electrons and ions are accelerated by the electric field towards the anode and cathode respectively. Due to stochastic collisions with gas atoms and molecules, they quickly reach a constant drift velocity \vec{v}_D , which can be calculated as a steady solution of the Langevin equation [86]:

$$\vec{v}_D = \frac{\mu E}{1 + \omega^2 \tau^2} \left[\hat{E} + \omega \tau \hat{E} \times \hat{B} + \omega^2 \tau^2 (\hat{E} \cdot \hat{B}) \hat{B} \right], \quad (4)$$

where E and B are the electric and magnetic field strengths with their respective unit vectors \hat{E} and \hat{B} , τ is the average time between collisions, $\omega = eB/m$ is the cyclotron frequency, and $\mu = e\tau/m$ is the mobility of the charge carriers. τ and consequently μ depend on the properties of the chamber gas [87].

If the electric and the magnetic fields are parallel – as is typically the case in a TPC –, equation (4) can be simplified using $\hat{E} = \hat{B}$, $\hat{E} \cdot \hat{B} = 1$, and $\hat{E} \times \hat{B} = 0$, yielding

$$\vec{v}_D = \mu \vec{E},$$

which is equal to the case without any magnetic field at all. Only if \vec{E} and \vec{B} are not parallel, so-called $\vec{E} \times \vec{B}$ effects become visible and the additional terms in equation (4) start to affect the drift of the charge carriers.

It should be noted that equation (4) applies both to drifting electrons and to ions. Due to their much larger mass, the mobility and therefore the drift velocity of ions is about 1000 times smaller than that of the electrons. In the presence of a strong magnetic field, the term $\omega\tau$ can get large (typically 1 to 5) for drifting electrons, such that equation (4) is dominated by its third term – the electrons basically follow the magnetic field lines, even though the drift is incited by the electric field. In contrast to that, $\omega\tau$ will always be small (typically $\mathcal{O}(10^{-4})$) for the heavy ions, so that they still follow the electric field lines.

Apart from keeping the drift velocity constant on a macroscopic scale, the collisions with gas atoms and molecules randomly influence the drift path of each single charge carrier, causing it to deviate from its ideal line of flight in a kind of random walk. On a macroscopic scale, an initially point-like charge cloud becomes wider (transversally, i. e. perpendicular to the drift direction) and longer (longitudinally, i. e. parallel to the drift direction) during the drift. This diffusion leads to a three-dimensional Gaussian profile with the widths

$$\sigma_T = D_T\sqrt{L} \quad \text{and} \quad \sigma_L = D_L\sqrt{L},$$

where D_T and D_L are the transversal and longitudinal diffusion coefficient respectively, and L is the drift length. A magnetic field that is parallel to the drift direction suppresses the transverse diffusion:

$$D_T(B) = \frac{D_T(0)}{1 + \omega^2\tau^2}$$

The diffusion coefficients D_T and D_L depend on the properties of the chamber gas.

5.2.3 The Chamber Gas

As with any gaseous detector, the choice of the chamber gas strongly affects the properties and eventually the performance of a TPC. Desirable characteristics are:

- a high drift velocity (to avoid accumulation of too many events inside the chamber, section 5.4.3),
- a very low transverse and a low longitudinal diffusion coefficient (to prevent deterioration of the spatial resolution, section 5.2.2),

- a sufficiently large specific energy loss dE/dx (to increase statistics for track reconstruction and particle identification),
- a high enough stability against electrical breakthroughs (to allow reliable operation of the amplification system, section 5.3),
- nonhazardous chemical properties (to address safety concerns like inflammability and damages to the hardware by ageing effects).

Many gas parameters depend on the electrical field strength, particularly the drift velocity [87], which is crucial for the reconstruction of the track position along the drift direction (cf. figure 5.2). In order to minimise influences of possible small field inhomogeneities, the working point of the chamber is typically chosen on a local maximum of the drift velocity as a function of the field strength. Most gases expose such a maximum as a consequence of the quantum-mechanical Ramsauer effect [88].

Chamber gases typically are mixtures of a noble gas and one or more quenchers in a concentration of a few up to several ten percent. The noble gas atoms can easily be ionised whereas the molecules of the quencher can absorb ultraviolet photons from recombination processes, thereby suppressing unwanted discharge cascades. The TESLA TDR [35] favoured a mixture of 93 % Ar, 5 % CH₄, and 2 % CO₂ – often dubbed “TDR gas” – for its high drift velocity and low transverse diffusion. In contrast to that, the ILC RDR calls for just 95 % Ar and 5 % CH₄ – sometimes called “P5” – because of its even more favourable diffusion coefficients, which are lower in the drift region, but higher in the amplification region. Since many gas parameters depend critically on the composition of the mixture and have an immediate impact on the overall chamber design and performance, the optimisation of the TPC gas mixture is still ongoing and several alternatives are being considered.

Most of the gas mixtures with acceptable properties contain carbohydrates, either in the simple form of CH₄ or as higher homologues such as iso-C₄H₁₀. In the past, it has been considered to avoid such substances because of the possible scattering of neutrons with hydrogen nuclei in the gas: if many neutrons from the detector background traverse the TPC, recoil protons might become a significant source of background signals in the chamber.

An alternative to standard carbohydrate-based quenchers would be CF₄, where the hydrogen has been replaced by fluorine and where the cross section for neutron scattering is much lower. However, CF₄ has problematic chemical properties: fluorine radicals can be released through radiolysis, and these may afterwards react with water vapour (which would always be contained in the chamber gas, at least in traces) to form hydrofluoric acid. As a strong

chemical agent, this acid could contribute to ageing effects and maybe even damage the amplification system over time [89].

The question whether hydrogen in the chamber gas should be avoided has already been addressed in earlier studies for TESLA [90], but providing an answer for the current ILC design that is based on full detector simulations is one of the goals of this thesis.

5.3 Signal Amplification and Gating

After drifting to the anode, the electrons from the ionised track have to be amplified before they can be detected by the readout electronics. This is accomplished by proportional gas amplification: in a relatively small spatial region with a strong electric field (a few 10 kV/cm), drifting electrons are accelerated so strongly that they acquire enough kinetic energy between collisions to ionise further gas atoms. This leads to a charge cascade that – depending on the detailed experimental set-up – grows approximately exponentially [81].

5.3.1 Proportional Wires

Classically, thin metal wires are used for signal amplification in gaseous chambers (not only TPCs): the required strong field is created by applying a high voltage to wires with a small radius. Drifting electrons are attracted by the wires and get amplified in an avalanche shortly before they reach the wire surface. In the case of a TPC, a layer of parallel wires is placed a few centimetres above the anode plane. Both the wires and the anode plane, on which a charge signal is induced by the amplification process, can be read out.

Wires have been the standard amplification device in gaseous detectors for a long time, but they cannot meet the requirements of the ILC detector. Due to the large electrostatic forces, they cannot be placed much closer than 1 cm apart from each other, and this distance influences the achievable spatial resolution as well as the $\vec{E} \times \vec{B}$ effects that distort the drift paths (section 5.2.2). Furthermore, wires need to be held under tension and therefore require a stable and rather massive support structure.

In order to substantially improve the performance that was, for example, achieved by the ALEPH TPC, there is common agreement that so-called Micro-Pattern Gas Detectors (MPGDs) should be used for the ILC TPC. Two possible amplification devices that are currently under study are Gas Electron Multipliers (GEMs) and Micro-Mesh Gas Amplifiers (Micromegas). Both kinds of devices use very small structures for signal amplification ($\mathcal{O}(100 \mu\text{m})$)

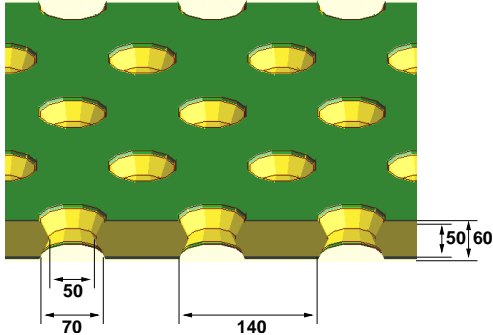


Figure 5.4: Geometry of a standard CERN GEM (values are given in micrometres)

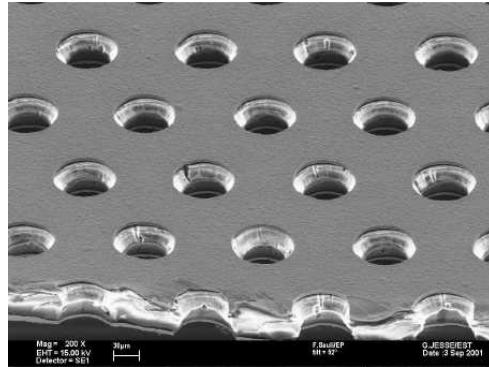


Figure 5.5: The same in reality, imaged with an electron microscope [92]

compared to $\mathcal{O}(1\text{ cm})$ in the case of wires) and have therefore an intrinsically better spatial resolution. Moreover, they allow the read-out of the fast electron signal, whereas the dominant process of signal formation with wires is the rather slow drift of ions.

5.3.2 Gas Electron Multipliers

GEMs are a novel concept of gas amplification devices that overcome the problem of wires [91]. They consist of a polyimide (better known as Kapton) foil with a thickness of $50\text{--}100\ \mu\text{m}$ that is covered by thin layers of copper (typically $5\ \mu\text{m}$ on each surface). The whole foil is covered by a regular pattern of small holes. GEMs that are available from CERN have a hexagonal arrangement of holes with $70\ \mu\text{m}$ diameter and $140\ \mu\text{m}$ centre-to-centre distance (figures 5.4 and 5.5), but different designs are produced by other suppliers as well.

When a voltage of several hundred Volts is applied to the surfaces of the GEM, the electric field inside the holes gets strong enough to amplify electrons that pass through (figure 5.6). This process can be quantified by three parameters [93, 94] (cf. figure 5.7):

- the collection efficiency C , which corresponds to the probability that a charge carrier that approaches the GEM enters a GEM hole (and does not end up on the front-side copper surface)
- the gain G , which is equal to the amplification factor inside the GEM hole

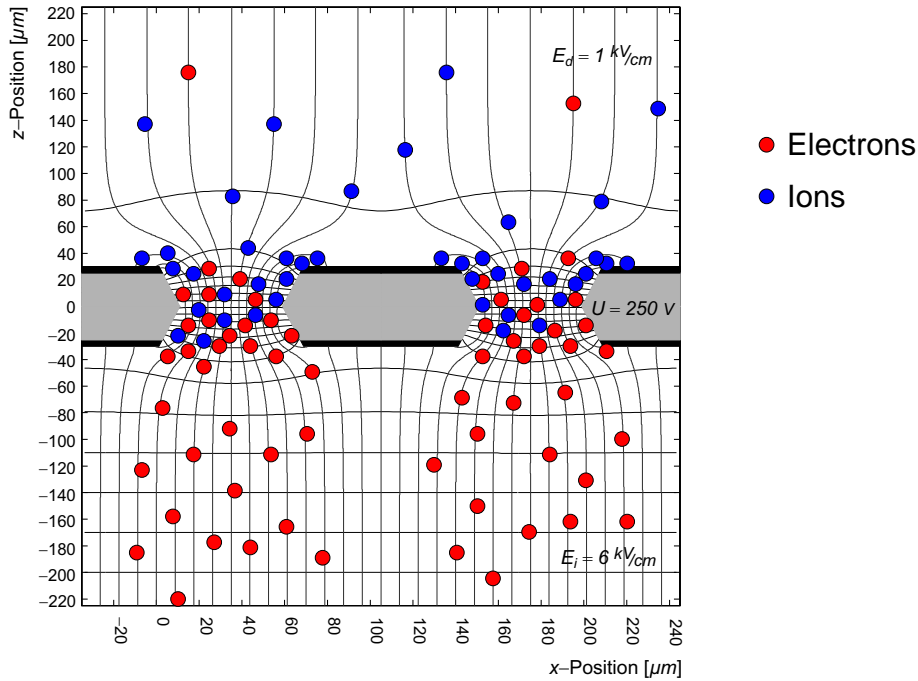


Figure 5.6: Working principle of a GEM foil (adapted from [93])

- the extraction efficiency X , which corresponds to the probability that a charge carrier inside the hole eventually leaves the GEM structure (and does not end up on the back-side copper surface)

The gain mainly depends on the applied voltage, whereas the collection and extraction efficiencies also depend on the field strengths in the surrounding volume. A single GEM foil can reach an effective gain $G_{\text{eff}} = C \cdot G \cdot X$ of up to 1000. Since $\vec{E} \times \vec{B}$ effects play a crucial role in GEMs (at least on the small scale of around $100 \mu\text{m}$), the efficiencies for electrons and ions can be significantly different.

GEMs are mostly used in structures of two or three foils stacked above each other, allowing a lower voltage in each single GEM and therefore a more stable operation. Typical distances in a GEM set-up are 1–2 mm between the foils and 1–5 mm between the final GEM and the anode plane where the amplified signal is read out. GEMs need a support structure to keep them flat and to ensure defined distances between them. This can either be achieved by frames that keep the foils tightened or by spacers that are fixed between the foils.

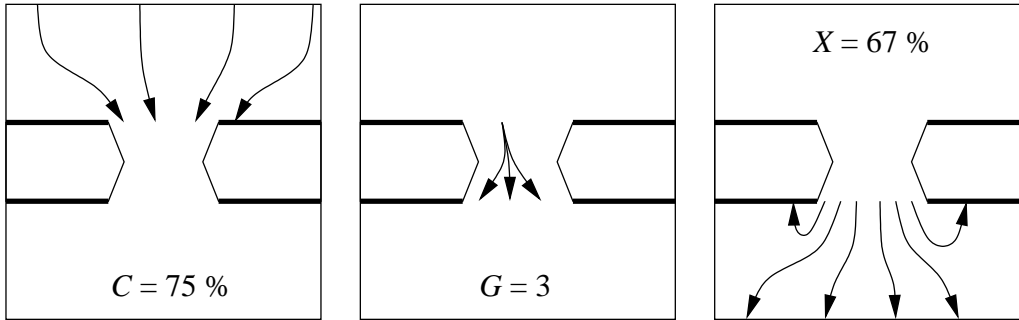


Figure 5.7: Illustration of the collection efficiency (left), the gain (middle), and the extraction efficiency (right) of a GEM. Collection and extraction efficiency are shown for electrons, but corresponding values can also be defined for ions drifting in the opposite direction. The indicated values have merely been chosen for clarification – they are not related to the values in a typical experimental set-up.

5.3.3 Micromegas

Similar to GEMs, Micromegas also use a thin region ($50\text{--}100\ \mu\text{m}$) with a high electric field (typically $30\ \text{kV/cm}$) for gas amplification. A very fine wire mesh is positioned in front of the anode plane and forms a large parallel-plate capacitor (figure 5.8). If a high voltage is applied to the mesh, drifting electrons get amplified as soon as they enter the high-field region between the mesh and the anode. To ensure a uniform amplification gain, the distance between the mesh and the anode needs to be kept constant. This is ensured by tiny pillars that act as spacers.

Micromegas reach typical amplification factors of 10^4 , which is sufficient for the readout of a gaseous detector like a TPC. The micro-mesh needs no further support structure except for the built-in spacing pillars, but the anode plane needs to be stiff enough to avoid a possible bending of the whole Micromegas set-up.

Extensive tests by various R&D groups have shown that GEMs [96, 97] and presumably also Micromegas [98] would be able to meet the performance requirements of the ILC TPC. However, it has not yet been decided which of the two technologies should be used in the end. Further comparative studies are currently ongoing.

5.3.4 Ion Backdrift and its Suppression

Any kind of amplification device creates not only secondary electrons, but also the same amount of ions. These ions move in the opposite direction – i. e.

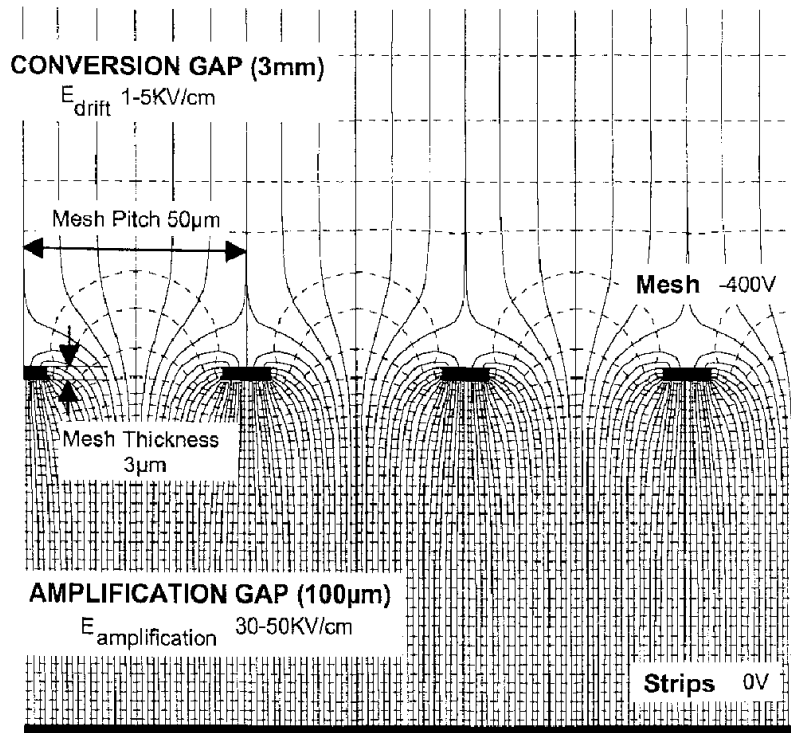


Figure 5.8: Geometry of a Micromegas [95]

away from the anode region into the main chamber volume – and furthermore have a much lower drift velocity, meaning that they could accumulate in the chamber gas and build up a significant space charge in the form of “ion discs” (figure 5.9). This might affect the drifting electron tracks through electrostatic attraction as well as inhomogeneities of the drift velocity (which depends on the electric field strength). In order to minimise this deteriorating influence on the spatial resolution of the chamber, the backdrift of ions should be suppressed.

One possible mechanism of backdrift suppression, often used together with wire amplification, is a so-called gating grid: an additional layer of metal wires is placed in front of the amplification structure. While the chamber is being read out immediately after an event, the gating wires are kept at an electric potential that corresponds to their position in the drift field – the wires are basically “invisible” to the drifting electrons and the gate is open. In the time between two events, alternating positive and negative high voltages are applied to the gating wires so that virtually all field lines terminate on the wires – the gate is closed and the backdrifting ions cannot enter the main chamber volume anymore (figure 5.10).

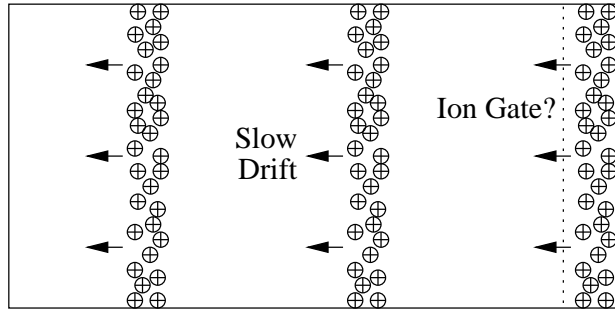


Figure 5.9: Ions that can escape from the amplification system drift back through the chamber volume. Since their drift velocity is so small, they form multiple thin discs that originate from different bunch trains.

The problem with this relatively simple yet effective scheme is that it cannot be immediately applied to the timing structure of the ILC: the bunch spacing of the machine is so small (compared to the readout time) that tracks from many events are drifting through the chamber at once, and the TPC is continuously read out during a whole bunch train. Closing a wire gate and thereby blinding the chamber during a bunch train would mean the loss and corruption of a significant amount of information.

The only feasible application of a gating grid (or similar mechanism) would be at the end of a whole bunch train, but this would imply a much larger distance of the grid (typically 10 cm) in order to be able to capture all ions from the whole bunch train. Besides, this approach would not save “later” tracks in a bunch train from having to pass through the ion disc that has already built up since the beginning of the train (cf. figure 5.9). All in all, it is therefore still under discussion whether a dedicated gating structure should be used in the ILC TPC or not.

Another promising approach is to exploit the “built-in” ion backdrift suppression of GEMs: since the slow, heavy ions basically exactly follow the electric field lines (section 5.2.2), they have a high probability of being caught in the distinct field pattern of a GEM foil and of ending up on its backside copper surface, i. e. their extraction efficiency can be tuned to be very small. In contrast to that, the drift path of electrons is dominated by the magnetic field lines, such that their extraction efficiency will be much larger. Using a multi-GEM structure with optimised electric field strengths and voltages, the amount of backdrifting ions can be suppressed approximately down to the level of the incoming electrons, i. e. down to the order of space charge that can in principle not be avoided in any case.

Micromegas provide a similar mechanism for the suppression of ion back-

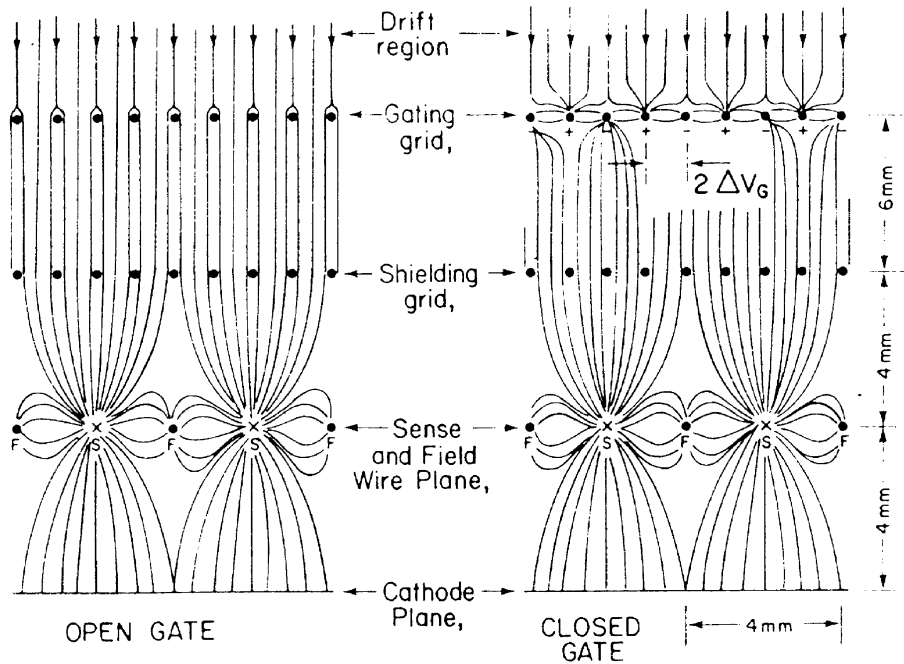


Figure 5.10: Working principle of gating wires, here shown for a drift chamber with wire amplification [99]. The open gate (left) does not influence the drifting electrons, whereas the closed gate (right) blocks the path for back-drifting ions.

drift: the electric field lines between the mesh cells and the anode plane form a funnel-shaped field configuration that will guide most ions to the mesh wires instead of the sensitive chamber region.

5.4 Pile-up and Readout

After their amplification, the signals that have drifted through the chamber towards the anode plane are read out, amplified and digitised by the front-end electronics of the chamber, sent to the data acquisition system, stored and finally analysed. The reconstruction software performs a pattern recognition to find coherent tracks and finally does a mathematical fit to determine the trajectories and momenta of the incident particles [100].

5.4.1 Anode Pads and Voxels

The anode plane is segmented into small pads that are read out as separate channels. The typical layout for a large TPC at a particle collider are trape-

zoidal pads that are arranged in concentric circular rows. The plans for the ILC TPC foresee pads with a size of about $5\text{ mm} \times 1\text{ mm}$, resulting in roughly 200 rows with 2000–10000 pads per row. The pads are very narrow in the azimuthal direction to allow for a precise point resolution in φ and therefore a high momentum resolution. The radial size is significantly larger in order to reduce the number of channels (and cost of the electronics) and also to collect enough primary electrons per pad to get a sufficient signal-to-noise ratio in the readout.

The signals that are sensed by the anode pads are digitised with a given sampling frequency. The duration of a so-called time bin, multiplied with the drift velocity, corresponds to a virtual longitudinal segmentation of the chamber volume, i. e. a slicing of the volume into thin discs, which are read out one after another. With a maximum drift length of about 2 m, a drift velocity of the order of $50\text{ }\mu\text{m/ns}$, and a typical sampling frequency of 20–40 MHz, the ILC TPC will contain approximately 1000–2000 time bins in each of the two halves.

Altogether, the radial segmentation by pad rows in r , the azimuthal segmentation by pads in φ , and the longitudinal segmentation by time bins in z divides the whole volume into so-called voxels, which correspond to the smallest unit of information that can be read out from the chamber. The whole ILC TPC will contain around $1\text{--}2 \cdot 10^9$ voxels. However, the largest fraction of these voxels will not contain any charge at a given point in time. The so-called occupancy of the chamber is defined as the fraction of voxels that contain some charge signal and that would therefore yield non-zero data after readout and digitisation.

A higher occupancy means a higher data rate that has to be transmitted out of the detector and written to a data storage, but also a more difficult task of pattern recognition and track fitting. However, it is generally believed that an occupancy of up to 1% would not pose a problem for an advanced pattern recognition algorithm and the subsequent fitting procedure, thus having virtually no impact on the performance of the TPC in terms of efficiency and resolution [63].

5.4.2 Overlay of Events

The time structure of the ILC will not leave a pause between bunch collisions that would be large enough to let all tracks from one event fully drift towards the anode, such that the chamber would be empty after each event and individual events could be cleanly separated. Instead, the bunch spacing (369 ns) is small compared to the maximum drift time ($\mathcal{O}(50\text{ }\mu\text{s})$), so that

tracks from 100–150 collisions will be overlaid in the chamber at any given point in time.

With a bunch separation of 330 ns and a typical drift velocity of $50 \mu\text{m}/\text{ns}$, the tracks of each event will be shifted by approximately 15 mm towards the anode before the next collision takes place. It should be noted that tracks from a later bunch crossing can easily be sensed before tracks from an earlier bunch crossing, e. g. if they have a smaller polar angle or if they are created closer to the anode.

5.4.3 Timing and Event Decomposition

A TPC translates the drift time of a charge signal into the spatial distance from the origin of the charge (i. e. the track of the incident particle) to the readout. However, the chamber can only measure the time of arrival on the readout structure directly – the beginning of the time interval needs to be taken from a different source of information.

In the case of a low collision rate without event overlaps, the time of the bunch collision can be taken as the moment in which all tracks are produced at once. The synchronisation of the machine clock and the detector clock then allows a direct measurement of the drift times. Similarly, in measurements with cosmic muons, the signal of a fast scintillator can provide an external time reference.

In contrast to that, is it not clear at first when a given track in the ILC TPC was produced, since it might in principle belong to any of the dozens of bunch crossings that are overlaid in the chamber at any given time. There are multiple ways to attach a timestamp to a track in the chamber in order to determine its absolute position in time and in the drift direction:

- If the track comes from the central axis, it was most likely produced in the interaction point. Using this assumption, the track can be assigned unambiguously to one bunch crossing, since the shift of 15 mm between each bunch crossing is large enough to be resolved by the chamber.

This will work for a large part of all medium- to high-energy tracks, except some decay products that do not originate from the interaction point.

- If the track ends without reaching the outer wall, it can be assumed that it has reached the anode endplate and left the chamber. The end of the track then corresponds to zero drift time. If the particle energy is not too low, a matching signal should appear in the calorimeter endcaps.

- By referring to an additional detector with sufficient timing capabilities and spatial resolution (e. g. fast silicon strip detectors that can differentiate between single bunch crossings, or even the ECAL), a matching of TPC tracks with the hits on this detector could be used to determine timestamps for the tracks.

The vertex detector is not a candidate for this task because it will probably integrate over roughly as many bunch crossings as the TPC, but the Silicon Intermediate Tracker (SIT) and the outer Forward Tracking Discs (FTDs) should be fast enough for a precise timestamping. Furthermore, the Silicon Envelope Tracker (SET) and the so-called Endcap Tracking Discs (ETDs) could provide another reference point at the outside of the TPC.

- When a low-energy track appears somewhere in the middle of the chamber (e. g. from Compton scattering) and is also stopped before reaching any boundary, there is generally no means – but also no need – to determine its absolute position.

Using these methods, it should be possible to assign basically all relevant tracks in the chamber to the events from which they originated. Furthermore, as already mentioned in section 2.1, the total event rate at a lepton collider is so low that a pile-up of multiple events with high-energy tracks in a given readout frame is rather unlikely.

5.4.4 Track Reconstruction and Charge Sharing

The digitised data from the TPC have to be filtered by a pattern recognition and track finding algorithm, and the parameters of the found tracks have to be determined by a fitting procedure – this can either happen in separate steps or in one go. There are several approaches to track fitting, either based on single reconstructed hits per pad row or on the global charge distribution as a whole [96, 101, 97].

In any case, all reconstruction methods have in common that their performance greatly improves if they do not act on single pads and on single time bins: as soon as a so-called charge sharing takes place between adjacent pads (and also between subsequent time bins), the original position of the track can be reconstructed much more precisely with the help of the centre-of-gravity method or more advanced techniques (figure 5.11).

This widening of the charge signal partially already happens through diffusion in the drift volume, even though the diffusion generally decreases the resolution because of the low primary statistics. In a GEM set-up, charge

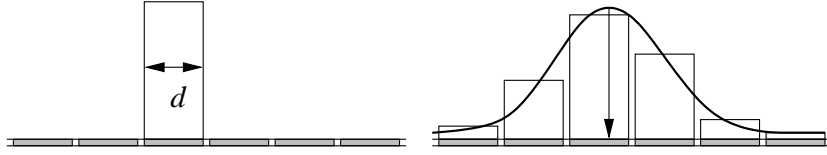


Figure 5.11: If a signal is found only on a single pad, its position cannot be determined with a precision better than $d/\sqrt{12}$ (“hodoscope limit”). In the case of charge sharing between several pads, the position can be reconstructed much more precisely.

sharing is achieved through the widening of the signal in the amplification structure, where the high electric field strengths result in large diffusion constants. In the case of Micromegas, an additional resistive foil may be used on top of the anode plane to spread the amplified signal over multiple pads [102].

5.5 Performance and Advantages

The transverse momentum resolution Δp_t of a tracking device – one of the basic figures of merit – is described by the Glückstern formula [103]:

$$\frac{\Delta p_t}{p_t^2} \propto \frac{\sigma_{r\varphi}}{BL^2} \sqrt{\frac{720}{n+4}},$$

where $\sigma_{r\varphi}$ denotes the spatial single-point resolution in the $r\varphi$ -plane, B is the magnetic field strength (which bends the particle trajectories depending on the momentum), L is the length over which the measuring points are distributed, and n is the number of single-point measurements that are used in the overall track fit.

On the one hand, a good (i. e. small) single-point resolution, a strong magnetic field, a large detector radius, and a large number of measuring points are helpful to reach a good momentum resolution. On the other hand, the magnetic field strength and the detector size have an immediate impact on the cost, meaning that a trade-off between performance and feasibility must be found. Since there are also several other subdetector systems besides the tracker, common studies to optimise the layout of the overall detector are currently ongoing.

Even though the design of the ILC detector is not yet finalised, there is strong confidence that a TPC will be able to meet the performance goals of the ILC tracker: with a single-point resolution of $\sigma_{r\varphi} \approx 100 \mu\text{m}$ (which has already been demonstrated by various R&D projects [96, 97]), with a magnetic field of 3–4 T, with an inner radius of 0.3 m and an outer radius of

1.5–1.8 m, and with approximately 200 pad rows, the TPC can reach a transverse momentum resolution of the order of $\Delta p_t/p_t^2 \approx 10^{-4} \text{ GeV}^{-1}$ [63]. The combination with the measured points from the silicon devices would then yield the required transverse tracking resolution of $5 \cdot 10^{-5} \text{ GeV}^{-1}$. In addition, the longitudinal resolution of $\sigma_{rz} \approx 2 \text{ mm}$ and the two-track separation of 2 mm and 5 mm in the transverse and longitudinal direction respectively, allow a highly robust and efficient pattern recognition, even in jets or in the presence of backgrounds.

Compared to silicon sensors, the spatial single-point resolution of a TPC is not exceptionally good, but this is easily compensated by the large number of measuring points in the hundreds of pad rows, compared to a few layers of silicon. Furthermore, the large number of points also allows a precise measurement of the strongly fluctuating dE/dx , thereby helping in the identification of particle types. The ILC TPC is designed for a precision of $\Delta(dE/dx)/(dE/dx) \leq 5\%$.

With regard to the overall concept of Particle Flow, the TPC has important advantages: due to the very low material budget, particles coming from the interaction point only traverse approximately 3% of a radiation length in the central region. This results in a low energy loss in front of the calorimeters, little multiple scattering, and a low conversion probability for photons. The material budget in the endplates is somewhat worse and lies typically around 15–30% of a radiation length. Furthermore, because of the large number of three-dimensional measuring points, a TPC will allow robust and highly efficient pattern recognition, which is a crucial input for Particle Flow algorithms. A TPC will even be able to recognise backscattering particles, particle decays, and kinks that are caused by the emission of neutral particles in flight.

Apart from the low material budget, the usage of gas as the sensitive material also means that a TPC is almost immune against radiation damage, except for ageing effects from quencher gases that might affect the amplification structures.

A problematic feature of a TPC is its slow readout and event pile-up, caused by the relatively slow drift velocity of electrons in the chamber gas. This is still acceptable for an ILC detector with its low background levels and event rates, but it is the reason why the usage of a TPC for the high-luminosity LHC experiments ATLAS and CMS would not have been feasible.

6 Simulation Tools

6.1 Guinea-Pig – Pairs Generator

Guinea-Pig [50, 104] is a tool for the simulation of beam-beam interactions at electron-positron colliders. It was originally developed for the study of electromagnetic and hadronic background in the interaction region of the TESLA collider and has since then been one of the standard tools for the simulation of beam-induced backgrounds.

Beam-beam interaction is handled on a semi-microscopic level: the particles in the colliding bunches (typically in amounts of the order of 10^{10}) are grouped together as so-called macroparticles, filled into a grid of spatial bins, and then tracked through the collision. The macroparticle approach is a trade-off between accuracy and execution speed, but the simulation takes several parameters into account that can be tuned such that Guinea-Pig produces reliable, stable results in a reasonable amount of time.

Guinea-Pig generates several kinds of output: the user can choose to have the spent beams, the beamstrahlung photons, electron-positron pairs, and minijets (i. e. hadronic scattering products of the beamstrahlung photons) written to output files. Apart from that, Guinea-Pig will determine the luminosity spectrum (i. e. the energy spectrum of colliding particles at the moment of a possible hard interaction) and the overall luminosity of the collision, thereby taking into account the beam-beam effects.

Guinea-Pig uses different models for the processes that contribute to the incoherent production of electron-positron pairs from the interaction of beamstrahlung photons (cf. section 3.2): the Breit-Wheeler process (two real photons) is modelled by a leading-order cross-section calculation, whereas the Bethe-Heitler process (one real and one virtual photon) and the Landau-Lifshitz process (two virtual photons) are calculated using the so-called Equivalent Photon Approximation (EPA), replacing virtual photons with an equivalent spectrum of real ones as long as their virtuality is not too large. This upper limit in the EPA model is taken to be $Q^2 = \hat{s}/4$, which is the recommended choice for Guinea-Pig.

The simulation results of Guinea-Pig cannot be compared to measurements because beamstrahlung pairs have not been seen at any existing particle collider yet, but comparisons have been made with the generator programs CAIN [105] (which uses the same models as Guinea-Pig, but a different implementation) and BDK [106] (which uses cross-sections calculated from matrix elements for the Bethe-Heitler process). These comparisons show good agreement on the level of 10 % between the different generators [56] (with Guinea-Pig predicting slightly higher, i. e. more conservative values), such that the

generation of pairs by Guinea-Pig seems to be reasonably reliable, even in the absence of experimental data.

In contrast to the process of electron-positron pair production, the production of minijets involves the hadronic structure of the photon and low-energy QCD, both of which are difficult to handle. Guinea-Pig has an internal cut-off of 1 GeV for the centre-of-mass energy of two photons that will produce a hadronic final state. First calculations that tried to take into account the full energy range down to the two-pion production threshold suggest that the number of minijets predicted by Guinea-Pig might be too low by a factor of five [59]. For a detailed understanding of these processes, further studies are needed.

There are two sets of parameters that determine the outcome of a Guinea-Pig simulation: the one set specifies internal settings of the simulation, such as the number and the size of simulated grid cells, enhancement factors, and internal cuts. The settings that were used for the simulations presented in this thesis mostly follow the suggested default values and can be found in table A.2. The minimum energy for pairs is chosen as $E_{\min} = 5$ MeV. The other set of parameters describes the properties of the colliding beams (cf. section 2.4). As an example, the settings for the ILC-NOM-500 parameter set are listed in table A.1.

Guinea-Pig version 1.12.1 was used for the simulation of pairs from 100 bunch crossings for each of the beam parameter sets ILC-NOM-500, ILC-NOM-1000, ILC-LOWP-500, ILC-LOWP-1000, and TESLA-500. Furthermore, a larger sample of 3000 bunch crossings for ILC-NOM-500 has been produced.

6.2 Mokka – Full Detector Simulation

Mokka [107] is a full detector simulation that was initially developed for studies of a calorimeter for the TESLA detector. In the course of time, it has been extended to accommodate also the tracking system and other pieces of the overall detector layout. More recent versions of Mokka can also model LDC and SiD detector geometries as well as test beam set-ups for specific detector components.

Mokka is currently the standard tool for LDC detector simulations. Written in C++ and using the Geant4 framework [108, 109], it can be understood as the successor of BRAHMS [110], which was the common full detector simulation for TESLA studies, written in Fortran and based on GEANT3 [111]. The counterparts of Mokka are the mainly GLD-specific Jupiter [112] and the mainly SiD-specific SLIC [113].

For the simulations presented in this thesis, Mokka version 6.1 was used together with Geant4 version 8.1.p01.

6.2.1 The Geant4 Framework

Geant4 is a toolkit to simulate the interaction of particles with matter. Initially conceived as a successor to GEANT3 and developed at CERN as a part of the overall LHC effort, Geant4 has become one of the standard tools not only for the simulation of detectors in high-energy physics, but also in medical physics or space applications.

Geant4 is written in C++ and follows a strict object-oriented approach to provide a well-structured system of classes to represent all typical ingredients of a detector simulation. It handles the definition of detector geometries, physical processes such as the interaction of particles with matter or particle decays, the definition of “sensitive” detector components and readout structures, the navigation through the detector geometry and the tracking of particles in the presence of matter and fields, but also user interfaces and the visualisation of detector geometries and simulated events.

As every application that is based on the Geant4 framework, Mokka has to define three major ingredients of the detector simulation: the geometry of the detector (i. e. shapes, materials, and sensitive components), a so-called physics list (i. e. a list of simulated particles plus the physical processes that they may undergo), and an interface to a generator of primary particles (i. e. a source of particles that will be shot into the detector to initiate a simulated event). These ingredients will be briefly described in the following sections. More detailed information can be found in appendix B.

6.2.2 Detector Geometry in Mokka

The simulations presented in this thesis use a detector geometry which is modelled corresponding to LDC version 2 [114] from the Detector Outline Document [63] and which contains most of the detector components listed in section 4.3 – beam tube, vertex detector, Silicon Intermediate Tracker, Forward Tracking Discs, forward calorimeters and mask, TPC, ECAL, HCAL, magnet coil, magnet yoke, and a magnetic field. A full view of the central detector region is shown in figure 6.1, and a close-up of the forward region is shown in figure 6.2.

The beams in the simulated detector geometry have a crossing angle of 14 mrad, resulting in an X-shaped beam tube (figure 6.3) and an asymmetric forward region – the forward calorimeters are aligned on the axis of the outgoing beam and not on the z -axis (figure 6.4). As already mentioned

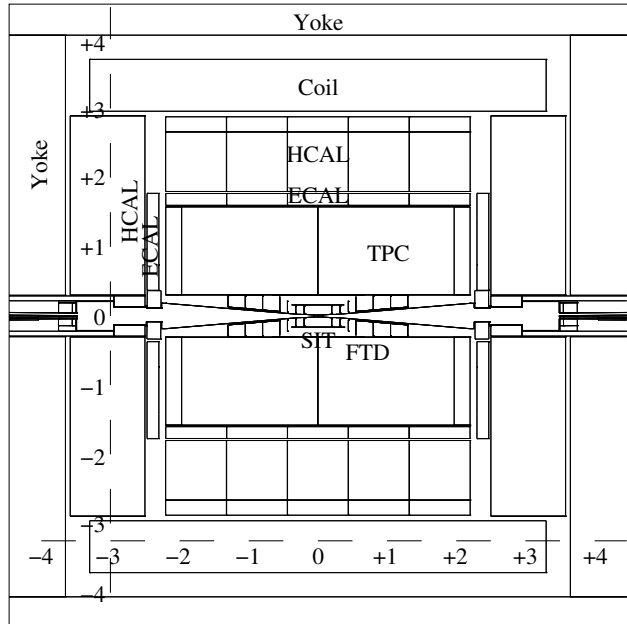


Figure 6.1: Central region of the simulated detector geometry (values are given in metres)

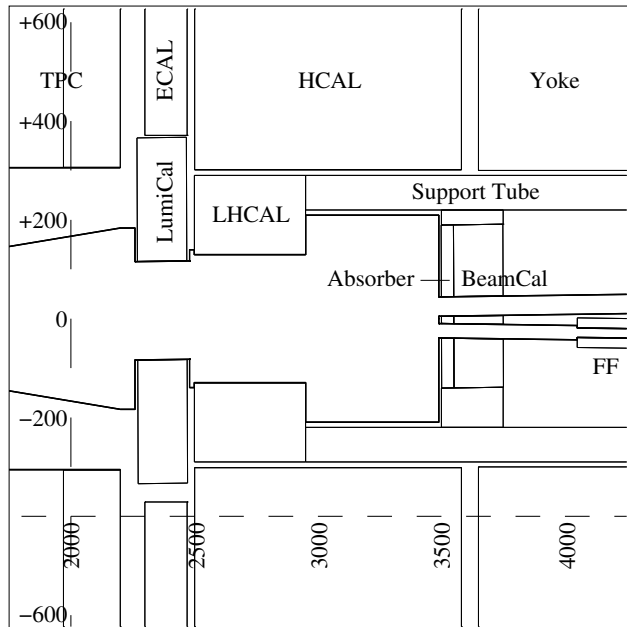


Figure 6.2: Forward region of the simulated detector geometry, compressed by a factor of 2 in z -direction (values are given in millimetres)

in section 4.4, the magnetic field configuration has an important influence on backgrounds in the case of a medium or large crossing angle. Therefore, the simulated detector geometry contains an anti-DID field, i. e. an additional dipole field is superimposed on the main solenoid such that the magnetic field lines get bent in the direction of the outgoing beams. The resulting field is illustrated in figure 6.5. Both the main solenoid [63, 115] and the anti-DID field [116] are defined by one-dimensional field maps that have been obtained from realistic field simulations (appendix B.1.13). The detector geometry also implements the (idealised) fields of the quadrupole magnets in the beam delivery and extraction system.

The simulation of a TPC with Geant4 is not straightforward: due to the low density of the chamber gas and the small probability of interactions (except ionisation), the Geant4 tracking system would normally use rather large steps when transporting particles through the chamber. This would result in very few, very large energy deposits in the gas – which utterly contradicts the working principle of a TPC.

In order to break the transportation steps down to small pieces, the TPC implementation that is used here limits the step length of the particles in the chamber: whenever a charged particle has travelled up to 5 mm in the chamber gas, the transportation is interrupted and the energy deposit that has taken place during the previous step is written to the output file. The choice of the maximum step length is a trade-off between the precision of the simulation and the amount of generated output, and the value of 5 mm can be considered as a reasonable compromise. It has the same magnitude as typical readout structures in an actual TPC for the ILC, i. e. the radial height of the anode pads, the azimuthal width of a signal cluster with charge sharing, and the longitudinal depth of a time bin that can be resolved.

A more detailed discussion on the TPC simulation in Mokka can be found in appendix B.1.6.

Finally, it should be noted that the forward calorimeters – LumiCal, LHCAL, and BeamCal – are merely modelled as solid tungsten blocks for the studies presented here. This means they will act as regular scattering targets in the simulation, but no information on detector hits will be written out. Likewise, the magnet yoke does not contain any muon chambers, but is only a solid block of iron.

6.2.3 Physics Models in Mokka

To define the different particle types that can appear in the simulation, the physical processes that they may undergo, and the specific models by which these processes are described, every Geant4 application needs to define a

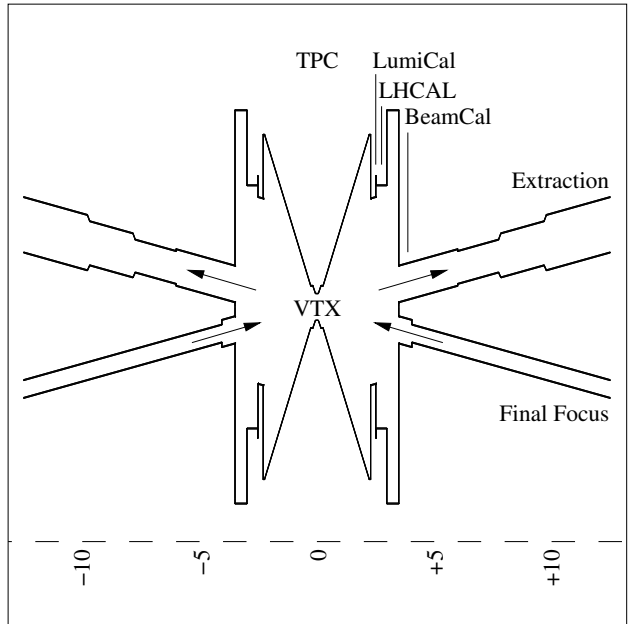


Figure 6.3: Geometry of the simulated beam tube in the xz -plane, compressed by a factor of 40 in z -direction (values are given in metres)

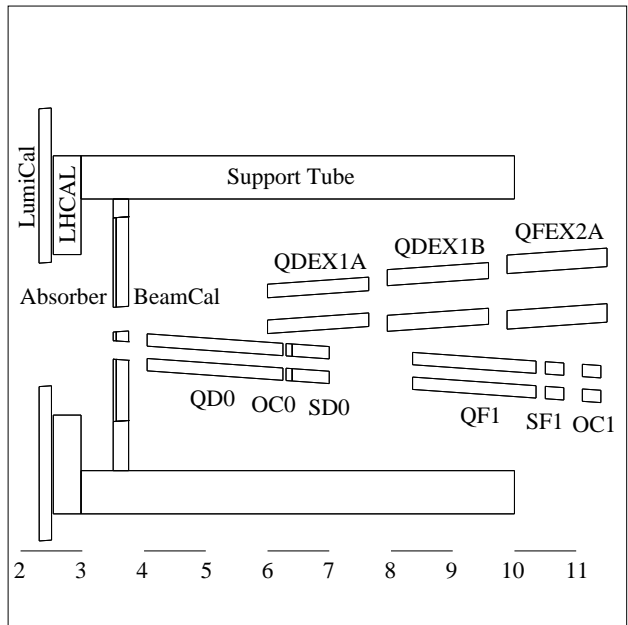


Figure 6.4: Geometry of the simulated forward mask in the xz -plane, compressed by a factor of 10 in z -direction (values are given in metres)

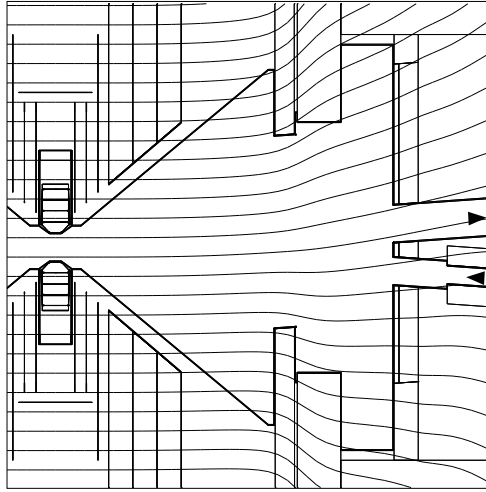


Figure 6.5: Forward region, compressed by a factor of 10 in z -direction. The magnetic field lines of an anti-DID field configuration [116] are superimposed.

so-called physics list. Users can implement custom physics lists with the particles, processes, and models of their choice, but Geant4 also provides a set of predefined lists that have been composed, tuned, and validated by the toolkit developers.

Mokka can use any of the predefined physics lists that are built into Geant4 or the so-called “Linear Collider Physics List” (LCPhys), which was intended specifically for linear collider studies [117]. For the simulations that are presented in this thesis, the Geant4 built-in list `QGSP_BERT_HP` has been used. This list offers the standard electromagnetic physics, but it provides a very detailed description of hadronic physics, especially with respect to neutrons at low energies.

This may sound contradictory at first because the simulation handles mainly electromagnetic particles, and hadrons play only a minor role. However, one of the goals of the simulation was to study the expected neutron-related backgrounds in the TPC and the vertex detector – this means that the production of neutrons in electromagnetic showers (through photonuclear and electronuclear reactions) must be modelled and that a good description of hadronic nuclear reactions and neutron transport is needed. `QGSP_BERT_HP` provides all this – a detailed list of its ingredients can be found in appendix B.2.

Still, `QGSP_BERT_HP` is a multi-purpose physics list that can be used for a full detector simulation. Other, more detailed models for specific processes are also available in Geant4 (e. g. for a better description of low-energy electromagnetic processes), but these could significantly reduce the performance

of the overall simulation. They might, however, be worthwhile to use for dedicated studies of certain subsystems, e.g. TPC-only or silicon-only simulations. For the study of neutron backgrounds, `QGSP_BERT_HP` is generally considered to be the best and most reliable choice [118, 119, 120].

An alternative would be the `LHEP_BIC_HP` physics list, which is very similar to `QGSP_BERT_HP`, but which uses a different nuclear cascade model and omits the Quark-Gluon-String Precompound model. A comparison between the physics lists is shown in section 7.8.1, and no significant differences are observed. The physics capabilities of the `LCPhys` list are similar to those of `QGSP_BERT_HP` as well, but the current version lacks the special support for low-energy neutrons. Therefore, `LCPhys` was not used here.

6.2.4 Primary Generator Particles in Mokka

Mokka can use several sources of primary particles: besides the built-in particle gun, Mokka can open and read generator files in the StdHep format [121], both in plain-text and in binary representation.

To facilitate the handling of files generated by Guinea-Pig, a specialised interface for files in the `pairs.dat` format has been added. Since the number of pair particles in one bunch crossing is very large (typically tens to hundreds of thousands), the Guinea-Pig interface handles events and runs in the simulation in an unusual way: one event contains just a single primary particle, such that one run may be used to represent a whole bunch crossing. This is done in order to avoid very large events with many thousands of primary particles, but it has to be kept in mind when overlaying beam-induced backgrounds and ordinary “physics” events.

Accelerator geometries with a crossing angle require a special treatment of primary particles: collisions under a given crossing angle lead to an x -boost of the centre-of-mass frame with respect to the laboratory frame. Most particle generators work in the centre-of-mass frame and do not take the additional boost into account, whereas the detector simulation has to take place in the laboratory frame. Therefore, a transformation of the primary particles is necessary in order to account for the crossing angle. This transformation has been included in Mokka, details can be found in appendix E.

It should be noted that Guinea-Pig does provide the possibility to include a crossing angle in its simulations, but this setting implies an imperfect mutual penetration of the bunches, thereby deteriorating the luminosity (figure 2.5). In the case of crab crossing (section 2.3), the crossing angle of the bunches themselves is again zero: the particle bunches penetrate each other (almost) perfectly and the full luminosity is retained – only the relative boost between the rest frame and the laboratory frame remains.

6.2.5 Output of Simulation Results

The Geant4 framework does not include a persistency model, i.e. there is no predefined way to write detector hits and other information to an output file. Therefore, Mokka uses the standard ILC persistency toolkit, LCIO (section 6.3.1). The output file of Mokka contains the simulated Monte Carlo particles (primaries from the particle generator as well as secondaries produced by Geant4, except in particle showers) and all resulting detector hits.

6.3 Marlin – Analysis Framework

Marlin [122, 123] (Modular Analysis and Reconstruction for the Linear Collider) is an analysis and reconstruction framework designed for simulated and measured data in ILC-related studies, written in C++. The concept of Marlin is that a set of code modules – so-called processors – subsequently acts on a data stream, thereby reading data objects from the stream, performing some kind of evaluation, and possibly adding new objects to the stream afterwards.

Each processor should execute a well-defined, encapsulated task, ranging from a simple calibration or pedestal correction to a complex fitting procedure or a sophisticated pattern recognition. Ideally, the modular approach allows to easily exchange and compare two processors that solve the same problem with different algorithms, to replace a simplified preliminary version of a processor with an improved implementation, or to apply the same processor chain on simulated and measured data by just adapting some preprocessing steps.

The Marlin framework itself just manages the data stream and invokes the processors that are specified in a steering file, thereby letting them read from and write to (but not delete anything from) the data stream. That stream is based on the LCIO data model (section 6.3.1), i.e. Marlin reads LCIO files that have been produced by a detector simulation or a data acquisition system, and LCIO objects are then passed from one processor to the next. However, apart from the pure framework, several packages of ready-made processors have become available in the past, which are maintained by expert groups and which attack specific problems such as vertexing (LCFIVertex), TPC simulation and analysis (MarlinTPC, section 6.3.4), or overall track reconstruction (MarlinReco). These tools can easily be included in the framework and be used for custom analyses.

Marlin has not exclusively been designed for LDC studies, but it has mainly been used by the LDC community up to now. Its GLD-focused equivalent are the “Satellites” that are bound to the Jupiter detector simulation,

whereas SiD-related studies have mainly used the Java Analysis Studio [124] with appropriate plug-ins in the past.

6.3.1 LCIO – Persistency Toolkit

LCIO [125] (Linear Collider Input/Output) is a data and persistency model designed for ILC detector studies, i. e. it is a toolkit that helps to organise detector- and analysis-related data in running applications (transient data) and to store this data on a storage medium (persistent data). LCIO exists in a C++ and a Java implementation plus a set of wrapper functions for Fortran.

LCIO provides classes for many typical kinds of information, ranging from low-level objects such as raw measured data or simulated data via medium-level objects that are needed during the reconstruction up to high-level objects at the end of the reconstruction chain (e. g. vertex information, tracks, clusters, reconstructed particles). LCIO will also store the Monte Carlo truth from the particle generator or the detector simulation, and it will manage inherent and arbitrary relations between objects (e. g. which Monte Carlo particle caused a given simulated hit or which reconstructed tracks and clusters seem to belong together).

LCIO allows to access and modify the intrinsic properties of these objects (such as raw data samples, hit energies, or track curvatures), but it offers only little additional “intelligent” functionality. This is done on purpose in order to keep LCIO lightweight and independent of a specific application.

Strictly speaking, LCIO is merely a data model, but not a data format: it defines an interface through which data of specific classes can be read, accessed, and written, but it does not handle the actual low-level I/O operations by which the data is stored on a medium in some encoded form. However, SIO (Simple Input/Output) is currently the only available persistency back-end for LCIO, such that all LCIO/SIO files are binary-compatible for the time being. This may change in the future if other I/O back-ends become available. Up to now, occasional suggestions to use ROOT [126] for this purpose have been fended off with the argument that ROOT is only available for C++, but not for Java.

In contrast to many of the other software tools that are still mostly concept- and region-specific, LCIO has truly spread across the globe: all major ILC-related software packages support LCIO, either as their core persistency model or at least as an option. LCIO has even been integrated into older tools such as BRAHMS in order not to leave them completely decoupled from the software developments of today.

6.3.2 Analysis of Background Simulations

From the point of view of analysis and reconstruction, beam-induced backgrounds are comparatively unspectacular: to a large extent the detectors register almost randomly scattered hits from low-angle primary particles and from backscattering secondaries. There is neither the possibility nor the need to reconstruct any specific objects, so Marlin is merely used as a means to access the simulation output (e.g. hits on a given detector) and to keep it available for counting and histogramming. No high-level reconstruction processors are involved in the analysis.

When, at a later stage of the simulation effort or even in the measured data, backgrounds and physics events are properly overlaid, there will be the need for a background suppression algorithm (section 9.2). It should be possible to filter out most of the beam-induced backgrounds by means of pattern recognition as long as background occupancies are not too high. Background hits typically come either in peculiar patterns or completely disassociated from other tracks and clusters – several examples are shown in section 7.

6.3.3 Analysis for the TPC

Mokka writes out undigitised hits for most of the tracking detectors: the energy deposits of a particle in a given layer of the detector are summed up and then assigned to an averaged point in space. However, the energy deposit is not mapped to any kind of specific pixel or strip structure or even distributed across several of such elements.

The reason for this approach is the idea that the time-consuming full detector simulation – i.e. the interaction of particles with matter – should be done only once, whereas the digitisation could then be applied in a second step (typically in a Marlin digitisation processor) for varying readout geometries and specifications. For the thin and dense silicon trackers, this slightly simplified method is valid, and the notion of an “undigitised hit” yields reasonable results. Therefore, whenever “hits” on a silicon tracking device are mentioned in this thesis, they are undigitised.

For the TPC as a very large detector with low density and no internal segmentation, the situation is different and more difficult. As explained in appendix B.1.6, the concept of artificial gas layers has been used in the past, but it is problematic when dealing with low-energy backgrounds. Instead, the Mokka TPC writes out all energy deposits in the sensitive volume (separated at most by the maximum step length, which is set to 5 mm) and assigns them to some point in continuous three-dimensional space. These deposited

energies then need to be filled in discrete voxels in order to derive meaningful quantities such as the occupancy.

The TPC digitisation works as follows: the dimensions of the sensitive volume, the height of the pad rows, the width of the pads, and the depth of the time bins are input parameters. The width of the pads in each row is minimally adjusted to ensure an integer number of pads per row. Gaps between the pads on the anode plane are not taken into account. Each energy deposit in the chamber (identified by its x -, y -, and z -coordinate) is then mapped to a voxel (identified by its row, pad, and bin index). If the voxel already contains an energy deposit, the energies are added.

To account for the charge sharing that is due to the transverse diffusion in the drift and amplification regions (cf. figure 5.11 on page 63), each energy deposit is assigned to three adjacent pads, with the outer pads each carrying one third of the energy (i. e. primary charge) of the central one. This model is a simplification, but it is based on the assumption that the readout geometry would always be matched to the gas properties such that the signals are shared between a few (though not necessarily exactly three) pads. This mechanism is only implemented in the φ -direction because the readout pads are usually much smaller in φ than in r , and charge sharing between pad rows is only a small effect.

The overlay of hits from several bunch crossings (usually 100 in the simulations that are presented here) is done with a proper representation of the drift in the chamber: hits from each subsequent bunch crossing are shifted by the drift velocity multiplied by the bunch spacing (i. e. $50 \mu\text{m}/\text{ns} \cdot 369 \text{ ns} \approx 18 \text{ mm}$), and the time interval between the moment of the bunch crossing and the actual occurrence of the hit is taken into account in the same way. This time interval is often short (less than 50 ns), but sometimes significant delays can be observed (section 7.4.2).

To determine the TPC occupancy, signals from many bunch crossings are overlaid, but only data that will be read out in a certain time interval is taken into account. Some of the signals from earlier bunch crossings (close to the anode) have already left the chamber before, whereas some of the signals from later bunch crossings (far from the anode) are not able to make it to the readout in time. In order not to lose this data, a simple wrapping procedure is applied: to model the state of the TPC in the middle of a bunch train, the front part of earlier bunch crossings is wrapped back into the rear part of the chamber, as if the data had come from a much later bunch crossing. The in principle infinite, continuous time range in which the hits occur is mapped to a finite, “looping” toroidal space region from which the hits are read out.

This method – which reduces the amount of required data by a factor of two – is fine for unstructured background hits, but it may produce too large

correlations in certain cases. For example, if an exceptionally intense curler leaves the readout frame through the anode plane, it will immediately re-enter the chamber through the cathode plane, only shifted backwards in the z -direction. Statistical fluctuations may be slightly increased, but no effect on the overall simulation results is expected.

6.3.4 MarlinTPC – Full Software Chain

MarlinTPC [127] is a package of Marlin processors that cover various kinds of TPC-specific topics. Regarding measured data, processors for tasks like pedestal subtraction, time-shift correction, and calibration are available. Regarding simulations, there are processors for a detailed low-level simulation of events in the TPC and others that establish an interface to high-level simulations such as Mokka. For the reconstruction of events, MarlinTPC provides hit and track finders, track fitting algorithms, and the calculation of residuals and resolutions.

The MarlinTPC package is actively being developed by several TPC groups world-wide and is continuously being improved and extended. Up to now, much of the development has focused on the analysis of measured and simulated data from small test set-ups (such as presented in [128]) and medium-sized prototypes (such as presented in [97]). Code that can be applied to the full-sized ILC TPC with realistic events and backgrounds is still under development. Therefore, MarlinTPC has not been used for the studies that are presented in this thesis, except for an outlook in section 9.2.

6.4 Grid Computing – Mass Production

6.4.1 Computing in High-Energy Physics

With the ever-rising complexity of experiments and increasing amounts of experimental data, the need for computing resources in high-energy physics has continuously grown over time: recorded data from detectors needs to be stored, events have to be reconstructed, and the resulting reconstructed objects have to be analysed to obtain meaningful results and to measure physical observables. Complementary to that, simulations have to be done for detector studies, for tests of reconstruction algorithms, and for Monte-Carlo-based analyses.

In contrast to various other sciences and also different fields of physics, computing tasks in high-energy physics can often be broken down to small pieces that are more easily manageable. The experimentalists' requirements concerning the number of recorded or simulated events are merely driven

by the search for processes with a small probability (i. e. cross-section) and the need for sufficient statistics. A single event, however, is usually not too complicated, and subsequent events are – at least on the fundamental level – independent of each other.

It is therefore possible to treat each event in a simulation separately and, if needed, to apply possible detector effects such as event pile-up or saturation effects only in a second processing step. Events can be simulated independently one after another, and in typical detector simulations there is no state information carried from one event to the next. This implies that the order of the single events is unimportant and that multiple events can even be simulated on different computers at the same time. These computers do not need to communicate with each other during the simulation, i. e. there is no need for parallel computing (in the stricter meaning) on a large, powerful, and expensive “super computer”. Instead, it is sufficient to split a large simulation task into small chunks, distribute these to a set of ordinary computers, and finally to collect and merge the output data of each of the small jobs.

6.4.2 The LHC Computing Grid

The LHC experiments have boosted the need for computing resources to the next level: on the one hand, the sheer amount of data that will be recorded during the nominal operation of the LHC is enormous, and it is practically only limited by the ability to convey data away from the detectors over the network and to write it to some kind of long-term storage. On the other hand, there is the demand for massive computing power for Monte Carlo production, event reconstruction, and data analysis.

The LHC community has therefore agreed to respond to the existing computing challenge by the relatively new concept of the Grid [129, 130]. Over the last few years, the so-called LHC Computing Grid (LCG) [131] has been built up, which is supposed to provide the nationally distributed computing resources that will be needed for a successful operation of the LHC experiments. In the meantime, other projects such as the HERA experiments, the ILC, or theoretical physics have joined the LCG effort.

The LCG is structured in so-called tiers, with the CERN computing centre being the central Tier-0, a few major national computing centres acting as Tier-1 sites for their respective countries, and all other participating centres running as Tier-2 sites. The sites of the tiers differ in size and also in their specific tasks such as data storage, general-purpose computing support and specialised analyses. The German Tier-1 is located at GridKa in Karlsruhe, whereas DESY in Hamburg hosts one of the German Tier-2 centres

for ATLAS and CMS. Some of the LCG sites – but by far not all, at least up to now – also support the ILC.

6.4.3 Profit and Experiences

The studies that are presented in this thesis would almost have been impossible without the usage of Grid resources, especially with regard to computing power. Approximately 60 000 jobs were run, using the equivalent of roughly 20 years of computing time on a state-of-the-art CPU (e. g. 3 GHz Intel Xeon) and producing a total amount of 750 GB of simulated data. The Grid was used for the full detector simulation with Mokka, whereas the particle generator Guinea-Pig and the Marlin-based analysis software were executed locally.

Most jobs were run on the ever-strengthening Computing Element `grid-ce3.desy.de` at DESY in Hamburg, which currently provides a total amount of 850 CPUs, but other important production resources were `lcg-ce0.ifh.de` at DESY in Zeuthen, `cclcgceli02.in2p3.fr` at the Centre de Calcul IN2P3 in Lyon, and `ce.bfg.uni-freiburg.de` at the University of Freiburg im Breisgau. At DESY, the Grid resources of the National Analysis Facility [132] were used as soon as they became available in early 2008. The simulated data that is presented in this thesis is currently stored on the Storage Elements `srm-dcache.desy.de` and `globe-door.ifh.de`. It can be found under `/grid/ilc/vogel` in the ILC-specific file catalogue (which currently runs on `grid-lfc.desy.de`).

Considering the continuously growing number of computing centres that support the ILC and furthermore taking into account that most sites are still upgrading and extending their resources as the date of the LHC start-up comes nearer, only a small fraction of all resources that are currently available for the ILC has actually been exploited for this thesis.

Looking back, the overall failure rate of Grid jobs for the simulations presented in this thesis lay well below the percent level, except for the very few occasions when some core component of the Grid infrastructure was malfunctioning, such that basically all submitted jobs would fail at once. The Grid may not (yet) be as reliable and failure-proof as a conventional local batch cluster, but the availability of tremendous computing resources outweighs the drawbacks by far.

7 Simulation Results

In the following sections, results from the simulation of pair-induced backgrounds are presented. Unless otherwise noted, all data have been obtained from Guinea-Pig with the nominal ILC beam parameter set for a centre-of-mass energy of 500 GeV (table 2.1) and the Mokka geometry model that is described in section 6.2.2, including a crossing angle of 14 mrad and an anti-DID magnetic field.

7.1 Remark on Statistics

All values and diagrams are given for 100 simulated bunch crossings, either summed up or averaged. When uncertainties of values or error bars of data points are shown, they correspond to the statistical fluctuations per bunch crossing, i. e. the root mean square (RMS) of a dataset with 100 elements. The statistical uncertainty of the mean value for $N = 100$ bunch crossings would be smaller by a factor of $\sqrt{N} = 10$. This reduced value is used only when results are extrapolated to a much larger number of bunch crossings, i. e. to estimate the total neutron fluence after 500 fb^{-1} for the vertex detector (table 7.1) and the HCAL endcap (figure 7.48).

The fluctuation per bunch crossing is shown to demonstrate the large variations that can appear between the single bunch crossings. Even though each bunch crossing contains around 10^5 primary particles (i. e. electrons and positrons created by beamstrahlung scattering and originating from the interaction point), only a very small fraction of them actually contributes to the background signals in the detector, and the effects of this small number of particles can differ greatly. As an example, a single medium-energy curler with low longitudinal momentum can create an enormous number of hits in the TPC, whereas the chamber sees only a small number of hits in most of the other bunch crossings (section 7.4.2).

As a consequence, the central limit theorem does not necessarily hold, and many distributions are non-Gaussian. As an example, the distribution of the number of hits on the vertex detector per bunch crossing (cf. section 7.2.1) is shown for the innermost and the outermost layer (figures 7.1 and 7.2). The former distribution, with a mean value of 401 and an RMS of 74, is approximately Gaussian, whereas the latter, with a mean value of 27 and an RMS of 23, is clearly asymmetric and has a distinct tail towards larger numbers. This is to illustrate that the stated uncertainties should generally not be interpreted as the width of a Gaussian curve (or any other parameter of a statistical model), but merely as an assessment of the intrinsic fluctuations that will appear between different simulation runs.

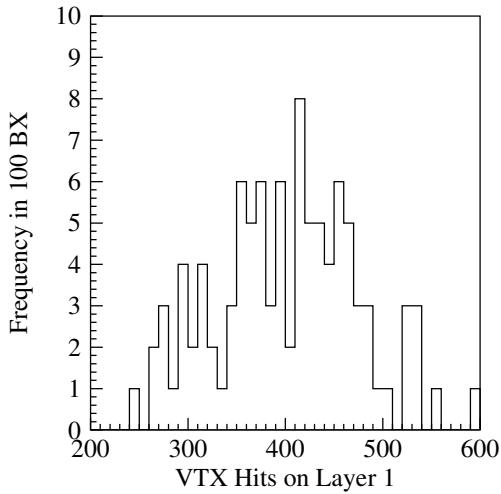


Figure 7.1: Distribution of the number of hits on the innermost layer (layer 1) of the vertex detector

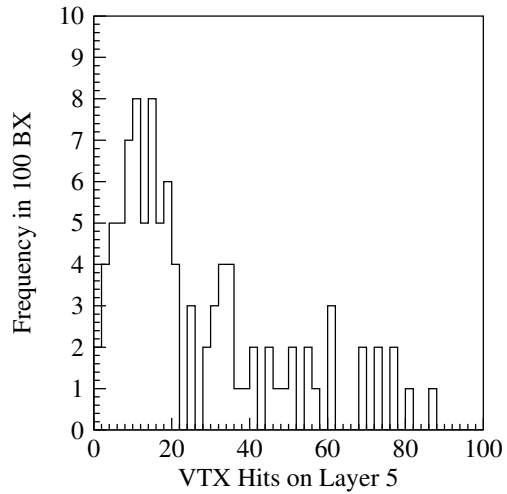


Figure 7.2: Distribution of the number of hits on the outermost layer (layer 5) of the vertex detector

In the case of strongly skewed distributions, asymmetric errors are shown. Instead of mean and RMS, the given numbers then correspond to the median and the lower and upper 1σ bounds, denoting the interval in which 68% of all values from the data sample can be found.

Both the vertex detector and the TPC have a read-out system that will integrate over 100–200 bunch crossings, which is of the same order as the data set that is evaluated here. This means that the statistics from 100 simulated bunch crossings are sufficient to obtain a realistic picture of the expected detector backgrounds. A more detailed discussion on the uncertainties of the simulation results can be found in section 7.9.

7.2 Vertex Detector

Of all components in the overall detector layout, the vertex detector is most sensitive to beam-induced backgrounds: it is located extremely close to the interaction point, cannot be shielded, must have a very small material budget, should be sufficiently fast, and is – as a silicon-based device – prone to radiation damage.

The number of hits on the vertex detector is a very simple yet important and frequently-used figure of merit to quantify background levels for a given detector layout.

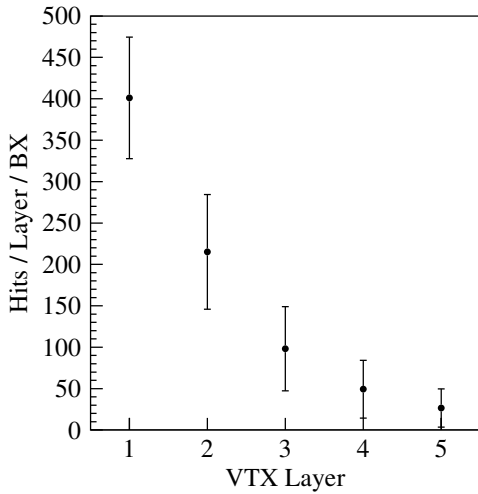


Figure 7.3: Hits on the vertex detector per bunch crossing, in absolute numbers

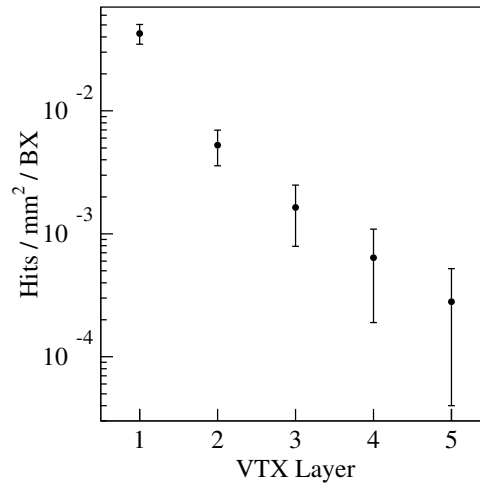


Figure 7.4: Hits on the vertex detector per bunch crossing, normalised per unit area

7.2.1 Hits on the VTX

Number of Hits Figure 7.3 shows the average number of hits per bunch crossing on the five layers of the vertex detector (table B.2), figure 7.4 shows the same numbers normalised to the area of the layers. It should be kept in mind that the area of the layers does not only increase with their radius, but that the innermost layer is less than half as long as the others. This means that the number of hits on layer 1, which is already twice as high as on layer 2 in absolute terms, is almost an order of magnitude higher than on layer 2 when normalised per unit area.

The recorded hits (i.e. the energy deposit) on the vertex detector can also be translated into a radiation dose that gets absorbed by the silicon sensors, but it turns out that this dose is far below any critical limit even for a run time of many years [133]. A similar analysis for the case of neutrons – which will usually not leave a hit in the detector material – can be found in section 7.2.2.

Since the innermost layer of the vertex detector has the highest number of hits in absolute as well as in relative terms, its design is clearly the driving force for the performance of the vertex detector. The background hits in a single bunch crossing will certainly not be an issue, but the vertex detector will typically be a rather slow device, which integrates over several tens to hundreds of bunch crossings. Still, it must be possible to apply a pattern recognition algorithm in order to find hits that belong together with a high

efficiency and a low fake rate, and to fit tracks to these hits with a sufficient resolution. In the current reconstruction scheme, it is foreseen that the vertex detector can work as a stand-alone device without requiring data from other tracking detectors for its track reconstruction – however, this is merely an advantageous feature and not a strict requirement for the functionality of the overall tracking system.

The actual readout speed of the detector – and therefore the number of bunch crossings which will be overlaid in one readout frame – depends on the technical implementation, and several rather different detector technologies are currently under discussion. A conventional SLD-like CCD detector [70], which would collect data during a whole bunch train to be read out only between trains, could not stand the background rates of the ILC. Possible solutions could be, among others (see [39] for a comprehensive list):

- FPCCDs [134] are CCDs with very fine pixels ($5 \times 5 \mu\text{m}^2$), which are read out after a complete bunch train. FPCCDs can partially reject background signals by measuring the angle of incident particles inside a single sensitive layer, but a drawback is that they have to be operated below room temperature due to their long signal integration time.
- CPCCDs [135] and DEPFETs [136] reduce the background occupancy by having multiple readout frames (≈ 20) per bunch train.
- MAPS [137] and ISIS [135] detectors are foreseen to store around 20 data samples per train, either as voltages in capacitors at the readout node or as charges in tiny CCD registers within each pixel.
- Chronopixels [138] would apply a single-bunch timestamp to each hit, thereby using small pixels ($10 \times 10 \mu\text{m}^2$) and only digital hit information.

All of these detector technologies claim that they could handle background levels similar to those indicated in figure 7.4.

If, due to a change of machine specifications (e.g. section 7.7.3), detector design (particularly the forward region, e.g. section 7.7.4), or improved simulations in the future (section 7.9), background levels turn out to be too high, there are some generic countermeasures:

- Increasing the strength of the magnetic field in order to let the pairs curl more tightly around the field lines (cf. figure 3.5). This remedy would come at the expense of an increased cost for the coil, and it could give rise to safety concerns due to the higher energy that is stored in the field.

- Increasing the radius of the vertex detector to keep a better clearance from the pairs [56] (cf. figure 3.3). This would deteriorate the impact parameter resolution, and it would probably require a longer sensitive area in order to retain the angular coverage, thereby potentially compromising the mechanical stability of the vertex detector as a whole.
- Switching to another detector technology that might have worse performance, but a higher tolerance against backgrounds. Such a decision would immediately affect the performance of the vertex detector itself, and the impact on the overall tracking would have to be evaluated.
- Sticking with a given detector technology, but relaxing the specifications in order to increase the tolerable background levels (e. g. by shortening the sampling time), maybe at the expense of an increased material budget or a higher power dissipation of the readout electronics. This option might or might not influence the performance of the vertex detector, but it could deteriorate the overall tracking (e. g. through increased multiple scattering) or lead to a more complicated detector design (e. g. for cooling of the vertex detector).

It would have to be studied whether these modifications (except the first item, of course) should be applied to the whole vertex detector or only to the innermost layer.

Time Distribution Figure 7.5 shows a time distribution of hits on the first layer of the vertex detector. Each entry corresponds to the time interval between the moment of the bunch crossing (i. e. the start of the simulation at $t = 0$) and the occurrence of a hit ($t = t_{\text{hit}}$). The primary particles that are generated by Guinea-Pig do not carry time information (i. e. they start exactly at $t = 0$), but the time needed for the mutual penetration of the bunches is completely negligible compared to the given time scale of nanoseconds.

The time distribution shows a distinct pattern: most of the hits occur very shortly ($t < 1$ ns) after the bunch crossing, i. e. they are caused by particles that come from the interaction point and immediately hit the vertex detector (“direct hits”). The tail of this peak is caused by secondaries which are produced close to the interaction point (e. g. in the wall of the beam tube, in the rest of the vertex detector, or in the other silicon detectors) and which are then backscattered to the first layer. This tail falls off rapidly.

A second wave of particles begins to arrive almost exactly at $t = 23$ ns. Assuming that particles travel at the speed of light, this time interval corresponds to a distance of 7.0 m, i. e. 3.5 m in each direction. This is a clear

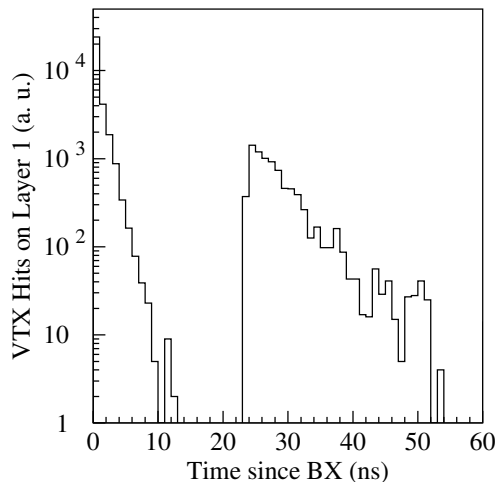


Figure 7.5: Time distribution of hits on layer 1 of the vertex detector.

indication that the hits are caused by particles backscattered from the Beam-Cal, which begins at $z = 3550$ mm (“indirect hits”). Particles that are immediately backscattered from the surface need the least time, whereas others that happen to make it out of a deeper shower may take longer, such that the second tail in the distribution is somewhat broader than the first.

The ratio of direct and indirect hits strongly depends on the design of the forward region: the number of direct hits can hardly be influenced for a given vertex detector geometry, a given set of beam parameters, and a given strength of the magnetic field, but the number of indirect hits varies with the detailed design of the forward mask (including the crossing angle) and the choice of the magnetic field configuration (DID, no DID, anti-DID). The detector design that is used here is already close to the optimum, as various comparative studies (section 7.8) show. In figure 7.5, the ratio of direct to indirect hits is around 80 % : 20 %.

It should be kept in mind that an extreme time resolution as in figure 7.5 will hardly be achievable for the vertex detector (except maybe with some very exotic technologies) – therefore the information shown in the histogram is only available in the simulation, but not in the measured data.

Spatial Distribution Figures 7.6 and 7.7 show the spatial distribution of hits on the first layer of the vertex detector, plotted against the azimuthal angle φ and against the longitudinal position z . Both histograms show separate entries for direct hits ($t_{\text{hit}} < 20$ ns) and indirect hits ($t_{\text{hit}} > 20$ ns).

The azimuthal distribution of direct hits is basically flat since electron-positron pairs are produced isotropically in φ . Particles with a low transverse

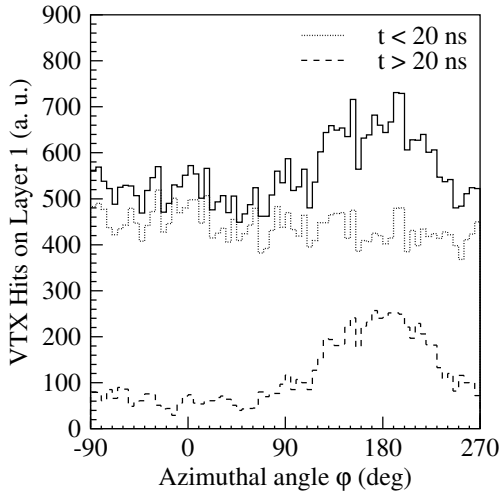


Figure 7.6: Azimuthal distribution of hits on layer 1 of the vertex detector. $\varphi = 0$ corresponds to the direction of the outgoing beam, $\varphi = 180^\circ$ corresponds to the direction of the incoming beam.

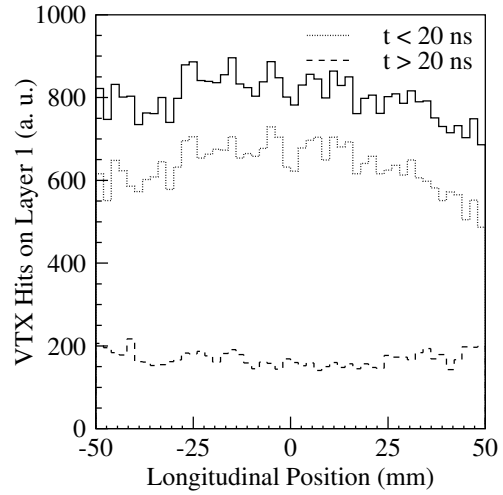


Figure 7.7: Longitudinal distribution of hits on layer 1 of the vertex detector.

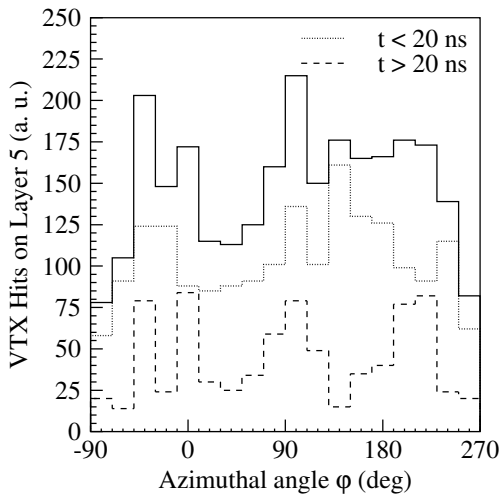


Figure 7.8: Azimuthal distribution of hits on layer 5 of the vertex detector.

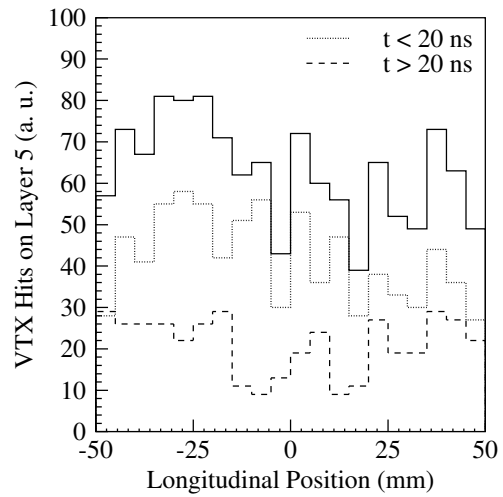


Figure 7.9: Longitudinal distribution of hits on layer 5 of the vertex detector.

momentum will be deflected by the space charge of the oncoming beam, resulting in distinct, different patterns for electrons and positrons, but particles that can reach the vertex detector are almost not affected. Furthermore, the boosting effect of the crossing angle (appendix E) is too small to be visible in figure 7.6.

The azimuthal distribution of indirect hits depends strongly on the magnetic field configuration. In the case of a well-tuned anti-DID field, the particles that are backscattered from the downstream hole of the BeamCal – which is the dominant source of backscatterers – are guided through the centre of the vertex detector (figure 6.2), resulting in a uniform azimuthal distribution of hits. In the case of an imperfect tuning of the anti-DID, a more or less prominent asymmetry can be observed. A DID field (instead of an anti-DID) or no DID field can lead to strong azimuthal asymmetries (section 7.7.2). The distribution in figure 7.6 has a significant excess in the negative x -direction (i. e. $\varphi \approx 180^\circ$), which is caused by a slightly too strong anti-DID field in the simulation. This effect gets weaker on the outer layers and can hardly be seen anymore on layer 5 (figure 7.8).

Even though the histograms in figures 7.6 and 7.8 contain the sum of 100 bunch crossings, rather strong statistical fluctuations appear. A source for these fluctuations are tightly curling particles that punch through a sensitive layer of the vertex detector many times, thereby leaving a long trace of hits that have almost identical φ -positions.

The longitudinal distribution of hits (figure 7.7) is approximately flat, but with a certain shape in the contributions of direct and indirect hits: direct hits appear more often at the centre of the detector ($z \approx 0$), i. e. under large polar angles. This is the net result of the focusing of pairs into the forward direction on the one hand (favouring small ϑ) and the geometrical effect of angular coverage on the other hand (favouring large ϑ). With the given detector geometry, the latter dominates slightly.

Indirect hits appear more often at the borders of the vertex detector, which can be explained by the energy loss and stopping of low-energy backscatterers that approach the vertex detector from either side. The fact that these effects for direct and indirect hits almost compensate each other and result in a flat overall distribution is purely coincidental, but nevertheless advantageous because no part of the vertex detector has to deal with a particularly high hit density. The hits on the outermost layer 5 show a similar distribution (figure 7.9), but with much less statistics.

7.2.2 Particles Passing Through the VTX

By construction, the sensitive detectors that are implemented in Mokka will write out a hit only if a particle deposits a certain minimum amount of energy (for the silicon detectors this limit is typically 20 % of the mean energy deposit of a minimum ionising particle, section B.1.2). This implies that the Mokka detectors are insensitive to neutral particles (i. e. photons and neutrons) as long as they don't happen to be absorbed by the detector material, which is unlikely in the case of the silicon detectors because of their – desirable – low material budget.

In order to get a handle on neutral particles that traverse the vertex detector (and the radiation damage they may cause), Mokka was extended by means of “virtual” sensitive surfaces. These surfaces are defined in the code for particle tracking (as a `G4UserTrackingAction`), but they are not part of the detector geometry. Whenever any particle traverses one of the surfaces during a tracking step, its current position, starting position, energy, particle type, and the time since the bunch crossing are written to an additional output file. If a particle traverses a surface more than once (e.g. because the surface is cylindrical or because the particle has changed its direction of flight in the meantime), it is also recorded more than once.

The defined surfaces correspond to the five layers of the vertex detector (approximated by cylinders), three circular planes perpendicular to the beam (one in front of the LumiCal, one close to the vertex detector, and one in between), and some cylinders of increasing radii inside the HCAL endcap (section 7.6).

Charged Particles Figures 7.10 and 7.11 show the number of electrons and positrons that traverse the five sensitive surfaces in the vertex detector. The numbers are slightly smaller than the number of hits (figures 7.4 and 7.3) due to technical reasons: the cylinders are only an approximation, and particles could hit the silicon sensor and be stopped without traversing the sensitive surface. Therefore, the numbers in figure 7.10 and 7.11 should only be understood as a cross-check.

However, one advantage of the sensitive surfaces is that they provide information about the particles' origins and energies. (The detector hits recorded by Mokka also contain additional data about their respective Monte Carlo particles, but this information has been found to be incomplete and unreliable [139].) Figure 7.12 shows the origins of electrons and positrons that traverse any of the five sensitive surfaces in the vertex detector. Most particles either come directly from the interaction point or are created in the immediate vicinity of the vertex detector (e.g. by photon conversion or

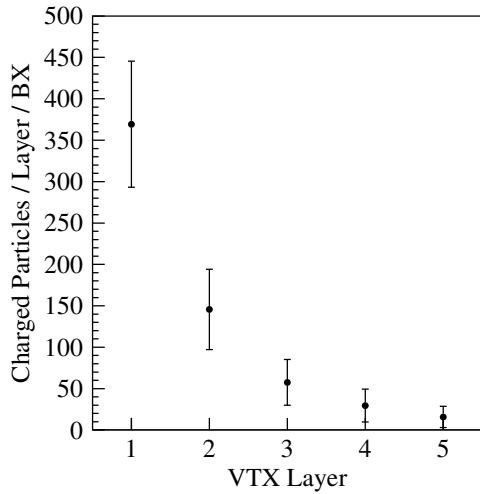


Figure 7.10: Electrons and positrons traversing the vertex detector per bunch crossing, in absolute numbers

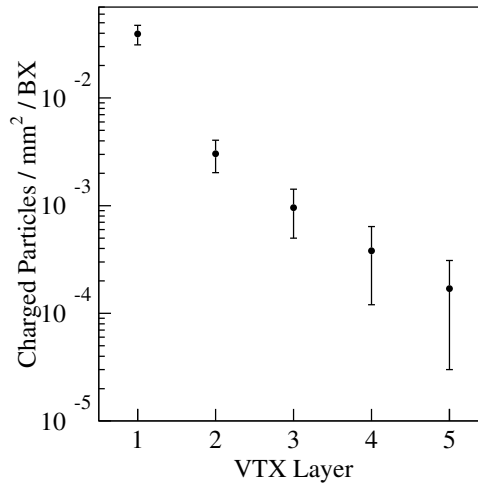


Figure 7.11: Electrons and positrons traversing the vertex detector per bunch crossing, normalised per unit area

other scattering processes), but further clear sources are the BeamCal and the innermost part of the beam delivery and extraction system. The LumiCal and the Forward Tracking Discs play negligible roles.

Figure 7.13 shows the energy spectrum of electrons and positrons as they traverse any of the five sensitive surfaces in the vertex detector. The histogram is separated into entries from near sources ($z < 1$ m) and entries from far sources ($z > 1$ m). The high-energy flank of the spectrum directly corresponds to the energy distribution of primary particles that have high enough transverse momenta to reach the vertex detector directly. The low-energy tail relates to particles that are produced by secondary processes very close to (or even inside) the sensitive parts of the vertex detector. It is likely that the lower end of the spectrum is also influenced by the internal implementation of electromagnetic physics (appendix B.2.3), even though no sharp cut-off (which would typically be at 1 keV) is visible in figure 7.13.

The “far” spectrum is considerably narrower than the “near” spectrum: an upper bound on the particle energy comes from the fact that only backscattering particles from electromagnetic showers can reach the vertex detector, and the energy spectrum of these particles apparently has a very steep fall-off at around 100 MeV. The lower limit on the energy spectrum is caused by the necessity to traverse a certain amount of material before reaching the vertex detector, particularly the wall of the beam tube. Backscatterers hit the wall of the beam tube under a shallow angle of 83 mrad such that its effective

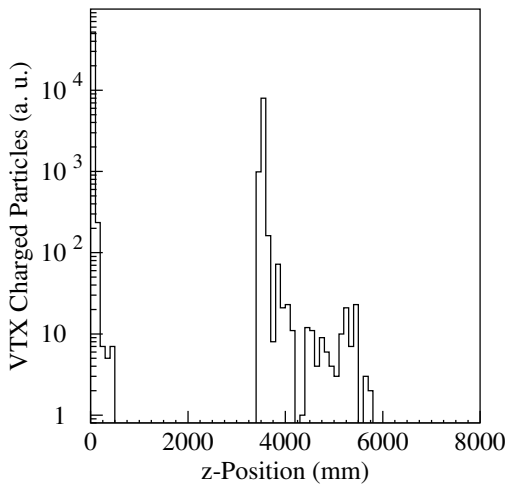


Figure 7.12: Origins of electrons and positrons traversing the vertex detector

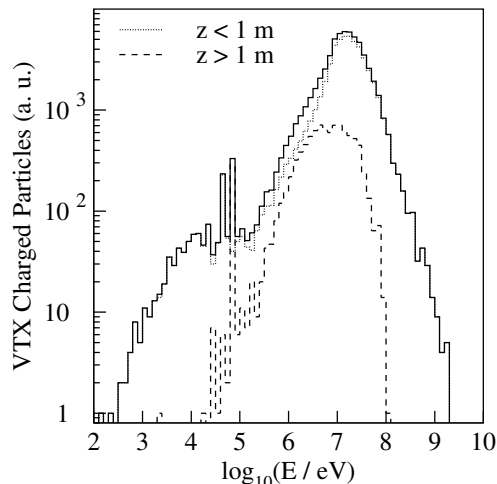


Figure 7.13: Energy distribution of electrons and positrons traversing the vertex detector

thickness is much larger than just 1 mm of beryllium. While the “far” spectrum still follows the “near” spectrum down to energies of some 100 keV, backscatterers with even lower energies (down to the order of 10 keV) are strongly suppressed. Extremely low-energy backscatterers cannot reach the vertex detector anymore at all.

Photons Figure 7.14 shows the average number of photons that traverse the five sensitive surfaces in the vertex detector per bunch crossing, figure 7.15 shows the same numbers normalised to the area of the layers. It should be noted that these photons are not necessarily related to hits in the vertex detector: they can be absorbed by the material, thereby producing secondary electrons and leaving an energy deposit, but they can also merely traverse the detector material without any interaction. Mokka knows no such thing as a “neutral hit” because photons on their own cannot deposit energy in the material – but only energy deposits will be written out as detector hits.

Compared to the charged particles (figures 7.10 and 7.11), the number of photons that traverse the different layers depends far less on the layer radius. The absolute number of transitions stays approximately the same for the outer layers, and is significantly lower for the innermost layer due to its shortness (table B.2). This means that the normalised density of transitions approximately falls with $1/r$, even though there is no fundamental reason for this specific relation. The qualitative difference between photons and charged particles comes from the facts that photons are not affected by the magnetic

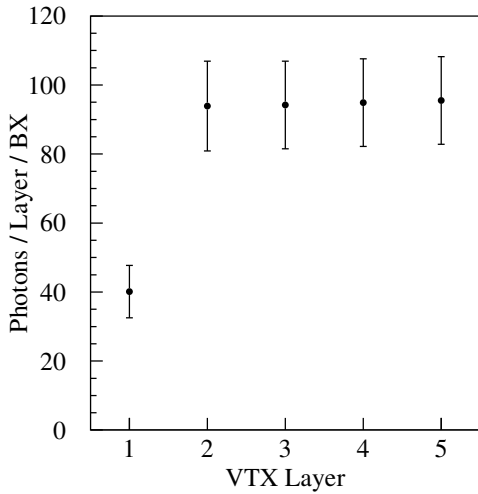


Figure 7.14: Photons traversing the vertex detector per bunch crossing, in absolute numbers

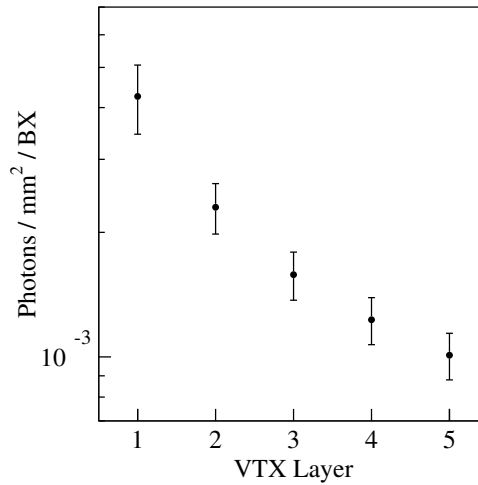


Figure 7.15: Photons traversing the vertex detector per bunch crossing, normalised per unit area

field (so that they are not necessarily confined to the innermost parts of the detector) and that they can possibly traverse thin layers of material without losing energy and being absorbed (so that photons of not too low energies can go through several layers of the vertex detector).

Figure 7.16 shows the origins of photons that reach the vertex detector. Even more pronounced than in the case of charged particles (figure 7.12), most of the photons originate in the immediate vicinity of the vertex detector, either through the radiation of bremsstrahlung or through the annihilation of positrons (cf. figure 7.17). Other sources are the BeamCal, but also the LumiCal and parts of the beam delivery and extraction system. Charged backscatterers from the LumiCal will usually not reach the vertex detector because the aperture of the LumiCal is too large and charged particles follow the magnetic field lines, but this restriction does not apply to photons. Still, the LumiCal is only a minor source of photons. The extraction system is a region of very high electromagnetic activity because virtually all pairs that have not struck another detector component before will be over-focused by the extraction quadrupoles to create a shower in the magnet material. Photons could escape from the magnets, but the angular coverage by the BeamCal and the LumiCal is so large that only few photons can actually reach the inner detector. Therefore the beam delivery and extraction system is also merely a minor source of photons in the vertex detector.

The energy spectrum of the photons is shown in figure 7.17, again split between near sources ($z < 1$ m) and far sources ($z > 1$ m). The “near”

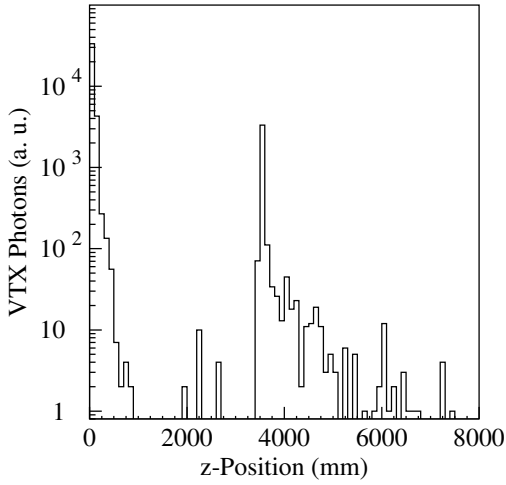


Figure 7.16: Origins of photons traversing the vertex detector

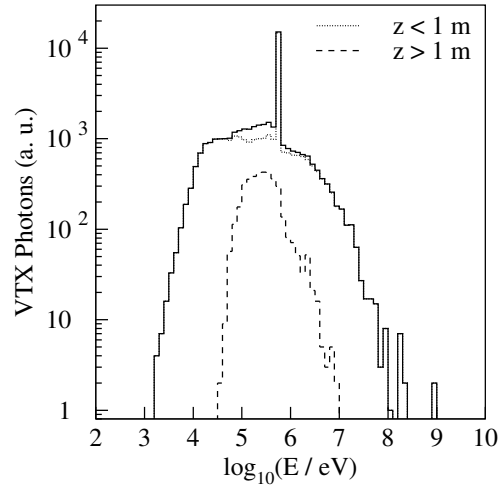


Figure 7.17: Energy distribution of photons traversing the vertex detector

spectrum has a very distinct peak around 500 keV, which is obviously caused by the annihilation of positrons in the material close to the vertex detector. Photons from far sources are strongly suppressed, with an abrupt cut-off around 50 keV – the range of such low-energy photons is too short to let them pass through the wall of the beam pipe and reach the vertex detector.

Neutrons Figure 7.18 shows the origins of neutrons that traverse any of the five sensitive surfaces in the vertex detector. The BeamCal, which is one of the places with the highest electromagnetic activity, is the most important source of neutrons, which are typically produced through photonuclear and electronuclear processes in electromagnetic showers. Other sources are the LumiCal and also the inner surface of the ECAL (barrel and endcap), since neutrons are not affected by the magnetic field. Neutrons can be reflected by dense surfaces (which increases their path of flight and therefore their chance of hitting a specific part such as the vertex detector), but they can also cause nuclear reactions such as neutron capture or inelastic scattering, leaving an excited nucleus behind. The deexcitation of such a nucleus will often produce further secondary neutrons (and photons), which is the reason why the inner surface of the ECAL also appears as a source of neutrons.

The energy spectrum of neutrons as they traverse the vertex detector is shown in figure 7.19. The neutron energies range from several electronvolts up to around 10 MeV, and the usage of high-precision models for processes of such low-energy neutrons (section 6.2.3) – as it was done in the studies

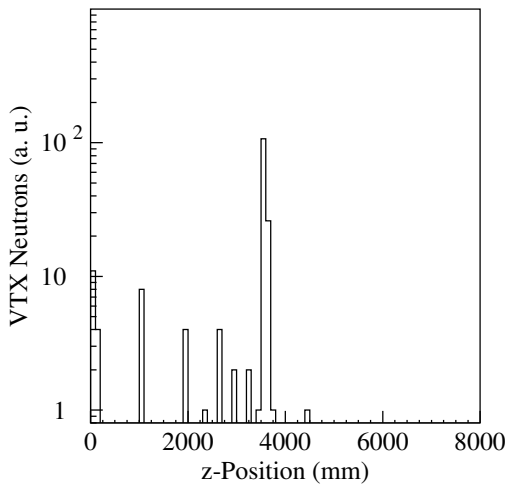


Figure 7.18: Origins of neutrons traversing the vertex detector

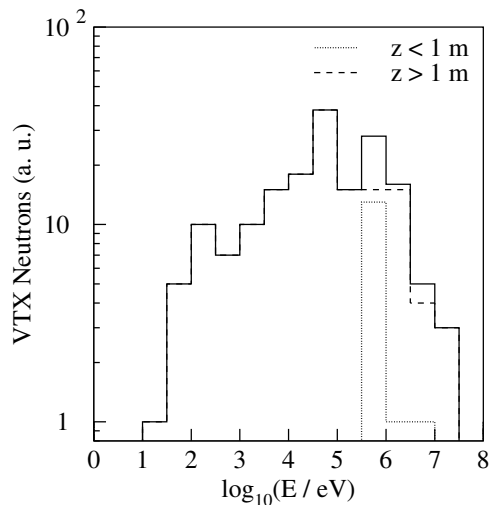


Figure 7.19: Energy distribution of neutrons traversing the vertex detector

that are presented here – should greatly help to improve the reliability of the simulations. However, the exact shape of the energy spectrum still depends on the specific choice of the models for hadronic physics. The spectrum in figure 7.19 was simulated with the physics list `QGSP_BERT_HP`, which uses the model of a Bertini Intranuclear Cascade (section B.2.6). A comparison with `QGSP_BIC_HP`, which uses a Binary Cascade model, can be found in section 7.8.1.

Neutrons do not play any significant role in the creation of background signals in the vertex detector, but they are nevertheless important because of the radiation damage that they will inflict on silicon devices. In this context, the neutron fluence, i. e. the flux integrated over time and normalised per unit area, is much more relevant than the number of neutrons that cross the vertex detector in a single bunch crossing, since this number is typically very small. Therefore, the neutron fluence is extrapolated to a total amount of $3.4 \cdot 10^{11}$ bunch crossings, which corresponds to the integrated design luminosity of 500 fb^{-1} (section 2.4).

The expected radiation damage that is caused by neutrons in silicon varies strongly with the neutron energy. A simple approach is to count only neutrons with energies above 1 MeV, but a better description can be achieved by the model of Non-Ionising Energy Loss (NIEL). The NIEL model introduces a scaling factor to relate the damage potential of a neutron with a given energy to the damage potential of a neutron of 1 MeV (similar to the “quality factor” that relates the biologically relevant human equivalent dose

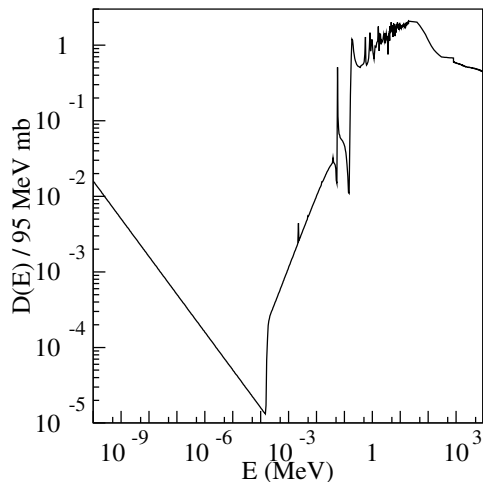


Figure 7.20: Relative neutron-induced displacement damage in silicon in dependency of the incident neutron energy [140]. The plot combines measured data from different sources for $0.1 \text{ meV} < E < 20 \text{ MeV}$ [141], $20 \text{ MeV} < E < 800 \text{ MeV}$ [142], and $800 \text{ MeV} < E < 9 \text{ GeV}$ [143].

to the plain energetic radiation dose). Scaling factors for neutrons in silicon [140, 141, 142, 143] are shown in figure 7.20 (and the simple rule of thumb to count only neutrons above 1 MeV is apparently not too bad).

Table 7.1 shows the expected neutron fluence for the five layers of the vertex detector, calculated from the simulation of 100 bunch crossings, weighted by NIEL scaling, extrapolated up to $2.3 \cdot 10^{11}$ bunch crossings, and normalised per unit area. The errors correspond to the scaled statistical uncertainty from 100 bunch crossings. The simulation results indicate that neutrons from beam-induced backgrounds should not be a problem for the vertex detector: typical silicon technologies that are currently under consideration for the ILC detector should be able to withstand a fluence of 10^{12} neutrons/cm², which is orders of magnitude more than the numbers in table 7.1.

7.3 Other Silicon Trackers

7.3.1 Silicon Intermediate Tracker

Figures 7.21 and 7.22 show the average number of hits from charged particles per bunch crossing on the two layers of the Silicon Intermediate Tracker (table B.3). The absolute numbers for the two layers are similar, but the outer layer is much larger than the inner one, such that its relative hit density is considerably lower.

Layer	unscaled n/100 BX	NIEL-scaled n/100 BX	total 10^7 n/cm ²
1	7 ± 3.5	4.0 ± 2.5	14.4 ± 9.2
2	22 ± 5.6	8.1 ± 3.1	6.8 ± 2.6
3	31 ± 7.2	9.6 ± 3.6	5.5 ± 2.0
4	54 ± 9.0	20.7 ± 5.2	9.2 ± 2.3
5	58 ± 9.0	17.4 ± 4.4	6.3 ± 1.6
all	172 ± 29	59.8 ± 16.1	7.2 ± 1.9

Table 7.1: Neutron fluence in the vertex detector for 100 bunch crossings and for the integrated design luminosity of 500 fb^{-1}

Different from the vertex detector, the SIT will be implemented as a silicon strip device. On the one hand this implies a much smaller number of channels (and therefore a higher relative occupancy for a given number of hits), but on the other hand it enables a much faster readout of the sensors (and therefore less pile-up of background signals) – the SIT might possibly be read out after every single bunch crossing to support the timestamping of tracks.

In any case, the number of hits from beam-induced backgrounds is supposed to be absolutely uncritical for the SIT.

7.3.2 Forward Tracking Discs

Figures 7.23 and 7.24 show the average number of hits per bunch crossing on the seven Forward Tracking Discs of one detector half. The strong decrease for the outer discs is due to their increasing inner radius, because most background particles (primaries as well as backscatterers) are confined to the innermost parts of the detector geometry by the magnetic field.

The spatial distribution of hits on the innermost disc is shown in figure 7.25. Again it is clearly visible that most of the background activity is located close to the central axis: the hit density ranges from $(0.20 \pm 0.07) \text{ hits/cm}^2/\text{BX}$ at the inner radius down to $(3 \pm 3) \cdot 10^{-3} \text{ hits/cm}^2/\text{BX}$ at the outer radius of the innermost disc.

Figure 7.26 shows the time structure of the hits on the innermost disc. The distribution is similar to that of the vertex detector (figure 7.5), even though the separation between direct hits and backscatterers is not quite as strict. Upon closer examination, the rising edge around $t = 23 \text{ ns}$ can even be resolved into two peaks (not visible in figure 7.26) – backscatterers from

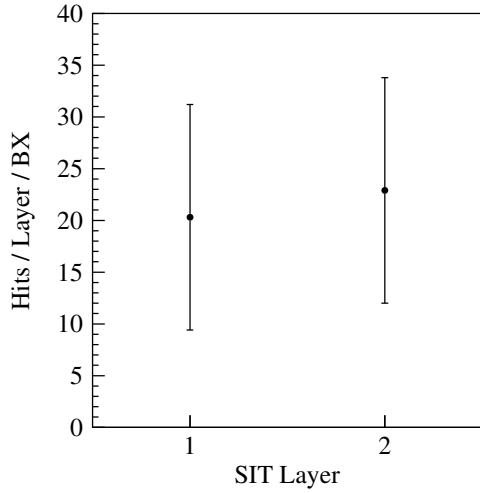


Figure 7.21: Hits on the Silicon Intermediate Tracker per bunch crossing, in absolute numbers

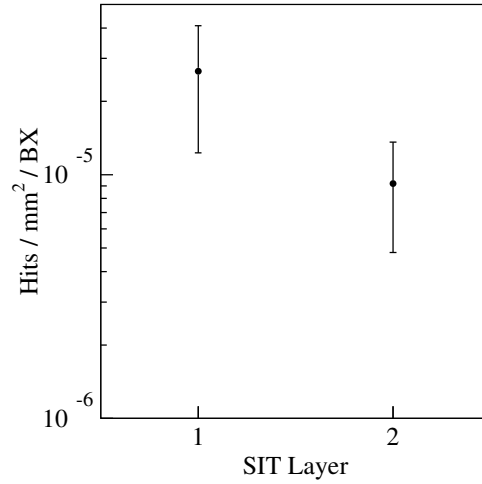


Figure 7.22: Hits on the Silicon Intermediate Tracker per bunch crossing, normalised per unit area

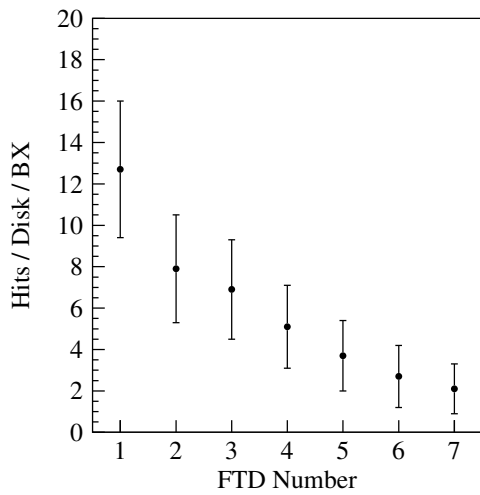


Figure 7.23: Hits on the Forward Tracking Discs of one detector half per bunch crossing, in absolute numbers

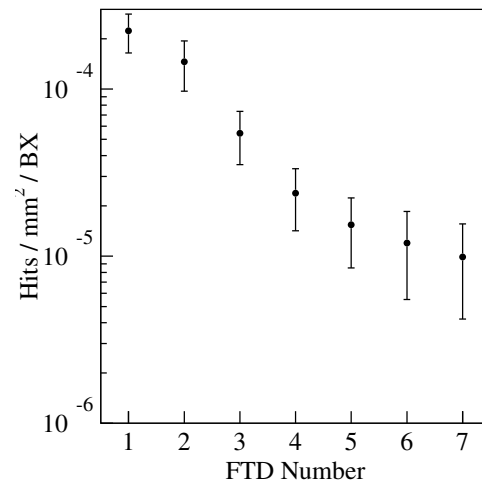


Figure 7.24: Hits on the Forward Tracking Discs per bunch crossing, normalised per unit area

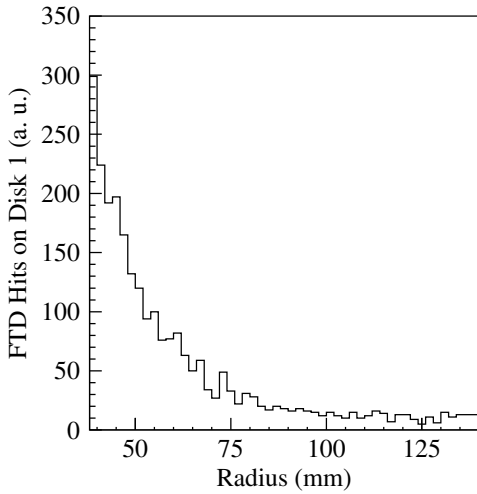


Figure 7.25: Radial distribution of hits on the Forward Tracking Discs

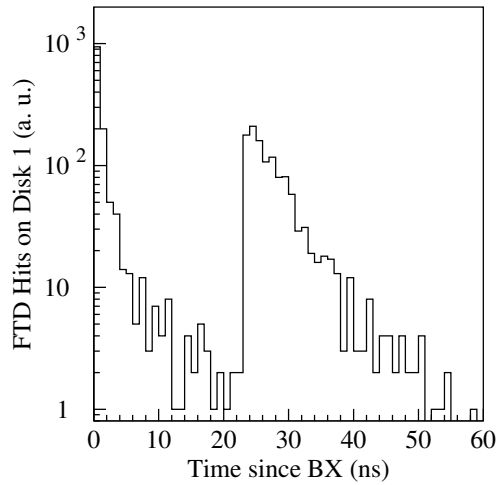


Figure 7.26: Time distribution of hits on the Forward Tracking Discs

the BeamCal on the same side of the detector arrive slightly earlier, whereas backscatterers from the BeamCal at the opposite side of the detector need a bit longer to reach the disc at $|z| = 200$ mm. As in the case of the vertex detector, the time structure will probably be unusable for the FTDs unless their sensors are particularly fast.

The occupancy from background hits is important for the Forward Tracking Discs because it may limit the pattern recognition performance for a given integration time of the inner pixel sensors: the relatively large distance between the discs makes it difficult to find matching hits, particularly in the case of low-energy tracks, and a large background occupancy can easily lead to tracking ambiguities. Recent studies indicate that a combination of three inner discs with slow pixel sensors (integrating over 20 bunch crossings) and four outer discs with fast micro-strip sensors will achieve the required performance [144], but more work is needed on this issue.

Furthermore, it should be noted that the magnetic field configuration plays an important role for the FTDs: the anti-DID field guides backscattered particles from the outgoing hole of the BeamCal back to the centre of the detector, where they will (almost) not interfere with the FTDs. In contrast to that, a DID field may lead backscatterers straight into the sensitive area of some of the inner FTDs, resulting in a “hot spot” with a significantly higher hit density, which may severely compromise the performance of the discs. An example is shown in section 7.7.2.

appearance	first	further
Particles entering from the outside		
photons	886 ± 53	61 ± 11
neutrons	71 ± 9	70 ± 14
electrons	0 ± 0^2	0 ± 0^{11}
Particles created on the inside		
electrons	292 ± 130	—
photons	1 ± 1^2	—
protons	2 ± 1^2	—

Table 7.2: Particles in the TPC per bunch crossing, averaged over 100 bunch crossings. Particles that enter the TPC for the first time as they move along their trajectory are counted in the left column. If they happen to enter the TPC again afterwards, they are counted in the right column. Asymmetric errors correspond to the 1σ bounds around the median, as explained in section 7.1.

7.4 Time Projection Chamber

7.4.1 Particles in the TPC

Like all detectors that are implemented in Mokka, the TPC will only write out a detector hit when a particle deposits a certain amount of energy in the sensitive gas volume (appendix B.1.6). To get a feel for the amount and the properties of all particles which enter the TPC (or which are created inside the chamber), Mokka was extended by means of a “virtual” sensitive cylinder that has the same size as the TPC gas volume. This cylinder is not a part of the detector geometry, but it is only known to the code for particle tracking (as a `G4UserTrackingAction`).

Whenever a particle enters the sensitive cylinder, its current position, starting position, energy, particle type, and the time since the bunch crossing are written to an additional output file. Two auxiliary flags indicate whether the particle was just created (i. e. whether its trajectory begins inside the TPC) and whether the particle enters the TPC for the first time or not. Particles can enter the TPC multiple times if they get reflected by some surface outside the chamber or if they happen to traverse the opening for the beam tube in the middle of the TPC.

Table 7.2 shows the average amount of particles which either enter the TPC from the outside or which are created inside the chamber volume. The table is not exhaustive, but the abundances of all other particle types are

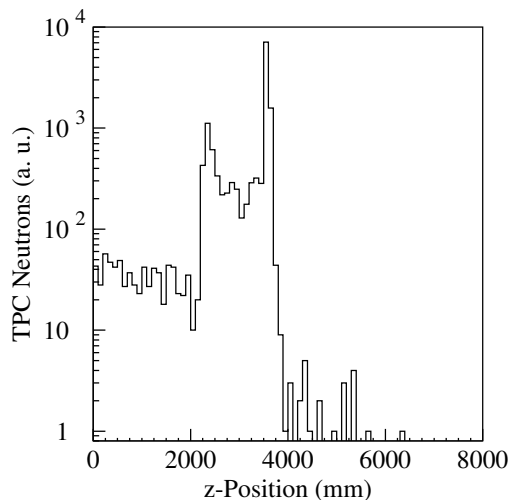


Figure 7.27: Origins of neutrons that enter the TPC volume

completely negligible. Numbers are given for a single bunch crossing, with the – partly very large – uncertainty corresponding to the statistical fluctuation per bunch crossing. Whereas photons can re-enter the TPC only by travelling through the inner opening, the fraction of re-entering neutrons is considerably larger: a significant number of neutrons is reflected back into the chamber by the inner surface of the ECAL. Only few electrons (and even fewer positrons) have enough energy to enter the TPC volume, but those typically re-enter the chamber many times because they curl on large helical trajectories.

Particles Entering from the Outside As expected, neutrons and photons are basically the only beam-induced background particles that are able to reach the TPC because they are not influenced by the magnetic field. In contrast to that, the largest number of charged backscattering particles originates at the BeamCal and is confined to the innermost regions of the detector by the magnetic field, reaching only the vertex detector if at all. The amount of primary particles which come directly from the interaction point and which have a high enough transverse momentum to reach the TPC is very small on average. However, if such particles only have a small longitudinal momentum and curl forward slowly, they can occasionally create a very large number of hits in the TPC.

Figure 7.27 shows the origins of neutrons that enter the TPC. Similar to the corresponding data for the vertex detector (figure 7.18), the most important source is the BeamCal. The contribution from the inner surface of the ECAL is larger just for geometrical reasons: if a nuclear process in the ECAL material releases one or more neutrons out of the surface, they will

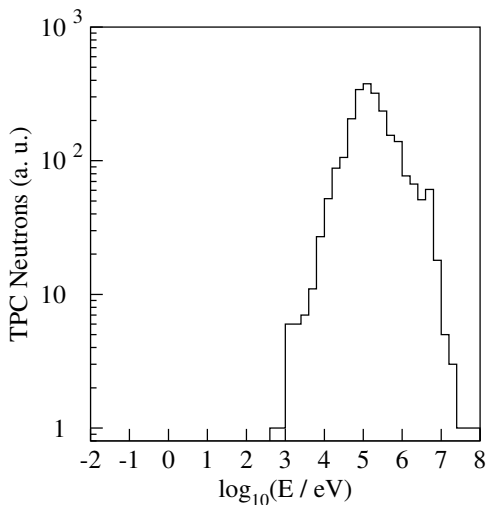


Figure 7.28: Energy distribution of neutrons that enter the TPC volume, at their point of origin

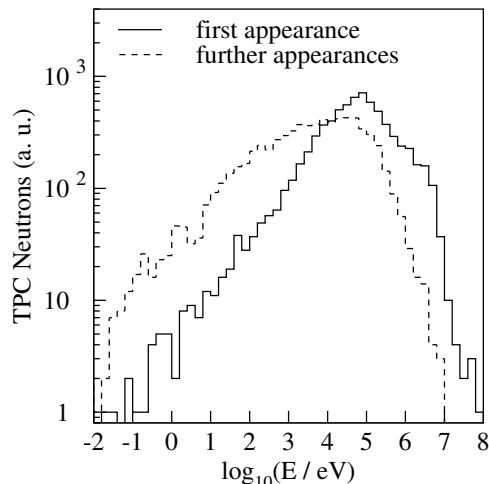


Figure 7.29: Energy distribution of neutrons that enter the TPC volume, at the moment of their entry into the chamber

almost inevitably enter the TPC volume, but not necessarily hit the rather small vertex detector.

Figures 7.28 and 7.29 show the energy spectra of neutrons at their point of origin and at the moment of their entry into the TPC volume respectively. Figure 7.29 is split into contributions from those neutrons entering the chamber for the first time and those entering repeatedly. As expected, the overall energy distribution tends to shift downwards as the neutrons undergo more and more interactions with the detector material. Still, almost all neutrons do not reach thermal energies in the simulation, which means that they are presumably captured away by nuclei before.

The origins and the energies of photons that enter the TPC are shown in figures 7.30 and 7.31. As in the case of neutrons, the most important sources are the BeamCal, the inner surface of the ECAL, and the vicinity of the interaction point. Large amounts of photons are produced in electromagnetic showers in the forward calorimeters, and some will also be released in the deexcitation of nuclei after hadronic processes, e. g. neutron capture or scattering in the ECAL.

It should be noted that the large distance between the LumiCal and the BeamCal helps to reduce the amount of photons that can reach the TPC: by far the largest number of all photons originate at the surface of the BeamCal, but most of them cannot reach the TPC because the direct line of flight is obstructed by the LumiCal. The remaining solid angle gets smaller

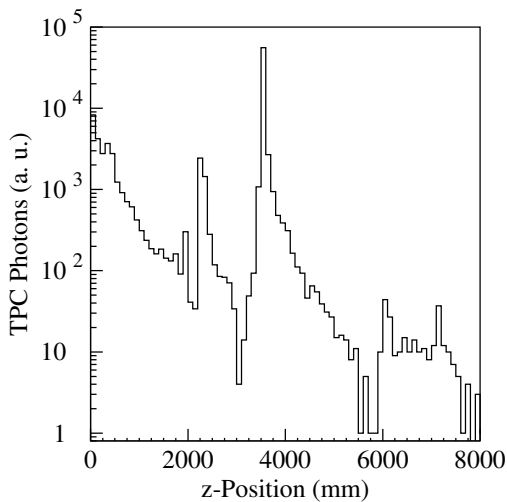


Figure 7.30: Origins of photons that enter the TPC volume

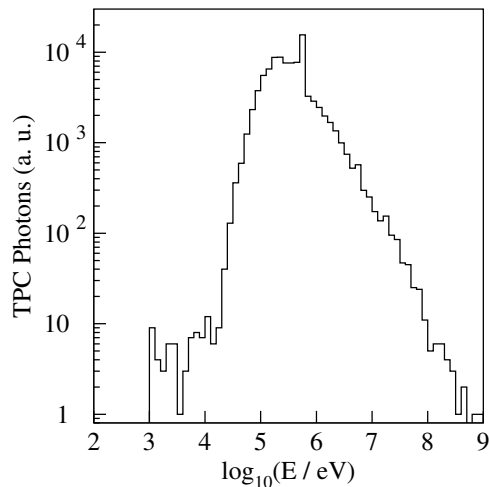


Figure 7.31: Energy distribution of photons that enter the TPC volume

as the distance between LumiCal and BeamCal increases (figure 7.32). For comparison, simulation results for other designs of the forward region can be found in section 7.7.1. A similar effect applies to photons from the beam delivery and extraction system: such photons do have a chance to hit the vertex detector, but there is only a small chance for them to reach the TPC.

Particles Created on the Inside Electrons make up the by far largest fraction of particles that are created inside the chamber volume. The dominant production processes are the ionisation of gas molecules by charged particles, the photoelectric effect, and Compton scattering of photons. Photon conversion, however, plays only a minor role because the energies of most incident photons are too low.

It must be kept in mind that not every electron that would be created in the real chamber also appears in the simulation: the internal range cut of Geant4 ensures that only particles with a range larger than the cut will actually be simulated and tracked through the detector geometry. In the simulations that are presented here, the range cut was set to $100 \mu\text{m}$, which corresponds to an energy of approximately 2 keV for electrons in argon. Particles with a range lower than the cut will not be simulated by Geant4, but only be counted as a local energy deposit of their parent. This concept roughly corresponds to the notion of delta-rays, i. e. ionisation products that are visible as particles of their own alongside an ionised track.

Having that said, an energy spectrum of electrons (at their respective

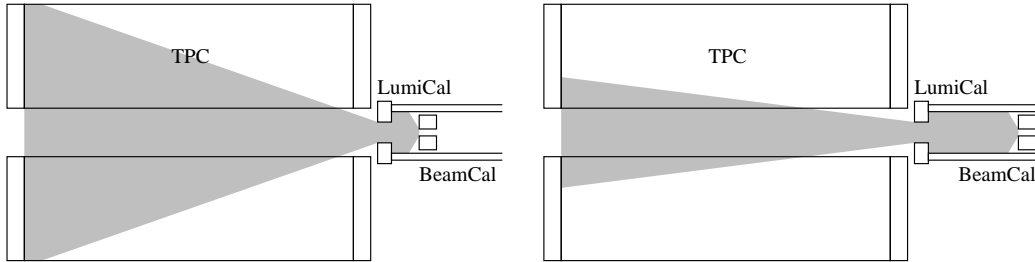


Figure 7.32: A larger distance between LumiCal and BeamCal reduces the backscattering of photons into the TPC.

origins inside the chamber) can be found in figure 7.33. A steep low-energy edge, which corresponds to an internal cut-off in the Geant4 physics list, can be seen at 1 keV. The rest of the spectrum corresponds to the energy distributions of the respective production processes for electrons, convoluted with the energy spectrum of photons in the chamber.

The number of protons that are created in the TPC is very small, but not zero. This shows that the expected process of neutron-proton scattering (with neutrons entering the TPC from the outside and protons being present as hydrogen in the quencher gas) is simulated by Geant4, but that its contribution to beam-induced backgrounds in the chamber is small. As expected for the scattering of particles of equal mass, the energy spectrum of protons (figure 7.34) is similar to the spectrum of neutrons in the chamber (figure 7.29).

The energy that is deposited in the chamber by recoiling protons makes up around 2.5 % of the total deposited energy, which indicates that the contribution of neutron-proton scattering is small, but not completely negligible. However, it should be taken into account that protons with their high dE/dx and a range of the order of millimetres will typically deposit their energy along a very short track, which may just appear as one blob of primary ionisation. Therefore, protons have no significant impact on the occupancy of the chamber and on pattern recognition, but merely on the total amount of primary charge.

As a consequence, the hydrogen content of the chamber gas is not crucial with respect to the resulting beam-induced backgrounds in the TPC – there seems to be no need to choose a hydrogen-free gas mixture for the suppression of backgrounds.

As a cross-check, the process of neutron-proton scattering in the TPC is also calculated with the help of measured cross-sections: the maximum of the neutron energy spectrum is around 10–100 keV, and the total cross-section for elastic neutron-proton scattering in this energy range has been

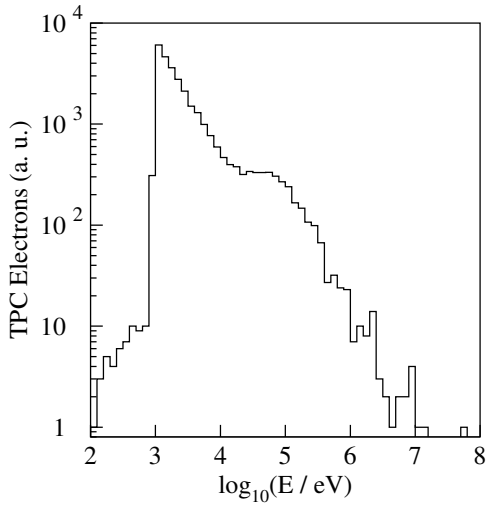


Figure 7.33: Energy distribution of electrons that are created inside the TPC volume

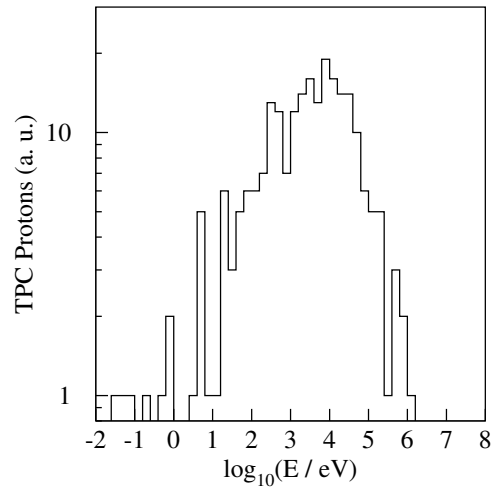


Figure 7.34: Energy distribution of protons that are created inside the TPC volume

measured to be approximately 20 barn (figure 7.35). TDR gas under standard conditions (5 % of CH_4 , $6 \cdot 10^{23}$ molecules per 22.4ℓ) has a proton density of $5 \cdot 10^{18}$ protons/ cm^3 . Assuming that 150 neutrons with an approximate mean path length of 100 cm enter the TPC per bunch crossing, one expects

$$150 \cdot (5 \cdot 10^{18} \text{ cm}^{-3}) \cdot 100 \text{ cm} \cdot (20 \cdot 10^{-24} \text{ cm}^2) = 1.6$$

scattered protons per bunch crossing, which agrees well with the simulation results (bottom row of table 7.2). This calculation is, of course, only a rough back-of-the-envelope estimate, but it shows that the outcome of the Geant4 simulation has the right order of magnitude.

Another cross-check with an (unrealistically high) CH_4 concentration of 20 % in the TPC gas is shown in section 7.8.2.

7.4.2 Hits in the TPC

Due to the technical implementation of the TPC in Mokka (appendix B.1.6), the “TPC hits” that get written out by the simulation are neither compatible with the notion of an occupied TPC voxel nor with the concept of a hit as it emerges during the reconstruction of tracks from measured or simulated data. Mokka TPC hits are merely energy deposits along the trajectories of charged particles, separated by no more than the maximum step length (set to 5 mm), but not digitised or otherwise binned in any way.

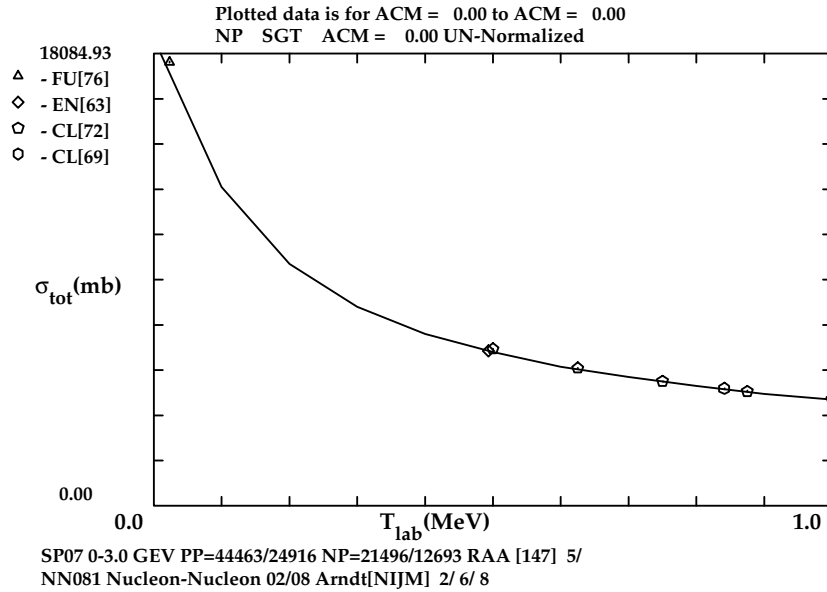


Figure 7.35: Measured total cross-section (“SGT”) for neutron-proton scattering at $0 \text{ MeV} < T_{\text{lab}} < 1 \text{ MeV}$, generated by [145]. The measured points are taken from [146]. The vertical axis ranges from 0 barn to approximately 18 barn.

To calculate properties such as the TPC occupancy or primary charge densities, the Mokka hits need to be filled into three-dimensional voxels (section 7.4.3). Moreover, to obtain reconstructed hits that could be used for an actual track fit, the Mokka hits would need to undergo a full-fledged digitisation, pulse finding, hit finding, and hit reconstruction algorithm. (Earlier TPC implementations in Mokka, which were all based on virtual “gas layers”, could have a simple Gaussian smearing applied to their hits, but this is not possible for the Mokka driver “tpc04”.) The complete digitisation and reconstruction software chain is still under development (section 6.3.4), but it is more needed for the analysis of physics events than for background studies.

Despite their lack of an immediate physical meaning, the plain Mokka hits can still be useful to get a qualitative impression of the background signals in the TPC – hit distributions in space and time already reveal some distinct characteristics of the beam-induced backgrounds in the TPC.

Spatial Distribution Figure 7.36 shows an overlay of the TPC hits from 100 bunch crossings, seen from the endplate of the chamber, i. e. projected onto the xy -plane. Figure 7.37 shows the same hits seen from the side, i. e.

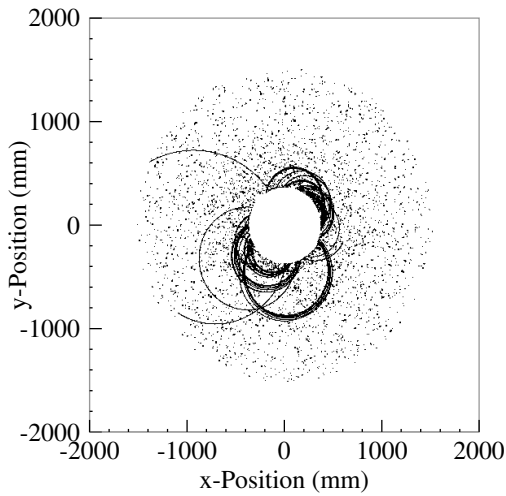


Figure 7.36: Mokka hits in the TPC from 100 bunch crossings, seen from the front. Most of the hits belong to “salt and pepper” backgrounds.

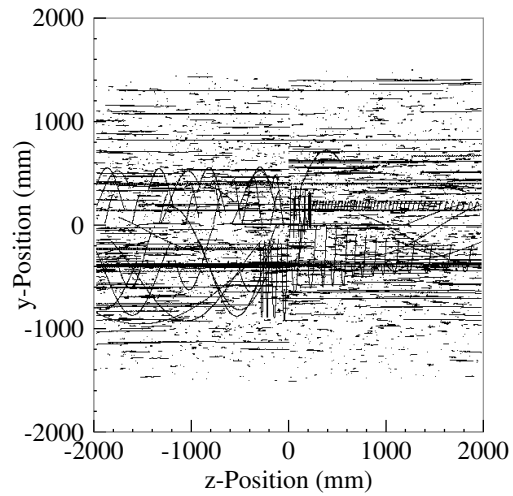


Figure 7.37: Mokka hits in the TPC from 100 bunch crossings, seen from the side. This view reveals the peculiar structure of the microcurlers.

projected onto the yz -axis. The drift of charges in the chamber between each bunch crossing is not taken into account here.

The front view shows only very few tracks of particles that have enough energy to leave the chamber through its outer wall. A couple of medium-energy curlers appear rather close to the inner wall, with some of them performing many turns in the magnetic field and producing a large number of densely distributed hits in the chamber. The rest of the signals consists of more or less randomly distributed blobs, sometimes called “salt and pepper” backgrounds.

Only the side view reveals that most of these blobs correspond to thin trails of hits which are aligned in the z -direction and which extend over lengths from a few centimetres up to the full length of the chamber. These patterns are created by low-energy electrons which curl very tightly around the magnetic field lines, but which still have enough energy to cover a sizable distance while they ionise the chamber gas. Such electrons are produced by photons through the photoelectric effect or Compton scattering, and therefore their ionisation patterns have no visible connection to other tracks – the “microcurlers” seem to appear out of nowhere and are often stopped again before they can even reach the end of the chamber. It is both impossible and needless to reconstruct such tracks. Instead, it should be rather easy to have the microcurlers filtered out by a pattern recognition algorithm in the

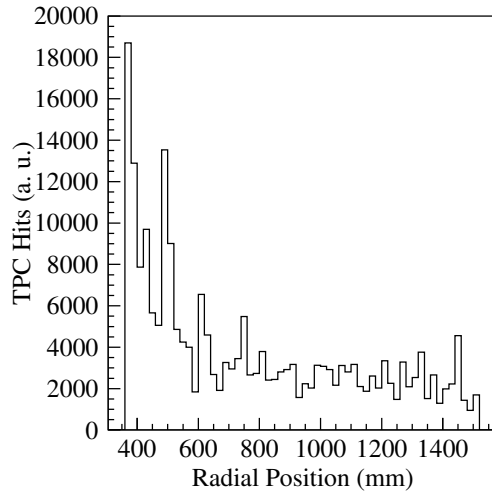


Figure 7.38: Radial distribution of hits in the TPC

reconstruction software.

The radial distribution of hits in the TPC is shown in figure 7.38. The histogram is not normalised per unit volume, i.e. it does not take into account that the circumference of the corresponding volume elements increases proportional to the radius. Except for a region of high activity close to the inner wall, the number of hits per bin remains roughly constant, which means that the average hit density falls approximately with $1/r$ towards the outer wall. Statistical fluctuations are high due to the curlers and microcurlers, which can sometimes produce very large numbers of hits in a small radial region.

Time Distribution Figure 7.39 shows a time distribution of the TPC hits: the radial distance of each hit from the z -axis is plotted against its time, measured from the moment of the bunch crossing. The result is similar to those for the vertex detector (figure 7.5) and the Forward Tracking Discs (figure 7.26): immediately after the bunch crossing, almost only tracks originating from the interaction point appear in the TPC. Very few disconnected microcurlers are caused by photons that are created close to the interaction point (e.g. by bremsstrahlung in the material of the beam tube wall).

About 20 ns later, a strong wave of backscattered photons enters the chamber, releasing large numbers of microcurlers throughout the volume. Again, the time offset corresponds to the distance to the BeamCal and back. Since the TPC itself has a length of almost 4 m, the distribution is inherently broader than in the case of the small vertex detector. The slight inclination of the dark band in figure 7.39 is caused by the fact that the photons need a

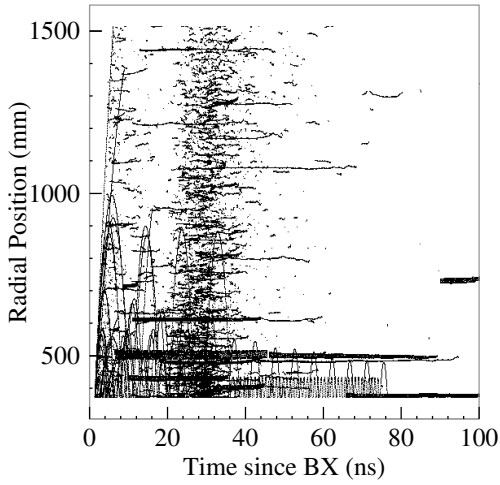


Figure 7.39: Time distribution of hits in the TPC, plotted against the radial position

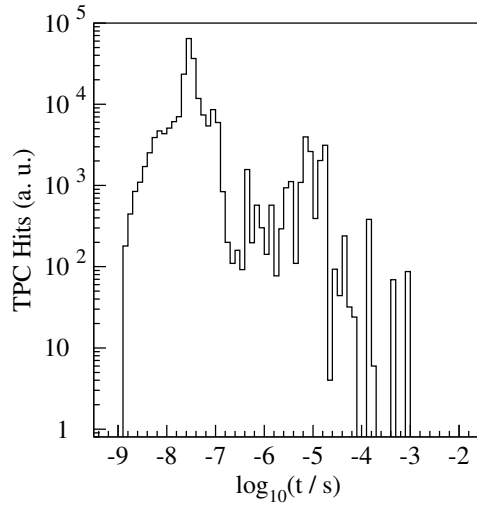


Figure 7.40: Time distribution of hits in the TPC. Note that the double-logarithmic scale ranges from the order of nanoseconds to several milliseconds.

bit more time to reach the outer regions of the chamber.

After approximately 40 ns, the activity in the TPC fades out: only a few slow curlers with a low longitudinal momentum are still travelling through the chamber, and a few further photons release new electrons in the gas. Some of these photons may come from more distant sources, but most are emitted in the deexcitation of nuclei that are the products of hadronic processes such as neutron scattering or capture. Figure 7.40 – a logarithmic time distribution of TPC hits that covers a much larger interval – shows that these incidental photon emissions continue for a very long time (up to 1 ms, i. e. the length of a whole bunch train), but their relative contribution to the total charge in the TPC is small: about 12% of all hits appear more than 100 ns after the bunch crossing, 8% appear more than $1\ \mu\text{s}$ later, and 3% have a delay of more than $10\ \mu\text{s}$.

7.4.3 Occupancy of the TPC

To get an estimate for the TPC occupancy that is caused by beam-induced backgrounds, the Mokka hits from 100 bunch crossings are filled into three-dimensional voxels as described in section 6.3.3. The relative occupancy is then the number of voxels with a non-zero energy (or primary charge) content, divided by the total number of voxels.

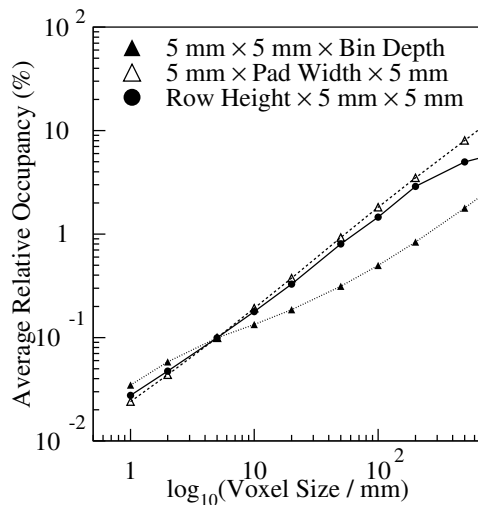


Figure 7.41: The relative occupancy for varying voxel sizes in three dimensions (overlay of 100 bunch crossings)

Strictly speaking, only those voxels will be counted that contain enough primary charge to be actually registered by the readout electronics. Assuming an appropriate gain of the amplification system (typically 10^3 – 10^4) and very sensitive readout electronics, a primary charge of a few electrons per voxel could be sensed and would result in a non-zero readout signal [147]. This corresponds to an approximate threshold of 100 eV deposited energy per voxel. Anyhow, it turns out that the largest fraction of voxels contains much more primary charge than that (figure 7.44).

All occupancy values are determined for an overlay of background signals from 100 bunch crossings. This number of bunch crossings that will pile up in the chamber during one readout frame is not yet fixed – depending on the size of the chamber and the drift velocity of the gas, around 100 to 160 bunch crossings will finally be overlaid. All occupancy values can be corrected for such variations by scaling them up accordingly.

Variation of the Voxel Size Neither the pad size nor the readout sampling frequency of the TPC for the ILC detector have been finally fixed yet. To understand the influence of the voxel size on the TPC occupancy, the occupancy is determined for various voxel sizes. Starting from the arbitrary size of $5 \times 5 \times 5 \text{ mm}^3$, the radial size (i. e. the height of pad rows in ρ), the azimuthal size (i. e. the pad width in φ), and the longitudinal size (i. e. the depth of time bins in z) is varied independently towards very small and also very large values.

The result is shown in figure 7.41: starting from a value of 0.1% for the medium voxel size of $5 \times 5 \times 5 \text{ mm}^3$, the relative occupancy generally increases and decreases along with the voxel size, as expected. An interesting observation, however, is the fact that the dependency on the longitudinal voxel size is only weak, keeping in mind that the scales in figure 7.41 are logarithmic.

This behaviour can be explained by the peculiar spatial structure of the beam-induced backgrounds, which could already be seen in figure 7.37. As shown in the middle row of figure 7.42, hits that are mostly aligned in the z -direction (as in the case of the many microcurlers) let the relative occupancy depend only weakly on the longitudinal voxel size. If, for comparison, the TPC contained mostly tracks from particles with a high transverse momentum (upper row of figure 7.42), the relative occupancy would hardly depend on the radial voxel size. Likewise, if the TPC backgrounds consisted of randomly distributed, unstructured hits (lower row of figure 7.42), the relative occupancy would be strictly proportional to the voxel size in all three dimensions.

Figure 7.41 also shows that the occupancy curve for the longitudinal voxel size rises more steeply again as it approaches the order of 100 mm. This size is a typical scale for the length of the microcurler structures, and if the voxels become larger than that scale, the lengthy trails behave point-like again. This order of magnitude is of course irrelevant for the TPC because the readout voxels will certainly be much shorter, but it might play a role for other detectors that are segmented into larger structures, such as the Silicon Intermediate Tracker with its long silicon strips.

Finally, it should be noted that the results for very small longitudinal voxel sizes (around 2 mm and below) are not reliable: due to the maximum step length that is implemented in the simulation (appendix B.1.6), two Mokka hits from a given particle in the TPC are guaranteed to be no further apart than 5 mm, but in between there may be a gap. If the voxel size is smaller than the maximum step length, binning effects are possible and the occupancy may be underestimated due to empty voxels between two consecutive hits. However, due to the distinct pattern of the background signals, this problem affects only the longitudinal voxel size. As a result, the fall-off at the left end of the z -curve in figure 7.41 is probably a binning artifact.

Radial Dependency of the Occupancy Using a more or less realistic voxel size of $5 \times 1 \times 5 \text{ mm}^3$ (i. e. pads of 5 mm height and 1 mm width with a time bin depth of 10 samples at 100 MHz readout frequency and

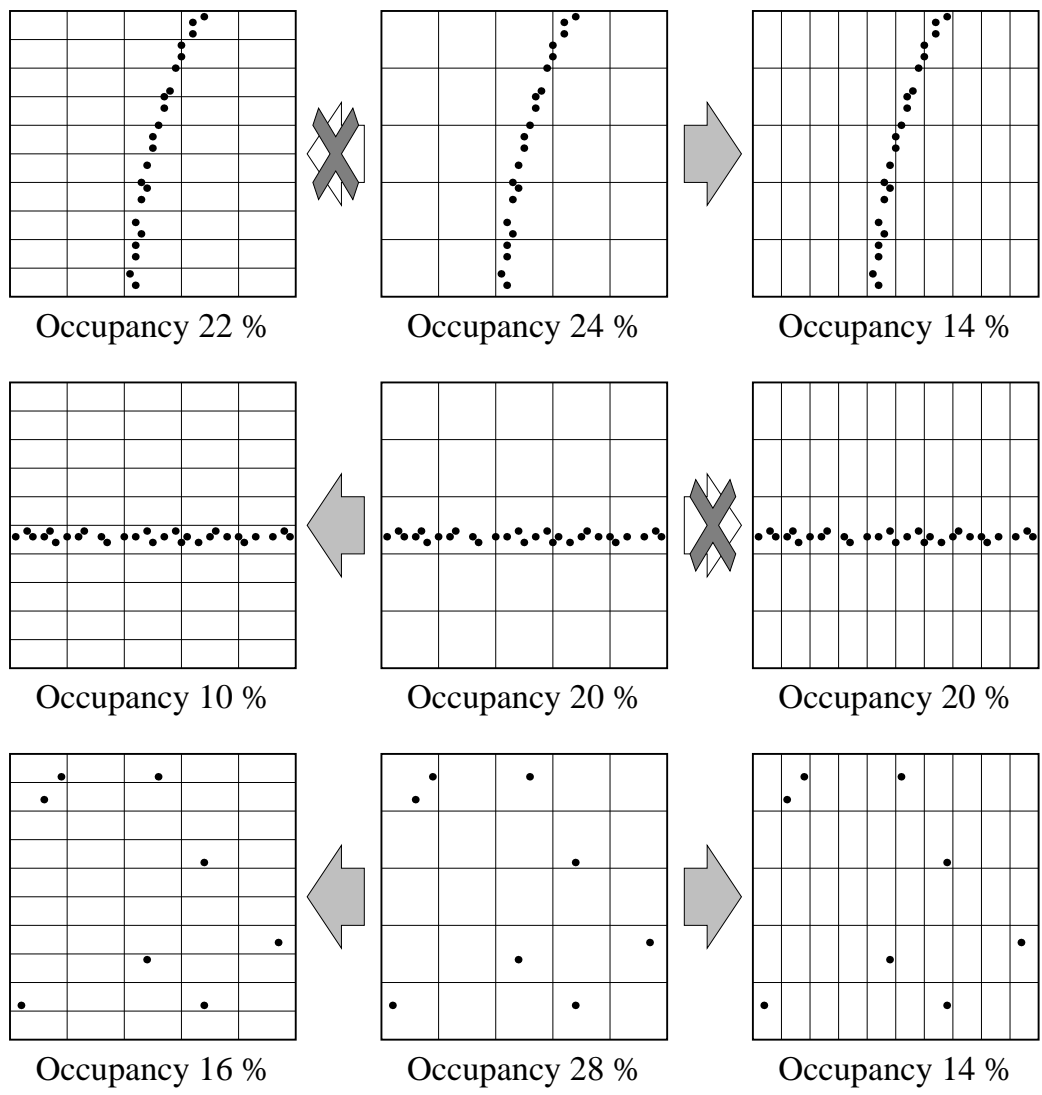


Figure 7.42: The relative occupancy depends weakly on the voxel size in a given dimension if the hits are mostly aligned in that direction. Because microcurlers produce hit patterns like in the middle row, the relative occupancy in figure 7.41 depends only weakly on the longitudinal voxel size.

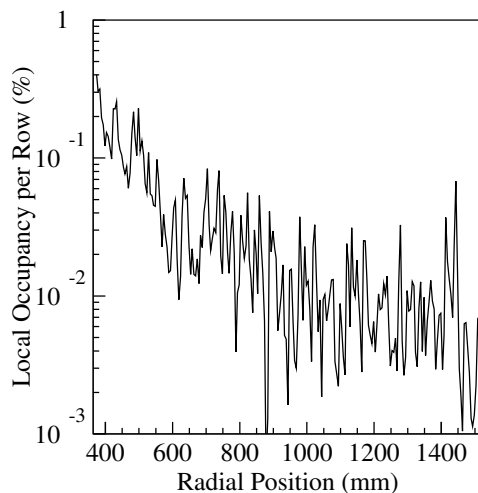


Figure 7.43: Local relative occupancy per pad row in dependency of the radial position (overlay of 100 bunch crossings)

50 $\mu\text{m}/\text{ns}$ drift velocity), the local relative occupancy is calculated for each of the 229 pad rows. The result, which is shown in figure 7.43, reproduces the qualitative impression from the undigitised hits in figure 7.36: the occupancy is highest close to the inner wall of the TPC, where it almost reaches 1 %, but it drops off quickly towards the outer regions of the chamber, with values ranging from 0.1 % well down to 0.01 %. The statistical fluctuations between different pad rows are large because a single microcurler (or also the far side of a medium- p_t curler) may occupy a large number of voxels that are all in the same pad row.

Primary Charges in the Chamber Figure 7.44 shows a spectrum of the energy deposit (or number of primary electrons) that is contained in each non-empty voxel. The variations are very large: a single voxel may contain a few primary electrons, but also hundreds or thousands. It should be noted that the spectrum does not have the shape of a Landau distribution (as it could be expected for the energy loss in thin layers of gas) since the signals are not caused by continuous tracks in the gas, but by particles with various, mostly low energies. These particles curl more or less tightly around the magnetic field lines and they are often stopped somewhere in the middle of the chamber, such that a naïve dE/dx measurement does not yield sensible results.

The mean charge density of primary electrons in dependency on the radial position in the chamber is shown in figure 7.45. This time, all voxels in a

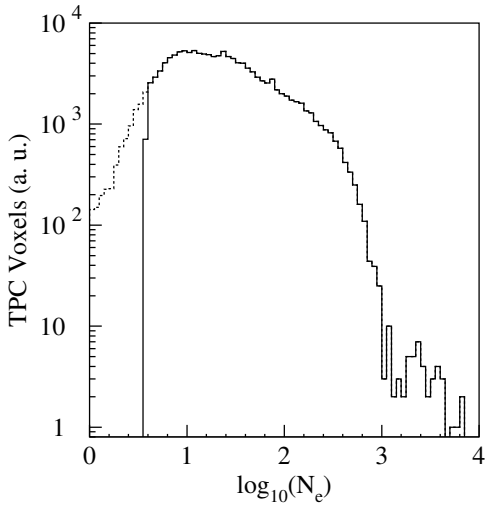


Figure 7.44: Distribution of the primary charge per non-empty voxel. The rising edge corresponds to an assumed electronics threshold of four primary electrons per voxel.

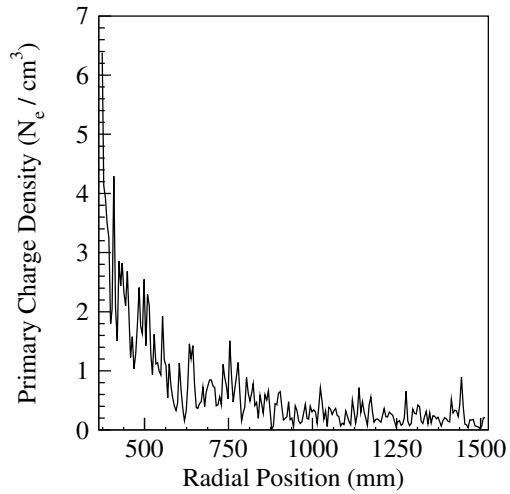


Figure 7.45: Primary charge density in the sensitive TPC volume in dependency of the radial position (overlay of 100 bunch crossings). Neither the gas amplification nor backdrifting ions are taken into account here.

given pad row are taken into account for the average value. The absolute numbers are therefore orders of magnitude lower than in figure 7.44, where only occupied voxels were considered. Again, the highest charge density (a few primary electrons per cubic centimetre) is found close to the inner wall of the chamber, whereas the values for the outer regions of the chamber are substantially lower.

Implications for the TPC Performance An occupancy of 1% is commonly taken as a critical limit that could still be tolerated by the TPC without a significant loss in resolution and also tracking efficiency [63, 39]. The simulation results show that this global occupancy is never reached for any realistic voxel size, and that the local occupancy approaches 1% only in regions that are very close to the inner wall of the chamber. Furthermore, these numbers do not even take the particular structure of the background signals into account: most of the hits are not scattered randomly but aligned in shorter or longer trails along the z -direction. This means that only a relatively small number of readout pads are affected by the backgrounds (cf. figure 7.36), but that these pads will often be blinded for a longer time when they are reached by an extended stream of charges (cf. figure 7.37).

In a pattern recognition algorithm, it should not be hard to find and to eliminate signals from microcurlers and small disconnected energy deposits (caused by photons) that appear at random positions in the chamber. Only very few patterns of background signals resemble usual particle tracks. Furthermore, since the background occupancy is completely negligible in the outer regions of the chamber, a track finding algorithm could also work its way outside-in to distinguish track hits from backgrounds more easily in regions where the background occupancy is higher.

The studies that are presented here do not yet address the problem of backdrifting ions in the chamber (section 5.3.4). Tools are currently under development in order to simulate the amplification of primary charges in a GEM structure, the extraction of backdrifting ions out of the GEM foil into the drift volume of the chamber, the formation of a slowly-drifting ion disc, and the influence of such a disc (or even multiple discs) on the drifting primary charges in the chamber volume (MarlinTPC, section 6.3.4). The studies that are foreseen with MarlinTPC will also take beam-induced backgrounds into account (section 9.2).

7.5 Electromagnetic Calorimeter

The ECAL has been included in the simulations and the resulting ECAL hits are available in the resulting output files, but no analysis or evaluation has been done for the studies that are presented in this thesis.

7.6 Hadronic Calorimeter

The Hadronic Calorimeter is, to a large extent, well shielded against beam-induced backgrounds: charged particles from electromagnetic showers in the BeamCal (and possibly the beam delivery and extraction system) cannot penetrate the tungsten support tube, which fully encloses the forward detectors and magnets, and the ECAL shields the inner HCAL surface from any background particles travelling through the TPC. Only neutrons and photons have a chance to traverse the tungsten tube and to reach the inner parts of the HCAL endcaps, but they may possibly inflict radiation damage on the silicon photomultipliers that are used for the steel-scintillator HCAL design.

In order to get a handle on these particles, the simulation uses the same kind of sensitive surfaces as described in section 7.2.2. These surfaces are located at $2500 \text{ mm} < |z| < 3500 \text{ mm}$ and they have radii of $r = 300 \text{ mm}, 400 \text{ mm}, 600 \text{ mm}, 900 \text{ mm}, 1200 \text{ mm},$ and 1500 mm , i. e. they just fit into the HCAL endcaps.

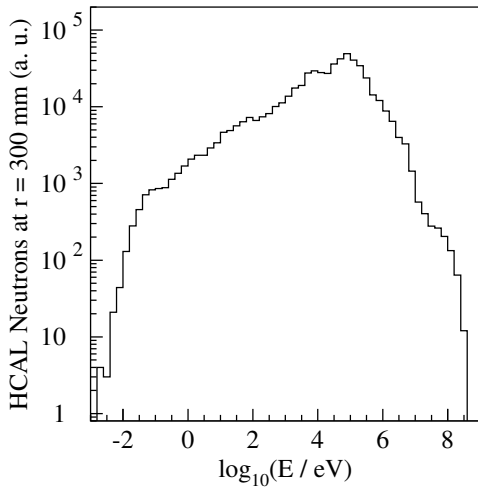


Figure 7.46: Energy distribution of neutrons in the HCAL endcap at $r = 300$ mm

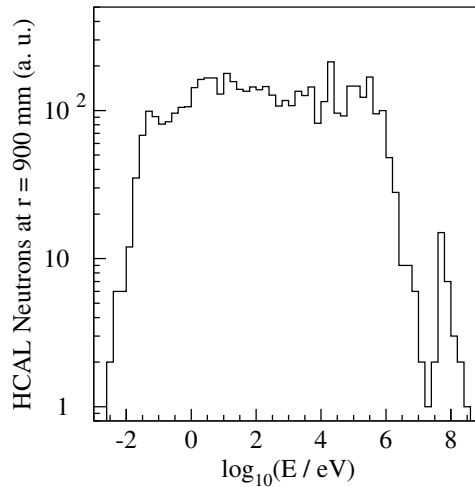


Figure 7.47: Energy distribution of neutrons in the HCAL endcap at $r = 900$ mm

7.6.1 Neutrons in the Endcap

Figures 7.46 and 7.47 show the energy spectra for $r = 300$ mm and $r = 900$ mm, respectively. The spectra are roughly similar, but it can be seen that more neutrons have been moderated down to very low energies at the surface that is located further outwards.

The total neutron fluence – weighted by NIEL scaling factors, scaled to the integrated design luminosity of 500 fb^{-1} , and normalised per unit area as in section 7.2.2 – is shown in figure 7.48. Again, the errors correspond to the scaled statistical uncertainty from 100 bunch crossings. The upper boundary of the plot marks the radiation dose of 10^{10} neutrons/cm², which is currently considered to be the maximum allowed dose before the silicon photomultipliers will start to degrade significantly [148]. The simulation indicates that only the pieces at very small radii get close to this limit.

This result, which lies on the critical border, shows that further, more detailed simulations with an improved description of the latest HCAL geometry and material composition may be needed – the current results cannot grant the highly desirable safety margin of at least a factor of 10 (section 7.9). In case the problem persists in future simulations, it may be worthwhile to consider the usage of a dedicated neutron moderator (e.g. a layer of hydrocarbon-based plastic or paraffin) or even a neutron absorber (e.g. a thin sheet of cadmium to cover the outside of the tungsten support tube) in the experimental set-up. Another – maybe accessory – measure would of course

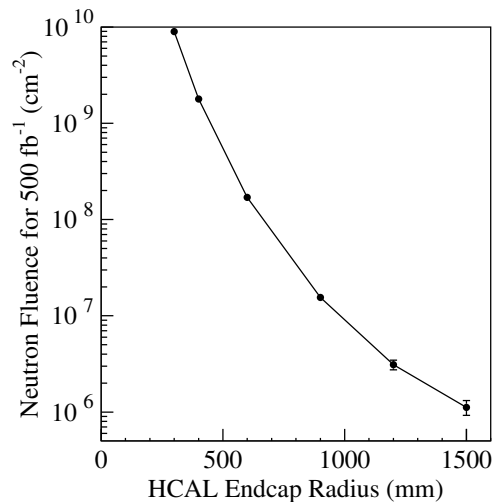


Figure 7.48: Total neutron fluence for 500 fb^{-1} in the HCAL endcaps, in dependency of the radial position. The upper boundary corresponds to the critical fluence of 10^{10} neutrons/cm².

be to have some spare scintillator tiles at hand to replace the original photomultipliers in the innermost parts of the endcaps if they have eventually degraded too much.

7.6.2 Photons in the Endcap

Similar to neutrons, there is also a maximum allowed dose for photons in the silicon photomultipliers of the HCAL [149]. The simulation shows that the background-related photon dose stays more than two orders of magnitude below that limit of 10^{12} photons/cm² even very close to the beam pipe.

It should still be noted that the tungsten support tube for the BeamCal plays a crucial role for the suppression of backgrounds in the HCAL endcaps. Some comparative studies with alternative designs of this tube can be found in section 7.7.6.

7.7 Design Options

7.7.1 Forward Region Layout

The layout of the forward region has substantially changed and developed over time. One of the key issues of this development are the final focus quadrupoles, which are the last elements of the roughly 2-km-long beam delivery system and which – at least partially – reach into the detector itself. The final focus quadrupoles set an outer limit on the position of the detector

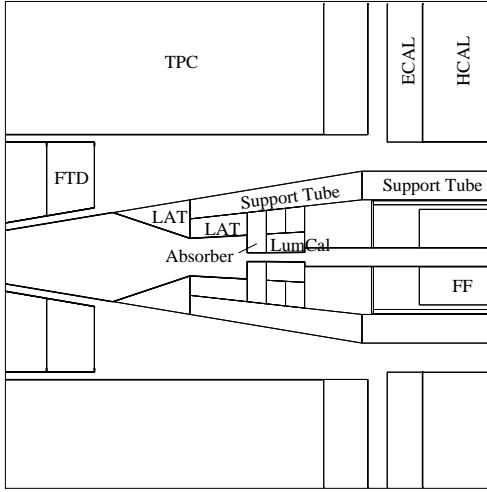


Figure 7.49: Simulated forward region according to the TESLA TDR (compressed by a factor of 2 in z -direction)

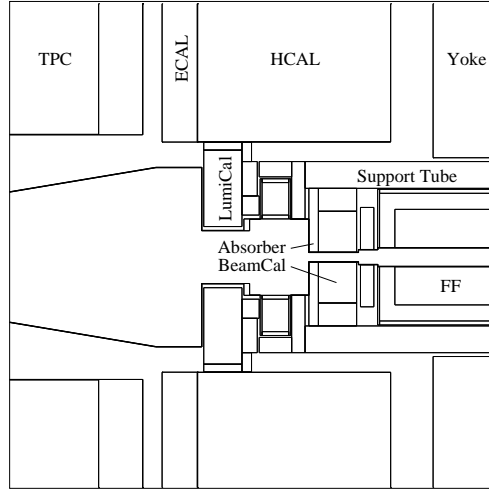


Figure 7.50: Simulated forward region according to the improved layout of 2004 (compressed by a factor of 2 in z -direction)

devices in the forward region: the low-angle calorimeters must be placed in front of the magnets. Only low-angle photons, which are not influenced by the magnetic fields, could possibly be detected in a much more distant calorimeter (a device named “GamCal” at $z \approx 200$ m is currently under discussion) [150].

On the one hand, a large distance of the final quadrupoles – and therefore a large focal length L^* – is desirable to keep possible backscattering sources far away from the inner regions of the detector, containing the highly sensitive vertex detector and also the TPC. On the other hand, L^* is limited by technical constraints: the longer the focal length, the higher are the requirements on the field quality and the mechanical precision of the quadrupoles. Only a certain maximum L^* can be accepted in order not to risk a deterioration of the beam spot size, which would lead to a decreased luminosity of the collider.

The forward region of the detector from the TESLA TDR [35] (figure 7.49) was still dominated by the final focus magnets with a focal length of $L^* = 3.00$ m. The innermost forward calorimeter (then called “LumCal”, but corresponding to today’s BeamCal) was placed at $2200 \text{ mm} < z < 2400 \text{ mm}$, i.e. still within the TPC, which had a longer sensitive volume of 2500 mm then. The “Low-Angle Tagger” with its distinct conical shape (roughly corresponding to today’s LumiCal), positioned at $1400 \text{ mm} < z < 2100 \text{ mm}$, would reach far into the sensitive volume of the TPC. In this design, both

forward calorimeters act as significant scattering targets, and large numbers of particles can enter the TPC.

At the end of 2004, an improved layout of the forward region (figure 7.50) was presented [151]. Assuming that a final focus length of $L^* = 4.05$ m is technically feasible, the innermost calorimeter (since then called BeamCal) could be moved outwards to $3650 \text{ mm} < z < 3850 \text{ mm}$, i. e. hidden deep inside the HCAL endcap. The second calorimeter (named “LumCal”) lost its special conical shape and was shifted to $3050 \text{ mm} < z < 3250 \text{ mm}$, i. e. shortly behind the ECAL endcap. This layout is much more favourable with respect to detector backgrounds since both forward calorimeters are much further away from the inner detector. The BeamCal is well-shielded not only by its tungsten support tube, but also by the HCAL endcap as a whole and partially by the LumCal, which blocks the path of backscattered photons heading for the TPC. However, the design relies on improved final focus magnets with an increased L^* .

Finally, the advent of LDC version 2 with its shortened TPC of only 1970 mm brought yet another slight improvement of the forward region (figure 6.2): leaving the BeamCal basically at its previous place ($3550 \text{ mm} < z < 3750 \text{ mm}$), but pulling the LumiCal inwards into the ECAL endcap (now at $2270 \text{ mm} < z < 2470 \text{ mm}$), the angular coverage against backscattering photons from the BeamCal is increased, and even fewer particles can reach the TPC (cf. figure 7.32). The choice to put the LumiCal immediately behind the TPC endplate implies that the front and the inner surface of the LumiCal should be hit by as few particles as possible since any particles backscattering from the LumiCal would be produced right next to the TPC. A comparison of different inner radii for the LumiCal can be found in section 7.7.4.

Table 7.3 compares the number of particles that enter the TPC for the different forward region designs, using the 500-GeV TESLA beam parameter set (table 2.1). The improvement is clearly visible, both in terms of photons and neutrons that reach the TPC, and hence also in the number of electrons and protons that are created inside the chamber.

7.7.2 Crossing Angles

The choice of a beam crossing angle and especially the superposition of an additional DID or anti-DID field over the main solenoid field has a crucial impact on beam-induced backgrounds. With regard to physics, head-on collisions (as foreseen for TESLA) would be the cleanest and best solution, but the technical challenge lies in the separation of the incoming and outgoing beams at some point of the beam delivery and extraction system (typically behind the final focus). TESLA planned to use electrostatic sepa-

	TESLA TDR head-on	Stahl 2005 head-on	LDC v2 14 mrad
Particles entering from the outside			
photons	7843 ± 205	6234 ± 152	1680 ± 61
neutrons	19990 ± 418	1222 ± 70	263 ± 30
electrons	$69 \pm \frac{73}{39}$	$50 \pm \frac{45}{34}$	$2 \pm \frac{19}{2}$
Particles created on the inside			
electrons	5327 ± 1152	2963 ± 338	517 ± 200
photons	32.4 ± 8.8	11.0 ± 3.6	$2 \pm \frac{1}{2}$
protons	280 ± 19	22.1 ± 5.2	$4 \pm \frac{3}{2}$

Table 7.3: Particles in the TPC per bunch crossing for different designs of the forward region, averaged over 100 bunch crossings (TESLA-500 beam parameters)

rators for this purpose, but in the meantime it has been doubted that such devices would work reliably enough in a high-radiation environment. Therefore, head-on collisions are currently only considered as an alternative option for the ILC.

Physics under a small crossing angle (typically 2 mrad between the beams) differs only little from head-on collisions, but the delicate electrostatic separators can be avoided. However, the beam extraction is still difficult: due to the small spatial separation of the beams, the outgoing beam would have to go through a second, off-axis aperture in the final focus quadrupoles. Even though recent progress in the fabrication of magnets has led to the conclusion that this is technically feasible, it would still be a very expensive solution.

A large crossing angle (typically 20 mrad between the beams) will allow a relatively uncomplicated extraction of the outgoing beam because the beam tubes and the magnets for both beams will fit well next to each other. However, a large crossing angle will influence physics processes and backgrounds in the detector: depending on the configuration of the magnetic field (DID, no DID, anti-DID), low-energy background particles will miss the hole for the outgoing beam if the magnetic field lines do not point in that direction (cf. section 4.4).

Recent developments in superconducting magnet technology have made it possible to produce very thin quadrupoles with a small outer radius [152]. For geometrical reasons, this enables the crossing angle to be reduced to 14 mrad, again with the beam tubes and magnets for both beams placed immediately next to each other and sharing a common cryostat. This reduction of the

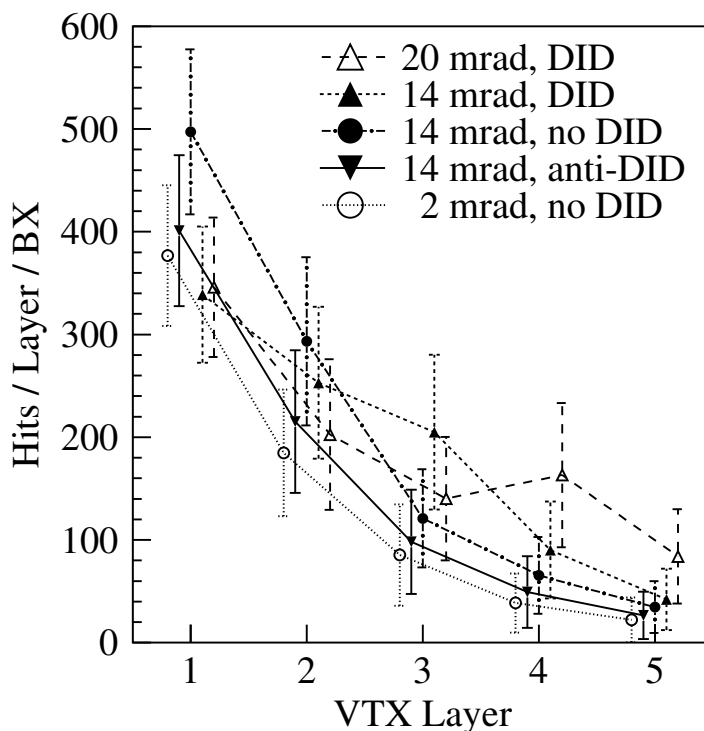


Figure 7.51: Hits on the vertex detector per bunch crossing for different crossing angles and magnetic field configurations

crossing angle is generally advantageous, but the questions and problems of the magnetic field configuration remain the same, though slightly less pronounced. For cost reasons, the initial idea to have one interaction region with a large and one region with a small crossing angle has been changed to one interaction region with a medium crossing angle of 14 mrad and two detectors with push-pull operation (section 2.3).

Figure 7.51 shows the number of hits on the five layers of the vertex detector for different crossing angles and magnetic field configurations. Keeping in mind that only part of the hits are caused by backscattering particles (and that only those can possibly be influenced), the strong impact of the crossing angle and the choice of the magnetic field configuration can clearly be seen.

As shown for the case of 14 mrad, the anti-DID configuration generally gives the best background suppression, since all outgoing particles – regardless of their energy – will be guided straight to the hole for the outgoing beam (figures 7.52 and 6.5). The particles that miss the hole or hit the inner surface of the BeamCal may produce backscatterers, but those backscatterers will again go through the centre of the detector and may not even hit the

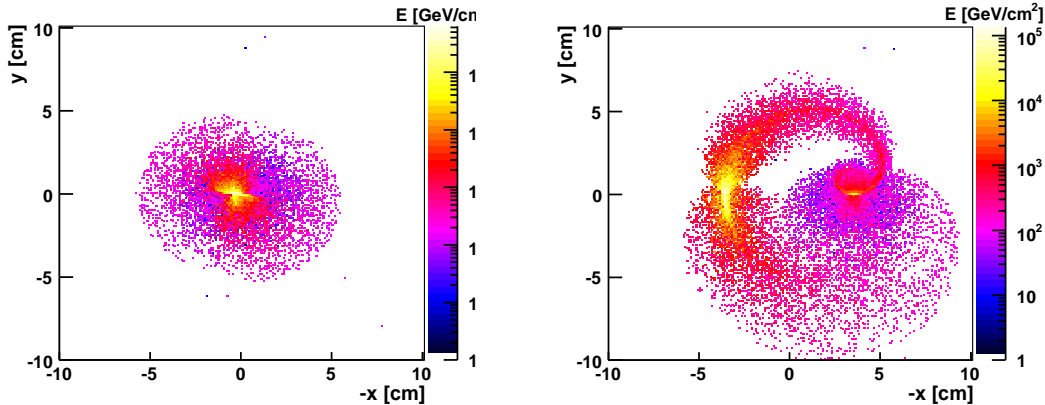


Figure 7.52: Energy distribution in the plane of the BeamCal surface for different magnetic field configurations [75]. **Left:** The picture actually shows the case of 2 mrad without an additional field, but 14 mrad with an anti-DID are very similar. Most particles reach the hole for the outgoing beam. **Right:** In the case of 14 mrad with a DID, only high-energy particles reach the hole for the outgoing beam (left spot), whereas low-energy particles are guided into the hole for the incoming beam (right spot). Particles with intermediate energies are swept across the BeamCal surface by the magnetic field.

first layer of the vertex detector if the anti-DID is well-tuned. (Figure 7.6 suggests that this is not yet fully the case because hits on the innermost layer of the vertex detector still have an azimuthal asymmetry.)

In contrast to that, the DID configuration gives an increased number of background hits because more particles from the electron-positron pairs will hit the surface of the BeamCal: only high-energy particles will make it into the hole for the outgoing beam, whereas low-energy particles will follow the magnetic field lines towards the hole for the incoming beam (figure 7.52 and [63]). Particles with intermediate energies will end up somewhere between the two holes, thereby creating a very distinct crescent-shaped pattern since the whole set-up effectively acts as an energy spectrometer.

Backscatterers from the outgoing hole – which is still the hottest region of the BeamCal – will, as before, follow the magnetic field lines (figure 7.53) and reach the vertex detector with an offset from the central axis. The result is an increased number of hits on the outer layers of the vertex detector (figure 7.51), namely on layer 3 for a crossing angle of 14 mrad and on layer 4 for 20 mrad. Consequently, the number of hits on the innermost layer is somewhat lower for the DID configuration. Furthermore, there is a very significant hot spot on the FTDs where they intercept the stream of backscattered particles (figures 7.55 and 7.56).

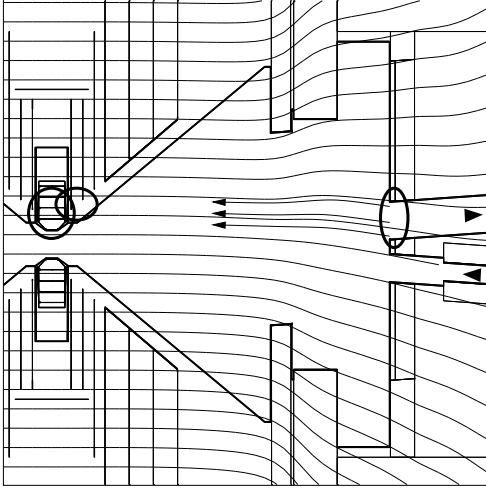


Figure 7.53: Forward region, compressed by a factor of 10 in z -direction. The magnetic field lines of a DID field configuration [153] are superimposed. Backscatterers from the BeamCal are guided into the FTDs and the vertex detector.

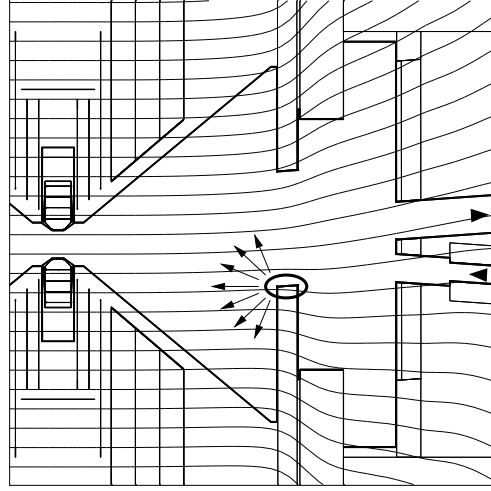


Figure 7.54: Forward region with a decreased inner LumiCal radius of 60 mm. The marked region is a strong source of backscattering photons that can easily reach the TPC.

The field configuration with a plain solenoid and no DID or anti-DID yields the worst results, particularly on the innermost layers: particles with high enough energies will still reach the hole for the outgoing beam (cf. figure 7.52), but all low-energy particles will hit the centre of the BeamCal and not the hole for the incoming beam, as in the case of a DID. With regard to the crossing angle itself, the small angle of 2 mrad gives the least backgrounds, as expected. In the DID case, the differences between the medium and large angle of 14 mrad and 20 mrad, respectively, are mainly due to the transverse offset of backscattered particles. In the case of an anti-DID, the results for 14 mrad and 20 mrad are almost equal (not shown in figure 7.51).

The effects of the magnetic field configuration on the TPC are similar: table 7.4 shows that the anti-DID field configuration for 14 mrad and 20 mrad give similar results (with the larger crossing angle being somewhat worse), but the DID field results in two to three times higher TPC backgrounds. One reason is the increased total amount of backscattering from the BeamCal surface, but another problem is that more backscattered particles will hit the inner surface of the LumiCal and induce particle showers (similar to the situation in figure 7.54, but mirrored in x -direction). This issue may even

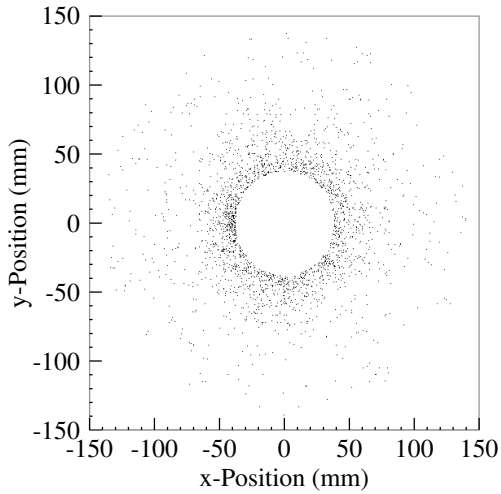


Figure 7.55: Hits on the innermost Forward Tracking Disc in the case of an anti-DID field configuration. Backscattered particles from the BeamCal are mostly guided through the centre of the disc without hitting the detector.

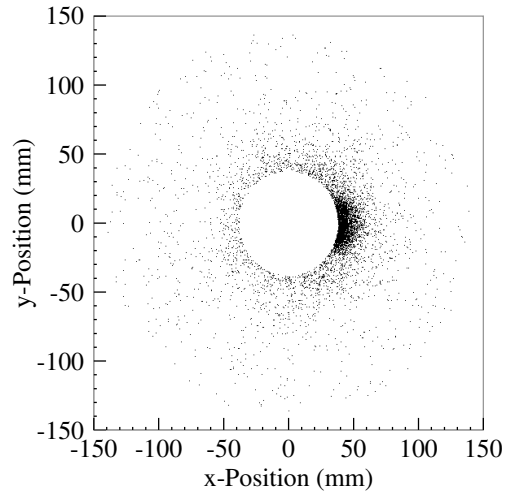


Figure 7.56: Hits on the innermost Forward Tracking Disc in the case of a DID field configuration. The stream of backscattered particles from the BeamCal has an offset from the z -axis and causes a hot spot on the disc.

become more severe for smaller inner radii of the LumiCal (cf. section 7.7.4).

As a conclusion, the anti-DID configuration is advantageous with regard to background suppression, particularly under medium to large crossing angles. Apart from that, the anti-DID will also improve the possible LumiCal performance with respect to the luminosity measurement through Bhabha-scattered electrons and positrons [74]. The anti-DID would effectively double the spin misalignment of the incoming particles (section 4.4), but the current opinion is that this should not affect the polarimetry too severely [154]. A further question is the possible impact of the anti-DID field on the TPC, which relies strongly on parallel electric and magnetic fields and which would then become subject to $\vec{E} \times \vec{B}$ effects (section 5.2.2). Even though the effects of a well-defined inhomogeneity of the magnetic field could – in principle – be corrected, it is still not clear whether the TPC performance may finally be compromised. Experimental studies to cover this issue are foreseen in the near future [155]. Another option is to design the anti-DID in such a way that there is a homogeneous field region in the centre of the chamber, and to bend the field lines only further outward [78]. This way, the central part of the chamber (i. e. close to the central cathode) could be used for track-based calibration measurements.

	14 mrad anti-DID	14 mrad DID	20 mrad anti-DID	20 mrad DID
Particles entering from the outside				
photons	947 ± 57	2154 ± 68	1188 ± 63	3360 ± 93
neutrons	142 ± 20	241 ± 32	209 ± 27	500 ± 36
electrons	$1 \pm \frac{11}{1}$	$6 \pm \frac{26}{6}$	$2 \pm \frac{17}{2}$	$15 \pm \frac{25}{13}$
Particles created on the inside				
electrons	292 ± 130	660 ± 162	390 ± 152	1069 ± 184
photons	$1 \pm \frac{2}{1}$	$2 \pm \frac{2}{2}$	$1 \pm \frac{2}{1}$	$4 \pm \frac{2}{2}$
protons	$2 \pm \frac{2}{1}$	$4 \pm \frac{2}{2}$	$3 \pm \frac{1}{1}$	$8 \pm \frac{3}{3}$

Table 7.4: Particles in the TPC per bunch crossing for different crossing angles and magnetic field configurations, averaged over 100 bunch crossings

7.7.3 Beam Parameters

Figures 7.57 and 7.58 show the number of hits on the five layers of the vertex detector for different beam parameter sets (cf. section 2.4). The nominal ILC beam parameters for 500 GeV (ILC-NOM-500) yield the lowest number of hits – the same numbers are also shown in figures 7.3 and 7.4. The numbers for TESLA beam parameters (TESLA-500) are higher, but the difference immediately relates to the different design luminosities ($2.0 \cdot 10^{34} \text{ cm}^{-2}\text{s}^{-1}$ for ILC-NOM-500 vs. $3.4 \cdot 10^{34} \text{ cm}^{-2}\text{s}^{-1}$ for TESLA-500). It should be noted that this comparison is for illustrative purposes only, since the design of the original TESLA detector was significantly different from the LDC detector.

The beam parameters for the “Low Power” option (ILC-LOWP-500) yield a factor of 2.5 more background hits on the vertex detector, since the stronger focusing and the smaller beam spot size lead to the production of more beamstrahlung and an increased number of electron-positron pairs (section 3.1). However, the Low Power beams contain only half the number of bunches per train, which means that the integrated number of hits per unit of time is in fact not much higher than for nominal beam parameters. Therefore, the impact of the Low Power option on vertex detector backgrounds is not as bad as it may look in figures 7.57 and 7.58.

As already shown in figure 3.4, increasing the centre-of-mass energy from 500 GeV to 1 TeV almost doubles the amount of electron-positron pairs that are produced in the beam-beam interaction. This increase is also reflected in the background hits on the vertex detector for ILC-NOM-1000 and ILC-LOWP-1000.

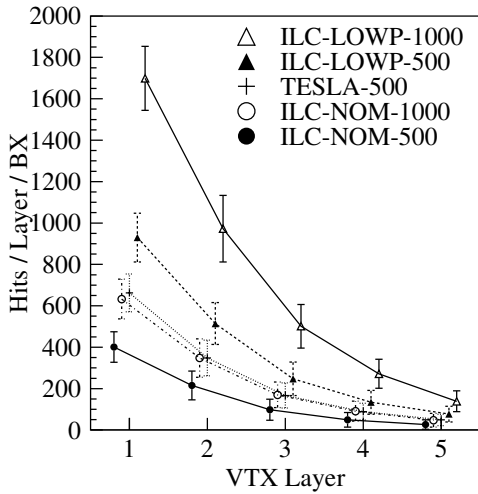


Figure 7.57: Hits on the vertex detector per bunch crossing for different beam parameters, in absolute numbers

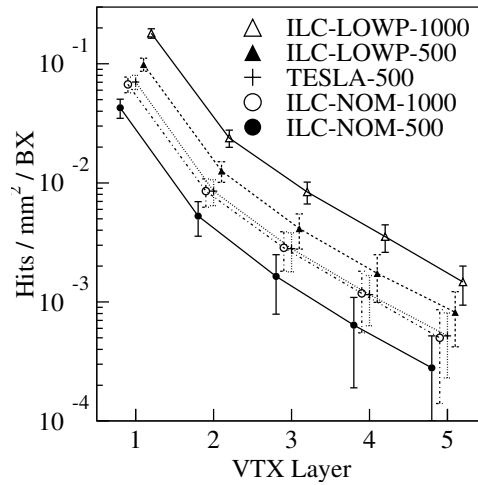


Figure 7.58: Hits on the vertex detector per bunch crossing for different beam parameters, normalised per unit area

Results for other detector devices are not shown here because they basically scale in the same way as the vertex detector hits.

7.7.4 LumiCal Inner Radius

The detector geometry that is used for the simulations presented in this thesis (with a crossing angle of 14 mrad) uses a LumiCal with an inner radius of 100 mm. For comparison, the design for 2 mrad foresees an inner radius of 60 mm, whereas the design for 20 mrad uses 120 mm [156]. The relatively large value of 100 mm has been chosen to ensure that the LumiCal will not become a significant scattering target, neither for particles that come directly from the interaction point nor for backscatterers from the BeamCal that might hit the inner surface of the LumiCal. However, a smaller radius (80 mm or even 60 mm) would be desirable for the luminosity measurement with Bhabha-scattered particles from the beams, which is the most important task of the LumiCal (hence its name).

Table 7.5 shows the number of particles that enter the TPC in dependency of the inner LumiCal radius. As expected, the numbers get constantly smaller as the LumiCal radius decreases because the angular coverage of backscattering photons from the BeamCal gets better (figure 7.32). However, as the inner radius reaches 60 mm, backgrounds in the TPC get drastically larger. Figures 7.59, 7.60, 7.61 and 7.62 provide an explanation: they show the ori-

	100 mm	90 mm	80 mm	70 mm	60 mm
Particles entering from the outside					
photons	952 ± 52	797 ± 47	669 ± 72	565 ± 56	2078 ± 165
neutrons	140 ± 25	119 ± 20	99 ± 20	84 ± 17	110 ± 19
electrons	1 ± $\frac{1^2}{1}$	1 ± $\frac{4}{1}$	1 ± $\frac{3}{1}$	0 ± $\frac{3}{0}$	5 ± $\frac{20}{3}$
Particles created on the inside					
electrons	290 ± 115	281 ± 187	224 ± 135	216 ± 198	850 ± 206
photons	1 ± $\frac{2}{1}$	1 ± $\frac{2}{1}$	1 ± $\frac{1}{1}$	1 ± $\frac{1}{1}$	3 ± $\frac{3}{2}$
protons	2 ± $\frac{2}{1}$	2 ± $\frac{1}{2}$	1 ± $\frac{2}{1}$	1 ± $\frac{2}{1}$	1 ± $\frac{2}{1}$

Table 7.5: Particles in the TPC per bunch crossing for decreasing inner LumiCal radii, averaged over 100 bunch crossings

gins of all particles that traverse a given surface immediately in front of the LumiCal, and it can clearly be seen that a “hot spot” forms on one side of the inner LumiCal surface if the inner radius gets to small. When particles hit the inner LumiCal surface in this hot spot, particle showers will be induced. This leads to the production of photons, which can in turn easily reach the TPC.

The fact that the hot spot appears only on one side of the LumiCal – namely on the side of the incoming beam – is a hint that the phenomenon is related to the anti-DID field. The crossing angle alone cannot be the reason because the LumiCal is aligned on the axis of the outgoing beam. Figure 7.54 suggests that the bending of the anti-DID field is the reason why particles hit the LumiCal at the observed hot spot. As a conclusion, an inner radius of 80 mm can be considered a safe choice with respect to TPC backgrounds, but with further optimisation of the anti-DID field, also 70 mm or even 60 mm may be feasible without affecting TPC backgrounds.

It should be noted that the influence of the LumiCal on the vertex detector is rather small: charged particles that originate from the LumiCal surface can hardly reach the vertex detector because it is much smaller than the LumiCal, and charged backscatterers can basically move only in z -direction. Most of the photons that reach the vertex detector come from the BeamCal, such that the LumiCal does not play a major role, either.

7.7.5 BeamCal Absorber

The BeamCal, which is the prime source of backscattering particles in the detector, is covered by a layer of graphite absorber. This low- Z material is

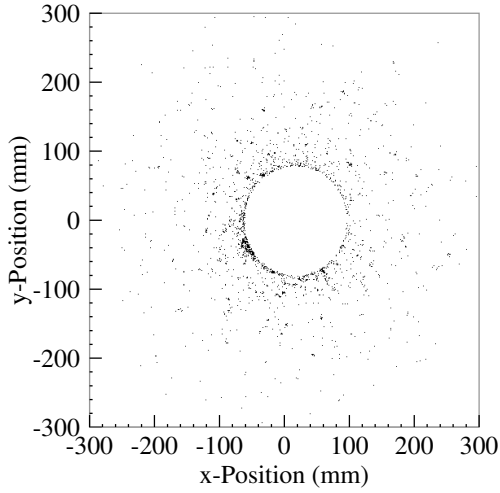


Figure 7.59: Backscattering sources in the LumiCal for an inner radius of 80 mm, front view. The LumiCal is not a significant source of backscattering particles.

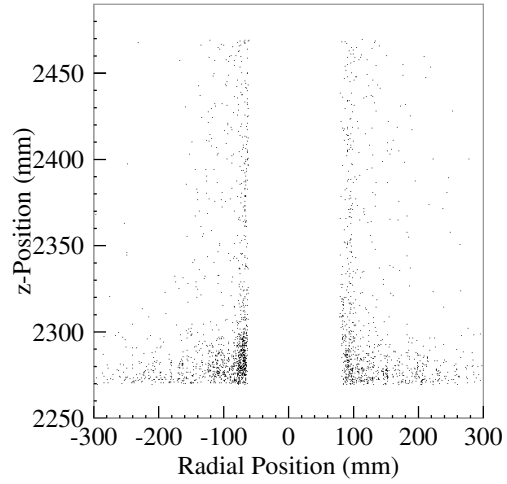


Figure 7.60: Backscattering sources in the LumiCal for an inner radius of 80 mm, top view

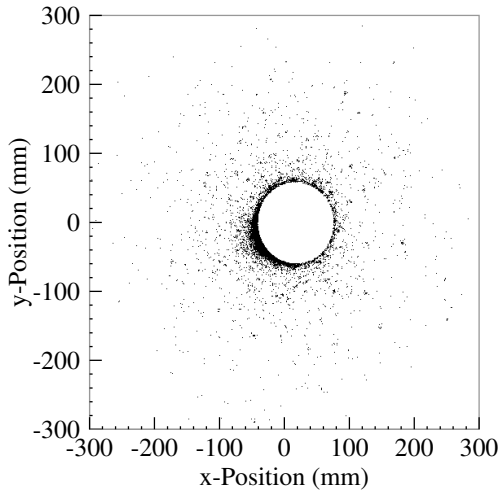


Figure 7.61: Backscattering sources in the LumiCal for an inner radius of 60 mm, front view. The inner surface of the LumiCal gets struck by particles and forms a region of high activity.

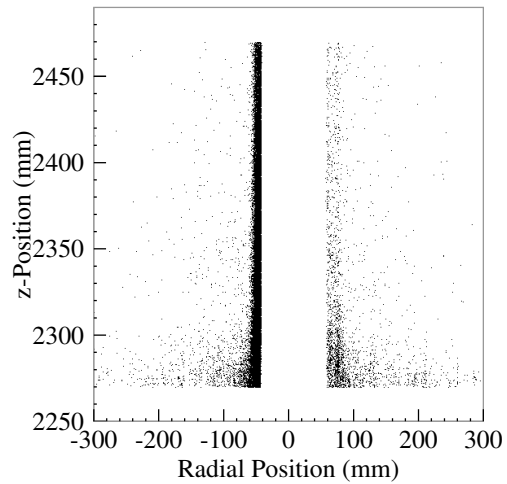


Figure 7.62: Backscattering sources in the LumiCal for an inner radius of 60 mm, top view

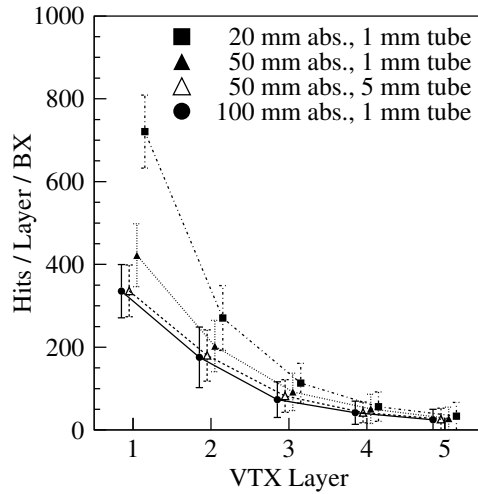


Figure 7.63: Hits on the vertex detector per bunch crossing for different thicknesses of the BeamCal absorber and the beam tube inside the BeamCal

meant to attenuate electromagnetic particle showers and to prevent backscattered particles from reaching the inner detector. For this purpose a thicker absorber will generally be better. However, the graphite absorber may also deteriorate the spatial resolution and the energy resolution of the BeamCal if it is too thick, such that an optimised thickness – and possibly further means to suppress backscattering – need to be found.

Figure 7.63 shows the number of hits on the five layers of the vertex detector for different absorbers. A thickness of 50 mm is clearly much better than only 20 mm: the total number of hits is reduced almost by a factor of two, and keeping in mind that only a part of the hits are caused by backscattered particles (section 7.2.1), the actual profit of the thicker absorber is even better. A further increase in thickness to 100 mm again reduces the number of hits slightly, but the rather small gain may not be worth the deteriorating effect of the absorber on the BeamCal itself.

Instead, another promising approach for the suppression of backscattering can be seen: many of the remaining backscatterers are produced at the inner surface of the BeamCal, which gets struck by electron-positron pairs under a very shallow angle of incident. A first step is to replace the steel beam tube wall by beryllium in this “hot region”, but this modification alone does not yet help a lot: even though particles have very shallow angles, 1 mm of beryllium is not enough to have a significant effect. However, if the thickness of the beryllium beam tube is increased to 5 mm, a significant suppression of backscattering can be observed. Again, the improvement is not large, but it would come basically for free: the innermost cells of the BeamCal

	long W	none	short W	short Fe	short Pb
Inner endcap surface at $r = 300$ mm					
n	5350 ± 201	9772 ± 270	5406 ± 198	9635 ± 311	$1.1\text{E}4 \pm 356$
γ	985 ± 52	$1.3\text{E}5 \pm 1.8\text{E}3$	1018 ± 48	9084 ± 155	1961 ± 63
e^-	$4 \pm \frac{3}{3}$	$115 \pm \frac{35}{24}$	$4 \pm \frac{4}{2}$	$16 \pm \frac{9}{6}$	$9 \pm \frac{5}{4}$
p	$0 \pm \frac{0}{0}$	$2 \pm \frac{1}{1}$	$0 \pm \frac{0}{0}$	$0 \pm \frac{0}{0}$	$0 \pm \frac{0}{0}$
E	4.0 ± 0.4	108 ± 2	4.0 ± 0.4	14.8 ± 0.5	8.3 ± 0.5
Surface inside the endcap at $r = 900$ mm					
n	50.5 ± 17.5	185.7 ± 31.3	90.1 ± 21.1	143.2 ± 28.2	149.2 ± 30.0
γ	34.7 ± 9.1	116.5 ± 18.5	56.2 ± 10.7	91.7 ± 13.1	90.7 ± 15.9

Table 7.6: Particles traversing the HCAL endcaps per bunch crossing for different designs of the support tube. The total energy E of particles that enter the HCAL endcap is given in GeV.

suffer from an extremely high occupancy and radiation dose, and they could be exchanged for a layer of beryllium without affecting the performance of the BeamCal too much. Therefore, placing an absorber also at the inside of the BeamCal might be an advantageous option for the suppression of backscattering.

7.7.6 Support Tube

The current detector geometry contains a support tube that carries the final focus quadrupoles and the BeamCal (figure 6.2). This tube also acts as a shielding device for photons and neutrons that are produced in particle showers in the BeamCal and the final focus magnets. However, since it is planned to be made of tungsten, the tube will be very heavy (about 15 t) and also rather expensive. Therefore it is worthwhile to study whether the tube could be shortened or be constructed from another material, such as ordinary stainless steel.

Table 7.6 shows the number of particles that traverse a sensitive surface at the inner radius of the HCAL endcap (cf. section 7.6) for different alternatives. Omitting the support tube altogether has a very large effect on HCAL backgrounds: the number of neutrons that enter the HCAL increases only moderately because tungsten is not an efficient neutron absorber, but the number of photons increases dramatically by a factor of 100.

A viable compromise, however, would be to shorten the tungsten support tube such that it extends only from the LHCAL to the BeamCal (cf.

figures 6.2 and 6.4). This would shield the HCAL against particles coming from the BeamCal and it would also sufficiently block the path for backscattering particles from the final focus quadrupoles. The rest of the mechanical support tube could then be made of steel, saving weight and cost, as long as the resulting radiation from the final focus magnets is not too high for the muon system in the yoke. This has not been studied since the muon system is not available in the used detector geometry.

Using steel for the support tube also helps to reduce the HCAL backgrounds again, but by far not as well as in the case of tungsten (particularly with regard to photons). Slightly better results are obtained for lead, even though lead would not be mechanically stable enough to be used for the whole tube in any case.

As it can be expected for geometrical reasons, backgrounds in the vertex detector and the TPC are not affected by the material choice and the design of the support tube, because the tube can only shield the HCAL and the magnet yoke from scattering products (figure 6.2).

7.8 Comparative Studies

7.8.1 Nuclear Cascade Models

The simulations that are presented in this thesis use the physics list “QGSP_BERT_HP”, which comes built into the Geant4 framework (section 6.2.3). It is known to provide a good description of hadronic physics, especially when neutrons are involved, but all available hadronic models – be it in Geant4 or in other software tools – generally suffer from imperfections. Therefore, as a cross-check, the simulations are re-run with two Geant4 physics list named “LHEP_BERT_HP” and “LHEP_BIC_HP”.

The latter physics list uses the Binary Internuclear Cascade model (“BIC”) for inelastic hadron-nucleon scattering at low energies ($E < 10$ GeV), in contrast to the Bertini Intranuclear Cascade (“BERT”). The Binary Cascade is based on the assumption that interactions of primary or secondary particles in the nucleus happen with individual nucleons, whereas the Bertini Cascade treats the nucleus as a whole. Neither model is based on first principles, but both are known to agree reasonably well with measured data [120]. On a microscopic level, the Bertini cascade typically produces a larger number of neutrons during the deexcitation of nuclei (up to a factor of two compared to the Binary Cascade), whereas the neutrons from the Binary Cascade have higher energies.

At higher energies, both alternatives only use the parameterisations from GHEISHA (“LHEP”), in contrast to the so-called Quark-Gluon-String Precom-

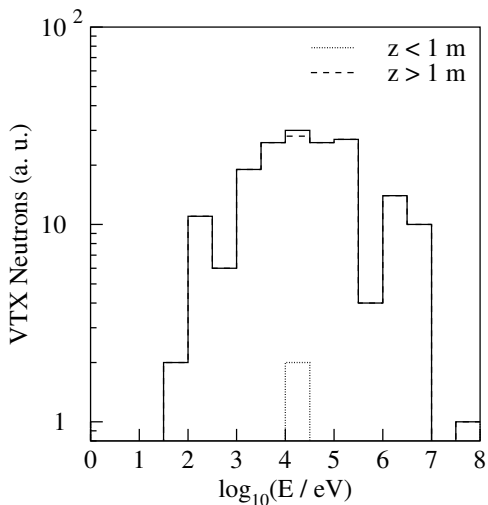


Figure 7.64: Energy distribution of neutrons traversing the vertex detector, using the physics list LHEP_BERT_HP

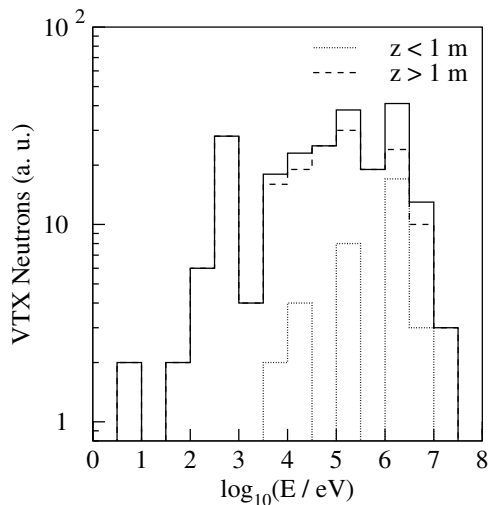


Figure 7.65: Energy distribution of neutrons traversing the vertex detector, using the physics list LHEP_BIC_HP

pound model (“QGSP”) for $E > 25$ GeV, but these energy ranges are hardly relevant for the interactions of beam-induced background particles. All three physics lists apply the same high-precision models (“HP”) for low-energy neutrons ($E < 20$ MeV), using databases with measured cross-sections for interactions with various nuclei. All other kinds of physical processes (decay, electromagnetic physics, elastic hadron physics) are modelled identically in the lists (cf. section B.2).

The Bertini model is known to yield a larger number of neutrons, whereas neutrons produced in a Binary Cascade tend to have higher energies. Even though statistics are low, this can partly be reproduced in the simulations (figure 7.19 compared to figures 7.64 and 7.65), but the effect on the number of vertex detector hits is negligible (the results are basically equal to those shown in figures 7.3 and 7.4). The same holds for the number of particles that enter the TPC (table 7.7).

As a conclusion, the exact choice of the physics list is not too crucial for the simulation of beam-induced backgrounds. Most particles that have an impact on detector backgrounds either come directly from the interaction point, or they are created in electromagnetic processes, which are well understood and well described in Geant4. Hadronic physics play only a minor role, and the subtle differences of the available hadronic models hardly influence the simulation results. However, if neutron-related backgrounds are to be studied, it is important that photonuclear and electronuclear processes are

	QGSP BERT	LHEP BERT	LHEP BIC
Particles entering from the outside			
photons	947 ± 57	948 ± 51	952 ± 49
neutrons	142 ± 20	137 ± 22	138 ± 22
electrons	$1 \pm \frac{11}{1}$	$1 \pm \frac{12}{1}$	$1 \pm \frac{15}{1}$
Particles created on the inside			
electrons	292 ± 130	297 ± 118	326 ± 149
photons	$1 \pm \frac{2}{1}$	$1 \pm \frac{1}{1}$	$1 \pm \frac{2}{1}$
protons	$2 \pm \frac{2}{1}$	$2 \pm \frac{1}{1}$	$2 \pm \frac{1}{1}$

Table 7.7: Particles in the TPC per bunch crossing for different physics lists, averaged over 100 bunch crossings

available and that high-precision neutron models (the “HP” variant of many available physics lists) are used.

7.8.2 Methane Content of the TPC Gas

To cross-check that the expected process of neutron-proton scattering (i. e. the interaction of incident neutrons with protons in the chamber gas) is properly simulated in Geant4, a test simulation with an increased CH_4 content of the chamber gas is run. The usage of a mixture with 20 % of CH_4 instead of the usual 5 % should increase the amount of neutron-proton collisions by a factor of 4. Table 7.8 shows that this expectation is confirmed, even though statistics are very low. The numbers of electrons that are created in the chamber are still equal within the statistical uncertainty.

Together with the estimate of the expected collision rate in section 7.4.1, this result confirms that neutron-proton scattering in the chamber gas does actually happen in the simulations, and it supports the conclusion that the hydrogen content of the chamber gas is not crucial with respect to beam-induced backgrounds.

7.9 Uncertainty Estimation

Several sources contribute to the uncertainty of the results that are presented in this thesis. This leads to an estimate of safety margins that should be kept to ensure a safe and reliable operation of the detector. Since the backgrounds are generally not interesting in their own right, typically only upper bounds

	5 % CH ₄	20 % CH ₄
Particles entering from the outside		
photons	947 ± 57	955 ± 44
neutrons	142 ± 20	146 ± 25
electrons	1 ± $\frac{11}{1}$	1 ± $\frac{13}{1}$
Particles created on the inside		
electrons	292 ± 130	303 ± 121
photons	1 ± $\frac{2}{1}$	1 ± $\frac{1}{1}$
protons	2 ± $\frac{2}{1}$	8 ± $\frac{4}{4}$

Table 7.8: Particles in the TPC per bunch crossing for normal and increased CH₄ content, averaged over 100 bunch crossings

are considered – backgrounds that are lower than expected would not cause any problem.

7.9.1 Statistics

The statistical fluctuations of values that are calculated for a single bunch crossing are intrinsically high in most cases – the number of hits on the vertex detector will typically vary by 30 % from bunch crossing to bunch crossing, whereas the number of occupied voxels in the TPC can easily fluctuate by factors of two or three, and occasionally much more. These fluctuations get averaged out to a certain extent since most detector components integrate over several (10–100) bunch crossings, but they still have to be taken into consideration.

On the one hand this means that the inevitable statistical fluctuations must not be neglected, and on the other hand it also implies that a precise determination of expected background rates with a very large statistical sample does not make sense in most cases. A large collection of bunch crossings with simulated backgrounds however is useful to overlay physics events with backgrounds and to test reconstruction algorithms under semi-realistic data conditions (section 9.2). A large amount of simulated data is also needed to get a handle on collective effects such as backdrifting ions from a whole bunch train (section 9.1).

7.9.2 Generator Level

On the generator level, the results for electron-positron pairs from Guinea-Pig should be reliable on a level of 10–20 %, as indicated by a comparison with

other generators [56] (cf. section 6.1). The description of hadronic scattering products, the so-called minijets, is more complicated because the hadronic structure of the photon and low-energy QCD are involved. Especially the energy region between the two-pion threshold (at 0.3 GeV) and the internal low-energy cut-off in Guinea-Pig (typically at 2.0 GeV) is difficult to handle.

Earlier studies (still done for TESLA) showed that no more than two hadronic background events are expected in 100 bunch crossings [58] – this number is negligible with regard to the detector performance. Newer calculations [59] suggest that the number of hadronic events might be larger by a factor of up to five (even though mostly in the range of very low energies), but hadronic events would still be only a minor source of detector backgrounds. However, it has to be kept in mind that background jets can be misidentified as fake physics events. The actual impact of such fake jets on physics analyses still needs to be studied.

7.9.3 Modelling of Physics Processes

Electromagnetic processes are well-understood, and the uncertainty of simulation results is typically on the percent level. Most of the Geant4 built-in physics lists – including the ones that were used for the simulations in this thesis – use a default implementation of electromagnetic processes, which is continuously validated and refined. A major improvement has been introduced with the transition to Geant4 version 8.0 [109] (which means it is already included in the simulations presented here), but in the meantime no significant problems, errors, or deviations from experimental data have been discovered.

In contrast to that, hadronic physics – and particularly neutron physics – are more difficult to handle. Again, the differences between the various Geant4 physics lists (QGSP vs. LHEP, Bertini Cascade vs. Binary Cascade) have only little impact because they apply to processes that are not dominant in the background simulations. The important processes – neutron production through photonuclear reactions and low-energy neutron transport with the help of cross-section data from the HP package – are modelled identically in the different physics lists.

For both of these processes, the intrinsic accuracy can be estimated as 20–50%, even though these values also depend on the quality of the available measured and evaluated cross-section data for the different materials and isotopes in the simulated geometry. For experimental set-ups that do not involve the transportation and attenuation of neutrons through large amounts of material (distances of the order of metres and more), an uncertainty and safety factor of two can be considered reasonable [120].

Previous studies that compared the different available physics implementations of GEANT3 (including interfaces to other codes such as FLUKA [157]) and Geant4 came to similar results [158]: the observed number of neutron hits from incident pions of 10 GeV in a simulated HCAL structure varied by up to 60 % across the different physics models. Even though these results are not immediately applicable to the experimental set-up that was used in this thesis, and even though they were done with an older version of Geant4 (presumably 5.x), they indicate at least the same level of inherent uncertainty for neutron-related studies.

7.9.4 Geometry Variations

Small modifications of the detector geometry or the magnetic field configuration can have a large influence on detector backgrounds – particularly where backscattering particles are involved. In some cases, the countermeasures to reduce backgrounds will have no impact on the detector performance, but in other cases a trade-off between background suppression and optimal detector performance has to be found.

The detector layout that was used for the presented studies (section 6.2.2) is already strongly optimised with respect to backgrounds – less advantageous designs with more backscattering could well yield a factor of two or three more backgrounds in some parts of the detector (section 7.7).

7.9.5 Other Sources

Backgrounds from other sources (section 3.5) have been found to be much weaker than those from the beam-beam interaction, but that does not mean they are completely negligible. For example, neutrons from the main beam dump will hardly reach the detector as long as there is no direct line of sight from the beam dump to the interaction region [53]. However, this may dramatically change for an extraction system with only one common beam dump for synchrotron radiation photons and the spent beams (as it is currently foreseen). Before such plans are finally established, the influences on the detector (e. g. neutron fluence in the vertex detector) need to be studied again. A similar example is the design of the extraction line magnets and collimators: if these components are not designed with careful consideration of the impact on the detector, background levels might rise to a critical level [62].

Still, if the beam delivery and extraction system is designed carefully and if its impact on detector backgrounds is taken into proper consideration, it should be possible to keep the related background sources under control.

This way, the electron-positron pairs – which are immediately caused by the collision of bunches and which are therefore unavoidable – would eventually be the dominant contribution to detector backgrounds.

7.9.6 Safety Margins

Bearing the various imponderabilities in mind, it becomes clear that sufficient safety margins must be kept whenever beam-induced backgrounds might put the performance (or even the operability) of detector components at risk. A safety factor of five, or better ten, should always be aimed for. This holds all the more for results that critically depend on the modelling of neutrons. In cases where neutrons doses appear to be critical, further studies with more specialised tools such as FLUKA or MCNPX [159] may become necessary (section 9.3).

7.10 Relation to Other Studies

This thesis is not the first study of beam-induced backgrounds at a linear collider. Various analyses dealing with the different sources of detector backgrounds – final focus synchrotron radiation, halo muons, beamstrahlung photons and their collimation, minijets, extraction line losses, and beam dumps – have been cited in section 3. Many older studies that were done for the TESLA project can be found in [35]. Apart from that, there have been other studies of electron-positron pair backgrounds in the recent years.

Results for the three major detector concepts were presented at the Snowmass Linear Collider Workshop in 2005 [160], focusing mainly on the vertex detector and – in the case of SiD – on the main silicon tracker. The results cannot be directly compared because of the different magnetic field strengths and vertex detector radii, but they exhibit qualitatively similar behaviour, e. g. with respect to beam parameter sets, crossing angles, and particle sources. The LDC studies are also quantitatively comparable and show a good agreement with the results presented in this thesis. Deviations on the level of 30 % can readily be explained by the usage of different simulation tools (BRAHMS and GEANT3 vs. Mokka and Geant4), different models and implementations of physical processes, and variations in the detector geometry.

A detailed study of pair generators and background levels on the vertex detector [56] focused on the influence of the magnetic field strength and the vertex detector radii for different beam parameter sets. The resulting numbers of hits on the vertex detector are somewhat lower than those presented in this thesis, but this can be explained by the fact that only direct

hits were considered in the analytical analysis – secondary effects such as backscattering will only be visible in a full detector simulation.

In conclusion, it can be said that the simulations performed for this thesis currently provide the most comprehensive results that are available for pair backgrounds in an LDC-like detector at the ILC, using a full detector simulation with the latest detector geometries, a detailed description of the magnetic field, and the best available models for neutron-related physics processes. The presented analyses cover a wide range of detector components – vertex detector, inner silicon trackers, TPC, and HCAL – and cover various issues that have not been studied before, or only with rather coarse estimations.

8 Summary

This thesis presents simulations of beam-induced electron-positron pair backgrounds at the ILC and their impact on the different components of a detector according to the Large Detector Concept. The main tools are Guinea-Pig, a generator for beam-beam interactions at electron-positron colliders, and Mokka, a full detector simulation for the ILC that is based on the Geant4 framework. The detector simulation uses a detailed geometry, including a beam crossing angle of 14 mrad and an anti-DID field configuration, and a wide range of physical processes, including models for neutron production in electromagnetic showers and neutron transportation.

The simulations show that backgrounds are at an acceptable level for all detector components: the innermost – and most critical – layer of the vertex detector will get around 400 hits per bunch crossing (or 0.04 hits/mm²/BX), which is still tolerable for the different detector technologies that are currently under consideration. The neutron fluence in the vertex detector will not do any harm as long as radiation doses are not massively increased by other sources, such as the beam dump.

The background occupancy of the TPC does not exceed a value of 0.1 % after integration over 100 bunch crossings, except in regions very close to the beam tube, where it still stays below 1 %. These values are considered uncritical for pattern recognition and tracking, which holds even more if the distinct structure of background hits – typically long microcurlers that occupy many voxels, but only few readout pads – is taken into account. Again, the neutron flux is uncritical and does not call for a hydrogen-free gas mixture in the chamber. Recoil protons from neutron-proton scattering in the gas create a non-vanishing, yet small amount of primary ionisation in the chamber. They contribute to few percent of the total primary charge, but only to a negligible fraction of the total occupancy because of their short ranges.

The neutron fluence in the HCAL is uncritical except for those parts of the endcaps that are very close to the beam tube: silicon photomultipliers in the innermost 10 cm may degrade after several years of running since the neutron fluence reaches levels of 10¹⁰ neutrons/cm². The photon fluence in the endcaps will be harmless as long as the HCAL is properly shielded against the BeamCal, which is the main source of secondary backgrounds.

Concerning the various options for the magnetic field configuration that are under discussion, the anti-DID is clearly preferable compared to configurations with a DID or no DID at all: in the case of a 14-mrad crossing angle, it reduces TPC backgrounds approximately by a factor of two and it avoids asymmetric hot spots on the inner silicon devices. Regarding the

overall design of the forward region, the current layout with a large final focus length L^* , a distant BeamCal, and a near LumiCal is advantageous because it helps to shield the TPC against backscattering photons from the LumiCal. A further measure to reduce backscattering to the vertex detector could be a thin beryllium (or graphite) absorber layer not only at the front of the BeamCal, but also at its inner surface.

Keeping in mind that the presented results mostly depend on indirect effects such as backscattering, that subtle changes of the experimental set-up can have strong effects, and that several of the involved physical models have non-negligible intrinsic uncertainties, it is clear that final conclusions about beam-induced backgrounds cannot be drawn at this point. Refined studies with improved tools should further accompany the design of the accelerator and the detectors as the plans for the ILC evolve in the future.

9 Outlook

This thesis may be one step towards a better understanding of beam-induced backgrounds and their impact on the detector, but further work needs to be done. Several issues are currently already being worked on, and others are foreseen for the future.

9.1 Ion Backdrift in the TPC

Every ionisation process in the TPC will not only create electrons, but also ions. The ions have a much smaller drift velocity than the electrons (typically 1000 times slower) and will accumulate in the chamber not only during a complete bunch train, but even across several trains. Apart from this primary ionisation, secondary ions can drift back from the amplification region into the main chamber volume, thereby forming a thin disc that corresponds to one bunch train (figure 5.9). Again, several of such ion discs can slowly drift through the chamber at a given point in time if they are not removed by an additional ion gate which is positioned in front of the amplification structures and which is activated in the time gap between two bunch trains.

To estimate the influence of ions in the chamber, simulated background signals from a whole bunch train (produced in the course of the work on this thesis) are accumulated in the chamber, including proper timing. The corresponding primary electrons are then transported to the anode by simulating their drift in the chamber gas. The amplification in a triple-GEM structure, including all transportation coefficients, is modelled according to previous measurements with a GEM test chamber [94]. The ions resulting from the amplification process are then transported back through the GEM structure and drift towards the chamber cathode. All steps are computed with the corresponding modules of the MarlinTPC package.

Figure 9.1 shows an intermediate result of these simulations: the number of backdrifting ions (after amplification and transportation through the GEM structure) in the chamber is plotted against their radial position. The upper histogram corresponds to the simulation of a triple-GEM structure with standard settings for voltages and electric fields, the lower histogram was obtained with special settings that are optimised to reduce the ion backdrift (details can be found in [94]) – the improvement is clearly visible. It should be noted that figure 9.1 is merely a snapshot of work in progress [161].

The next step will be to calculate the electrostatic field that is caused by the ions, to superimpose this field over the nominal – and ideally homogeneous – drift field in the TPC, and to study its effect on drifting electrons. The question is how strongly the field imperfections will influence the re-

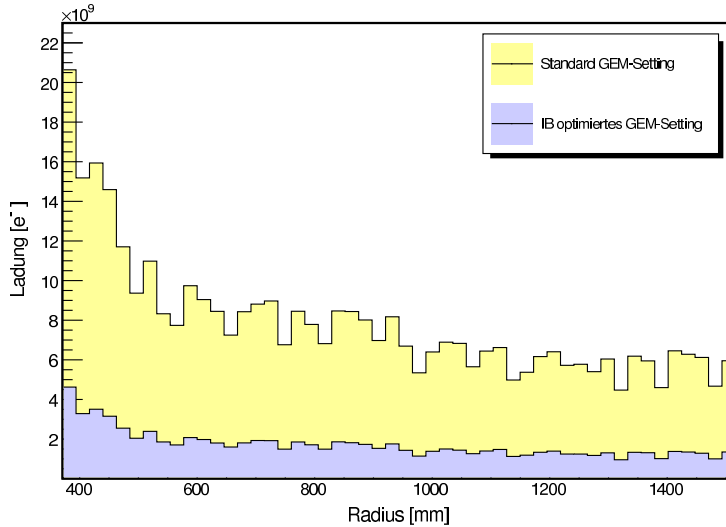


Figure 9.1: Radial charge distribution in a disc of backdrifting ions from a whole bunch train, simulated for standard settings and optimised settings in a triple-GEM structure [161]

construction of the original particle tracks, possibly by changing the drift velocity or by introducing an additional transverse offset. These studies are a medium-term goal of the MarlinTPC group.

The last item related to backdrifting ions is to study a possible correction of the disturbing effects mentioned above. One possibility would be to model an average ion disc with its charge distribution and electric field and to correct for the effects of such an idealised disc in the track reconstruction. Another possibility would be to calculate the actual charge distribution in each single ion disc by making use of the measured electron signals from each bunch train, and by post-simulating the transportation of ions through the GEM structure and their backdrift. Such studies, which are a long-term goal of the TPC simulation effort, could provide an answer to the question whether an ion gate in the chamber is actually needed or not.

The problem of an imperfect electric field and the possibility to correct for its effects is also related to TPC measurements that are planned for the next year: the Large Prototype that is currently being built by the LC-TPC collaboration [162] in the framework of the EUDET project [163] shall also be operated in an inhomogeneous magnetic field while measuring particle tracks from an electron test beam [155]. These measurements will also improve the understanding of field inhomogeneities (albeit primarily magnetic, in this case) and appropriate countermeasures in the track reconstruction.

9.2 Event Reconstruction and Analysis

Concerning the overall ILD reconstruction and analysis software in the Marlin framework, it will become necessary to perform a proper overlay of backgrounds and physics events and to include realistic beam-induced backgrounds in the full reconstruction and analysis process. The various detector components will need specific algorithms to recognise and to discard background signals, typically via pattern recognition. Afterwards, the results of analyses with and without backgrounds can be compared. Only these studies can ensure that beam-induced backgrounds will not eventually affect the detector performance.

9.3 Further Simulations of Backgrounds

As soon as a new detector geometry for the ILD concept – possibly including an updated forward region – has been established, the results presented in this thesis should be reviewed and verified. The process of detector optimisation and the merging of the former LDC and GLD concepts is currently in full swing, and first conclusions can probably be expected in a few months.

The neutron fluence in the innermost parts of the HCAL endcaps approaches a critical level (section 7.6.1), but it is strongly influenced by the shielding effect from the support tube – made of tungsten or some other material – that encloses the BeamCal (section 7.7.6). If the possible radiation damage of the silicon photomultipliers gives rise to operability concerns, it might be worthwhile to cross-check the simulation results with another simulation code such as FLUKA. In this case it would probably be sufficient for the simulations to focus on the forward region (figure 6.2), without necessarily modelling the whole rest of the detector.

Finally, it must not be forgotten that electron-positron pairs are only one of the possible background sources at the ILC. As already mentioned in section 3.5, several issues – such as neutrons from the beam dumps or backscattering from beam losses in the extraction system – still need to be studied in further detail.

Appendix

A Guinea-Pig Parameter Settings

Guinea-Pig [50] is a tool for the simulation of beam-induced backgrounds. It is controlled by two sets of parameters that must be defined in a steering file named `acc.dat`. The first set, named `$ACCELERATOR`, describes the properties of the colliding beams (cf. section 2.4). The second set, named `$PARAMETERS`, contains internal settings for the simulation itself and defines which kind of data should be written to output files. Tables A.1 and A.2 list the settings that were used for the generation of electron-positron pairs with the nominal ILC beam parameters.

Name	Value	Unit
<code>energy</code>	250	GeV
<code>espread</code>	0.003	relative
<code>which_espread</code>	0	flag (= none)
<code>particles</code>	2.0	10^{10}
<code>n_b</code>	2820	
<code>f_rep</code>	5	Hz
<code>charge_sign</code>	-1	sign (= opposite)
<code>emitt_x</code>	10	10^{-6} m rad
<code>emitt_y</code>	0.040	10^{-6} m rad
<code>beta_x</code>	21	mm
<code>beta_y</code>	0.4	mm
<code>sigma_x</code>	655	nm
<code>sigma_y</code>	5.7	nm
<code>sigma_z</code>	300	μm

Table A.1: Guinea-Pig `$ACCELERATOR` settings for nominal ILC beam parameters with 500 GeV centre-of-mass energy (ILC-NOM-500). Most of the parameters correspond directly to those given in [42]. The values `n_b` and `f_rep` are currently not used since all results are given per bunch crossing.

Name	Value	Unit
rndm_load	1	flag (= yes)
rndm_save	1	flag (= yes)
n_x	64	
n_y	64	
n_z	36	
n_t	3	
n_m	200000	
cut_x	$6.0 \cdot \text{sigma}_x$	1 relative
cut_y	$6.0 \cdot \text{sigma}_y$	1 relative
cut_z	$3.0 \cdot \text{sigma}_z$	1 relative
do_compt	0	flag (= no)
do_eloss	1	flag (= yes)
do_hadrons	0	flag (= no)
do_isr	1	flag (= yes)
do_jets	0	flag (= no)
do_lumi	0	flag (= no)
do_pairs	1	flag (= yes)
do_photons	1	flag (= yes)
do_prod	0	flag (= no)
electron_ratio	0.05	
photon_ratio	0.05	
pair_ratio	1	
store_pairs	1	flag (= yes)
track_pairs	1	flag (= yes)
grids	7	
pair_ecut	$5 \cdot 10^{-3}$	GeV
pair_q2	2	flag (= $\hat{s}/4$)
beam_size	1	flag (= yes)
ext_field	0	flag (= no)

Table A.2: Guinea-Pig \$PARAMETERS settings that were used for the generation of electron-positron pairs. All parameters are explained in detail in [50], and most values follow the default suggestions given there.

B Mokka Technicalities

B.1 The Detector Geometry

Mokka uses a very flexible approach when it comes to the description of detector geometries: the program offers a large number of “detector models”, each of which consists of a set of “subdetectors”. A Mokka subdetector consists of a piece of executable code – a “geometry driver” – plus a set of geometry data which gets read by the driver at runtime and which determines the properties of the constructed geometry.

Mokka follows the approach not to keep any static, hard-coded values in its drivers, therefore all geometry data is stored in external databases. This allows one driver, i. e. one piece of code, to construct different detector geometries if it is linked to different databases. Furthermore, the geometry construction can be influenced by means of “geometry parameters” that influence properties of the overall detector geometry. These parameters can easily be modified at runtime and allow the study of variable, “scaling” detector geometries.

The coordinate system of the LDC detector models in Mokka follows the common standard [164]: the y -axis points upward, the z -axis follows the beam axis, pointing in the direction of electrons. In the case of a crossing angle, the z -axis is the angle bisector between the incoming and the outgoing beam (i. e. the detector axis), again pointing in the direction of electrons. The x -axis is directed such that a right-handed Cartesian system is formed. In the case of a crossing angle, the momenta of beam electrons as well as beam positrons have a positive x -component.

All chemical elements and most compound materials in Mokka are taken from the NIST material database, which is provided by the `G4NistManager` of Geant4. This database contains all relevant elements with their isotopes in natural abundances (if available) and describes their nuclear properties. It also describes an extensive set of materials that are composed of single elements, including molecular properties and bulk properties such as the density under standard conditions. A few further Mokka-specific materials that are not contained in the NIST database are defined inside Mokka.

The simulations that are presented in this thesis were done using a specialised Mokka detector model that was derived from the common model `LDC01_01Sc`. That common model reflects, to a large extent, the state of the LDC detector plans at the stage of LDC version 2 [63, 114]. A cross-section of the central region of the detector model is shown in figure 6.1 on page 68.

Certain modifications have been made with respect to the beam tube, the mask region, the TPC and the magnetic field, since these components of the

detector are of special relevance when it comes to the simulation of beam-induced backgrounds. In the meantime, some of these extensions have been integrated into newer common models (LDC01_05Sc and upward), but others have also been left out because they were too specialised and the penalty in terms of execution time would have been too high for ordinary detector simulations. The extensions are nevertheless available within Mokka and could be re-activated whenever they are needed for further studies.

The following sections give an overview of all detector components that have been used for the background simulations. More detailed explanations are provided only in those cases where a component differs from the one that is used in the common model LDC01_01Sc.

B.1.1 Beam Tube

The Mokka subdetector `tubeX01` constructs the beam tube from the interaction point up to a distance of 12.5 m, including two branches with a crossing angle of 14 mrad. The inner part of the tube follows the proposal for LDC version 2, opening at an angle of 83 mrad (and pointing straight to the interaction point) in order to minimise the multiple scattering of Bhabha-scattered particles, which are essential for the luminosity measurement with the LumiCal. The rest of the beam tube is designed to match with the current proposals for the forward instrumentation and the nearest magnets of the beam delivery and extraction system.

A schematic drawing of the beam tube, seen from the top and compressed by a factor of 40 in z -direction, is shown in figure 6.3 on page 70. A detailed list of geometrical values is provided in table D.1.

The inner parts of the beam tube (up to the front face of the LumiCal) consist of beryllium, the rest is made of steel. The innermost section that is surrounded by the vertex detector has an assumed thickness of 0.5 mm, all other pieces are 1 mm thick. The beam tube is filled with a gas mixture that is supposed to be a realistic estimate of the expected rest gas in the interaction region [165]. The composition of the gas is listed in table B.1.

The main component of the rest gas is hydrogen, which is contained in the steel of the beam tube and which cannot be completely eliminated by annealing the tubes. Mass spectrometric measurements of the rest gas in the HERA beam tube have shown that another, minor component with a molecular mass of 28.0 units exists, possibly N_2 or CO. The actual ratio of these components cannot be determined, so equal abundances are assumed in the simulation.

The beam tube geometry has become publicly available in the common Mokka detector model LDC01_05Sc.

Component	p (mbar)	vol-%	mass-%	ρ (kg/m ³)
H ₂	$5.25 \cdot 10^{-8}$	84	27.4	$4.6 \cdot 10^{-12}$
CO	$0.5 \cdot 10^{-8}$	8	36.3	$6.2 \cdot 10^{-12}$
N ₂	$0.5 \cdot 10^{-8}$	8	36.3	$6.2 \cdot 10^{-12}$
Total	$6.25 \cdot 10^{-8}$	100	100	$1.7 \cdot 10^{-11}$

Table B.1: Composition of the rest gas in the beam tube [165]

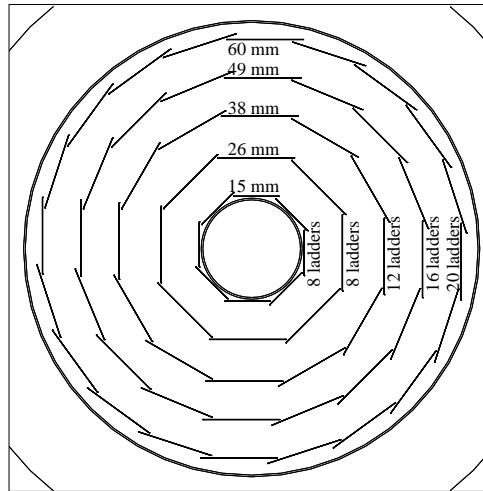


Figure B.1: Geometry of the simulated vertex detector

B.1.2 Vertex Detector

The Mokka subdetector `vxd01` provides a quasi-realistic model of the vertex detector (VTX) as it was proposed in the TESLA TDR [35]. The vertex detector consists of five layers, each segmented into an increasing number of so-called ladders, which slightly overlap in the φ -direction (figure B.1). Details are listed in table B.2. Additionally, the modelled geometry contains support structures, simplified electronics modules, and a lightweight cryostat, which encloses the whole vertex detector.

The sensitive part is made of silicon and has a thickness of $50 \mu\text{m}$, and an additional layer of supporting beryllium is also $50 \mu\text{m}$ thick. This results in an effective material thickness of $0.3\% X_0$ for all layers in total. Energy deposits above 3.4 keV (20% of a MIP) in the sensitive part will be written out as undigitised detector hits.

This version of the vertex detector is not part of `LDC01_01Sc`, but it is used in several older and newer detector models.

Layer	Radius (mm)	Total length (mm)	Ladders	Area (mm ²)
1	15	100	8	$0.94 \cdot 10^4$
2	26	250	8	$4.08 \cdot 10^4$
3	38	250	12	$5.97 \cdot 10^4$
4	49	250	16	$7.70 \cdot 10^4$
5	60	250	20	$9.42 \cdot 10^4$
Total				$2.81 \cdot 10^5$

Table B.2: Geometry of the vertex detector

Layer	Radius (mm)	Total length (mm)	Area (mm ²)
1	160	760	$7.64 \cdot 10^5$
2	300	1320	$2.49 \cdot 10^6$

Table B.3: Geometry of the two SIT layers

B.1.3 Silicon Intermediate Tracker

The Mokka subdetector `sit00` constructs a very simplistic Silicon Intermediate Tracker (SIT) to create a link between the vertex detector and the TPC. It merely consists of two plain silicon cylinders of $300 \mu\text{m}$ thickness, which will write out energy deposits above 20 keV (20% of a MIP) as undigitised hits. The geometry of the two layers can be found in table B.3.

This version of the SIT has been the standard implementation for a long time, but more detailed descriptions are currently being developed.

B.1.4 Forward Tracking Discs

The Mokka subdetector `ftd01` constructs the seven Forward Tracking Discs (FTDs), which are intended as an extension of the silicon tracking system into the low-angle forward region, which is only poorly (or not at all) covered by the TPC. The design of the discs follows LDC version 2: the discs are surrounded by a thin support ring and fill the space between the conical beam tube and the TPC almost completely. Details on the geometry can be found in table B.4.

All discs have a thickness of $300 \mu\text{m}$. In order to account for the presence of additional support material, the discs 4 to 7 are constructed of silicon with an unnaturally high density. Even though multiple scattering in the discs is modelled approximately correctly by this method, it leads to wrong

Disc	r_{inner} (mm)	r_{outer} (mm)	z (mm)	Single area (mm ²)
1	38	140	200	$0.57 \cdot 10^5$
2	48	140	320	$0.54 \cdot 10^5$
3	59	210	440	$1.28 \cdot 10^5$
4	68	270	550	$2.14 \cdot 10^5$
5	90	290	800	$2.39 \cdot 10^5$
6	111	290	1050	$2.26 \cdot 10^5$
7	132	290	1300	$2.09 \cdot 10^5$

Table B.4: Geometry of the Forward Tracking Discs.

values for the energy deposition. Therefore, an improved model of the discs is currently under development.

B.1.5 Forward Mask

The Mokka subdetector `maskX01` provides a representation of the forward region as described in recent sketches of the FCAL collaboration [156]. It constructs the LumiCal, the LHCAL, the BeamCal with a graphite absorber in front, the tungsten support tube, which carries the BeamCal and acts as a radiation protection for the HCAL, and finally the innermost magnets of the beam delivery and extraction system, up to a distance of 12.5 m.

The crossing angle is taken into account by placing the LumiCal and the BeamCal on the axis of the outgoing beam, i. e. shifted in x -direction and rotated by half the crossing angle. A detailed description of the modelled geometry can be found in table D.2, and the mask is also shown in figure 6.4 on page 70. All of the constructed geometry elements are insensitive, which means that – in these simulations – the forward calorimeters only act as scattering targets.

A more detailed, sensitive description of the LumiCal has recently become available and a proper description of the BeamCal is currently being developed. For the time being, the forward mask geometry is available in the detector model `LDC01_05Sc`, but without the LumiCal in order to make room for the improved implementation named `SLcal01`.

B.1.6 Time Projection Chamber

The Mokka subdetector `tpc06` constructs a Time Projection Chamber (TPC) consisting of an inner and outer barrel, a thin cathode in the centre, two endplates, and a (mostly) sensitive gas volume.

Following the description in BRAHMS, the barrel cylinders consist of thin layers of aluminium that give a realistic fraction of a radiation length (1.3% X_0 for the inner barrel and 1.7% X_0 for the outer barrel) compared to the current state of the art in field cage design. The cathode is a 100 μm thick sheet of copper and the endplates are described as a relatively detailed sandwich of various materials (modelling GEMs, the readout plane, electronics, cabling and insulation), resulting in an effective material thickness of approximately 20% X_0 . The construction of such a lightweight endplate in reality is seen as an ambitious goal, but nevertheless deemed feasible.

The TPC is located at $305 \text{ mm} < r < 1580 \text{ mm}$ and $z < 2200 \text{ mm}$, but the sensitive gas volume only stretches across $371 \text{ mm} < r < 1516 \text{ mm}$ and $z < 1970 \text{ mm}$, leaving room for a realistic barrel structure and for the endplate. The TPC is filled with the so-called TDR gas mixture, containing 93% of Ar, 5% of CH_4 , and 2% of CO_2 .

To model the readout of a TPC in Geant4 is not straightforward: the main process by which signals are produced in a TPC is ionisation of the gas by charged particles. This process is included in the physics lists of Geant4, but the problem is that it acts only as a “continuous” process. To understand the implications of this concept, it is necessary to explain how Geant4 tracks particles through the detector geometry.

A particle in the simulation, represented by a `G4Track` object, is transported in terms of discrete steps, represented by `G4Step` objects. The Geant4 tracking system solves the particle’s equation of motion typically by taking its momentum and possible fields into account. The transportation then happens in terms of small straight “chords”, many of which may be composed to form a curved trajectory. However, these chords are used only to find a good approximation for the solution of the equation of motion – they are known to the internal Geant4 tracking system, but not to the calling application (Mokka, in this case).

A `G4Step` ends – and a hook of the calling application may be invoked – as soon as one of the following is true:

- The boundary of a volume in the detector geometry is reached. A `G4Step` will never cross a volume boundary.
- A “discrete” process happens. These are all processes that involve the occurrence of one or more new particles in the simulation, such as decay, bremsstrahlung, pair production, delta-ray emission, or hadronic interactions. Ionisation is not one of them.
- The maximum step length, if defined, has been reached.

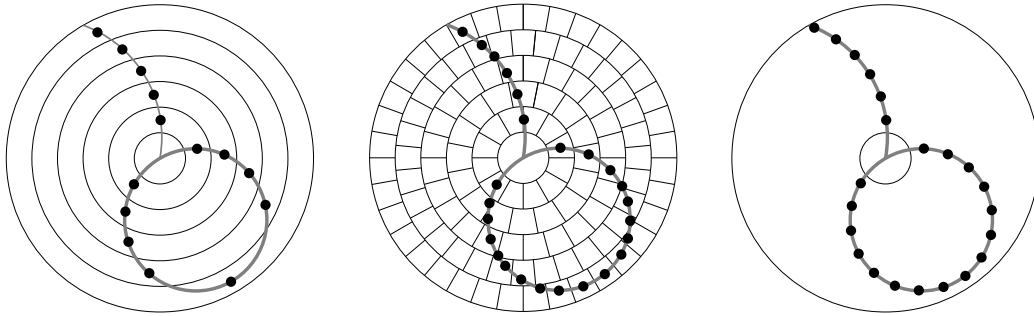


Figure B.2: Possible segmentations of the TPC volume to break simulation steps into smaller pieces. **Left:** Radial segmentation with artificial gas layers. **Middle:** Three-dimensional segmentation with artificial voxels. **Right:** Limitation of the maximum allowed step length, i. e. a segmentation along the line of flight.

Since the TPC gas has a low density, discrete processes are rare, and particles would typically be transported through the TPC volume with a small number of large steps. The energy loss caused by ionisation would only be calculated at the end of each step and then be assigned to the step as a whole. This would leave the TPC with small number of poorly-located, large energy deposits, rendering it practically useless for tracking and the measurement of dE/dx .

There are several strategies to overcome these issues:

- Artificial volume boundaries can be introduced by segmenting the TPC gas into many cylindrical layers, each of which corresponds to a pad row on the readout plane (figure B.2, left). Thus, steps are forced to stop at each volume boundary, and the energy deposits in each layer can be assigned to the according pad row.

This approach is fine for high-energy tracks with a large transverse momentum component, but it leads to a significant thinning of track points for curlers that travel a longer distance inside one layer. The situation is even worse for low-energy particles that tightly curl inside a single layer. In both cases, only one or few track points with unrealistically large energy deposits will be written out as detector hits.

- To solve the problem of curlers, the TPC volume can be artificially segmented not only in layers (corresponding to pad rows), but also in wedges (corresponding to pads) and discs (corresponding to time bins), which leads to a full three-dimensional voxelisation of the TPC (figure B.2, middle). While this is technically possible, it significantly

slows down the internal navigation and tracking due to the enormous number of voxels ($5 \cdot 10^9$). This slow-down renders the approach infeasible, even though it would in principle be the best representation of a TPC.

- Another approach would be to increase the probability for the production of secondary particles. Geant4 has an internal “range cut” that determines whether an energy deposit will lead to the production of a secondary particle (and thereby end the current step) or whether the secondary particle will be ignored and the energy deposit will instead be accounted for only after the step has ended for some other reason. The cut is given in terms of an expected range in the current material, not in terms of an energy.

If the range cut in the TPC was set very low, every energy loss – through ionisation or any other processes – could lead to a tiny “delta-ray”, at the same time producing a secondary particle and ending the current step. However, there are two problems: firstly, it is unclear whether the ionisation process that is built into Geant4 still works correctly under these preconditions. In contrast to dedicated tools like HEED [166], Geant4 was never intended to simulate the interactions of charged particles with gas on a microscopic level, and one would have to confirm that the clustering of secondary charges (and even the total energy loss) is modelled correctly if steps are extremely small. Secondly, the execution speed might be reduced significantly because every track in the TPC would produce a large “shower” of very low-energy particles.

- Another idea might be just to accept the large steps with their large energy deposits, and to distribute the deposited energy (i. e. the secondary charges) along the track only in a post-processing step – possibly even with the help of a sophisticated, specialised tool like HEED. The problem, however, is to reconstruct the actual trajectory of the particle, which is in principle unknown when no endpoints of steps are provided by the simulation.

It would be possible to try and reconstruct the trajectory using the Monte Carlo truth or information from other subdetectors, but the outcome of such a procedure would at least be questionable.

- Finally, a regular interruption of the internal tracking process can be enforced by specifying a maximum step length, which corresponds to a segmentation of the track along its trajectory (figure B.2, right).

This approach has practically no speed penalty, but the choice of the maximum step length requires a trade-off: too small steps may lead to a very large number of detector hits, whereas too large steps may lead to binning problems during the digitisation of the hits, because the steps will not correspond to the pattern of the readout structure.

The Mokka subdetector `tpc06` uses the last approach: a maximum step length of 5 mm is specified for the sensitive gas volume, such that detector hits will be written out with a maximum distance of 5 mm. These hits are not digitised within the simulation, i.e. they are not filled into voxels or otherwise post-processed to resemble the output from a real detector.

Following the examples of its predecessors, the TPC implementation allows to set a minimum energy cut: particles with an energy below a given limit will never create any hits in the TPC. This may be useful for the suppression of background signals, but for the background simulations presented in this thesis, the limit is set to zero. The Geant4 range cut – which defines e.g. the lower production threshold for delta-rays – is set to $100\ \mu\text{m}$, which should be sufficiently well below the two-track separation of a real TPC.

B.1.7 Endcap Tracking Discs

The Endcap Tracking Discs (ETDs), formerly also called Forward Chambers (FCH), are a possible intermediate detector between the TPC endplate – which is relatively thick and may therefore give rise to non-negligible multiple scattering – and the ECAL endcap. They were intended to provide a precise measurement of the entry point into the calorimetric system in order to improve Particle Flow performance. Since the ETDs are still under discussion, they are not included in the simulation.

B.1.8 Silicon Envelope Tracker

The Silicon Envelope Tracker (SET) is a possible intermediate detector between the TPC barrel and the ECAL barrel, providing a precise measurement of the entry point into the ECAL, similar to the ETDs. The need for an SET is still being debated, and the detector is not included in the simulation.

B.1.9 Electromagnetic Calorimeter

The Mokka subdetector `SEca101` constructs an electromagnetic calorimeter (ECAL) based on silicon-tungsten technology, with 10 layers of 2.1 mm thickness and 20 more layers of 4.2 mm thickness. The sensitive part consists of silicon layers of 0.5 mm thickness, logically divided in cells of $10 \times 10\ \text{mm}^2$

size and embedded in a layer of G10, a fibreglass-epoxy composite material. The ECAL barrel fills the region $1600 \text{ mm} < r < 1770 \text{ mm}$, the endcap is positioned at $2300 \text{ mm} < z < 2470 \text{ mm}$.

This version of the ECAL roughly corresponds to the plans in LDC version 2 and is the standard in LDC01_01Sc and similar models.

B.1.10 Hadronic Calorimeter

The Mokka subdetector SHca102 constructs a hadronic scintillator-steel calorimeter (HCAL). The calorimeter has 40 layers with 20 mm of steel as radiator material and 5 mm of polystyrene as scintillator material. In order to be able to study various cell sizes, the sensitive scintillator is logically divided into very small cells of $10 \times 10 \text{ mm}^2$, so that the hits in these cells can later be combined into cells of the desired size. (This post-processing step is sometimes referred to as “ganging”.) The HCAL barrel fills the region $1800 \text{ mm} < r < 2880 \text{ mm}$, the endcap is located at $2500 \text{ mm} < z < 3580 \text{ mm}$.

The subdetector SHca102 is also used in LDC01_01Sc and similar models, even though its geometry is only an approximation to the current plans for the HCAL layout. An improved implementation has become available in the meantime and is used in the latest detector models.

B.1.11 Magnet Coil

The Mokka subdetector SCoil01 constructs a simple aluminium cylinder with $2960 \text{ mm} < r < 3710 \text{ mm}$ and $z < 3300 \text{ mm}$, according to LDC version 2. This is the standard for LDC01_01Sc and all later models so far.

B.1.12 Magnet Yoke

The subdetector yoke02 provides a simple octagonal iron yoke that encloses the whole detector. The distinct “plug” that was needed to ensure the required field quality for the longer coil in LDC version 1 (i. e. a piece of the yoke that would reach into the inside of the coil) is missing here. The simulated yoke is not instrumented with muon chambers and therefore completely insensitive. Its dimensions are $4060 \text{ mm} < r < 6060 \text{ mm}$ and $3650 \text{ mm} < z < 5650 \text{ mm}$.

This version of the yoke is also used in LDC01_01Sc and similar models, but an improved description, including sensitive muon chambers, has become available in the meantime and is used in the latest detector models.

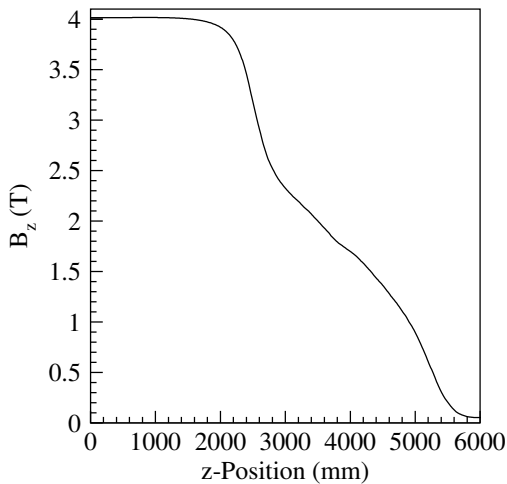


Figure B.3: B_z -component of the main solenoid field, calculated for a realistic coil and yoke [63, 115]

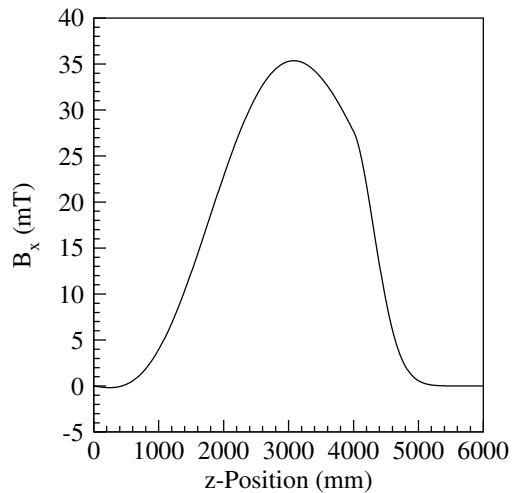


Figure B.4: B_x -component of the superimposed anti-DID field [116]

B.1.13 Magnetic Field

The Mokka subdetector `fieldX01` provides a description of the magnetic field for the whole detector. (Even though the field is of course no subdetector in the literal sense, it is included in the geometry management like an ordinary detector component.) The main contribution comes from the solenoid field, using a one-dimensional field map derived from realistic field simulations. An anti-DID field (cf. section 4.4) is superimposed on the solenoid field such that a field line that starts at the interaction point (i.e. the origin of the coordinate system) hits the centre of the hole for the outgoing beam in the BeamCal.

The main solenoid field is limited to a radius of 3200 mm because the field approximation from a one-dimensional map can only be valid inside the coil. Instead, the field of the return yoke is modelled by a simplified cylindrical and homogeneous magnetic field that points into the opposite direction.

The field description is completed by the quadrupole fields of the innermost magnets of the beam delivery and extraction system. The quadrupoles are modelled as ideal fields, without contributions from the yokes or from fringe fields. Higher-order magnets (sextupoles and octupoles) are present as scattering targets, but their fields are not included.

Details on the geometric properties of the various contributions to the magnetic field are listed in table D.3. More information on the calculation of the fields can be found in appendix C.3.3. The field maps that are used for

the simulation are shown in figures B.3 and B.4, the resulting overall field distribution (compressed by a factor of 10 in the z -direction) is shown in figure 6.5 on page 71.

This representation of the magnetic field has not been included in any common geometry model because too much computing time is needed for the tracking of particles in the rather complicated magnetic field. All common models use the approximation of an ideally homogeneous field that vanishes beyond a given z -position, which is sufficient for the currently ongoing detector performance studies.

B.2 The Physics List QGSP_BERT_HP

This section gives an overview of the ingredients of the Geant4 physics list QGSP_BERT_HP, which has been used for all simulations presented in this thesis. Further details on the different models, their implementation, and the theoretical backgrounds can be found in the Geant4 Physics Reference Manual [167] and the comprehensive references provided therein.

B.2.1 Particles

The list models the photon (γ), the six leptons ($e, \mu, \tau, \nu_e, \nu_\mu, \nu_\tau$), the nucleons (p, n), some simple nuclei ($D, T, {}^3\text{He}, \alpha$), and most mesons (π, K, D, B, \dots) and baryons ($N, \Delta, \Lambda, \Sigma, \Omega, \Xi$) that can e. g. be found in [1], except the higher heavy-flavour states. The heavy gauge bosons, the Higgs boson, and supersymmetric particles are not implemented in Geant4. Partons exist, but they do not have any physical processes attached to them – such particles will typically be processed by dedicated particle generators and not by a detector simulation.

B.2.2 Particle Decay

All unstable particles have their mean lifetime and their major decay channels assigned. Most decays are implemented as two-, three-, or N -body phase space decays with isotropic angular distributions in the centre-of-mass frame. Specialised models exist for Dalitz-like decays ($h^0 \rightarrow \gamma + \ell^+ + \ell^-$), the muon decay, leptonic tau decay, and semileptonic kaon decays. For many of the short-lived particles, decay is the only available process.

B.2.3 Standard Electromagnetic Physics

QGSP_BERT_HP contains the standard electromagnetic physics that are also found in most of the other built-in physics lists.

- Photons may undergo the photoelectric effect (using the Sandia parameterisation for absorption cross-sections and atomic shell data for electron energies), Compton scattering (using the Klein-Nishina model, which gives good results for $1 \text{ keV} < E_\gamma < (100/Z) \text{ GeV}$), and gamma conversion (using the Bethe-Heitler model, which is good for $1.5 \text{ MeV} < E_\gamma < 100 \text{ GeV}$).
- Electrons and positrons are affected by multiple scattering (using the Urbán model, which does not simulate individual scattering processes, but only their effective spatial displacement and angular deflection after a simulated particle step). Their energy loss and the production of delta-rays follows the Møller-Bhabha model (good for $1 \text{ keV} < E_e < 100 \text{ GeV}$). The fluctuations of the energy loss are calculated by a simple model (partially taken from the GLANDZ code in GEANT3), which distinguishes thick and thin absorbers and which approaches the Landau limit for thin absorbers. The bremsstrahlung model is based on the EEDL parameterisation (good for $1 \text{ keV} < E_e < 100 \text{ GeV}$). Additionally, positrons can annihilate with atomic electrons (using the Heitler model for the annihilation cross-section and the kinematics of the final state).
- Muons also use the Urbán model of multiple scattering, but different models for energy loss (Bragg for $E_\mu < 0.2 \text{ MeV}$, Bethe-Bloch for $0.2 \text{ MeV} < E_\mu < 1 \text{ GeV}$, Bethe-Bloch with radiative corrections for $E_\mu > 1 \text{ GeV}$), bremsstrahlung, and pair production.
- Charged hadrons undergo multiple scattering (Urbán model) and energy loss through ionisation and delta-rays (Bragg and Bethe-Bloch models).

B.2.4 Extra Electromagnetic Physics

QGSP_BERT_HP supports photonuclear (sometimes also called gammanuclear) and electronuclear physics, using a parameterised model that covers different energy regions for the incident photon: the Giant Dipole Resonance (GDR) dominates for $10 \text{ MeV} < E_\gamma < 30 \text{ MeV}$, the so-called quasi-deuteron region reaches up to the pion threshold, the Δ region continues up to 450 MeV , the Roper resonance region extends to 1.2 GeV , and the Reggeon-Pomeron region is reached for even higher energies. Photonuclear absorption cross-sections are available in a database for around 50 nuclei. Electronuclear reactions are basically described with the Equivalent Photon Approximation (EPA).

Having photonuclear processes enabled in the simulation is essential for the production of neutrons in electromagnetic showers – if a physics list without photonuclear physics is used, no neutrons will be produced from electron-positron pairs by Geant4 at all.

Synchrotron radiation and nuclear interactions of muons also belong to the “extra” section of electromagnetic physics, but they are neither required nor switched on by default.

B.2.5 Elastic Hadron Physics

The cross-sections for elastic and quasi-elastic hadron-nucleus scattering are mostly calculated from various parameterisations for different energies and particles. A speciality of the `QGSP_BERT_HP` physics list is a detailed description of elastic processes with neutrons: for energies of $E_{\text{therm}} \lesssim E_n < 20$ MeV, the neutron model uses the detailed ENDF/B-VI database, which contains elastic scattering cross-sections for many different nuclei. The transportation of neutrons is greatly improved by this supplementary data, and the extension “HP” is often understood as “high precision” (sc. neutrons).

B.2.6 Inelastic Hadron Physics

Inelastic hadronic scattering processes – including capture and fission reactions – are modelled through various parameterisations, depending on the energy range:

- For high energies ($E > 25$ GeV), the so-called Quark-Gluon-String Precompound model (“`QGSP`”) is used for the interaction of hadrons (p, n, π , K) with nuclei, enabling the production of secondary hadrons and the emission of nucleons and larger fragments from excited nuclei.
- At low energies ($E < 10$ GeV), the interactions with nuclei and the subsequent nuclear deexcitation are modelled with a Bertini Intranuclear Cascade (“`BERT`”), taking into account pre-equilibrium particle emission, nuclear explosions, fissions, and particle evaporation at the equilibrium state. The calculation of the intranuclear cascade is based on the `INUCL` code. Evaporation models exist for nucleons, heavier fragments (such as D, T, α), and photons with continuous and discrete energy distributions. Nuclear energy levels that are needed for discrete photon transitions are read from the ENSDF database.
- The remaining intermediate energy range is covered by the Low Energy Parameterised model (“`LEP`”), which is basically equivalent to the `GHEISHA` code in `GEANT3`.

Again, the special case of low-energy neutrons ($E_{\text{therm}} \lesssim E_n < 20 \text{ MeV}$) uses the ENDF/B-VI database with cross-sections (“HP”) for inelastic scattering, capture, and fission processes of many nuclei. Data for all relevant isotopes are available for many elements, whereas in some cases only data for the most abundant isotope or for the natural mixture of isotopes are known. For the few exceptions where no data is available at all, the simulation falls back to parameterised cross sections.

Radioactive decays – i. e. deexcitations of long-lived, metastable nuclei – are available in Geant4, but not included in the built-in physics lists.

B.2.7 Stopping Physics

The list `QGSP_BERT_HP` enables the nuclear capture of negative muons, pions, and kaons at rest. The hadronic processes can be separated in two different components: first the primary absorption process and the interaction of the hadron with one or more nucleons, then the deexcitation of the remnant nucleus. Nucleons can be released in both stages.

B.2.8 Ion Physics

This section enables models for inelastic processes of deuterons, tritons, and alpha particles that may have been emitted in deexcitations of nuclei.

B.2.9 User Special Cuts

A pseudo-process named `G4UserSpecialCuts` must be attached to particles in order to enable the limitation of the step length in certain volumes of the detector geometry (such as the sensitive TPC volume). This process is not included in `QGSP_BERT_HP` and the other built-in physics lists by default, but it is later added in Mokka for all charged, long-lived particles.

C Geometry Drivers for Mokka

Several pieces of code – so-called geometry drivers – have been contributed to the simulation application Mokka to allow for a detailed modelling of the detector geometry, particularly the forward region. The older, already existing drivers may well have been sufficient for simulations of the overall detector (where the forward region is often just an annoying gap in the 4π coverage), but they could not be used for detailed studies like the ones presented in this thesis, where minor details of the detector model can have major effects.

The following sections are provided as a short overview of the functionality of these drivers. They also give some explanation of the database entries that determine the construction of detector geometries.

C.1 The Beam Tube Driver

C.1.1 General

The driver “`TubeX01`” constructs a beam tube that may consist of any number of tubular or conical elements. All elements are placed into the Geant4 world volume, i. e. the top-level volume that contains all other pieces of the simulated geometry. The wall material can be chosen freely for each element, and the inner openings or holes will be filled with the material “`beam`”, which models the estimated rest gas in the beam tube (table B.1 on page 147). The constructed geometry will always be symmetric to the plane $z = 0$, therefore only one half of the geometry data has to be provided in the database. Simple, symmetric shapes will be placed twice; more complicated, asymmetric shapes will be created as two different solids that are mirrored versions of each other.

C.1.2 Parameters

The most important parameter for the beam tube geometry is the crossing angle, stored in the global Mokka geometry parameter “`ILC_Main_Crossing_Angle`”. It is the full angle between the incoming and the outgoing beam, i. e. twice the angle between the beams and the z -axis.

Since beam tube geometries may differ significantly for different crossing angles, this parameter is not used to scale certain geometric measures continuously. Instead, the crossing angle determines which database will be read to construct the beam tube. This means that only a discrete set of crossing angles can be constructed – namely the ones for which a complete dataset has been defined. Even though this may sound like a severe restriction, it is almost none: only a limited set of angles is under discussion, and a freely

varying angle would require extreme caution not to produce collisions and overlaps in the geometry – not only in the simulated model, but also in the real layout of the beam delivery system.

Apart from the crossing angle, dependencies on any desired global Mokka geometry parameter can be introduced through the concept of “references” (section C.4).

C.1.3 Database Entries

The geometry database that gets selected through the internal Mokka geometry management and through the value of the parameter “`ILC_Main_Crossing_Angle`” needs one table with the name “`tube`”. Every row in this table corresponds to one element of the beam tube. The fifteen fields are:

- **crossType** (integer): selects how a possible crossing angle will influence the geometrical shape and placement of this element. Details are given below.
- **zStart** and **zEnd** (float): the position of the beginning and the end of this element, measured along the z -axis or along the axis of the incoming or outgoing beam (depending on **crossType**), given in millimetres. The innermost element of the beam tube should have **zStart** set to zero.
- **rInnerStart**, **rInnerEnd**, **rOuterStart**, and **rOuterEnd** (float): generally the inner and the outer radii of the element at its beginning (**zStart**) and its end (**zEnd**), measured from the z -axis or from the axis of the incoming or outgoing beam (depending on **crossType**), given in millimetres. The element will always be based on a conical shape (i. e. a `G4Cons` solid), but depending on **crossType**, some of the given radii may be interpreted differently.
- **material** (string): the name of the material that should be used for the wall of this element. All materials from the `G4NistManager` are available, plus a few more that are internal to Mokka. The inner openings or holes will always be filled with the `beam` material.
- **name** (string): an arbitrary name for identification, which will also be used in the names of the constructed Geant4 geometry objects.
- **zStartRef**, **zEndRef**, **rInnerStartRef**, **rInnerEndRef**, **rOuterStartRef**, and **rOuterEndRef** (string): may contain references for the respective fields (section C.4) or may be left empty.

Most of the database entries correspond to the parameters of a “G4Cons” constructor and are straightforward to use, but the “crossType” selector needs further explanation. It is an integer code for the detailed shape of the constructed element and its placement, ranging from 0 through 17. Additional names for enumerated constants are given in the driver code.

- 0 (`kCenter`): a plain G4Cons (cylindrically or conically tubular), placed on the z -axis. To be used for long pieces of the beam line.
- 1 (`kUpstream`) and 2 (`kDnstream`): same, but placed on the axis of the incoming or outgoing beam, respectively.
- 3 (`kPunchedCenter`): a solid cylinder or cone with radii `rOuterStart` and `rOuterEnd` from which one or two cylindrical off-centre holes are punched out by means of a `G4SubtractionSolid`. `rInnerStart` is interpreted as the radius of the hole on the axis of the incoming beam, `rInnerEnd` is interpreted as the radius of the hole on the axis of the outgoing beam. If either radius is zero, the hole will be missing. Mainly to be used for the disc-like element where the beam tube splits for the first time.
- 4 (`kPunchedUpstream`) and 5 (`kPunchedDnstream`): similar, but placed on the axis of the incoming or outgoing beam, respectively. One of the holes will be in the centre of the element, the other one will be shifted outward twice as much as in the case of `kPunchedCenter`. Neither `rInnerStart` nor `rInnerEnd` may be zero.
- 6 (`kUpstreamClippedFront`) and 7 (`kDnstreamClippedFront`): similar to `kUpstream` and `kDnstream`, but with a front face perpendicular to the z -axis (not to the beam axis). `zEnd` will be measured along the beam axis, but `zStart` will be recalculated to fit to an element placed on the z -axis. The front face will have a slightly elliptic shape, and the radii `rInnerStart` and `rOuterStart` will therefore not be exactly matched. Mainly to be used as a connection behind a disc of type `kPunchedCenter`.
- 8 (`kUpstreamClippedRear`), 9 (`kDnstreamClippedRear`), 10 (`kUpstreamClippedBoth`), and 11 (`kDnstreamClippedBoth`): as `kUpstreamClippedFront` and `kDnstreamClippedFront`, but with the rear face or with both faces parallel to the z -axis.
- 12 (`kUpstreamSlicedFront`), 13 (`kDnstreamSlicedFront`), 14 (`kUpstreamSlicedRear`), 15 (`kDnstreamSlicedRear`), 16 (`kUpstreamSliced`

Both), and 17 (`kDnstreamSlicedBoth`): similar to the `Clipped` types, but with one or both faces parallel to the axis of the respective other beam. To be used as a connection to a disc of type `kPunchedUpstream` or `kPunchedDnstream`.

This variety of shapes is needed to ensure a seamless fit between all the possible elements of the beam tube. A gap between two elements would be filled with air at standard pressure (the material of the Mokka world volume) and might become the source of a significant amount of backscattering.

C.2 The Mask Driver

C.2.1 General

The driver “MaskX01” constructs pieces of the mask, i. e. all kinds of dead material that is arranged around the beam tube. The mask may consist of any number of tubular or conical elements. All elements are placed into the Geant4 world volume, and their material can be chosen freely. Openings and holes will not be filled, which means that elements of the mask any enclose the beam tube without producing geometry overlaps. As for the beam tube, the constructed geometry will always be symmetric to the plane $z = 0$.

C.2.2 Parameters

Again, the most important parameter for the mask geometry is the crossing angle, stored in the global Mokka geometry parameter “`ILC_Main_Crossing_Angle`” and defined as described above. As in the case of the beam tube, different databases exist for a set of different crossing angles. The mask can depend on “references”, too.

C.2.3 Database Entries

The geometry database that gets selected through the internal Mokka geometry management and through the value of the parameter “`ILC_Main_Crossing_Angle`” needs one primary table with the name “`_components`”. Every row in this table corresponds to a group of mask elements that form one functional entity and that share a common set of visualisation attributes. The five fields are:

- **name** (string): an arbitrary name, which serves as an identifier for the component.

- `colorR`, `colorG`, `colorB` (float, should be in the range $[0, 1]$): the red, green, and blue contribution to the colour in which all elements of this component will be displayed. Transparency (i.e. the alpha channel) is currently not included, but could easily be added.
- `visAttrib` (string): the first character of this string will enable special visualisation attributes. “i” means invisibility, “w” means forced wire-frame display, and “s” means forced solid display. All other characters will be silently ignored.

For every component there must be a table with a name equal to the “name” field of the “_components” table. The structure of these is equal to the table for the beam tube (section C.1.3), with the only difference that the “cross Type” can only have values from 0 through 5 (i.e. `kCenter`, `kUpstream`, `kDnstream`, `kPunchedCenter`, `kPunchedUpstream`, and `kPunchedDnstream`).

C.3 The Magnetic Field Driver

C.3.1 General

The driver “FieldX01” defines the magnetic field for the whole detector. Strictly speaking, it does not construct any geometrical objects, but it supplies field vectors for any given point in space whenever it is queried by the internal Geant4 navigation and tracking system.

The driver specifies cylindrical or tubular regions in which solenoidal or quadrupole fields exist and in which the returned field vectors are calculated according to certain rules. These regions are not bound to any geometrical objects, which means their boundaries may be located anywhere. The regions can also overlap, and multiple fields that contribute to the same space point will be superimposed. Apart from the polarity of the field vectors of solenoidal fields and DID fields, the resulting overall field will be symmetric to the plane $z = 0$.

C.3.2 Parameters

As in the case of the beam tube, the crossing angle – stored in the global Mokka geometry parameter “`ILC_Main_Crossing_Angle`” and defined as described above – has an influence on the magnetic field. Different databases exist for a set of discrete crossing angles because a simple scaling of the field configuration with the angle may not always produce the desired results. Additional dependencies on global geometry parameters can be introduced by “references”, as in the case of the beam tube.

C.3.3 Database Entries

The geometry database that gets selected through the internal Mokka geometry management and through the value of the parameter “`ILC_Main_Crossing_Angle`” needs one table with the name “`magnetic`”. Every row in this table corresponds to one region with a certain type of magnetic field. The eleven fields are:

- `fieldType` (integer): selects the type of magnetic field for this region. Details are given below.
- `zStart` and `zEnd` (float): the position of the beginning and the end of this region, measured along the z -axis or along the axis of the incoming or outgoing beam (depending on `fieldType`), given in millimetres. Fields that cover the inner parts of the detector should have `zStart` set to zero.
- `rInner` and `rOuter` (float): the inner and the outer radius of the region, measured from the z -axis or from the axis of the incoming or outgoing beam (depending on `fieldType`), given in millimetres. Regions will always be cylindrical or tubular.
- `fieldValue` (float): usage depends on `fieldType`.
- `fieldData` (string): for some values of `fieldType`, this database field contains the name of another database table with additional field map data. Ignored otherwise.
- `zStartRef`, `zEndRef`, `rInnerRef`, and `rOuterRef` (string): may contain references for the respective database fields (section C.4) or may be left empty.

The “`fieldType`” determines which kind of magnetic field exists in the specified region. It is an integer code for the placement of the region and the calculation of the associated field, ranging from 0 through 6. Additional names for enumerated constants are given in the driver code.

- 0 (`kCenterQuad`): an ideal quadrupole that is centred on the z -axis. `fieldValue` contains the gradient in Tesla per metre; it can be positive or negative to select a focusing or defocusing quadrupole. A field with the gradient a is calculated as:

$$B_x = ay, \quad B_y = ax, \quad B_z = 0$$

The polarity of quadrupoles for $z > 0$ and $z < 0$ is the same, such that they act in the same way upon particles of the opposite charge that pass through them in the opposite direction.

- 1 (`kUpstreamQuad`) and 2 (`kDnstreamQuad`): same, but placed on the axis of the incoming or outgoing beam, respectively.
- 3 (`kSolenoid`): an ideal, homogeneous solenoid field in z -direction. `fieldValue` contains the field strength in Tesla.
- 4 (`kDID`): an ideal DID field in x -direction that flips its polarity at $z = 0$. `fieldValue` contains the field strength in Tesla. The superposition of this field over a solenoid field will result in field lines with an unphysical kink at $z = 0$. The DID (or anti-DID) field strength should be chosen such that

$$\tan \frac{|B_x|}{B_z} = \frac{1}{2}\vartheta,$$

where ϑ is the crossing angle.

- 5 (`kMapSolenoid`): a solenoid field that is based on a field map. `fieldData` contains the name of a table in the database “`fieldmaps00`” that contains the field map data. `fieldValue` is used as an overall scaling factor for the field vectors.

The current implementation takes a list of field values $B_z(0, 0, z)$ from $z = 0$ m to $z = 10$ m with a separation of $\Delta z = 10$ mm. The field vectors for points that are not located on the z -axis are then calculated with the help of the Maxwell equation $\vec{\nabla} \cdot \vec{B} = 0$. Under the assumption of azimuthal symmetry, in cylindrical coordinates this yields:

$$B_\rho(\rho, z) = -\frac{1}{2}\rho \frac{\partial}{\partial z} B_z(z), \quad B_z(\rho, z) = B_z(z)$$

The derivative is approximated by a simple numerical calculation of the difference quotient, and the data for intermediate points is obtained by linear interpolation. This calculation of a three-dimensional field map is clearly simplified and it becomes completely wrong as soon as the magnetic coil and the yoke are reached, but it should be a good approximation for small distances from the z -axis, i. e. for the region of main interest in this study.

- 6 (`kMapDID`): a DID field that is based on a field map. As above, `fieldData` contains the name of the field map table and `fieldValue` is used as an overall scaling factor.

The current implementation takes a list of field values $B_x(0, 0, z)$ from $z = 0$ m to $z = 10$ m with a separation of $\Delta z = 10$ mm. The polarity of field vectors for $z < 0$ gets flipped. The scaling factor in `fieldValue` may be used to (moderately) adjust a field map that was originally calculated for another solenoidal field strength, for a different crossing angle, or for a different layout of the forward region.

Higher-order fields (sextupoles, octupoles, ...) or more complex field maps (planar two-dimensional maps or full three-dimensional maps) are currently not implemented, even though the driver code itself could easily be extended to accommodate further field types.

C.4 Geometry Parameter References

C.4.1 General

To facilitate the global scaling of detector geometries, the geometry drivers for the beam tube, the mask, and the magnetic field can assign so-called references to any radius or z -position that is given in their respective databases. The idea is that these numbers are valid only if a certain global geometry parameter has a specific value, here called the “assumption”.

If the actual value of the global parameters – for whatever reason – differs from that assumption at runtime, the corresponding radius or z -position is adjusted likewise. This allows parts of the beam tube, pieces of the mask, or magnetic field regions to be relocated or to grow and shrink together with completely different parts of the overall detector geometry – provided that some global geometry parameter reflects these changes.

In the current implementation, the adjustment is always done in an additive way, i. e. a difference between the assumed value of a global parameter and the runtime value will lead to the same difference between the radius or z -position that is found in the database and the number that is actually used in the construction of the geometry. This is by far the most common way of scaling, even though a multiplicative adjustment – with ratios instead of differences – could in principle be implemented as well.

C.4.2 Parameters

References can be used to declare dependencies on any global geometry parameter that is available in Mokka. It is the task of the geometry designer to find and to implement a reasonable behaviour.

Good examples would be to let the radii of the innermost parts of the beam pipe depend on the inner radius of the vertex detector, to let the

LumiCal (and all related parts of the beam pipe) move in z -direction together with the ECAL, or to let the main solenoid field grow and shrink with the radius of the coil. A bad example would be to let the rear end of the final sextupole depend on the number of layers in the HCAL.

It is valid – and it may make perfect sense – to let the inner radius, the outer radius, and the z -position at the start and at the end of some geometry element depend on different references.

C.4.3 Database Entries

References are given via an additional database table named “`_references`”. Every row in this table corresponds to a global geometry parameter that can be used as a reference. The three fields are:

- `globalName` (string): the name of the global parameter as it is known to the Mokka geometry management.
- `localName` (string): a (typically shorter) alias name for the same parameter, to be used in the “`Ref`” fields of the geometry tables.
- `assumption` (float): the assumed value of the parameter for which the entries in the geometry tables are valid, typically in millimetres.

Since the names of global geometry parameters need to be unique, they are usually rather long and bulky. Because references live only in the local scope of the current driver, the shorter local alias names were introduced for convenience. As soon as the local name is given in any of the fields `zStartRef`, `zEndRef`, `rInnerStartRef`, and so forth, the corresponding value depends on the reference value and may be adjusted at runtime.

C.5 Error Checking

Like large parts of the current Geant4 geometry system, the drivers for the beam tube, the mask, and the magnetic field do not check for inconsistencies and errors like overlapping volumes. Some basic mistakes will throw a `G4Exception` at runtime, but most other problems may go unnoticed.

It is therefore the responsibility of the geometry designer to supply data that results in a valid and consistent detector geometry. Special attention must be paid to the scaling of geometries and to the introduction of sensible dependencies on reference values. A good viewer that can apply section cuts through the detector may provide some valuable assistance in the debugging and validation of geometries. Mokka can also draw field lines to visualise the magnetic field.

D Geometry Values

Tables D.1, D.2, and D.3 list the detailed geometries of the simulated beam tube, forward mask, and magnetic field, respectively, as they were used for the work presented in this thesis. The values are adapted from [156] and [168]. All dimensions are given in units of millimetres. The exact interpretation of the listed values, especially of the “crossType” T and the “fieldValue”, can be found in the respective sections of appendix C.

T	z_1	z_2	r_{i1}	r_{i2}	r_{o1}	r_{o2}	Mat.	Region
0	0	61	14	14	14.5	14.5	Be	VTX
0	61	172	14	22	14.5	23	Be	
0	172	264	22	22	23	23	Be	
0	264	2200	22	183	23	184	Be	
0	2200	2259	183	183	184	184	Be	
3	2259	2260	0	99	184	184	Be	
11	2260	2480	99	99	100	100	Fe	LumiCal
3	2480	2481	0	99	140	140	Fe	
0	2481	2499	139	139	140	140	Fe	LHCAL
0	2499	2500	129	129	140	140	Fe	
0	2500	2950	129	129	130	130	Fe	
0	2950	2951	129	129	210	210	Fe	
0	2951	3489	209	209	210	210	Fe	
3	3489	3490	14	19	210	210	Fe	
6	3490	3500	14	14	15	15	Fe	BeamCal
1	3500	4049	14	14	15	15	Fe	
1	4049	4050	9	9	15	15	Fe	
1	4050	12500	9	9	10	10	Fe	
7	3490	3500	19	19	20	20	Fe	BeamCal
2	3500	5999	19	19	20	20	Fe	
2	5999	6000	17	17	20	20	Fe	QDEX1A
2	6000	7741	17	17	18	18	Fe	
2	7741	7839	17	23	18	24	Fe	QDEX1B
2	7839	9681	23	23	24	24	Fe	
2	9681	9779	23	29	24	30	Fe	QFEX2A
2	9779	12500	29	29	30	30	Fe	

Table D.1: The geometry of the simulated beam tube in detail. A cross-section is shown in figure 6.3 on page 70.

T	z_1	z_2	r_{i1}	r_{i2}	r_{o1}	r_{o2}	Mat.	Name
2	2270	2470	100	100	350	350	W	LumiCal
0	2500	2950	130	130	290	290	W	LHCAL
5	3500	3550	15	20	165	165	C	Absorber
5	3550	3750	15	20	165	165	W	BeamCal
0	2950	10000	220	220	290	290	W	Support
3	3500	3750	0	165	220	220	W	
1	4050	6250	10	10	30	30	Fe	QD0
1	6300	6400	10	10	30	30	Fe	OC0
1	6400	7000	10	10	30	30	Fe	SD0
1	8350	10350	10	10	30	30	Fe	QF1
1	10500	10800	10	10	30	30	Fe	SF1
1	11100	11400	10	10	30	30	Fe	OC1
2	6000	7640	18	18	40	40	Fe	QDEX1A
2	7940	9580	24	24	50	50	Fe	QDEX1B
2	9880	11500	30	30	60	60	Fe	QFEX2A

Table D.2: The geometry of the simulated forward mask in detail. A cross-section is shown in figure 6.4 on page 70.

T	z_1	z_2	r_1	r_2	Value	Unit	Name
5	0	10000	0	3200	1	factor	Solenoid
6	0	10000	0	3200	1	factor	Anti-DID
3	0	5000	3200	6000	-2.52	T	Yoke
1	4050	6250	0	10	-65	T/m	QD0
1	8350	10350	0	10	40	T/m	QF1
2	6000	7640	0	18	-85	T/m	QDEX1A
2	7940	9580	0	24	-50	T/m	QDEX1B
2	9880	11500	0	30	40	T/m	QFEX2A

Table D.3: The geometry of the simulated magnetic field in detail. The field maps for the main solenoid and the anti-DID are shown in figures B.3 and B.4 on page 155. The two scaling factors of 1 correspond to a central magnetic field strength of 4 T and an anti-DID field that suits a crossing angle of 14 mrad.

E Lorentz Boost for Crossing Angles

E.1 Purpose

Several new detector geometries that have become available in Mokka make use of a beam crossing angle. This angle can have a crucial impact on beam-induced backgrounds, but many particle generators do not support a crossing angle, and basically all preexisting generator files have been produced without one. Therefore it is desirable to have the possibility to transform Monte Carlo particles from the centre-of-mass frame (in which they are usually generated) to the laboratory frame (in which the detector has to be simulated).

This transformation of Monte Carlo particles is a good approximation for the case of a beam crossing angle, provided that the actual accelerator performs crab crossing to retain its luminosity (section 2.3). The following calculation assumes that the centre-of-mass energy of the collision remains the same, i. e. that the beam energy is slightly higher than without a crossing angle. Whether this is correct depends on the actual specifications of the accelerator, but it turns out that the effect is tiny, in any case.

E.2 Calculation

In the rest frame (denoted by an asterisk), the incoming particles move only in the z -direction and collide head-on with the beam energy E_B^* . In the case of highly relativistic particles with negligible mass (as it is the case for electrons here), the four-momenta are given by:

$$p_1^* = \begin{pmatrix} E_B^* \\ 0 \\ 0 \\ +E_B^* \end{pmatrix}, \quad p_2^* = \begin{pmatrix} E_B^* \\ 0 \\ 0 \\ -E_B^* \end{pmatrix}$$

The available centre-of-mass energy is $\sqrt{s} = 2E_B^*$. Under the assumption that this centre-of-mass energy should remain constant, the transformation to the laboratory frame is achieved by a Lorentz boost in x -direction:

$$\Lambda_x = \begin{pmatrix} \gamma & \gamma\beta & 0 & 0 \\ \gamma\beta & \gamma & 0 & 0 \\ 0 & 0 & 1 & 0 \\ 0 & 0 & 0 & 1 \end{pmatrix}$$

The transformed four-momenta of the incoming particles in the laboratory frame are then:

$$p_1 = \begin{pmatrix} \gamma E_B^* \\ \gamma\beta E_B^* \\ 0 \\ +E_B^* \end{pmatrix}, \quad p_2 = \begin{pmatrix} \gamma E_B^* \\ \gamma\beta E_B^* \\ 0 \\ -E_B^* \end{pmatrix}$$

As expected for any Lorentz transformation, the centre-of-mass energy of the collision is still $\sqrt{s} = 2E_B^*$.

In the laboratory frame, an incoming particle should have the angle α (i. e. half the crossing angle) with respect to the z -axis:

$$\frac{p_{1,x}}{p_{1,z}} = \gamma\beta \stackrel{!}{=} \tan \alpha$$

Using $1 - \beta^2 = 1/\gamma^2$, this condition fixes the transformation parameters:

$$\gamma\beta = \tan \alpha, \quad \gamma = \sqrt{1 + \tan^2 \alpha}$$

Since the Lorentz transformation applies to the whole coordinate frame (and not only a single incoming or outgoing particle), the four-momentum of any particle in the laboratory frame can be expressed as:

$$p = \begin{pmatrix} E \\ p_x \\ p_y \\ p_z \end{pmatrix} = \Lambda_x p^* = \begin{pmatrix} E^* \sqrt{1 + \tan^2 \alpha} + p_x^* \tan \alpha \\ p_x^* \sqrt{1 + \tan^2 \alpha} + E^* \tan \alpha \\ p_y^* \\ p_z^* \end{pmatrix}$$

It should be noted that the transformation parameters γ and $\gamma\beta$ depend neither on the properties of the individual particles nor on the beam energy, but only on the angle. It should also be noted that, in order to keep the centre-of-mass energy constant, the beam energy in the laboratory frame only needs to be increased by a tiny amount, which is actually smaller than the energy spread of the accelerator itself:

$$\begin{aligned} \frac{E_B}{E_B^*} &= \gamma = \sqrt{1 + \tan^2 \alpha} \approx 1 + \frac{1}{2}\alpha^2 \\ &\approx 1.000025 \quad \text{for } \alpha = 7 \text{ mrad} \end{aligned}$$

The surplus energy gets used up to boost all products of the interaction in x -direction.

E.3 Implementation

In Mokka, the Lorentz transformation Λ_x can be applied to all primary particles (originating from whatever data source) immediately before starting the simulation of an event. The angle α (half the crossing angle, as above) can be set using the command `/Mokka/init/lorentzTransformationAngle` in the Mokka steering file. In the current implementation, the vertex positions (which are anyway neglected by Geant4 in many cases) are not transformed.

List of Figures

1.1	Fermions in the Standard Model	11
1.2	Bosons in the Standard Model	12
1.3	Forces in the Standard Model	13
2.1	The Livingston plot	20
2.2	Higgs boson coupling constants	21
2.3	Schematic layout of the ILC	23
2.4	Bunch structure of the ILC	24
2.5	Crab crossing	26
3.1	Illustration of the pinch effect	31
3.2	Energy spectrum of electron-positron pairs	33
3.3	Polar angle and transverse momentum of pairs	33
3.4	Number of pairs for different beam parameter sets	33
3.5	Sketch of pairs inside the detector	35
4.1	Quadrant of the Large Detector Concept	43
5.1	Schematic layout of a TPC	47
5.2	Basic principle of a TPC	48
5.3	Energy loss in the ALEPH TPC	49
5.4	Geometry of a standard CERN GEM	54
5.5	Photo of a standard CERN GEM	54
5.6	Working principle of a GEM foil	55
5.7	Collection, gain, and extraction of a GEM	56
5.8	Geometry of a Micromegas	57
5.9	Ion backdrift in a TPC	58
5.10	Working principle of gating wires	59
5.11	Charge sharing on the anode pads	63
6.1	Central region of the simulated detector geometry	68
6.2	Forward region of the simulated detector geometry	68
6.3	Geometry of the simulated beam tube	70
6.4	Geometry of the simulated forward mask	70
6.5	Forward region with magnetic field lines, anti-DID	71
7.1	Distribution of the number of hits on the VTX, layer 1	81
7.2	Distribution of the number of hits on the VTX, layer 5	81
7.3	Hits on the vertex detector, absolute	82
7.4	Hits on the vertex detector, normalised	82
7.5	Time distribution of VTX hits	85
7.6	Azimuthal distribution of VTX hits, layer 1	86
7.7	Longitudinal distribution of VTX hits, layer 1	86
7.8	Azimuthal distribution of VTX hits, layer 5	86
7.9	Longitudinal distribution of VTX hits, layer 5	86

7.10	Electrons and positrons traversing the VTX, absolute	89
7.11	Electrons and positrons traversing the VTX, normalised	89
7.12	Origins of electrons and positrons in the VTX	90
7.13	Energy distribution of electrons and positrons in the VTX	90
7.14	Photons traversing the VTX, absolute	91
7.15	Photons traversing the VTX, normalised	91
7.16	Origins of photons traversing the VTX	92
7.17	Energy distribution of photons traversing the VTX	92
7.18	Origins of neutrons traversing the VTX	93
7.19	Energy distribution of neutrons traversing the VTX	93
7.20	Neutron-induced displacement damage in silicon	94
7.21	Hits on the SIT, absolute	96
7.22	Hits on the SIT, normalised	96
7.23	Hits on the FTDs, absolute	96
7.24	Hits on the FTDs, normalised	96
7.25	Radial distribution of hits on the FTDs	97
7.26	Time distribution of hits on the FTDs	97
7.27	Origins of neutrons in the TPC	99
7.28	Energy distribution of neutrons in the TPC, origin	100
7.29	Energy distribution of neutrons in the TPC, entry	100
7.30	Origins of photons in the TPC	101
7.31	Energy distribution of photons in the TPC	101
7.32	BeamCal position and backscattering into the TPC	102
7.33	Energy distribution of electrons in the TPC	103
7.34	Energy distribution of protons in the TPC	103
7.35	Measured cross-section for neutron-proton scattering	104
7.36	Mokka hits in the TPC, front view	105
7.37	Mokka hits in the TPC, side view	105
7.38	Radial distribution of hits in the TPC	106
7.39	Radius-vs.-time distribution of hits in the TPC	107
7.40	Time distribution of hits in the TPC	107
7.41	Relative TPC occupancy for different voxel sizes	108
7.42	Influence of hit structures on the occupancy variation	110
7.43	Local relative TPC occupancy per pad row	111
7.44	Distribution of the primary charge per TPC voxel	112
7.45	Primary charge density in the TPC volume	112
7.46	Energy distribution of neutrons in the HCAL, $r = 300$ mm	114
7.47	Energy distribution of neutrons in the HCAL, $r = 900$ mm	114
7.48	Neutron fluence in the HCAL endcaps	115
7.49	Simulated forward region, TESLA TDR	116
7.50	Simulated forward region, layout of 2004	116

7.51	VTX hits for different crossing angles and fields	119
7.52	Energy distribution on the BeamCal for anti-DID and DID . . .	120
7.53	Forward region with magnetic field lines, DID	121
7.54	Forward region with decreased inner LumiCal radius	121
7.55	Hits on the innermost FTD, anti-DID field	122
7.56	Hits on the innermost FTD, DID field	122
7.57	Hits on the VTX for different beam parameters, absolute . . .	124
7.58	Hits on the VTX for different beam parameters, normalised . .	124
7.59	Backscattering in the LumiCal for $r = 80$ mm, front view . . .	126
7.60	Backscattering in the LumiCal for $r = 80$ mm, top view	126
7.61	Backscattering in the LumiCal for $r = 60$ mm, front view . . .	126
7.62	Backscattering in the LumiCal for $r = 60$ mm, top view	126
7.63	Hits on the VTX for different BeamCal absorbers	127
7.64	Energy distribution of neutrons in the VTX, LHEP_BERT_HP . . .	130
7.65	Energy distribution of neutrons in the VTX, LHEP_BIC_HP . . .	130
9.1	Radial charge distribution in an ion disc	140
B.1	Geometry of the simulated vertex detector	147
B.2	Possible segmentations of the TPC volume	151
B.3	B_z -component of the main solenoid field	155
B.4	B_x -component of the superimposed anti-DID field	155

List of Tables

2.1	ILC beam parameter sets	28
4.1	Comparison of the four ILC detector concepts	39
7.1	Neutron fluence in the VTX	95
7.2	Particles in the TPC	98
7.3	Particles in the TPC for different forward regions	118
7.4	Particles in the TPC for different magnetic fields	123
7.5	Particles in the TPC for decreasing inner LumiCal radii	125
7.6	Particles in the HCAL endcaps for different support tubes	128
7.7	Particles in the TPC for different physics lists	131
7.8	Particles in the TPC for different CH ₄ contents	132
A.1	Guinea-Pig \$ACCELERATOR settings for ILC-NOM-500	143
A.2	Guinea-Pig \$PARAMETERS settings for pairs	144
B.1	Composition of the rest gas in the beam tube	147
B.2	Geometry of the vertex detector	148
B.3	Geometry of the Silicon Intermediate Tracker	148
B.4	Geometry of the Forward Tracking Discs	149
D.1	Geometry of the simulated beam tube	169
D.2	Geometry of the simulated forward mask	170
D.3	Geometry of the simulated magnetic field	170

Bibliography

- [1] Particle Data Group, Wei-Ming Yao, et al. Review of Particle Physics. *J. Phys.*, G33, 2006.
- [2] Murray Gell-Mann. A schematic model of baryons and mesons. *Phys. Lett.*, 8:214–215, 1964.
- Harald Fritzsch, Murray Gell-Mann, and Heinrich Leutwyler. Advantages of the color octet gluon picture. *Phys. Lett.*, B47:365–368, 1973.
- [3] Sheldon Lee Glashow. Partial symmetries of weak interactions. *Nucl. Phys.*, 22(4):579–588, February 1961.
- Steven Weinberg. A model of leptons. *Phys. Rev. Lett.*, 19(21):1264–1266, November 1967.
- Abdus Salam. Weak and electromagnetic interactions. In Nils Svartholm, editor, *Elementary Particle Theory*, pages 367–377, Stockholm, Sweden, 1968. Almquist and Wiksell. Proceedings of the 1968 Nobel Symposium, Lerum, Sweden.
- [4] Peter W. Higgs. Broken symmetries, massless particles and gauge fields. *Phys. Lett.*, 12:132–133, September 1964.
- Peter W. Higgs. Broken symmetries and the masses of gauge bosons. *Phys. Rev. Lett.*, 13(16):508–509, October 1964.
- François Englert and Robert Brout. Broken symmetry and the mass of gauge vector mesons. *Phys. Rev. Lett.*, 13(9):321–323, August 1964.
- Gerald S. Guralnik, Carl R. Hagen, and Thomas W. B. Kibble. Global conservation laws and massless particles. *Phys. Rev. Lett.*, 13(20):585–587, November 1964.
- [5] LEP Working Group for Higgs boson searches, Robert Barate, et al. Search for the Standard Model Higgs boson at LEP. *Phys. Lett.*, B565:61–75, 2003. hep-ex/0306033.
- [6] The LEP Electroweak Working Group. Constraint on the mass of the Higgs boson. LEPEWWG Web Site, 2008. <http://cern.ch/LEPEWWG/>.
- [7] Thomas Hambye and Kurt Riesselmann. Matching conditions and Higgs mass upper bounds revisited. *Phys. Rev.*, D55:7255–7262, 1997. hep-ph/9610272.

- [8] TriTertButoxy. Elementary particle interactions. Provided on the Wikimedia Commons, February 2008. http://commons.wikimedia.org/wiki/Image:Elementary_particle_interactions.svg.
- [9] The LEP Collaborations ALEPH, DELPHI, L3, OPAL, the LEP Electroweak Working Group, and the SLD Electroweak and Heavy Flavour Groups. A combination of preliminary electroweak measurements and constraints on the Standard Model. hep-ex/0412015, 2004.
- [10] WMAP Collaboration, David N. Spergel, et al. Wilkinson Microwave Anisotropy Probe (WMAP) three year results: Implications for cosmology. *Astrophys. J. Suppl.*, 170:377, 2007. astro-ph/0603449.
- [11] Benjamin W. Lee, Chris Quigg, and Harry B. Thacker. Weak interactions at very high energies: The role of the Higgs-boson mass. *Phys. Rev.*, D16:1519–1531, September 1977.
- [12] Julius Wess and Bruno Zumino. Supergauge transformations in four dimensions. *Nucl. Phys.*, B70:39–50, 1974.
Pierre Fayet and Sergio Ferrara. Supersymmetry. *Phys. Rept.*, 32:249–334, 1977.
- [13] John R. Ellis, John S. Hagelin, Dimitri V. Nanopoulos, Keith A. Olive, and Mark Srednicki. Supersymmetric relics from the Big Bang. *Nucl. Phys.*, B238:453–476, 1984.
- [14] Hans Peter Nilles. Supersymmetry, supergravity and particle physics. *Phys. Rept.*, 110:1–162, 1984.
- [15] Theodor Kaluza. Zum Unitätsproblem der Physik. *Sitzungsberichte der Preußischen Akademie der Wissenschaften*, pages 966–972, 1921.
Oskar Klein. Quantentheorie und fünfdimensionale Relativitätstheorie. *Z. Physik*, 37:895–906, 1926.
- [16] Lisa Randall and Raman Sundrum. A large mass hierarchy from a small extra dimension. *Phys. Rev. Lett.*, 83:3370–3373, 1999.
- [17] JoAnne L. Hewett and Thomas G. Rizzo. Low-energy phenomenology of superstring-inspired E_6 models. *Phys. Reports*, 183:193–381, November 1989.
Paul Langacker, Mingxing Luo, and Alfred K. Mann. High-precision electroweak experiments: A global search for new physics beyond the Standard Model. *Rev. Mod. Phys.*, 64(1):87, January 1992.

- [18] Steven Weinberg. Implications of dynamical symmetry breaking. *Phys. Rev.*, D13:974–996, 1976.
- Steven Weinberg. Implications of dynamical symmetry breaking: An addendum. *Phys. Rev.*, D19:1277–1280, 1979.
- Leonard Susskind. Dynamics of spontaneous symmetry breaking in the Weinberg-Salam theory. *Phys. Rev.*, D20:2619–2625, 1979.
- [19] Wilfried Buchmüller, Reinhold Rückl, and Daniel Wyler. Leptoquarks in lepton quark collisions. *Phys. Lett.*, B191:442–448, 1987.
- [20] Oliver Brüning (ed.) et al. LHC Design Report, Volume I: The LHC Main Ring. Technical Report CERN-2004-003-V-1, CERN, June 2004.
- [21] Stefano Catani et al. QCD. hep-ph/0005025, May 2000.
- [22] Ian Hinchliffe and Paula Eerola (eds.). ATLAS Detector and Physics Performance Technical Design Report, Volume II. Technical Report CERN/LHCC-99-15, CERN, May 1999.
- Genrikh L. Bayatian et al. CMS Technical Design Report, Volume II: Physics Performance. *J. Phys.*, G34:995–1579, 2007.
- [23] Rolf-Dieter Heuer, David Miller, François Richard, and Peter Zerwas (eds.). TESLA Technical Design Report, Part III: Physics at an e^+e^- Linear Collider. Technical Report DESY-2001-011, DESY, March 2001.
- [24] Gudrid A. Moortgat-Pick et al. The role of polarized positrons and electrons in revealing fundamental interactions at the Linear Collider. *Phys. Rept.*, 460:131–243, May 2008. hep-ph/0507011.
- [25] Geoffrey T. J. Arnison et al. Experimental observation of isolated large transverse energy electrons with associated missing energy at $\sqrt{s} = 540$ GeV. *Phys. Lett.*, B122:103–116, February 1983.
- Paolo Bagnaia et al. Evidence for $Z^0 \rightarrow e^+e^-$ at the CERN $\bar{p}p$ collider. *Phys. Lett.*, B129:130–140, September 1983.
- [26] Gideon Alexander et al. Measurement of the Z^0 line shape parameters and the electroweak couplings of charged leptons. *Z. Phys.*, C52:175–208, 1991.
- [27] Tor Raubenheimer (ed.). Zeroth-Order Design Report for the Next Linear Collider. Technical Report SLAC-R-0474-VOL-1, SLAC, 1996.

- Nan Phinney (ed.). 2001 report on the Next Linear Collider: A report submitted to Snowmass 2001. In *APS/DPF/DPB Summer Study on the Future of Particle Physics, Snowmass, CO, USA*, July 2001. SLAC-R-571.
- [28] Rasmus Ischebeck. Accelerator physics media gallery. <http://tesla.desy.de/~rasmus/media/>.
- [29] Koya Abe et al. GLC Project: Linear Collider for TeV Physics. Technical Report KEK-Report-2003-7, KEK, September 2003.
- [30] Abdelhak Djouadi, Joseph Lykken, Klaus Mönig, Yasuhiro Okada, Mark Oreglia, and Satoru Yamashita (eds.). ILC Reference Design Report, Volume 2: Physics at the ILC. Technical Report ILC-REPORT-2007-001, ILC Global Design Effort and World-Wide Study, August 2007.
- [31] Georg Weiglein et al. Physics interplay of the LHC and the ILC. *Phys. Rept.*, 426:47–358, 2006. hep-ph/0410364.
- [32] The CDF Collaboration, F. Abe, et al. Observation of top quark production in $\bar{p}p$ collisions. *Phys. Rev. Lett.*, 74:2626–2631, March 1995. hep-ex/9503002.
- The D0 Collaboration, Shahriar Abachi, et al. Observation of the top quark. *Phys. Rev. Lett.*, 74:2632–2637, March 1995. hep-ex/9503003.
- [33] John David Jackson. *Classical Electrodynamics*. John Wiley & Sons, third edition, December 1998.
- [34] Reinhard Brinkmann, Klaus Flöttmann, Jörg Roßbach, Peter Schmüser, Nicholas Walker, and Hans Weise (eds.). TESLA Technical Design Report, Part II: The Accelerator. Technical Report DESY-2001-011, DESY, March 2001.
- [35] Ties Behnke, Sergio Bertolucci, Rolf-Dieter Heuer, and Ronald Dean Settles. TESLA Technical Design Report, Part IV: A Detector for TESLA. Technical Report DESY-2001-011, DESY, March 2001.
- [36] World Wide Study Group for the Physics and Detectors for the Linear Collider. Understanding matter, energy, space and time: The case for the Linear Collider, April 2003. http://physics.uoregon.edu/~lc/wwstudy/lc_consensus.pdf.

- [37] James Brau, Yasuhiro Okada, and Nicholas Walker (eds.). ILC Reference Design Report, Volume 1: Executive Summary. Technical Report ILC-REPORT-2007-001, ILC Global Design Effort and World-Wide Study, August 2007.
- [38] Nan Phinney, Nobukasu Toge, and Nicholas Walker (eds.). ILC Reference Design Report, Volume 3: Accelerator. Technical Report ILC-REPORT-2007-001, ILC Global Design Effort and World-Wide Study, August 2007.
- [39] Ties Behnke, Chris Damerell, John Jaros, and Akiya Miyamoto (eds.). ILC Reference Design Report, Volume 4: Detectors. Technical Report ILC-REPORT-2007-001, ILC Global Design Effort and World-Wide Study, August 2007.
- [40] Olivier Napoly. The luminosity for beam distributions with error and wake field effects in linear colliders. *Part. Accel.*, 40:181–203, 1993.
- [41] US Linear Collider Steering Group. Accelerator Technology Options Report, March 2004. <http://www.slac.stanford.edu/xorg/accelops/>.
- [42] Tor Raubenheimer. Suggested ILC beam parameter range, February 2005. <http://www-project.slac.stanford.edu/ilc/acceldev/beampar/SuggestedILCBeamParameterSpace.pdf>.
- [43] Fumio Furuta et al. Experimental comparison at KEK of high-gradient performance of different single-cell superconducting cavity designs. In *Proceedings of the European Particle Accelerator Conference (EPAC 2006), Edinburgh, United Kingdom*, pages 750–752, June 2006.
- [44] Hasan Padamsee, Jens Knobloch, and Tomas Hays. *RF Superconductivity for Accelerators*. Wiley-VCH, Berlin, Germany, second edition, January 2008.
- [45] Gilbert Guignard (ed.). A 3 TeV e^+e^- linear collider based on CLIC technology. Technical Report CERN-2000-008, CERN, July 2000.
- [46] Particle Physics Project Prioritization Panel (P5). US particle physics: Scientific opportunities – A strategic plan for the next ten years, May 2008. http://www.er.doe.gov/hep/HEPAP/reports/P5_Report06022008.pdf.

- Robert B. Palmer. Muon colliders. Talk given at the P5 Meeting, Brookhaven, NY, USA, March 2008. http://www.bnl.gov/npp/p5_bnl_agenda.asp.
- [47] CERN. LEP Design Report, Volume 2: The LEP Main Ring. Technical Report CERN-LEP-84-01, CERN, June 1984.
- [48] Kaoru Yokoya. A computer simulation code for the beam-beam interaction in linear colliders. Technical Report KEK-Report-85-9, KEK, October 1985.
- [49] Kaoru Yokoya and Pisin Chen. Beam-beam phenomena in linear colliders. *Lect. Notes Phys.*, 400:415–445, 1992.
- [50] Daniel Schulte. *Study of Electromagnetic and Hadronic Background in the Interaction Region of the TESLA Collider*. Doctoral thesis, Universität Hamburg, Germany, 1996. TESLA 1997-08.
- [51] Marco Venturini and Witold Kozanecki. The hourglass effect and the measurement of the transverse size of colliding beams by luminosity scans. In *Proceedings of IEEE Particle Accelerator Conference (PAC 2001), Chicago, IL, USA*, pages 3573–3575, June 2001. SLAC-PUB-8699.
- [52] Olivier Napoly. Collimation depth requirements for the TESLA interaction region. Technical Report DAPNIA/SEA-01-02, DAPNIA, February 2001.
- Frank Jackson. Effect of MDI design on BDS collimation depth. Talk given at the 9th ACFA ILC Physics & Detector Workshop & ILC GDE Meeting (BILCW 2007), Beijing, China. <http://ilcagenda.linearcollider.org/contributionDisplay.py?confId=1212&contribId=216>.
- [53] Gregor Wagner. Neutron background studies at the TESLA collider. Technical Report LC-DET-2001-048, LC Note, January 2001.
- [54] Pisin Chen. Disruption, beamstrahlung and beamstrahlung pair creation. In *DPF Summer Study 1988, Snowmass, CO, USA*, June 1988.
- [55] M. S. Zolotarev, E. A. Kuraev, and V. G. Serbo. Estimates of electromagnetic background processes for the VLEPP project. Translated from Russian as SLAC-TRANS-0227, June 1987.

- [56] Cécile Rimbault, Philip Bambade, Klaus Mönig, and Daniel Schulte. Incoherent pair generation in a beam-beam interaction simulation. *Phys. Rev. ST Accel. Beams*, 9(3):034402, March 2006.
- [57] Stephan Gronenborn. Study of pair background due to beamstrahlung for different ILC parameter sets. Technical Report EUROTeV-Memo-2005-003-1, EUROTeV, September 2005.
- [58] Carsten Hensel. Beam-induced background at a TESLA detector. Technical Report LC-DET-2000-001, LC Note, January 2000.
Carsten Hensel. *Search for Nearly Mass-Degenerate Charginos and Neutralinos in e^+e^- Collisions*. Doctoral thesis, Universität Hamburg, Germany, December 2002. DESY-THESIS-2002-047.
- [59] Timothy Barklow. Update on $\gamma\gamma \rightarrow$ hadrons calculation. Talk given at the ALCPG Winter Workshop 2004, Stanford, CA, USA, January 2004. <http://www-conf.slac.stanford.edu/alcp04/WorkingGroups/BeamDeliveryInteractionRegion/index.html>.
- [60] Martin Sachwitz and Hans-Jürgen Schreiber. Muon background in the 500 GeV TESLA linear collider. Technical Report TESLA-1994-27, DESY, 1994.
Dmitri S. Denisov et al. Machine-related backgrounds in the SiD detector at ILC. hep-ex/0608001, December 2006.
Alexander I. Drozhdin, Nikolai V. Mokhov, Noriaki Nakao, Sergei I. Striganov, and Lewis Keller. Suppression of muon backgrounds generated in the ILC beam delivery system. In *Proceedings of the Particle Accelerator Conference (PAC 2007)*, Albuquerque, NM, USA, pages 2945–2947, June 2007.
- [61] Ilya Agapov, Grahame Blair, John Carter, and Olivier Dadoun. The BDSIM toolkit. Technical Report EUROTeV-Report-2006-014-1, EUROTeV, March 2006.
BDSIM web site. <https://twiki.pp.rhul.ac.uk/twiki/bin/view/JAI/Simulation>.
- [62] John Carter, Ilya Agapov, Grahame Blair, and Olivier Dadoun. International Linear Collider simulations using BDSIM. *Pramana*, 69(6):1133–1136, December 2007.

- [63] LDC Working Group, Danuta Kisielewska, et al. Detector Outline Document for the Large Detector Concept, August 2006. <http://www.ilcldc.org/documents/dod/>.
- [64] LDC web site. <http://www.ilcldc.org>.
- [65] The SiD Concept Group. SiD Detector Outline Document, May 2006. <http://hep.uchicago.edu/~oreglia/siddod.pdf>.
SiD web site. <http://silicondetector.org>.
- [66] GLD Concept Study Group, Koya Abe, et al. GLD Detector Outline Document. physics/0607154, July 2006.
GLD web site. <http://ilcphys.kek.jp/gld/>.
- [67] The 4th Concept Group, Patrick Le Du, et al. Detector Outline Document for the Fourth Concept Detector (“4th”) at the International Linear Collider, 2006. <http://www.4thconcept.org/4doc.pdf>.
Fourth Concept web site. <http://www.4thconcept.org>.
- [68] ILD web site. <http://www.ilcild.org>.
- [69] ILD optimisation web site. <http://www-flc.desy.de/ldcoptimization/>.
- [70] Koya Abe et al. Design and performance of the SLD vertex detector: A 307 megapixel tracking system. *Nucl. Instrum. Meth.*, A400:287–343, 1997.
- [71] Vasilij L. Morgunov. Calorimetry design with energy flow concept. In *Proceedings of the 10th International Conference on Calorimetry in High Energy Physics (CALOR 2002), Pasadena, CA, USA*, pages 70–84, March 2002.
- [72] Jean-Claude Brient. Improving the jet reconstruction with the particle flow method: An introduction. In *Proceedings of the 11th International Conference on Calorimetry in High-Energy Physics (Calor 2004), Perugia, Italy*, pages 445–451, April 2004.
- [73] Mark Andrew Thomson. Particle flow calorimetry at the ILC. *AIP Conf. Proc.*, 896:215–224, March 2007.
- [74] Christian Grah. Fast and precise luminosity measurement at the ILC. Technical Report EUROTeV-Report-2006-095, EUROTeV, September 2007.

- [75] Christian Grah and Andrey Saprosov. Fast luminosity measurement and beam parameter determination. Technical Report EUROTTeV-Report-2007-006, EUROTTeV, October 2007.
- [76] Brett Parker and Andrei Seryi. Compensation of the effects of a detector solenoid on the vertical beam orbit in a linear collider. *Phys. Rev. ST Accel. Beams*, 8(4):041001, April 2005.
- [77] Brett Parker et al. The superconducting magnets of the ILC beam delivery system. In *Proceedings of the Particle Accelerator Conference (PAC 2007)*, Albuquerque, NM, USA, pages 3196–3198, June 2007.
- [78] Andrei Seryi, Takashi Maruyama, and Brett Parker. IR optimization, DID and anti-DID. In *Proceedings of the 36th ICFA Advanced Beam Dynamics Workshop (Nanobeam 2005)*, Kyoto, Japan, October 2005. SLAC-PUB-11662.
- [79] Andrei Seryi. Discussion of anti-DID (“DIDNT?”). Web Page of the SLAC Beam Delivery Meeting on 2005-09-27, September 2005. <http://www-project.slac.stanford.edu/lc/bdir/Meetings/beamdelivery/2005-09-27/index.htm>.
- [80] David R. Nygren. The Time Projection Chamber: A new 4π detector for charged particles. In *Proceedings of the 1974 PEP Summer Study*, Berkeley, CA, USA, pages 58–78, 1975. PEP-0144.
- [81] Walter Blum and Luigi Rolandi. *Particle Detection with Drift Chambers*. Springer, Berlin, Germany, 1993.
- [82] William R. Leo. *Techniques for Nuclear and Particle Physics Experiments*. Springer, Berlin, Germany, second edition, 1994.
- [83] Christopher K. Bowdery, editor. *ALEPH Handbook*, volume 1. CERN, second edition, 1995.
- [84] The ALEPH Collaboration, Damir Buskulic, et al. Performance of the ALEPH detector at LEP. *Nucl. Instrum. Meth.*, A360:481–506, 1995.
- [85] Lev Davidovich Landau. On the energy loss of fast particles by ionisation. *J. Phys. USSR*, 8:201, 1944.
P. V. Vavilov. Ionisation losses of high-energy particles. *Sov. Phys. JETP*, 5:749–751, 1957.

- Stephen M. Seltzer and Martin J. Berger. Energy loss straggling and of protons and mesons: Tabulations of the Vavilov distribution. *National Academy of Sciences Publication, Nuclear Science Series Report*, 39:1133, 1964.
- [86] Thomas Lohse and Werner Witzeling. The Time Projection Chamber. In Fabio Sauli, editor, *Instrumentation in High Energy Physics*, chapter 2. World Scientific, Singapore, 1992.
- [87] Anna Peisert and Fabio Sauli. Drift and diffusion of electrons in gases: A compilation. Technical Report CERN-84-08, CERN, July 1984.
- [88] Carl Ramsauer. Über den Wirkungsquerschnitt der Gasmoleküle gegenüber langsamen Elektronen. *Annalen der Physik*, 369:513–540, 1921.
- [89] M. Alfonsi et al. Aging measurements on triple-GEM detectors operated with CF₄-based gas mixtures. *Nucl. Phys. Proc. Suppl.*, 150:159–163, January 2006.
- [90] Vasiliy Morgunov. Neutron background at TPC. Talk given at the 5th ECFA-DESY Linear Collider Workshop, Obernai, France, October 1999. <http://ireswww.in2p3.fr/ires/ecfadesy/talks/morgunov/morgunov.html>.
- [91] Fabio Sauli. GEM: A new concept for electron amplification in gas detectors. *Nucl. Instrum. Meth.*, A386:531–534, 1997.
- [92] CERN Gas Detectors Development group (GDD) web site. <http://cern.ch/gdd/>.
- [93] Blanka Sobloher. Simulationsstudien zu GEM-Folien für die Auslese einer TPC. Diploma thesis, RWTH Aachen, Germany, March 2002.
- [94] Sven Lotze. *Ion Backdrift Minimisation in a GEM-Based TPC Readout*. Doctoral thesis, RWTH Aachen, Germany, April 2006.
- [95] Yannis Giomataris, Philippe C. Rebourgeard, Jean Pierre Robert, and Georges Charpak. Micromegas: A high-granularity position-sensitive gaseous detector for high particle-flux environments. *Nucl. Instrum. Meth.*, A376:29–35, 1996.
- [96] Dean Karlen, Paul Poffenberger, and Gabe Rosenbaum. TPC performance in magnetic fields with GEM and pad readout. *Nucl. Instrum. Meth.*, A555:80–92, September 2005. physics/0509051.

- [97] Matthias Enno Janssen. *Performance Studies of a Time Projection Chamber at the ILC and Search for Lepton Flavour Violation at HERA II*. Doctoral thesis, Universität Hamburg, Germany, May 2008. DESY-THESIS-2008-011.
- [98] Dennis C. Arogancia et al. Study in a beam test of the resolution of a Micromegas TPC with standard readout pads. 0705.2210, May 2007. Submitted to Nucl. Instrum. Meth.
- [99] Amos Breskin, Georges Charpak, S. Majewski, F. Mathy, G. Melchart, Anna Peisert, G. Petersen, and Fabio Sauli. High-flux operation of the gated multistep avalanche chamber. *Nucl. Instrum. Meth.*, 178:11–25, December 1980.
- [100] Rainer Mankel. Pattern recognition and event reconstruction in particle physics experiments. *Rept. Prog. Phys.*, 67:553, 2004. physics/0402039.
- [101] Ralf Diener. Study of reconstruction methods for a Time Projection Chamber with GEM gas amplification system. Diploma thesis, Universität Hamburg, Germany, May 2006. DESY-THESIS-2006-040.
- [102] Madhu S. Dixit, Jacques Dubeau, Jean-Pierre Martin, and Kirsten Sachs. Position sensing from charge dispersion in micro-pattern gas detectors with a resistive anode. *Nucl. Instrum. Meth.*, A518:721–727, February 2004. physics/0307152.
- [103] Robert L. Glückstern. Uncertainties in track momentum and direction, due to multiple scattering and measurement errors. *Nucl. Instrum. Meth.*, 24:381–389, 1963.
- [104] Guinea-Pig web site. http://www-project.slac.stanford.edu/lc/bdir/programs/guinea_pig/gp_index.html.
- [105] P. Chen, G. Horton-Smith, T. Ohgaki, A. W. Weidemann, and K. Yokoya. CAIN: Conglomerat d’ABEL et d’Interactions Nonlinéaires. *Nucl. Instrum. Meth.*, A355:107–110, 1995.
- [106] F. A. Berends, P. H. Daverveldt, and R. Kleiss. Monte Carlo simulation of two-photon processes. *Comput. Phys. Commun.*, 40:309, June 1986.
- [107] Paulo Mora de Freitas and Henri Videau. Detector simulation with Mokka and Geant4: Present and future. Technical Report LC-TOOL-2003-010, LC Note, March 2003.
Mokka web site. <http://mokka.in2p3.fr>.

- [108] The Geant4 Collaboration, Stefano Agostinelli, et al. Geant4: A simulation toolkit. *Nucl. Instrum. Meth.*, A506:250–303, 2003.
- The Geant4 Collaboration, John Allison, et al. Geant4 developments and applications. *IEEE Trans. Nucl. Sci.*, 53:270–278, February 2006.
- [109] Geant4 web site. <http://cern.ch/geant4/>.
- [110] Ties Behnke, Grahame Blair, Markus Elsing, Klaus Mönig, and Martin Pohl. BRAHMS: A Monte Carlo for a detector at a 500/800 GeV linear collider. Technical Report LC-TOOL-2001-005, LC Note, January 2001.
- BRAHMS web site. http://www-zeuthen.desy.de/lc_repository/detector_simulation/dev/BRAHMS/.
- [111] René Brun, Francis Bruyant, Michel Maire, Andy C. McPherson, and Pietro Zancarini. GEANT3. Technical Report CERN-DD/EE/84-1, CERN, September 1987.
- GEANT3 web site. <http://cern.ch/wwasd/geant/>.
- [112] Jupiter web site. <http://acfahep.kek.jp/subg/sim/simtools/>.
- [113] SLIC web site. <http://www.lcsim.org/software/slic/>.
- [114] Ties Behnke. LDC version 2, February 2006. http://www.ilcldc.org/documents/dod/lcdv2_23022006.pdf.
- [115] Olivier Delferrière. Private Communication.
- [116] Andrei Seryi. Anti-DID field map for LDC. Web Page of the SLAC Beam Delivery Meeting on 2005-10-04, October 2005. <http://www-project.slac.stanford.edu/lc/bdir/Meetings/beamdelivery/2005-10-04/index.htm>.
- [117] Dennis Wright. Linear collider physics list, March 2005. http://www.slac.stanford.edu/comp/physics/geant4/slac_physics_lists/ilc/ilc_physics_list.html.
- [118] Hans-Peter Wellisch. Physics lists for linear collider neutron fluxes. Geant4 Web Site, October 2004. http://cern.ch/geant4/physics_lists/geant4.6.1/linear/.
- [119] Dennis Wright. Private Communication.
- Vasilij Morgunov. Private Communication.

- [120] Alexander Howard. Private Communication.
Alexander Howard. Final Geant4 benchmark comparison with TARC data. Talk given at the LCG Physics Validation Meeting for LHC Simulations on 2007-11-21, CERN, November 2007. <http://indico.cern.ch/conferenceDisplay.py?confId=22867>.
- [121] StdHep web site. <http://cepa.fnal.gov/psm/stdhep/>.
- [122] Frank Gaede. Marlin and LCCD: Software tools for the ILC. *Nucl. Instrum. Meth.*, A559:177–180, 2006.
Marlin web site. <http://ilcsoft.desy.de/marlin/>.
- [123] ILC Soft web site. <http://ilcsoft.desy.de>.
- [124] Norman A. Graf. Java Analysis Studio and Java-based reconstruction and analysis tools. In *Proceedings of the Linear Collider Workshop (LCWS 2002), Jeju, Korea, August 2002*.
JAS web site. <http://jas.freehep.org>.
- [125] Frank Gaede, Ties Behnke, Norman Graf, and Tony Johnson. LCIO, a persistency framework for Linear Collider simulation studies. Technical Report LC-TOOL-2003-053, LC Note, July 2003.
LCIO web site. <http://lcio.desy.de>.
- [126] René Brun and Fons Rademakers. ROOT: An object-oriented data analysis framework. *Nucl. Instrum. Meth.*, A389:81–86, 1997.
ROOT web site. <http://root.cern.ch>.
- [127] Jason Abernathy et al. MarlinTPC: A Marlin-based common TPC software framework for the LC-TPC collaboration. Technical Report LC-TOOL-2007-001, LC Note, September 2007.
MarlinTPC web site. <https://twiki.cern.ch/twiki/bin/view/ILCTPC/MarlinTPC>.
- [128] Uwe Renz. Development of a GEM-based gas detector with MediPix2 pixel readout. Diploma thesis, Universität Freiburg, Germany, 2007.
- [129] Carl Kesselman and Ian Foster. *The Grid: Blueprint for a New Computing Infrastructure*. Morgan Kaufmann, November 1998.
- [130] Ian Foster. What is the Grid? A three-point checklist, July 2002. <http://www-fp.mcs.anl.gov/~foster/Articles/WhatIsTheGrid.pdf>.

- [131] Jürgen Knobloch (ed.). LHC Computing Grid Technical Design Report. Technical Report CERN-LHCC-2005-024, CERN, June 2005. <http://cern.ch/lcg/tdr/>.
- [132] Yves Kemp. A National Analysis Facility at DESY. Talk given at the Open Session of the 65. Physics Review Committee, DESY, Hamburg, Germany. <https://indico.desy.de/conferenceDisplay.py?confId=865>.
- [133] Ringo Schmidt. Optimisation of a testbeam setup and background estimates for detectors at the ILC using Monte Carlo simulations. Diploma thesis, Brandenburgische Technische Universität Cottbus, Germany, August 2007.
- [134] Yasuhiro Sugimoto and Tadashi Nagamine. Fine-pixel CCD R&D in Japan. *ECONF*, C0508141:ALCPG1420, 2005.
- [135] LCFI Collaboration, Steve Worm, et al. Progress with vertex detector sensors for the International Linear Collider. *Nucl. Instrum. Meth.*, A582:839–842, 2007.
LCFI collaboration web site. <http://hepwww.rl.ac.uk/lcfi/>.
- [136] Jaap J. Velthuis et al. A DEPFET-based beam telescope with submicron precision capability. *IEEE Trans. Nucl. Sci.*, 55:662–666, 2008.
DEPFET collaboration web site. <http://www.depfet.org>.
- [137] Yan Li et al. CMOS sensors for the vertex detector of the future International Linear Collider. *Nucl. Instrum. Meth.*, A572:300–304, 2007.
CMOS MAPS collaboration web site. <http://www.iphc.cnrs.fr/-CMOS-ILC-.html>.
- [138] J. E. Brau, N. B. Sinev, D. M. Strom, C. Baltay, H. Neal, and D. Rabinowitz. Development of an ILC vertex detector sensor with single bunch crossing tagging. In *Proceedings of the Linear Collider Workshop (LCWS 2007)*, Hamburg, Germany, May 2007.
Chronopixel collaboration web site. <http://physics.uoregon.edu/~lc/ilcvxd/>.
- [139] Ringo Schmidt. Private Communication.

- [140] Gunnar Lindström and Angela Vasilescu. Displacement damage in silicon, online compilation, August 2000. <http://sesam.desy.de/members/gunnar/Si-dfuncs.html>.
- [141] P. J. Griffin, J. G. Kelly, T. F. Luera, and J. VanDenburg. SNL RML recommended dosimetry cross section compendium. Technical Report SAND92-0094, Sandia National Laboratories, November 1993. and Private Communication 1996.
- [142] A. Yu. Konobeyev, Yu. A. Korovin, and V. N. Sosnin. Neutron displacement cross-sections for structural materials below 800 MeV. *J. Nucl. Mater.*, 186:117, 1992.
- [143] M. Huhtinen and P. A. Aarnio. Pion-induced displacement damage in silicon devices. *Nucl. Instrum. Meth.*, A335:580–582, 1993. and Private Communication.
- [144] Marcel Vos. Private communication.
 Marcel Vos. Far forward tracking requirements for the ILC. Personal Web Pages, September 2007. <http://ific.uv.es/~vos/ilc/ilcFastForward/>.
- [145] Richard A. Arndt, William J. Briscoe, Ron L. Workman, and Igor I. Strakovsky. Center for Nuclear Studies, Data Analysis Center: Virginia Tech Partial-Wave Analysis Facility (SAID). <http://gwdac.phys.gwu.edu>.
- [146] Y. Fujita, K. Kobayashi, T. Oosaki, and R. C. Block. Measurement of the neutron-proton total cross section using 24 keV iron-filtered neutrons. *Nucl. Phys.*, A258:1–9, February 1976.
 C. E. Engelke, R. E. Benenson, E. Melkonian, and J. M. Lebowitz. Precision measurements of the n-p total cross-section at 0.4926 and 3.205 MeV. *Phys. Rev.*, 129:324–337, January 1963.
 J. M. Clement, P. Stoler, C. A. Goulding, and R. W. Fairchild. Hydrogen and deuterium total neutron cross sections in the MeV region. *Nucl. Phys.*, A183:51–59, March 1972.
 P. J. Clements and A. Langsford. On the monotonic variation of the n-p total cross-section with energy in the range 1.0 to 7.9 MeV. *Phys. Lett.*, B30:25–26, September 1969.

- [147] Ronaldo Bellazzini et al. Reading a GEM with a VLSI pixel ASIC used as a direct charge collecting anode. *Nucl. Instrum. Meth.*, A535:477–484, 2004. physics/0403019.
- [148] Mikhail Danilov. A scintillator tile hadron calorimeter prototype with a novel SiPM readout for ILC. In *Proceedings of the 11th Vienna Conference on Instrumentation (VCI 2007)*, Vienna, Austria, February 2007. <http://indico.cern.ch/sessionDisplay.py?confId=3062&sessionId=9>.
- [149] Toshinori Ikuno. MPPC radiation resistivity study. Talk given at the ACFA Physics and Detector Workshop (TILC 2008), Sendai, Japan, March 2008. <http://ilcagenda.linearcollider.org/sessionDisplay.py?confId=2432&sessionId=10>.
- [150] William M. Morse. GamCal – A beamstrahlung gamma detector for beam diagnostics. In *Proceedings of the Linear Collider Workshop (LCWS 2007)*, Hamburg, Germany, May 2007.
- [151] Karsten Büßer and Achim Stahl. Detector concept of the forward region. Technical Report LC-DET-2004-034, LC Note, November 2004.
- [152] P. Wanderer et al. Completion of superconducting magnet production at BNL for the HERA luminosity upgrade. *IEEE Trans. Appl. Supercond.*, 12:305–308, March 2002.
- Brett Parker. Recent progress designing compact superconducting final focus magnets for the ILC. In *Proceedings of the 36th ICFA Advanced Beam Dynamics Workshop (Nanobeam 2005)*, Kyoto, Japan, October 2005. BNL-75691-2006-CP.
- [153] Andrei Seryi. DID field map for LDC. Web Page of the SLAC Beam Delivery Meeting on 2005-07-26, July 2005. <http://www-project.slac.stanford.edu/lc/bdir/Meetings/beamdelivery/2005-07-26/index.htm>.
- [154] K. Peter Schüler. Private communication.
- [155] Peter Schade. Development and construction of a large TPC prototype for the ILC. In *Proceedings of the International School of Subnuclear Physics (ISSP 2007)*, Erice, Italy, August 2007.
- [156] Figures for the LDC version 2 forward region. Provided on the FCAL Web Site. <http://www-zeuthen.desy.de/ILC/fcal/pages/Figures.html>.

- FCAL web site. <http://www-zeuthen.desy.de/ILC/fcal/>.
- [157] Alberto Fassò, Alfredo Ferrari, Johannes Ranft, and Paola R. Sala. FLUKA: A multi-particle transport code. Technical Report CERN-2005-010, CERN, 2005.
- FLUKA web site. <http://www.fluka.org>.
- [158] Vasiliy Morgunov. Attempt to estimate the prediction power of the calorimeter properties following from different hadron models in the simulation programs; and the systematic errors of such predictions. Talk given at the 1st ECFA Workshop on Physics and Detectors for a Linear Collider, Montpellier, France, November 2003. http://www.desy.de/~morgunov/talks_articles/Mont_Soft.ps.gz.
- [159] Laurie S. Waters et al. The MCNPX Monte Carlo radiation transport code. *AIP Conf. Proc.*, 896:81–90, March 2007.
- MCNPX web site. <http://mcnp.x.lanl.gov>.
- [160] Karsten Büßer. Pair backgrounds in the Large Detector with realistic solenoid and DID fields. Talk given at the ILC Physics and Detector Workshop (ALCPG 2005), Snowmass, CO, USA, August 2005. <http://www.slac.stanford.edu/econf/C0508141/proc/ilcaw5.htm>.
- Yasuhiro Sugimoto. BCAL and pair background. Talk given at the ILC Physics and Detector Workshop (ALCPG 2005), Snowmass, CO, USA, August 2005. <http://www.slac.stanford.edu/econf/C0508141/proc/alcp17.htm>.
- Takashi Maruyama. Backgrounds. Talk given at the ILC Physics and Detector Workshop (ALCPG 2005), Snowmass, CO, USA, August 2005. <http://www.slac.stanford.edu/econf/C0508141/proc/alcp9.htm>.
- [161] Thorsten Krautscheid. Private Communication.
- [162] LCTPC Collaboration. TPC R&D for an ILC detector. Technical Report LC-DET-2007-005, LC Note, June 2007.
- LCTPC web site. <http://www.lctpc.org>.
- Dan Peterson. Personal web pages on the Linear Collider and the LP-TPC. http://www.lepp.cornell.edu/~dpp/linear_collider/.
- [163] EUDET web site. <http://www.eudet.org>.

- [164] Adrian Vogel. The coordinate system for LDC detector studies. Technical Report LC-DET-2005-009, LC Note, October 2005.
- [165] Annette Brenger, Kay Rehlich, and Kirsten Zapfe. The vacuum system for the TESLA beam delivery system. Technical Report TESLA-2001-14, DESY, 2001.
- [166] Igor B. Smirnov. Modeling of ionization produced by fast charged particles in gases. *Nucl. Instrum. Meth.*, A554:474–493, 2005.
HEED web site. <http://cern.ch/ismirnov/heed.html>.
- [167] The Geant4 Collaboration. Physics reference manual. <http://cern.ch/geant4/support/index.shtml>.
- [168] Mark Woodley. Beam optics for the ILC beam delivery systems, April 2006. <http://www.slac.stanford.edu/~mdw/ILC/2006b/>.

Acknowledgements

First, I wish to thank my supervisor *Prof. Dr. Joachim Mnich* for his support during the time of my work. He suggested the topic of this thesis and provided me with much freedom to accomplish my studies, at the same time never losing sight of the long-term goals. I also thank *Prof. Dr. Peter Schleper* and *Prof. Dr. Eckhard Elsen* for taking over the duties of the second referees, and *PD Dr. Michael Martins* for his willingness to act as the chairman of my defence.

I would like to express my gratitude to the group leader *Ties Behnke* for giving me the possibility to work in the FLC group at DESY.

I am particularly grateful to *Karsten Büßer*, who was always willing to support me with interesting discussions and valuable suggestions, broadening my view and keeping me up to date about the latest BDS and MDI topics. *Peter Wienemann* and *Roman Pöschl* helped me find my way into the simulation software. It was Peter the Great who seduced me to use the Grid right from the start, and Maître Roman guided me into the obscurities of Mokka. I thank *Andreas Gellrich* and the other Grid administrators with whom I had contact for their ever-friendly support. Without Andreas, I probably could not have used so many CPU cycles on Computing Elements and occupied so much disk space on Storage Elements.

I acknowledge the hospitality of the Geant4 group at CERN, especially *Alexander Howard*. It was a great experience to visit the Geant4 headquarters and to discuss with the experts in the flesh. I would like to thank *Dennis Wright*, *Olivier Delferrière*, *Andrei Seryi*, *Christian Grah*, *Steve Aplin*, *Hannes Jung*, *Ingrid-Maria Gregor*, *Felix Sefkow*, *Erika Garutti*, *Marcel Vos*, *Peter Schüler*, and others for the various kinds of support they provided – be it details on physics lists, magnetic field maps, discussions on forward detector geometries, TPC implementations, help in summoning Pythia, or valuable explanations about vertex detector technologies, calorimetry, forward tracking, and polarimetry. I particularly appreciate the long-standing interest that *Ron Settles* showed in my studies.

I thank Karsten for thoroughly proof-reading this thesis, *Philip Bechtle* for checking the theory-prone introductory section, and *Barbara Warmbein* for her profound and bountiful assistance regarding the English language and its subtleties.

Jörgen Samson never got tired to answer my questions about C++, the compiler, the linker, the library, the system, and life in general. Furthermore, *Jörgen*, *Benjamin Lutz*, and *Christian Helebrant* did their best to keep `f1c36` running smoothly, and *Oliver Wendt* and *Lea Hallermann* kept my `/data` safe from harm – thank you for your efforts, often going unnoticed.

It was good to have *Ramona Matthes* around, the true heart of the group and the one to confide. I enjoyed sharing the office with *Krzysztof Komar*, *Felix Stöver*, the artist, *Christian Grefe*, and *Bakul Gaur*, who provided a nice and friendly atmosphere to work, talk, share points of view, and learn some tiny bits of Polish. *Cześć!* *Thorsten Lux* gave me a warm welcome and it was fun to work together with him in the first weeks and months. I am certainly not enlightened yet, but at least I was able to get a remote idea of the Buddha-nature.

I am sincerely grateful to the TPC group as a whole – the people mentioned above and *Markus Ball*, *Jeannine Beck*, *Klaus Dehmelt*, *Ralf Diener*, *Lea Hallermann*, *Andreas Imhof*, *Matthias Enno Janssen*, *Alexander Kaukher*, *Diana Linzmaier*, *Peter Schade*, and *Oliver Schäfer* – for offering me a mental home, even though I have actually never been very much involved in their daily business. It has been a great pleasure to be a part of the FLC group, with many present and former members who have been not only colleagues, but also friends – you know who you are and what I esteem you for. I thank especially Matthias, my predecessor to be ground through the mills of PhD bureaucracy, for his helpful and reassuring hints in the final phase of my work, *Svenja Niehage*, who was a great companion in the very summer of 2006, *Blanka Sobloher* for offering a sound chat every now and then, and *Nanda Wattimena*, who would not only take me to the surging floods once a week, but who would also ease my mind like a bridge over troubled water.

Finally, I would like to thank all the people at home for not giving up on me even though I was far away most of the time, and – most importantly – my parents and the rest of my family for encouraging me at all times and supporting me in every possible way.